Photodynamic anticancer and antimicrobial activities of aza-BODIPY and porphyrin-based photosensitisers and their non-linear properties

A thesis submitted in fulfilment of the requirements

for the degree of

DOCTOR OF PHILOSOPHY

at

Rhodes University

by

Nthabeleng Molupe

January 2024

Abstract

New aza-BODIPY dyes and porphyrins were synthesised and characterised so that photodynamic therapy (PDT) and photodynamic antimicrobial chemotherapy (PACT) activity studies could be performed. Several strategies were explored to achieve targeted nanoplatforms or biocompatible nanoplatforms to enhance the suitability of these compounds for use in PDT. Following earlier MSc research on the encapsulation of halogenated boron dipyrromethene (BODIPY) dyes into Pluronic® micelles, similar nanomicelles were prepared to encapsulate halogenated boron aza-dipyrromethene (aza-BODPY) dyes to enhance their aqueous solubility. However, the 1,7-di-methylthiophenyl-2,6-diiodo-3,5-diphenyl (**1**) and 1,7-di-methylthiophenyl-2,6-diiodo-3,5-dithien-3-yl (**2**) aza-BODIPY dyes that were prepared in this context were found to degrade when encapsulated. A different strategy was then followed in which gold nanoparticles (AuNPs) were conjugated to **1** and **2** *via* Au-S interactions to form biocompatible aza-BODIPY-AuNP conjugates (**1-AuNP** and **2-AuNP**). This strategy was successful, and favourable IC_{50} values of 3.60 and 10.0 μM for **1-AuNP** and **2-AuNP** were obtained during *in vitro* PDT activity studies against MCF-7 human breast cancer cells, respectively, while values of 11.0 and 12.8 μM were obtained for **1** and **2**.

To further explore the preparation of better-targeted aza-BODIPY photosensitiser dyes, folic acid (FA) was conjugated to 1,7-dihydroxyphenyl-2,6-diiodo-3,5-di-4-bromophenyl (**3**) and 1,7-di-4-bromo-2,6-diiodo-3,5-dihydroxyphenylphenyl (**4**) aza-BODIPYs *via* ester bonds. Not only was the conjugation to form **3-FA** and **4-FA** successful, but the conjugated dyes are water-soluble, which is advantageous for drug transport in the context of PDT. These conjugates were applied *in vitro* against MCF-

7 cancer cells and were found to have relatively high activities with IC_{50} values of 0.91 and 7.48 μM for **3-FA** and **4-FA**, respectively, while values of 11.3 and 13.0 μM were obtained for the non-conjugated **3** and **4** dyes.

In a similar manner, tin (IV) and indium (III) tetrapyridylporphyrins (**5** and **6**) were axially conjugated to folic acid *via* ester bonds (**5-FA** and **6-FA**). The conjugation was successful and enhanced the PDT activities of the dyes MCF-7 cancer cells *in vitro* from 48.2 to 29.6 μM for **5** and **5-FA**, and from 43.9 to 13.3 μM for **6** and **6-FA**. Relatively high dark toxicity was observed for **6-FA** of 26.1 μM. When the nitrogen atoms of the *meso*-pyridyl rings were quaternized (**5-FAQ** and **6-FAQ**) to further enhance the aqueous solubility of the complexes, it was not possible to calculate an IC_{50} value. When octanol-water partition coefficients (Log P) were calculated by the shake flask method, values of −0.70 and −1.70 were obtained for **5-FAQ** and **6-FAQ**, respectively. This provides evidence that the dyes are too water-soluble and not sufficiently lipophilic.

The PACT activity properties of the synthesised diiodinated aza-BODIPYs were studied against *Staphylococcus aureus* (*S. aureus*) through photoirradiation for 60 min with Thorlabs M660L4 (280 $mW.cm^{-2}$) and M730L4 (160 $mW.cm^{-2}$) light emitting diodes (LEDs) mounted on the illumination chamber of Modulight® 7710-680 medical laser system providing doses at the well-plate of 100 and 57 $J.cm^{-2}.min^{-1}$. Aza-BODIPYs **2**, **3** and **4** all inhibited the growth of *S. aureus* but with relatively low Log_{10} reductions of 1.37, 1.20 and 0.20. In contrast, aza-BODIPY **1** was found to have a Log_{10} reduction of 7.82. The PACT activities of free base and Sn(IV) 5-[4-(3-bromoethylcarboxyamidyl)phenyl]-10,15,20-triphenylporphyrins (**7** and **8**) prepared by Dr Balaji Babu (*New Journal of Chemistry* **2022**, *46*, 5288-5295) were tested against *S. aureus* to determine whether adding a triphenylphosphonium moiety to form free

base and Sn(IV) 5-[4-(triphenylphosphonium)ethylcarboxyamidyl)phenyl]-10,15,20-triphenylporphyrin (**18** and **19**) enhances the photo-induced antibacterial activity, in addition to optimising the PDT properties due to its mitochondria-targeting properties. The PACT activities obtained against *S. aureus* were not favourable, but **18** exhibited enhanced activity across the studied concentration range.

The potential utility of aza-BODIPY dyes **1-4** and their non-iodinated analogues (**1a-4a**) for optical limiting applications was analysed by carrying out a series of Z-scan measurements, since dyes of this type have large ground state dipole moments, and this can enhance the non-linear optical limiting response. All the aza-BODIPY dyes under investigation exhibited intense non-linear absorption (NLA) behaviour with Z-scan profiles that contain significant reverse saturable absorption (RSA) responses. Aza-BODIPYs **1**, **2a**, **2**, **3**, **4a**, and **4** decreased the transmitted intensity of the strong laser beam to less than 50% of the linear response in organic solutions with a fixed absorbance of 1.8 for the main aza-BODIPY spectral band and a laser pulse input energy of 42 μJ. Higher second-order hyperpolarizability (γ) values were obtained for iodinated dyes **1**, **2**, **3** and **4**. The highest value of 3.15×10^{-29} esu was obtained for **1**. A comparative study involving the four non-iodinated dyes **1**, **2**, **3** and **4** and seven 1,3,5,7-tetraaryl aza-BODIPY dyes reported previously in the PhD thesis of Gugu Kubheka at Rhodes University demonstrated that there was no clear trend correlation between the γ values calculated from the Z-scan measurements and calculated dipole moments.

Acknowledgements

I would like to sincerely thank my supervisor, Prof. John Mack, for all his assistance, patience, and support throughout this project and when I was writing this thesis. Working with you has been a wonderful pleasure. I am incredibly appreciative to Distinguished Prof. Tebello Nyokong for giving me the chance to conduct research in her laboratories and under their guidance. I would like to extend my gratitude to Prof. Rosa Klein for consistently motivating me. My heartfelt gratitude goes to my family for holding my hand throughout this challenging journey. I am also grateful for the support I received from my friends and colleagues in S22 and the Department of Chemistry.

A special thank you to Gail Cobus, Francis Chindeka and other supporting staff for their unwavering support throughout my studies. Above all, I would like to thank the Lord for his guidance throughout this journey.

Table of Contents

List of Schemes

List of Figures

List of Tables

List of Abbreviations

1PA	One-photon absorption
2PA	Two-photon absorption
Aza-BODIPY	Boron azadipyrromethene
AuNPs	Gold nanoparticles
B3LYP	Becke 3-parameter, Lee-Yang-Parr
CFU	Colony forming units
DCM	Dichloromethane
DDQ	2,3-Dichloro-5,6-dicyano-*p*-benzoquinone
DLS	Dynamic light scattering
DMA	Dimethylanthracene
DMEM	Dulbecco’s modified Eagle’s medium
DMF	Dimethylformamide
DMSO	Dimethylsulfoxide
DPBF	1,3-Diphenylisobenzofuran
DPBS	Dulbecco’s phosphate−buffered saline
EDC	*N*-ethyl-*N*'-(3-dimethylaminopropyl)carbodiimide
EDG	Electron donating group
EDS	Electron dynamic scattering
ESA	Excited state absorption

ESP	Electrostatic potential
EtOH	Ethanol
FA	Folic acid
FCS	Fetal calf serum
FDA	Food and Drug Administration
FR	Folic acid receptor
FT-IR	Fourier transform-Infrared
FWHM	Full width at half maximum
HOMO	Highest occupied molecular orbital
HPD	Hematoporphyrin derivative
IC	Internal conversion
ISC	Intersystem crossing
LED	Light-emitting diode
LUMO	Lowest occupied molecular orbital
MALDI-TOF-MS	Matrix-assisted laser desorption/ionisation-time of flight-mass spectrometry
MOs	Molecular orbitals
NIR	Near-infrared region
NIS	*N*-iodosuccinimide
NLA	Nonlinear absorption

NLO	Nonlinear optics
NMR	Nuclear magnetic resonance
NPs	Nanoparticles
OL	Optical limiting
PACT	Photodynamic antimicrobial chemotherapy
Pcs	Phthalocyanines
PDT	Photodynamic therapy
PS	Photosensitiser
RSA	Reverse saturable absorption
TCSPC	Time-correlated single photon counting
TD-DFT	Time-dependent Density functional theory
TEA	Triethylamine
TEM	Transmission electron microscopy
TFA	Trifluoroacetic acid
TPP	Tetraphenylporphyrin
TPyP	5,10,15,20-Tetrakis(4-pyridyl)porphyrin
UV-visible	Ultraviolet-visible
XPS	X-ray photoelectron spectroscopy
XRD	X-ray diffraction
ZnPc	Zinc phthalocyanine

List of Symbols

α	Linear absorption coefficient
A	Absorbance
β_{eff}	Effective nonlinear absorption coefficient
ε	Molar extinction coefficient
F	Fluorescence
h	Hours
$\hbar$	Planck's constant
hv	Light
I	Light intensity
I_{lim}	Limiting threshold fluence
$Im[\chi^{(3)}]$	Imaginary third order susceptibility
λ	Wavelength
Φ_F	Fluorescence quantum yield
γ	Second-order hyperpolarisability
Φ_Δ	Singlet oxygen quantum yield
η	Refractive index
$^1O_2$	Singlet oxygen
$^3O_2$	Triplet oxygen
P	Phosphorescence

S_0	Ground state
S_1	Singlet excited state
T_1	First triplet state
τ_F	Fluorescence lifetime
τ_T	Triplet lifetime
γ	Second-order hyperpolarisability

Chapter 1: Introduction

1.1. An overview of Photodynamic therapy

Photodynamic therapy (PDT) is a relatively new and promising therapeutic method that uses a combination of visible or near-infrared (NIR) light and a light-activated medication to treat cancerous and non-malignant illnesses [1-23]. Photosensitiser (PS) dye is a term used to describe a medication that is triggered by light in this context. By themselves, the light or photosensitisers used in PDT have little or no toxicity. Only the activation of the photosensitiser by light causes the formation of cytotoxic species, which causes the targeted tissue to be destroyed [1-4]. Oscar Raab, a medical student of Professor Herman von Tappeiner in Munich, Germany, originally published the concept of cell death being triggered by a combination of light and chemicals in 1900 [4, 8]. Oscar Raab discovered that acridine orange eradicated paramecia in the presence of light [4, 8]. Three years later, in partnership with a dermatologist called Albert Jesionek, Von Tappeiner used this discovery to treat skin malignancies with a combination of eosin and white light [4]. He went on to demonstrate that oxygen is required in photosensitisation processes, such as this, coining the phrase "photodynamic action" to describe the phenomena in 1907 [4].

Following Von Tappeiner and Jesionek's pioneering work, little research on clinical therapeutic applications of PDT was conducted until nearly 60 years later, when lasers were invented. In 1960, Mayo Clinic researchers discovered that injecting hematoporphyrin caused neoplastic tumours to glow preferentially [2, 4, 10-18]. PDT was first proposed as a cancer treatment in the 1970s by Thomas Dougherty, at the Roswell Park Cancer Institute [14]. Although the PDT action of porphyhrinoids was initially reported in Germany over a century ago, until Dougherty's studies, scientists were unable to develop a means to cure diseases with light-sensitive drugs. In 1973, Dougherty used PDT to successfully treat cancer in preclinical models for the first time

[14, 15]. He carried out the first human controlled clinical trial research three years later. PDT and the photosensitizer Photofrin® were approved by the US Food and Drug Administration (FDA) in 1994 for the treatment of advanced oesophageal cancer. To date, the FDA has approved it for the treatment of Barrett's oesophagus and a few forms of lung cancer [10, 14, 15]. Following this findings, additional photosensitisers were prepared by other researchers to destroy malignant tissues. In comparison to the parent hematoporphyrin or other porphyrins, a porphyrin derivative named "hematoporphyrin derivative" (HPD) was shown to have superior localising and photosensitising capabilities [2, 4]. Systematic research in tumour-bearing animals began only in the mid-1970s after Diamond *et al.* [4] published a seminal publication in 1972 in which the authors investigated both *in vitro* and *in vivo* the effect of light activation of hematoporphyrin in an experimental rat glioma. They discovered treatment results in both cases in 100% cell death *in vitro* through tumour necrosis and through growth inhibition *in vivo*. The scientists concluded that based on these findings, PDT offers a novel strategy for the treatment of brain malignancies [10-18]. Since then, significant ground-breaking research has been carried out to advance PDT as a therapeutic technique. Several large-scale clinical investigations of PDT have been conducted in human patients through the application of various photosensitisers, including HPD, to treat skin, bladder, oral cavity, bronchial, oesophagal, head and neck, brain, and rectal cancers [4].

Great progress has been made in realising the clinical potential of PDT almost a century after Raab's first observations [1-18]. The Canadian Health Agency approved Photofrin® (porfimer sodium), a refined and purified version of HPD, for PDT treatment of recurrent superficial papillary bladder cancer in 1993 [2, 4, 23]. This was the world's first formal approval of PDT and a watershed moment in the history of PDT. The

second big breakthrough came in 1998 when the FDA approved Photofrin® for the treatment of oesophageal and lung cancer [2, 4]. Photofrin® is currently approved for the treatment of bronchial, oesophageal, lung, cervical, and bladder cancer in numerous countries globally. Photofrin® was approved by the FDA in 2003 for the treatment of high-grade dysplasia in Barrett's oesophagus, which can develop into oesophageal cancer [9, 10]. This approval is notable since it was the first time PDT had been evaluated as a primary therapy option for a neoplastic disorder in its early stages.

The limitations of first-generation photosensitisers prompted the development of second-generation photosensitisers. Clinical trials are underway for several new photosensitisers so that the main disadvantages of HPD and Photofrin® can be addressed [9, 10]. Both HPD and its refined descendant Photofrin® create prolonged skin photosensitivity and have weak porphyrin-based absorption peaks at wavelengths short of the optimal transmission of the tissues in the phototherapeutic window (620−850 nm) [9, 10]. Second-generation photosensitisers include mTHPC (Foscan®), BPD-MA (Verteporfin®), and mono-N-aspartyl chlorin e6 (NPe6, Taloporfin®). mTHPC is a potent photosensitiser that is now being studied in clinical trials for skin, oral, mesothelioma, and prostate malignancies [13, 16]. mTHPC was licensed by the European Union in 2001 for use in the treatment of advanced head and neck cancer.

Porphyrin analogue dyes, such as phthalocyanines and chlorins, and non-porphyrin photosensitisers, such as phenothiazines and curcuminoids, are among the second-generation of photosensitiser dyes [2, 10, 12]. Porphyrin analogue dyes are generally better suited for use in PDT than non-porphyrin-based dyes, since some of these PS dyes take a long time to clear from the body, resulting in prolonged phototoxicity.

Researchers have concentrated on non-porphyrin-based PS dyes, which are easier to synthesise and functionalise and have fewer side effects due to the long-term cytotoxicity of porphyrin-based PS dyes [27-50]. Only a modest amount of research has been carried out on the usefulness of aza-BODIPY dyes (4,4′-difluoro-4-bora-3a,4a-diaza-*s*-indacenes or boron-azadipyrromethenes) as a novel second-generation class of PDT agents [27-34]. Several review studies have examined several functionalities and derivatives of PDT-based aza-BODIPY dyes, which produce moderate to high $^1O_2$ quantum yields [9-12]. The focus of this work is on exploring the potential utility of both porphyrins and aza-BODIPY dyes as potential PDT agents.

Photodynamic antimicrobial chemotherapy (PACT) is an alternative treatment for bacterial illnesses that precedes PDT in terms of applicability [13, 14]. A photosensitiser dye and visible region or ultraviolet light are applied in a similar way to PDT to kill bacteria *via* oxidative damage to the bacterial cell wall. PACT is currently used mostly to treat oral infections and sterilise blood products, and it is successful in killing bacteria that have gained resistance to practically all antibiotics [13, 14]. *Neisseria gonorrhoeae* and *Staphylococcus aureus (S. aureus)* are examples of these microorganisms. The fundamental benefit of PACT as a potential treatment is that the bacteria can be photo-inactivated repeatedly without building resistance against the reactive oxygen species that are generated [13, 14].

1.2. The mechanism of photodynamic therapy

The starting point of PDT is the generation of phototoxic oxygen species in the target tissue. This entails a two-step process, the first of which is the injection of a photosensitiser, followed by light illumination of the sensitised target tissue at a

wavelength that is optimal for sensitiser absorption [5-12]. Although the biological mechanisms underpinning PDT vary depending on the nature of the sensitiser, its tissue distribution, intracellular localisation locations, and other factors, the primary photochemistry involved in PDT-induced damage is the same for all photosensitisers. The energy level diagram in **Figure 1** depicts the photophysicochemical processes that lead to the generation of $^1O_2$ and other reactive oxygen species. The photosensitiser molecule is initially in its ground state (S_0). When a photon is absorbed by this photosensitiser, the dye is excited to its first singlet excited state (S_1). Due to high rates of intersystem crossing (ISC) rates, a large proportion of singlet excited state photosensitiser molecules convert to the lowest energy triplet state (T_1).

Unlike most molecules, molecular oxygen has a triplet ground state ($^3O_2$) and a low-lying singlet excited state ($^1O_2$). Direct excitation of oxygen from its triplet ground state to the singlet excited state is prohibited by selection rules, but energy transfer between the T_1 state of the photosensitiser molecule and $^3O_2$ [5-12]. This is referred to as a Type II mechanism. When electron transfer occurs *via* the Type I mechanism, reactive oxygen radical species are formed. Singlet oxygen is generally considered to be the principal cytotoxic species created during PDT [5-12]. In a biological context, $^1O_2$ is a strong oxidising agent and, consequently, very reactive, with a lifespan of less than 0.01−0.05 s [15]. Cell organelles such as the plasma membrane, endoplasmic reticulum, mitochondria and others are damaged by the interactions of $^1O_2$ with cellular targets, resulting in cell death by apoptosis or necrosis [15].

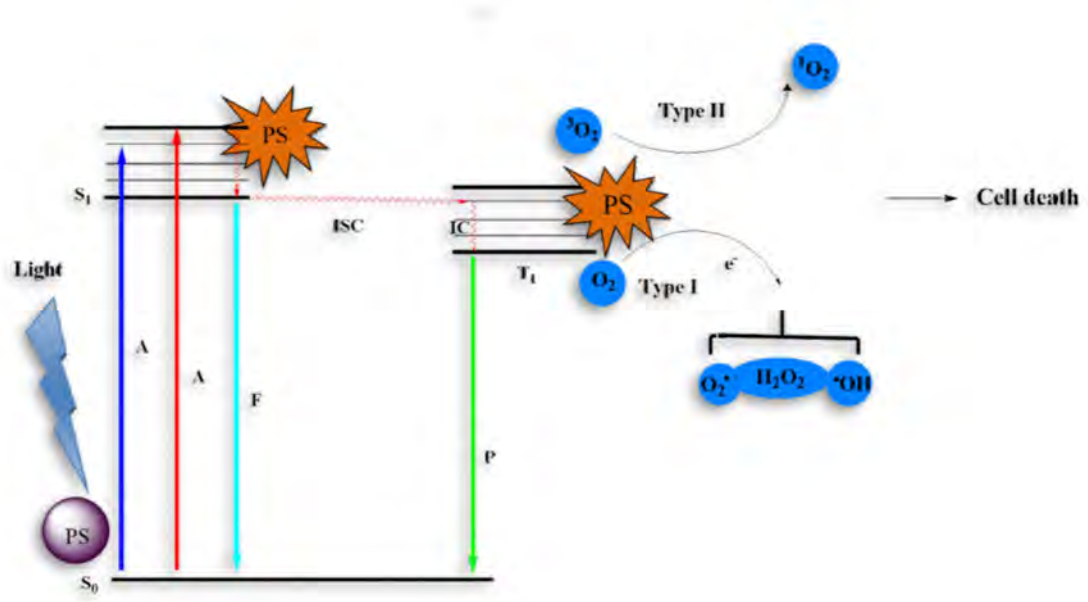

Figure 1. A Jablonski diagram showing the production of reactive oxygen species by the Type I and II mechanisms.

1.3. Structure and properties of aza-BODIPY dyes

In recent years, the usefulness of NIR fluorescent dyes in biological applications has been widely recognised. NIR light can permeate biological tissues more deeply and non-invasively than visible light, which is advantageous in applications such as intracellular labelling and PDT and PACT treatments. The parent structure of aza-BODIPY is shown in **Figure 2**, which is derived from conventional BODIPY (4,4′-difluoro-4-bora-3a,4a-diaza-*s*-indacenes also referred to as boron dipyrromethenes) by substituting the *meso*-carbon with an aza-nitrogen atom [9-12]. Because of the high extinction coefficients of their main spectral band in the NIR and modest fluorescence quantum yields, this class of dyes has recently received a lot of interest. Traditional BODIPY dyes can be defined as boron-bridged monomethine cyanine dyes from a structural standpoint (**Figure 2**) [9-12]. This results in reduced double bond rotation and greater rigidity in a planar structure, resulting in higher brightness than is the case

with cyanine dyes. Furthermore, the electron-deficient aza-BODIPY core contains a wealth of reactive sites, facilitating the incorporation of electron-donating or functional groups to improve all aspects of the photophysical properties and therapeutic qualities for bio-applications [9-12].

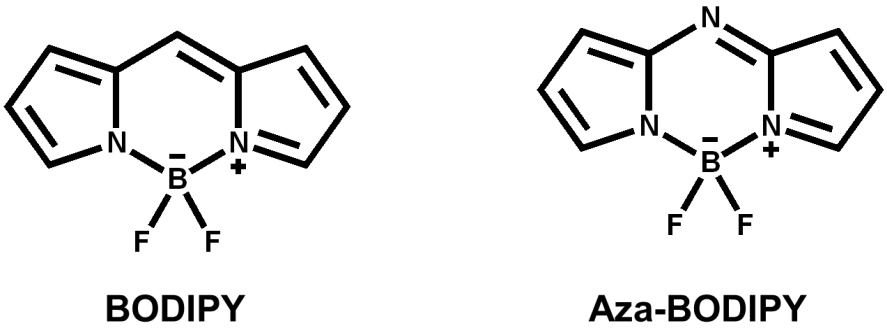

Figure 2. Generic structures of BODIPY and aza-BODIPY dyes.

1.3.1. General synthetic strategies

Aza-BODIPYs are relatively well-established commercial dyes in terms of precursor availability. **Figure 3** outlines the three major strategies for preparing aza-BODIPY parent compounds. Firstly, O'Shea *et al.* [30] postulated that symmetrical and asymmetrical products might be generated by using the Michael addition to cyclise nitromethane and substituted ketones, followed by complexation with boron trifluoride to obtain the target products. This approach is straightforward: the reaction conditions are mild, and aza-BODIPYs can be prepared with various substituents by altering the precursors used. However, the product yield tends to be modest (20–50%). Secondly, Carreira *et al.* [30] hypothesised that direct cyclisation of a substituted pyrrole and subsequent complexation with boron trifluoride could yield symmetrical or asymmetrical products. This approach produces a better yield (> 50%). Furthermore, in contrast with the target molecular structures accessible using O'Shea's method, this

reaction can introduce fused rings to the pyrrole, facilitating the formation of an expanded π-conjugation system [30]. Thirdly, Luk'yanets *et al.* [30] reported that a phthalonitrile and aryl magnesium bromide may be combined to produce a symmetrical product. The intended product might then be produced by boron trifluoride complexation. This approach, however, had the lowest yield (10–30%), since other products are also possible using these reaction conditions. The three approaches, when combined, form a solid foundation for synthesising most possible aza-BODIPY derivatives.

Previous research has demonstrated that aza-BODIPY absorbs and emits in the NIR range with a large red shift of roughly 100 nm compared to the parent BODIPY dye, with similar fluorescence lifetime values [27, 33]. The cause of this strong red shift will be explored further in Section 1.3.2 and Chapter 9. The aza-BODIPY scaffold's remarkable optical characteristics in the NIR biological transparency window make it particularly attractive for bio-applications. The structural design of novel aza-BODIPYs is critical for manipulating their photophysical properties, which ultimately define their utility for applications. Furthermore, a shift in aza-BODIPY absorption and emission maxima into the NIR region enhances their suitability for bio-applications.

A commonly adopted technique for red-shifting spectral bands is to attach aryl groups to the aza-BODIPY core. Introducing electron-donating groups (EDGs) at the 3,5-positions has been reported to be an effective strategy for giving aza-BODIPYs longer absorption/emission wavelengths and higher absorption/emission rates [27-33]. The introduction of EDGs on both the 3,5- and 1,7-positions in the context of the O'Shea method can result in pronounced red shifts [27-33]. This approach will be explored in this work.

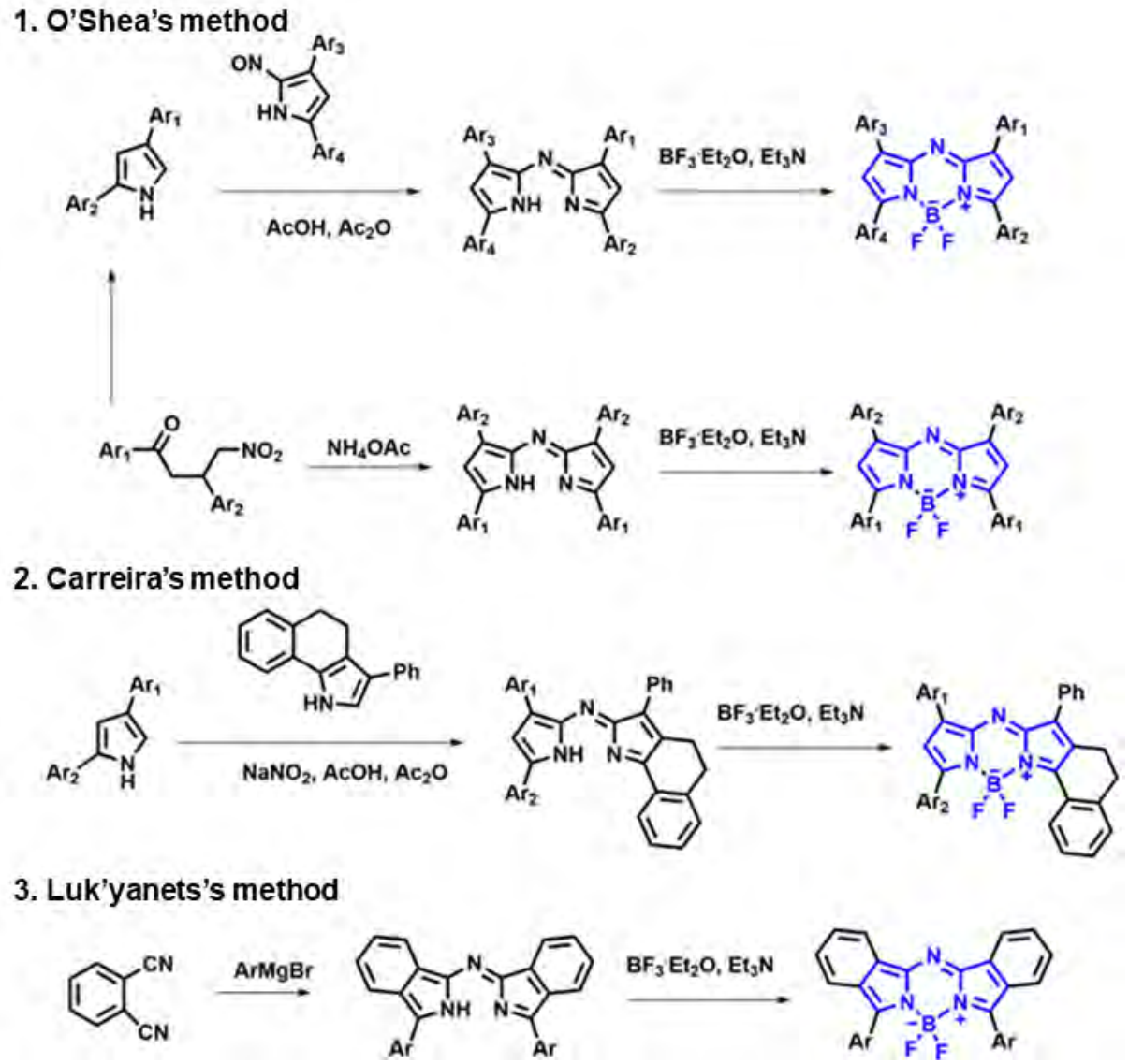

Figure 3. The synthetic strategies for aza-BODIPY dyes [30].

1.3.1.1. Functionalisation at the 2,6-positions

The 2,6-positions of 1,3,5,7-tetramethyl-aza-BODIPY dyes are readily modified. Introducing halogen atoms at these sites improves the dyes' utility as PDT and PACT photosensitiser dyes. The 2,6-positions have lower partial positive charges in theoretical calculations, leaving them vulnerable to electrophilic substitution [43]. The halogenation of the 2,6-positions is accomplished by substituting iodine or bromine atoms for the 2,6-position protons. Bromination and iodination do not affect the

planarity of the core structure [43]. Blue shifts observed in the absorption and emission band maxima of the aza-BODIPYs are quite minor when either halogen atom is introduced.

Aza-BODIPYs that have not been halogenated are highly fluorescent. When the photosensitiser dyes are activated, they are photoexcited into higher singlet states and, after internal conversion, ultimately relax from the S_1 state to the S_0 ground state via fluorescence [43]. ISC to the triplet state is usually limited in the absence of heavy atoms. The spin-forbidden ISC transition is favoured when halogens are introduced at the 2,6-positions of the core structure. This increases the rate of ISC while quenching fluorescence because of the population of the T_1 state. This phenomenon occurs when heavy atoms enhance spin-orbit coupling and is termed the heavy atom effect [43].

Various methods can be used for the halogenation of aza-BODIPY dyes. These include the regioselective bromination using *N*-iodosuccinimide (NIS) in DCM or the direct use of iodine under similar conditions [43]. The use of NIS was explored in this work due to the facile nature of the iodination reaction.

1.3.2. The absorption and emission spectra of aza-BODIPY dyes

The absorption and fluorescence bands of aza-BODIPYs, a heteroatom-substituted counterpart of BODIPYs in which a methine carbon atom at the *meso*-position is replaced with a nitrogen atom, have been observed at wavelengths greater than 650 nm [27-33]. Although the ligand structure of aza-BODIPY, aza-dipyrrin, was first reported more than 70 years ago, it remained largely unstudied until O'Shea *et al.* [30] repeated their initial serendipitous synthesis and reported the marked bathochromic shift of aza-BODIPY absorption and fluorescence relative to their BODIPY counterparts. Since then, researchers have concentrated their efforts on the potential

applications of aza-BODIPY dyes in bioimaging and sensing, as fluorescent probes and laser dyes and in therapeutics.

Because nitrogen is more electronegative than carbon, the considerable red shifts in absorption and fluorescence of an aza-BODIPY compared to its parent BODIPY can be attributed to the efficient stabilisation of the lowest unoccupied molecular orbital (LUMO) [44]. The *meso*-position in the LUMO has a large molecular orbital (MO) coefficient (**Figure 4**), while the highest occupied molecular orbital (HOMO) has a nodal plane at this location [44]. As a result, the LUMO undergoes a relative stabilisation when the frontier π-MO energies are compared to those of the analogous BODIPY. Because the HOMO–LUMO transition is the predominant mode of absorption for both BODIPY and aza-BODIPY, aza-BODIPY has a longer absorption than BODIPY due to the smaller HOMO–LUMO gap [44].

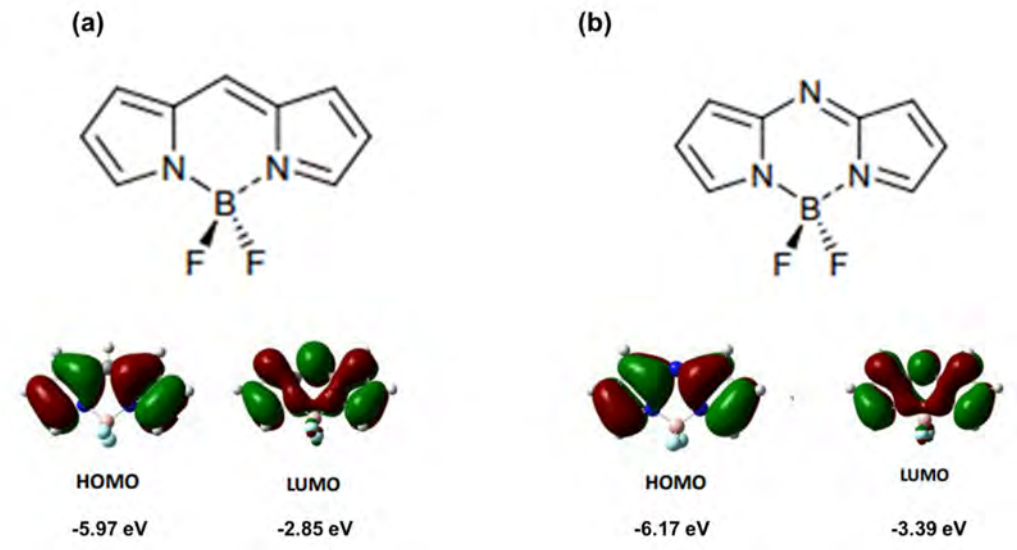

Figure 4. Structures and frontier MOs of (a) BODIPY and (b) aza-BODIPY. The MOs and their energies were calculated at the B3LYP/6-31G(d) level.

1.3.3. Photophysical and photochemical properties of aza-BODIPY dyes

The physicochemical features of aza-BODIPY dyes and the method of action of PDT and PACT can be described using a Jablonski diagram (**Figure 1**). A precise wavelength of light is used to illuminate the photosensitiser dye. Internal conversion allows the excited photosensitiser dye to shift from the S_0 to the lowest vibrational state of the S_1, where it can undergo fluorescence and ISC [27-33]. For improved rates of ISC in the T_1, which is a critical phase in PDT and PACT, the photosensitiser dye requires the introduction of heavy atoms into its structure [43]. Type II ($^1O_2$) and Type I (hydroxyl radical (•OH), hydrogen peroxide (H_2O_2) and $^3O_2$)) electron transfer processes can form ROS when the photosensitiser dye is in the T_1 state [27-33]. ROS kill tumour cells by inducing apoptosis and/or necrosis, while oxidative reactions break down bacterial cell walls.

1.3.3.1. Fluorescence quantum yields and lifetimes

The emission of light due to an electron transition from a singlet excited state to the ground state ($S_n \rightarrow S_0$) is known as fluorescence [46]. This process usually follows Kasha's rule, which states that only the transition from the lowest vibrational level of the S_1 produces emission [46]. In this case, the shape of the emission band is unaffected by the excitation wavelength. The emission spectrum is usually a near mirror image of the absorption spectrum because the electronic states of dyes with rigid structures have similar potential energy surfaces (**Figure 5**) [46]. Fluorescence can be useful in the context of PDT and PACT because tumours or bacterial cells can be identified using imaging techniques. Fluorescence lifetime measurements can be used to calculate how long it takes the photosensitiser dyes, on average, to relax to the S_0 state.

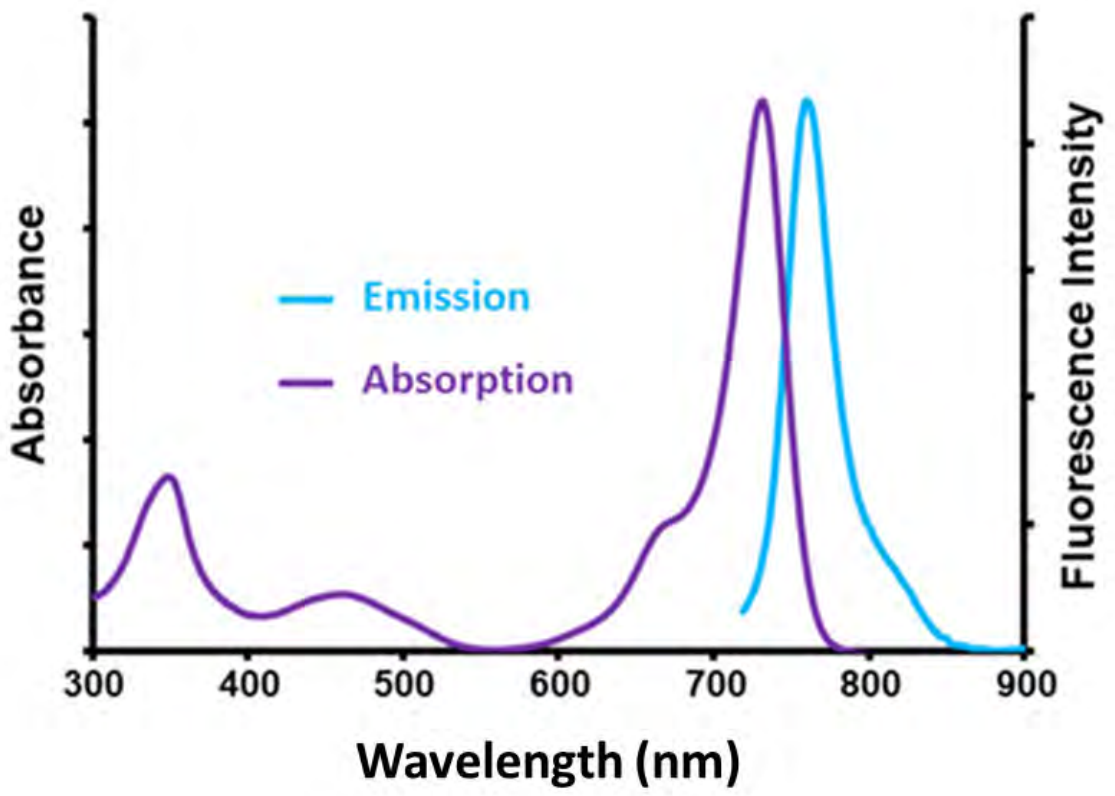

Figure 5. The absorbance and emission spectra of a typical aza-BODIPY dye.

The effectiveness of the fluorescence process is measured by the fluorescence quantum yield (Φ_F) value [46]. The Φ_F value is calculated using a comparative method that compares the integrated area beneath the dye's emission spectrum to that of a molecular dye with a known Φ_F value that serves as a standard. Equation 1 is used to calculate the sample's Φ_F value:

$$\Phi_F = \Phi_{F(std)} \times \frac{F.A_{std}.\eta^2}{F_{std}.A.\eta^2_{std}} \quad \text{..... (1)}$$

Where F and F_{std} are the integrated areas under the sample and standard emission curves, A and A_{std} are the sample and standard absorbances at the excitation wavelength, and η and η_{std} are the refractive indices of the sample and standard solvents, respectively. The known Φ value of the used standard is $\Phi_{F(std)}$. Standards include zinc phthalocyanine (ZnPc) (Φ_F = 0.20 in DMSO, 0.28 in ethanol) [44].

The fluorescence lifetime (τ_F) is the time it takes for the S_1 population to decrease by 1/e because of the fluorescence process. If the assumption can be made that a locally excited state is involved, the τ_F values will be independent of the emission and excitation wavelengths utilised. The τ_F values of aza-BODIPYs are usually short-lived, but their absorption and emission processes are known to be efficient [31-33]. Decay curves from the time-correlated single photon counting (TCSPC) instrument were used to calculate the lifetime values. **Figure 6** depicts a typical decay curve with residuals.

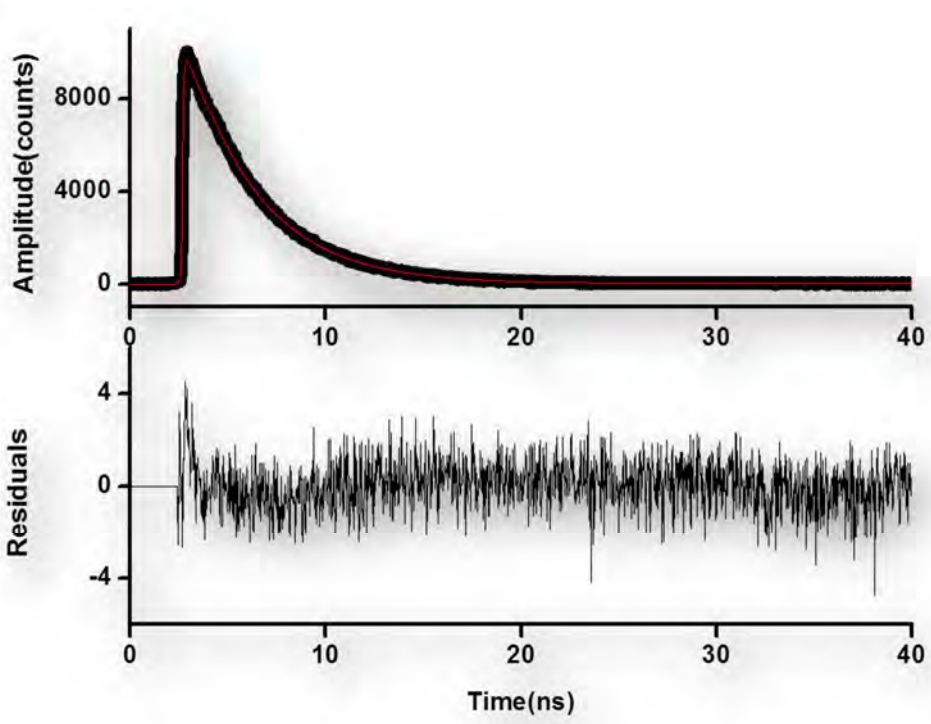

Figure 6. A typical fluorescence lifetime decay curve. The fluorescence intensity decay curve is shown by a solid black exponential line. The red exponential line shows the line of best fit. The lower panel provides the residual difference between the experimental and theoretical values.

1.3.3.2. Singlet oxygen quantum yields

Aza-BODIPY dyes are typically more fluorescent than porphyrins and have larger molar extinction values at the red end of the visible region [27-33]. The fundamental structure of aza-BODIPY dyes is very rigid due to the BF_2 moiety. If the structure is viewed as a modified *s*-indacene, this disturbs the delocalised π-system, resulting in the absence of a macrocyclic ring system analogous to that of porphyrins [27-46]. As a result, the HOMO−LUMO transition completely dominates the primary spectral band [27-33]. As a result, unlike porphyrins, which are heteroaromatic, aza-BODIPY dyes do not have aromatic π-systems. Although the low rate of ISC has hindered the use of aza-BODIPY dyes in $^1O_2$ applications, molecular dye structures can be modified to increase the rate of ISC by adding heavy atoms to populate the T_1 state and therefore increase the formation of $^1O_2$ [27-33]. Incorporating iodine atoms at the 2,6-positions is the strategy used in this research to enhance the singlet oxygen quantum yield (Φ_Δ) values of a range of aza-BODIPY dyes.

Singlet oxygen quantum yields provide a quantifiable measurement that is used to evaluate the effectiveness of the photosensitiser to utilise light energy to convert ground state molecular dioxygen to $^1O_2$, since this cytotoxic species plays a critical role in PDT and PACT. The value can be calculated by using a comparative chemical method or by monitoring the phosphorescence of $^1O_2$ with a germanium detector. In this investigation, the comparative chemical approach was applied. 1,3-diphenylisobenzofuran (DPBF) and dimethyl anthracene (DMA) are $^1O_2$ scavengers that can be used in this context. The amount of $^1O_2$ produced is measured in comparison with a known standard, such as free base tetraphenylporphyrin (H_2TPP) and methylene blue [47]. The dye/standard and scavenger mixed solutions are

irradiated at predetermined intervals. During the irradiation, the $^1O_2$ created by the dye reacts with the scavenger and degrades it. The change in the absorbance value of the maximum intensity of the $^1O_2$ scavenger in solution is used to monitor the production of $^1O_2$. Equation 2 below is applied:

$$\Phi_{\Delta}=\Phi_{\Delta(std)}\times\frac{\propto_{std}}{\propto_{PS}} \quad \text{.....(2)}$$

Where $\Phi_{\Delta(std)}$ is the $^1O_2$ quantum yield of the standard (methylene blue or H_2TPP), and α_{PS} and α_{std} are the photosensitiser and standard's ΔA slopes, respectively. This equation is only valid if the solvents and optical densities used for the sample and standard solutions are the same.

1.4. Overview of porphyrins

Porphyrins are macrocyclic chemicals that occur naturally and play an important part in the metabolism of living beings. The porphyrin ligand is a highly stable heteroaromatic system that follows Huckel's aromaticity rule, **Figure 7** [48-50]. Porphyrins obtained synthetically have been used in a variety of applications. Porphyrin chemistry stimulated research on porphyrin analogues such as aza-BODIPY dyes, and these analogues have properties that are often quite similar to those of porphyrins. The porphyrin structure consists of four pyrrole rings joined by methene bridges, each with a 3.7-micron inner cavity [48-50]. Porphyrins are, therefore, ideal ligands for coordination chemistry. The two protons on the pyrrole nitrogen are eliminated during coordination and replaced with negative charges [48-50]. Porphyrins can bind a wide range of metals with varying coordination numbers, and the resulting complexes are extremely stable.

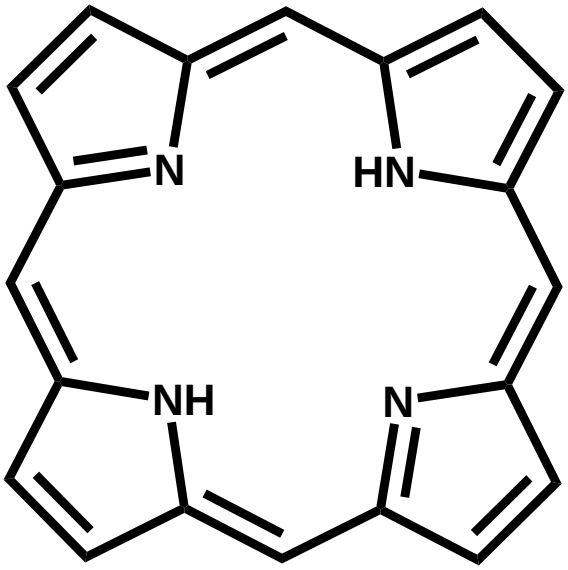

Figure 7. The generic macrocyclic structure of a porphyrin ligand.

The symmetrical planar structure of metalloporphyrins, and their photostability, adaptability, and distinctive electrical and optical properties make porphyrins appealing for use in applications such as PDT [48-50]. Because the wavelength of light used to activate the photosensitiser affects tissue penetration, the lowest energy porphyrin absorption bands ideally should be moved by changing the structure at the *meso*-positions and/or β-positions. The rate of ISC is increased by inserting a heavy central metal ion [48-50]. Porphyrin spectra are distinguished by an intense absorption band called the B (or Soret) band at *ca.* 420 nm, and less intense Q bands at the red end of the visible spectrum (550−750 nm) [48-50]. The Q bands are useful in the context of PDT, and the major purpose of this study is to red shift their band maxima into the therapeutic window (600−850 nm). However, because of the limited ability of the photosensitiser to transfer energy to $^3O_2$, the photosensitiser should also absorb below 800 nm in the heart of the therapeutic window.

1.5. Drug delivery agents

1.5.1. Gold nanoparticles and polymeric nanocarriers

The use of nanocarriers in drug delivery is critical for improving medicinal efficacy and biocompatibility in physiological conditions. Photosensitiser dyes such as phthalocyanines (Pcs) and porphyrins have been effectively attached to nanoparticles (NPs), including carbon nanotubes, as well as silicon, gold, and silver NPs [51, 52]. Photosensitiser dyes can also be transported using polymeric nanocarriers such as Pluronics® and liposomes [52]. Since the biocompatibility and efficacy in physiological settings of the aza-BODIPYs is limited by their hydrophobicity, solubilisation using mixed Pluronic® F-127 and L-121 micelles was initially investigated to build on earlier work with Pluronic® F-127 during the MSc research of the author [53, 54]. Unfortunately, unfavourable results were obtained, so the focus of the project shifted to using gold nanoparticles (AuNPs) as nanocarriers.

AuNPs of various morphologies and sizes (**Figure 8**) are becoming increasingly relevant in biological sciences due to their compatibility, reactivity, susceptibility to change, and tuneable optical qualities [55]. Because of their favourable properties, AuNPs can be used in clinical chemistry, bioimaging, cancer therapy, and targeted drug administration [55-68]. Synthetic procedures have been perfected that allow for controlled sizes, shapes, and dimensions. For example, drug delivery nanoparticles should be small enough to bypass physiological barriers or infiltrate target cells while also being large enough to transport enough therapeutic molecules/drugs to the site of action [55-68]. Due to the increased vasculature, spherical AuNPs < 100 nm easily permeate into the deep layers of skin and malignant tissues [55-68]. They have a good rate of circulation and removal from the body [55-68]. The coupling of AuNPs to aza-

BODIPY dyes *via* S-bonds and its use *in vitro* to inhibit MCF−7 cancer cells are described in this work.

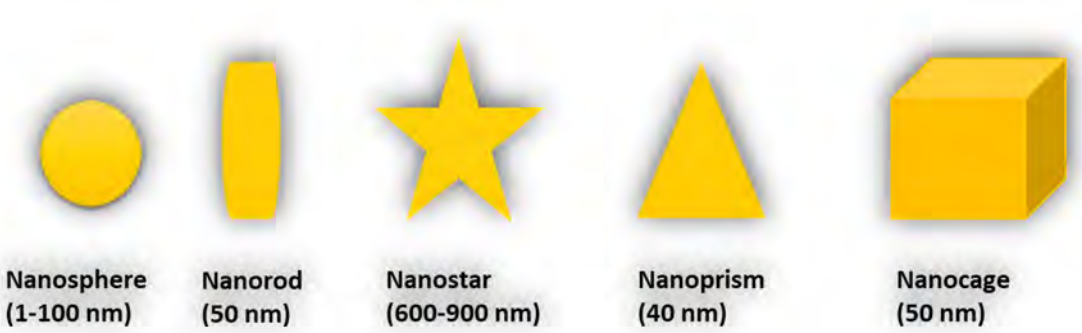

Figure 8. Gold nanoparticles of different morphologies and sizes.

1.5.2. *Folic acid*

Targeted (active) drug delivery is critical to effective cancer therapy to overcome these non-targeted and invasive surgical procedures. Active targeting techniques can boost the intracellular concentration of therapeutic medicines in cancer cells while preventing cytotoxicity in healthy cells [69-77]. Folic acid (FA) (**Figure 9**) is a cancer cell-targeted biomolecule with a high over-expressed receptor that helps tumours with poorly established vasculature circumvent a formidable membrane barrier [69-77]. FA is a type of vitamin that is required for nucleotide base production and cell proliferation. Physiological FA is delivered by receptor-mediated endocytosis *via* cell membrane-associated proteins or the folic acid receptor (FR) [66-77]. The FR is overexpressed in various human carcinomas, including breast, ovarian, lung, and others, and it is thought to be a tumour-specific target platform due to its intravenous drug accessibility [66-77]. Using ester bonds to conjugate FA to aza-BODIPY dyes is a novel approach adopted in this study. Water-soluble aza-BODIPYs were obtained because of this conjugation. The axial ligation allowed us to conjugate FA to porphyrins, providing new

porphyrin conjugates. The porphyrin-FA conjugates, on the other hand, were not soluble in water. The conjugates were quartenised to make them water-soluble.

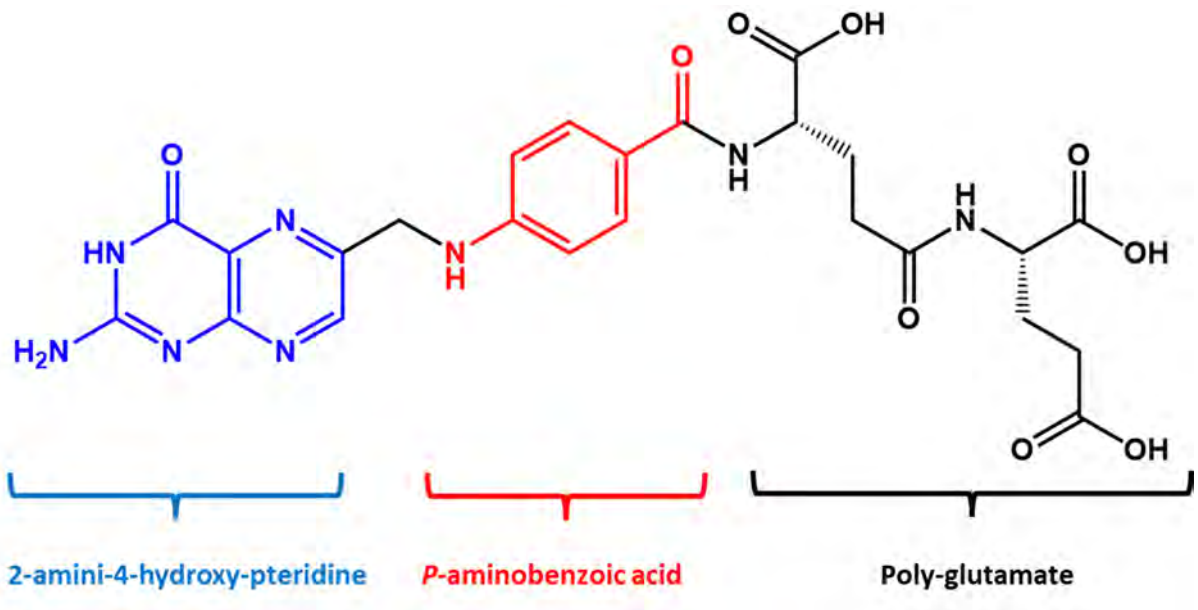

Figure 9. The molecular structure of folic acid.

1.6. Non-linear optics

Nonlinear optics is a specific and in-depth branch of nonlinear science. Although nonlinear effects in optics have been recognised for many decades, the development of the optical maser, or laser as it is referred to today, gave rise to modern nonlinear optics [78-80]. Second harmonic generation was demonstrated by precisely focusing a pulsed ruby optical maser onto crystalline quartz in a seminal study by Franken and colleagues in 1961 [78-80]. In the years that followed, a wide range of nonlinear phenomena in light-matter interaction were experimentally demonstrated. Many of these effects quickly found use in various industries, from telecommunications to imaging for medical care and characterisation [78-92].

The transition from bulk nonlinear optics to guided wave nonlinear optics represents a major step because early nonlinear optical effects were frequently associated with

relatively poor efficiency due to the short interaction distances between light and matter [78-92]. Shortly after optical fibre gained popularity as a transmission medium, the field of nonlinear guided wave optics began to grow. Because light-matter interaction durations may be prolonged by several orders of magnitude, this greatly boosted the effectiveness of nonlinear optical effects (from a few centimetres to tens of kilometres) [78-80]. This research topic has been greatly enhanced by the novel physics that has subsequently emerged, and researchers in the field have, in turn, provided significant developments.

In recent years, both fundamental and applied research has been centred on materials with enhanced nonlinear optical capabilities [78-92]. Inorganic and organic semiconductors, natural and manufactured nanomaterials, molecular dyes, and polymer systems, among many other materials, all exhibit nonlinear optical properties that are useful in a wide range of applications [78-92]. Due to their broad application and capacity to maximise a nonlinear response through specifically tailored modification of their molecular structure, organic nonlinear optical materials have drawn significant attention [78-80]. Well-known nonlinear optical organic materials such as pyrrole-based porphyrins, phthalocyanines and aza/azo-benzenes contain many delocalised π-electrons [78-96]. These materials also have band gaps of 2−3 eV and reasonably strong nonlinearities.

For major multi-disciplinary domains, such as fluorescence bio-mapping, photodynamic treatment, and organic photovoltaics, the development of new aza-boron-dipyrromethene (aza-BODIPY) molecular structures with unique linear photophysical and nonlinear optical (NLO) properties are significant [90, 91]. It should be emphasised that rapid excited-state charge transfer events and the NLO features of aza-BODIPY derivatives are of interest for a range of different real-world

applications [90, 91], including 3D micro-fabrication, optical data storage, optical signal processing, and optical limiting (OL) devices [78-96].

The comparatively weak absorption at 532 nm and throughout most of the visible range for NIR dyes such as aza-BODIPYs makes the dyes potentially suited as nonlinear optical limiters [90, 91]. Since the human eye is most sensitive to the green area of the visible spectrum, the second harmonic of Nd/YAG laser systems at 532 nm is particularly problematic from the perspective of the careless usage of laser points during the landing approaches of aircraft [78-96]. In recent years, a wide variety of NIR dyes, including BODIPY and, to a lesser extent, aza-BODIPY dyes, have had their optical limiting qualities examined using the open-aperture Z-scan approach.

The open-aperture Z-scan (**Figure 10**) method has been used to examine the nonlinear characteristics of a variety of optical materials and is regarded as the best approach for examining the nonlinear absorption (NLA) features of molecular dyes [97]. The sample cuvette is translated along the z-direction (i.e., the laser beam propagation direction) so that it lies both inside and outside a focus point produced by a lens. A polarised Gaussian laser beam is then directed perpendicular to the plane of the cuvette. Due to a change in transmission along the z-axis as the laser light intensity increases, normalised transmittance is displayed as a function of sample position, resulting in convex-shaped curves [78-97]. At high light intensities, a downward drop is consistent with reverse saturable absorption (RSA), which also exhibits high third-order susceptibility (Im[$\chi^{(3)}$]) and second-order hyperpolarisability (γ) values [97]. If excited state absorption (ESA) from the S_1 and/or T_1 states that are populated by a nanosecond pulse of laser excitation is stronger than the ground state one-photon absorption (1PA) would have been otherwise, an RSA response associated with NLA is detected (**Figure 11**) [97]. In contrast, saturable absorbance is observed, and there

is an increase in light transmission at the lens focus if the ESA is weaker than the 1PA from the ground state.

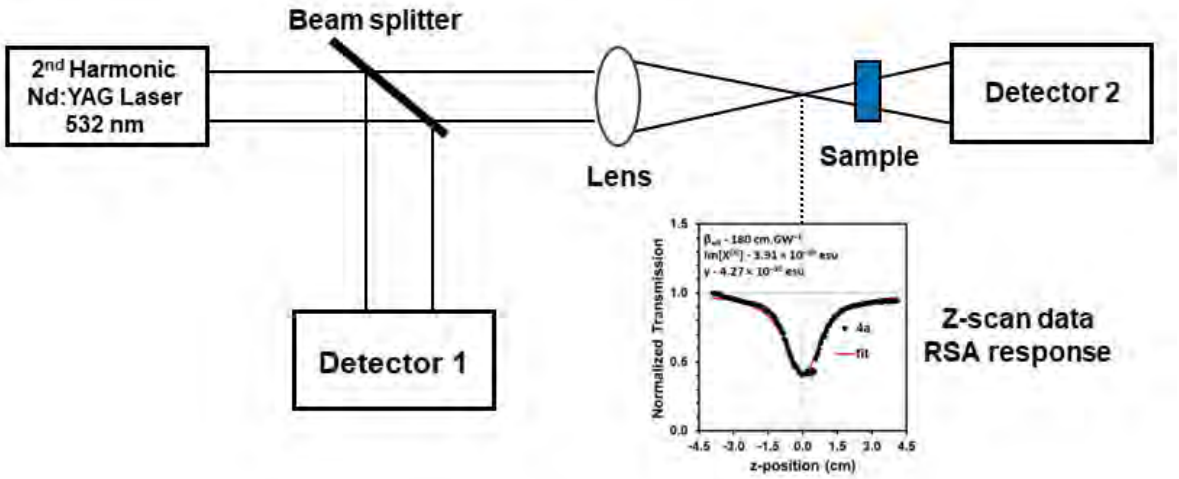

Figure 10. A schematic of the open-aperture Z-scan experimental setup (TOP) and an illustration of a reverse saturable absorption response (BOTTOM RIGHT).

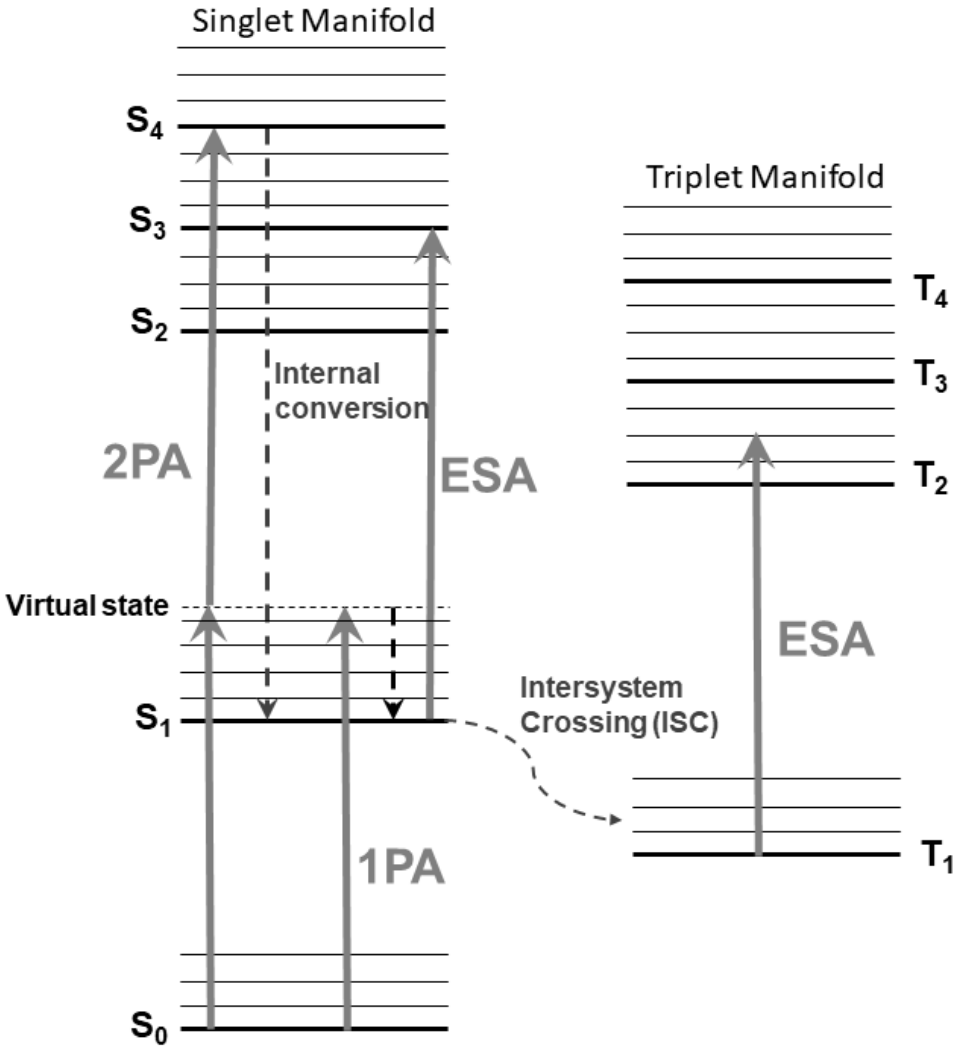

Figure 11. A Jablonski diagram depicting molecular-based NLO photophysical processes [97].

Equation 3 can be used to determine the normalised transmittance of the open-aperture measurement for a Gaussian laser pulse time profile.

$$T(z) = \frac{1}{\sqrt{\pi} q_0(z)} \int_{-\infty}^{\infty} \ln[1 + q_0(z) e^{-\tau^2}]\, d\tau \quad \text{..... (3)}$$

where the nonlinear magnitude is indicated by $q_0(z)$. The provided $q_0(z)$ value for beams with a circular response cross-section is given by Equation 4:

$$q_0(z) = \frac{2\beta_{eff} P_0 l_{eff}}{\pi \omega(z)^2} \quad \text{..... (4)}$$

where β_{eff} is the effective nonlinear absorption coefficient, P_0 is the laser pulse peak power, and l_{eff} is the effective pathlength specified by Equation 5:

$$l_{\text{eff}} = \frac{1-e^{(-\alpha L)}}{\alpha} \quad \text{..... (5)}$$

where α is the linear absorption coefficient, and L is the path length of the material. The beam width in Equation 4 as a function of sample position (z) can be determined using Equation 6:

$$\omega(z) = \omega_0\sqrt{1+\left(\frac{z}{z_0}\right)^2} \quad \text{..... (6)}$$

where z and z_0 are the sample's translational distances from the focus, z is the focus's Rayleigh length (z_0), defined as $\pi\omega_0^2/\lambda$ (λ is the laser's wavelength), and ω_0 is the focus's beam waist or the distance from the incident laser beam's centre to the point where its intensity drops to $1/e^2$ of its axis value. Equations 3−6 can be used to determine the effective nonlinear absorption coefficient or β_{eff}, given experimentally determined transmittance. The analytical version of Equation 7 can be utilised to directly derive $q_0(z)$ from the normalised transmittance:

$$T(z) = 0.363e^{\left(\frac{-q_0(z)}{5.60}\right)} + 0.286e^{\left(\frac{-q_0(z)}{1.21}\right)} + 0.213e^{\left(\frac{-q_0(z)}{24.62}\right)} + 0.096e^{\left(\frac{-q_0(z)}{115.95}\right)} + 0.038e^{\left(\frac{-q_0(z)}{965.08}\right)}$$

..... (7)

If Equation 6 is substituted into Equation 4, the $q_0(z)$ value can be defined as:

$$q_0(z) = \frac{Q_0}{1+\frac{z^2}{z_0^2}} \quad \text{..... (8)}$$

where Q_0 is given as:

$$Q_0 = \frac{2\beta_{\text{eff}}P_0 l_{\text{eff}}}{\pi\omega_0^2} \quad \text{..... (9)}$$

A Gaussian curve with a maximum of Q_0 at z = 0 can be derived from Equation 7. The peak value and full width at half maximum (FWHM) determined experimentally provide values for z_0 and Q_0, respectively. Equation 10 can be used to calculate the value of β_{eff}, an important parameter for determining the suitability of molecular dyes for optical limiting applications:

$$\beta_{eff} = \frac{\lambda z_0 Q_0}{2P_0 l_{eff}} \quad \text{..... (10)}$$

The imaginary component of the third-order nonlinear susceptibility ($Im[\chi^{(3)}]$) quantifies he response speed to an incident intense laser pulse and can be derived from β_{eff} using Equation 9:

$$Im\left[\chi^{(3)}\right] = \frac{n^2 \varepsilon_0 c \lambda \beta_{eff}}{2\pi} \quad \text{..... (11)}$$

Where ε_0, η and c are the permittivity of free space, the linear refractive index and the speed of light, respectively. The interaction between the permanent dipole of molecules and incident intense laser pulses results in a bias in the orientation of the dye molecules, resulting in induced hyperpolarizability. The second-order hyperpolarizability parameter can be derived from the $Im[\chi^{(3)}]$ value in the manner shown in Equation 12:

$$\gamma = \frac{Im\left[\chi^{(3)}\right]}{f^4 C_{mol} N_A} \quad \text{..... (12)}$$

Where N_A, C_{mol}, and f are Avogadro's constant, the molar concentration of the active species in the excited state, and the Lorentz local field factor, f = (η2 + 2) / 3,

respectively. In this study, NLO and fast relaxation processes were examined using open-aperture Z-scan measurements (see structures in **Table 1**).

1.7. Photosensitisers studied in this work

The aza-BODIPY dyes studied are shown in **Table 1. 1−4** are novel compounds. Iodine atoms are present at the 2,6-positions in all the complexes to enhance the rate of ISC and, hence, singlet oxygen generation. When choosing the substituents for **1a, 1, 2a** and **2**, the 4-methylthiobenzaldehyde was chosen for conjugation of the aza-BODIPYs to gold nanoparticles since gold nanoparticles have high affinity for sulfur. The 3-thienyl substituents of **2a** and **2** were chosen for red shifting the main absorption bands towards the NIR since electron donating groups have been reported to have that ability [32] For **3a**, **3**, **4a** and **4,** 4-hydroxyl group was specifically chosen for conjugation to the carboxylic acid group of folic acid to form an ester bond. The 4-bromide substituents were chosen for post modification of the compounds. Iodine atoms were chosen for substitution at the 2,6-positions of the aza-BODIPYs because they are heavier than bromine atoms. As such, they are expected to facilitate higher intersystem crossing, thus higher production of singlet oxygen quantum yields.

AuNPs were used to conjugate complexes **1** and **2**, while FA was used to conjugate complexes **3** and **4**. Singlet oxygen and its usefulness in inhibiting cancer cell growth *in vitro* is described in this study. **1**, **2**, **3** and **4** were synthesised and applied in PACT for the photoinactivation of *S. aureus.* The porphyrins used in this work are shown in **Table 1**. **5** and **6** have been reported previously, while **5-FA**, **5-FAQ**, **6-FA** and **6-FAQ** are new. **5**, **5-FA** and **5-FAQ** contain Sn(IV) as a central metal ion, while **6**, **6-FA** and **6-FAQ** contain indium (In) as a central metal. The presence of central metal is known to enhance ISC and the rate of singlet oxygen generation. 4-pyridine carboxaldehyde

was specifically chosen to enable post quaternisation of the compounds because charged porphyrins are soluble in aqueous media and are more biocompatible than their water-insoluble counterparts. The novelty of the porphyrins was achieved through the conjugation of folic acid at the axial position of the porphyrins. Further inactivation of *S. aureus* was performed using porphyrins (**18a**, **18**, **19a**, **19**), which were donated by a former postdoctoral researcher at Rhodes University (Dr Balaji Babu). Their full characterisation can be found in the literature [98]. The efficiency of these complexes in generating singlet oxygen and their usefulness in inhibiting cancer cell growth *in vitro* is described in this work.

Table 1. Photosensitisers prepared and applied in this work.

	Structure	Modification strategy	Applications
1a	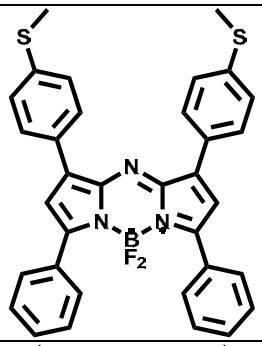		NLO PACT
1	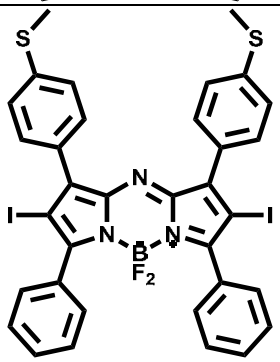	AuNPs	NLO PDT PACT
2a	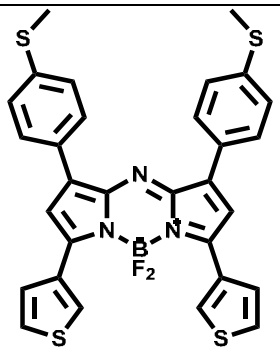		NLO PDT PACT
2	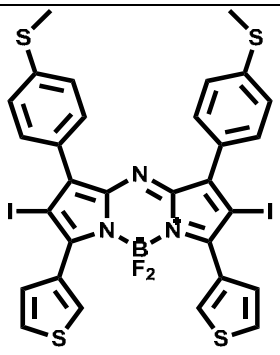	AuNPs	NLO PDT PACT

3a	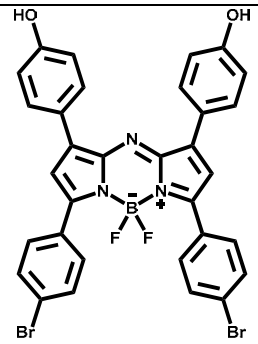		NLO PDT
3	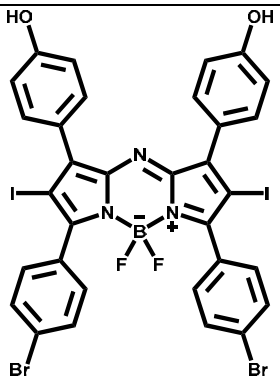		NLO PDT
3-FA	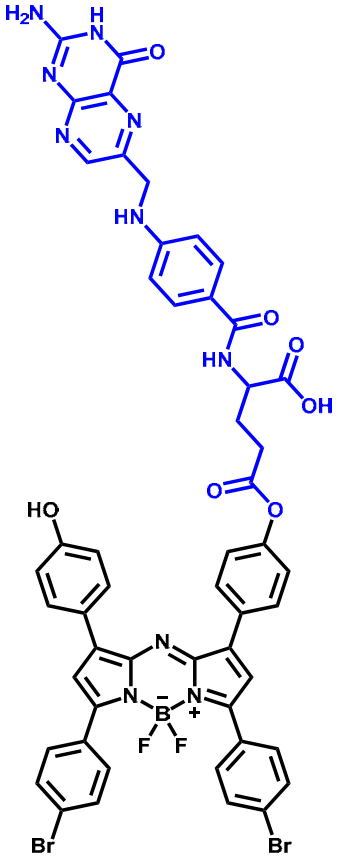	Folic acid	PDT

4a	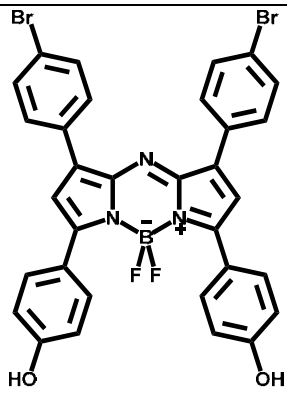		NLO PDT
4	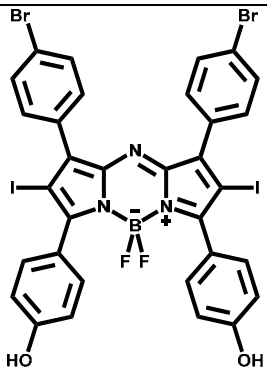		NLO PDT
4-FA	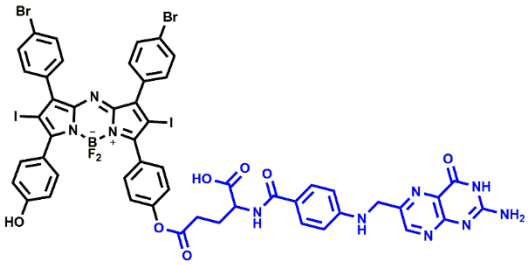	Folic acid	PDT
5	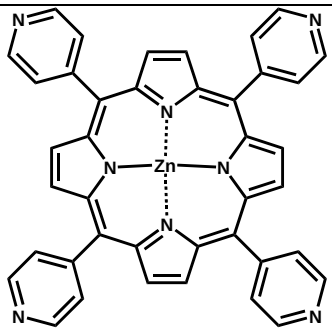		PDT

5-FA	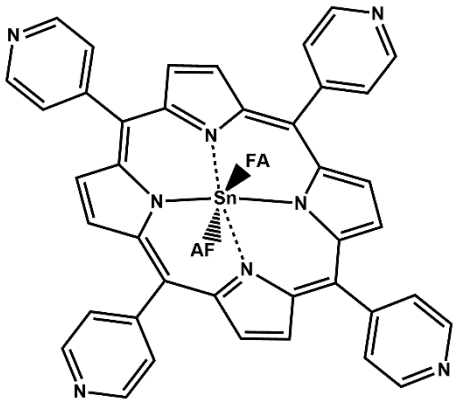	Folic acid	PDT
5-FAQ	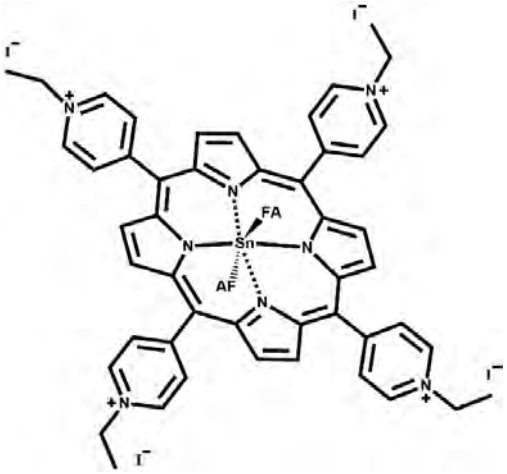	Folic acid	PDT
6	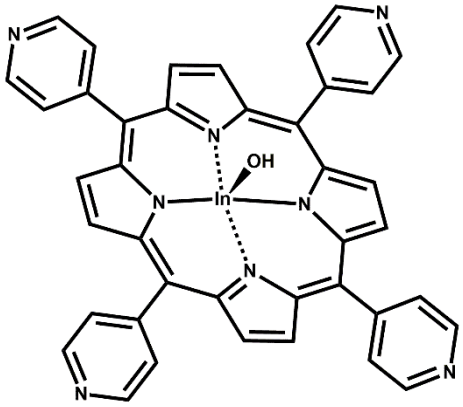		PDT

6-FA	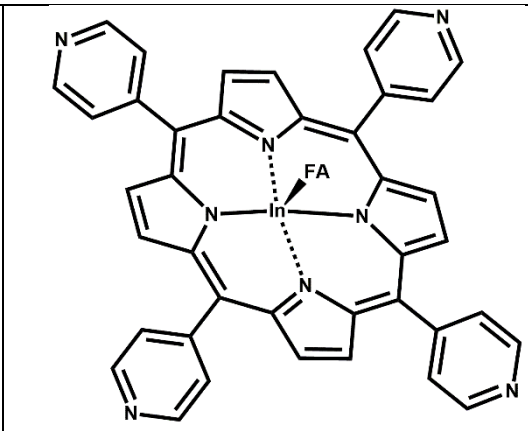	Folic acid	PDT
6-FAQ	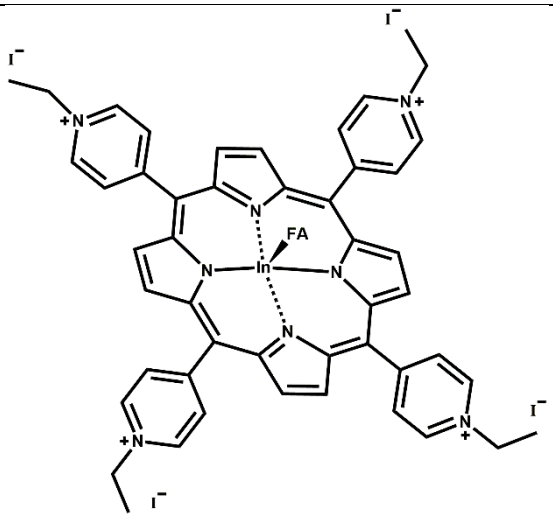	Folic acid	PDT
18a	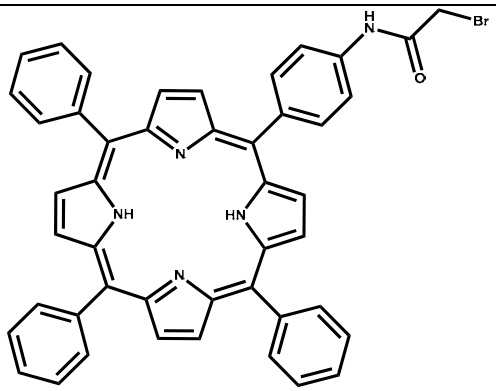		PACT
18	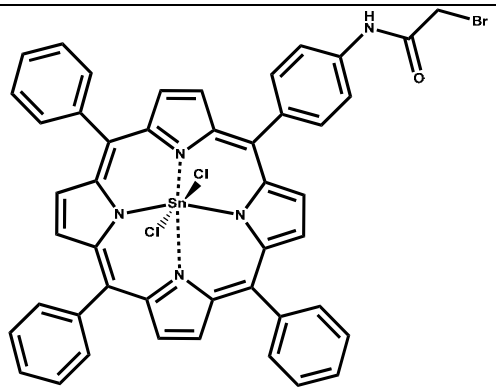		PACT

19a	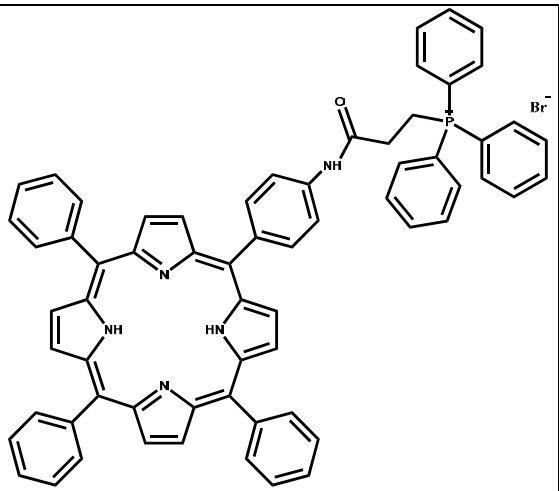	Triphenylphosphonium	PACT
19	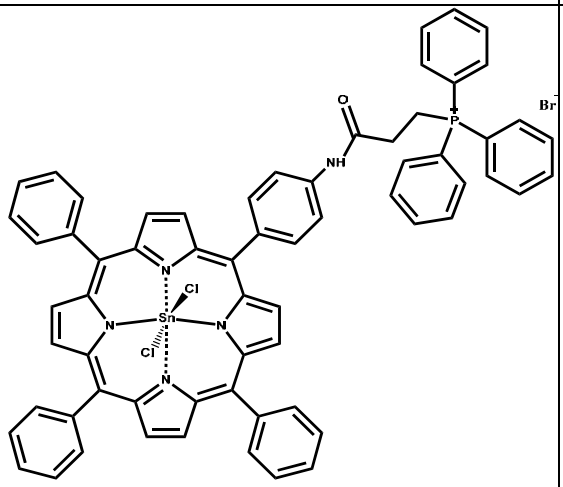	Triphenylphosphonium	PACT

1.8. Aims

The aims of this study can be summarised as follows:

1. Synthesis, characterisation and photophysical studies of 2,6-diiodinated-1,3,5,7-tetraaryl-aza-BODIPYs for photodynamic therapy.
2. Preparation of 2,6-diiodinated-1,3,5,7-tetraaryl-aza-BODIPYs conjugated to AuNP dyes for photodynamic therapy.
3. Application of 2,6-diiodinated-1,3,5,7-tetraaryl-aza-BODIPYs in PACT.

4. Preparation of 2,6-diiodinated-1,3,5,7-tetraaryl-aza-BODIPY-folic acid conjugates for targeted photodynamic therapy studies.
5. Synthesis of novel tetraapyridylporphyrin-FA derivatives and their application *in vitro* against MCF−7 cancer cells.
6. Application of the porphyrin derivatives **18a**, **18**, **19a**, **19** for PACT against *S. aureus.*
7. A study of the optical limiting properties of the aza-BODIPY and porphyrin dyes.
8. Molecular modelling studies to identify trends in the electronic structures and optical properties of the aza-BODIPY and porphyrin dyes.

Chapter 2: Experimental

2.1. Materials

Nitromethane, diisopropylamine, methylene blue, 1,3-diphenylisobenzofuran (DPBF), DMA, dimethylsulfoxide (DMSO), ethanol (EtOH), dimethylformamide (DMF), dichloromethane (DCM), 4-methylthiobenzaldehyde, acetophenone, 2-acetylthiophene, 4-pyridinecarboxylaldehyde, 4-hydroxybenzaldehye, 4-hydroxyacetophenone, 4-bromobenzaldehyde, 4-bromoacetophenone, iodoethane, *N*-iodosuccinimide (NIS), ammonium acetate, boron trifluoride diethyl etherate ($BF_3 \cdot OEt_2$), *N,N*-diisopropylethylamine (DIPEA), dicyclohexylcarbodiimide (DCC), *N*-hydroxysuccinimde (NHS), trifluoroacetic acid (TFA), H_2TPP, zinc tetraphenylporphyrin (ZnTPP), and triethylamine (TEA) were purchased from Sigma-Aldrich. Unless otherwise stated, all reagents obtained from commercial suppliers were used without further purification. Ultrapure water was sourced from a Milli−Q Water System (Millipore Corp, Bedford, MA, USA). Dry solvents were used for all reactions, and atmospheric air and moisture-sensitive reactions were carried out under argon gas. 100 unit/mL penicillin−100 µg/mL streptomycin–amphotericin B and Heat-inactivated fetal calf serum (FCS) were purchased from Biowest®. MCF-7 cell cultures were acquired from Cellonex®. Dulbecco's modified Eagle's medium (DMEM) and Dulbecco's phosphate−buffered saline (DPBS) were obtained from Lonza®. Water-Soluble Tetrazolium salt 1 (WST−1) cell-proliferation assay was obtained from Sigma-Aldrich.

2.2. Equipment

- ^1H nuclear magnetic resonance (NMR) measurements were performed on a Bruker AMX 600 MHz instrument.

- Mass spectral data were obtained on a Bruker Auto-FLEX III Smart beam matrix-assisted laser desorption/ionisation-time of flight (MALDI-TOF) mass spectrometer running in positive or negative ion mode with α-cyano-4-hydroxycinnamic acid as the matrix.
- Ultra-violet visible (UV-visible) absorption spectra were measured with a Shimadzu UV-2550 spectrometer.
- Fluorescence emission spectra were measured with a Varian Eclipse spectrofluorimeter.
- Fluorescence lifetimes were acquired using a time-correlated single photon counting spectrometer (FluoTime 300, Picoquant GmbH).
- Fourier transform-infrared (FT-IR) spectra were acquired from a Bruker Alpha FT-IR spectrometer fitted with a universal attenuated total reflectance (ATR) sampling accessory.
- Monochromatic laser light (400–700 nm) from an Ekspla NT 342B-20-AW nanosecond pulsed laser (20 Hz, 2.0 mJ/5 ns) was used to determine the $^1O_2$ quantum yields of compounds with either DPBF or DMA as the $^1O_2$ quencher.
- Transmission electron microscopy (TEM) was carried out on a Zeiss Libra model 120 instrument operated at 90 kV to determine the sizes and morphologies of the AuNPs and the AuNP conjugates.
- Dynamic light scattering (DLS) measurements were made on a Malvern Zetasizer Nano series Nano-ZS90 to determine the size of AuNPs and the gold nanoparticle conjugates.
- Powder X-ray diffraction (XRD) data were measured on a Bruker D8 Diffractometer fitted with a Lynx Eye detector and Cu K_α (λ=1.5405 Å) at a

scanning rate of 192 s per step. Zero background silicon wafer slide sample holders were used.

- Elemental compositions of gold nanoparticle conjugates were determined qualitatively by energy dispersive X-ray spectroscopy (EDS) using an INCA PENTA FET coupled to a VAGA TESCAM operated at a 20 kV accelerating voltage.
- The lengau cluster at the Centre for High Performance Computing in Cape Town provided the resources necessary to perform theoretical calculations with the Gaussian 09 software package [99] running on an Intel/Linux operating system. Geometry optimisations were performed with the Beck, three-parameter, Lee-Yang-Parr (B3LYP) exchange-correlation functional and SDD basis sets. The coulomb-attenuated B3LYP (CAM-B3LYP) functional was used for time-dependent DFT (TD-DFT) calculations with SDD basis sets. Molecular orbitals (MOs) were visualised on Avogadro [99, 100].
- MCF−7 cells human breast cancer cells were cultured in 25 cm^2 vented flasks (Porvair®), subcultured in 75 cm^2 vented flasks (Porvair®) in an incubator (Heal Force) under a humidified 5% CO_2 atmosphere at the physiological temperature of 37°C. A Zeiss-AxioVert A fluorescence light emitting diode (FL-LED) inverted microscope was used to view the cells under phase contrast. WST−1 cell proliferation neutral red reagent (Roche) was used to determine the cell viability through a Synergy 2 multi-mode microplate reader (BioTek®). PDT studies were conducted with a Thorlabs M660L4 (280 $mW.cm^{-2}$) or M730L4 (160 $mW.cm^{-2}$) LED mounted on the illumination chamber of Modulight® 7710-680 medical laser system providing doses at the well-plate of 100 and 57 $J.cm^{-2}.min^{-1}$,

respectively. A Fluorescence LED (FL-LED) inverted microscope was used to view the cells under phase contrast (Zeiss-AxioVert).

- The optical density of the bacteria culture was determined using the Ledetect 96 microplate reader (Labxim Products).
- PBS buffer, nutrient broth and agar, and the apparatuses used for the bacterial and cancer studies were sterilised with a China Medical Device RAU-530D autoclave.
- A Vortex mixer (Lasiec) was used to homogenise the bacteria suspension.
- Bacteria were harvested from suspensions with a Hermle Z233M-2 centrifuge from Lasiec.
- The colony-forming units (CFU)/mL values for the bacteria were determined with a Scan® 500 automatic colour colony counter.

2.3. Theoretical calculations

Geometry optimisations were performed at the B3LYP/6-31G(d) level of theory for the dyes studied by using the Gaussian 09 software package [99, 100]. Because the CAM-B3LYP functional includes a long-range adjustment, TD-DFT calculations were performed in the same way [99, 100].

2.4. Syntheses of aza-BODIPY dyes

2.4.1. 3-(4-(methylthio)phenyl)-1-phenylprop-2-en-1-one

The chalcone was synthesised through a base-catalysed Aldol condensation of 4-methylthiobenzaldehyde (639 mg, 6.02 mmol) and acetophenone (1000 mg, 6.92 mmol) in 40 mL ethanol at ambient conditions [101, 102]. 60% potassium hydroxide was added. The reaction was monitored with TLC, quenched after 4 h over ice, and

then allowed to stand overnight. The product was filtered. The yellow product obtained was recrystallised using ethanol and dried in air.

Yield: 95% (1531 mg). ^{1}H NMR (400 MHz, DMSO-d_6) δ_H, ppm 7.32 (d, J = 7.7 Hz, 2H), 7.06 (s, 1H), 7.01 (d, J = 8.3 Hz, 2H), 6.92 (s, 1H), 6.84 (d, J = 7.1 Hz, 1H), 6.75 (d, J = 15.2 Hz, 2H), 6.50 (d, J = 8.2 Hz, 2H), 1.71 (s, 3H).

2.4.2. 3-(4-(methylthio)phenyl)-3-nitro-1-phenylpropan-1-one

The nitro-derivative was obtained through the reflux of nitromethane (2.87 mL) to the chalcone (1750 mg, 10.6 mmol) in basic media using sodium hydroxide (2−4 pellets) and ethanol (50 mL) as solvent [101, 102]. After 20 h, the reaction was quenched, and the product was extracted with DCM. No purification was performed.

2.4.3. 1,7-(4-(methylthio)phenyl)-3,5-(-phenyl)-4a-diaza-s-indacene

The azadipyrromethene was synthesised following a modified procedure following methods reported in the literature [101, 102]. 3-(4-(Methylthio)phenyl)-3-nitro-1-phenylpropan-1-one (1.59 g, 0.0050 mol) and ammonium acetate (7.76 g, 0.10 mol) were dissolved in 30 mL butanol/acetic acid (3:2). The mixture was refluxed and monitored using TLC and UV-visible absorption spectroscopy over 12 h. After 12 h, the reaction was quenched. The azadipyrromethene was isolated using silica chromatography with DCM as an eluent and then air-dried.

Yield: 73.2% (1.10 g). ^{1}H NMR (600 MHz, $CDCl_3$) δ_H, ppm 8.01 (d, J = 8.1 Hz, 4H), 7.96 (d, J = 7.5 Hz, 4H), 7.56 (t, J = 7.4 Hz, 4H), 7.33 (d, J = 8.1 Hz, 4H), 7.18 (s, 2H), 6.32 (s, 2H), 2.59 (s, 6H). MALDI-TOF MS: anticipated mass (Calcd for $C_{34}H_{27}N_3S_2$): 541.16 amu; observed mass: m/z = 542.43 $[M+H]^+$.

*2.4.4. 4,4'-Difluoro-1,7-(4-dimethylthio)phenyl)-5,7-(phenyl)-4-bora-3a,4a-diaza-s-indacene (**1a**)*

The target aza-BODIPY derivative **1a** was obtained by complexing the azadipyrromethene (86.2 mg, 0.159 mmol) with boron trifluoride diethyl etherate (291 mg, 2.04 mmol) and DIPEA (206 mg, 1.59 mmol) under reflux in DCM (20 mL) for 12 h [101, 102]. Silica chromatography was used to separate the metallic blue product in appreciable yield.

Yield: 77% (721 mg). ^{1}H NMR (400 MHz, $CDCl_3$) δ_H, ppm 8.05–7.99 (m, 8H), 7.50–7.46 (m, 6H), 7.32 (d, *J* = 8.5 Hz, 4H), 6.98 (s, 2H), 2.57 (s, 6H). MALDI-TOF MS; anticipated mass (Calcd for $C_{34}H_{26}B_1N_3F_2S_2$): 589.54 amu; observed mass: m/z = 589.83 $[M]^+$.

*2.4.5. 4,4'-Difluoro-1,7-(4dimethylthio)phenyl)-5,7-(phenyl)-2,6-diiodo-4-bora-3a,4a-diaza-s-indacene (**1**)*

1a (422 mg, 0.716 mmol) and NIS (40.3 mg, 0.179 mmol) in DCM (20 mL) were reacted in ambient conditions for 16 h [101]. The product was precipitated, washed with ethanol, and dried *in vacuo*.

Yield: 80% (120 mg). ^{1}H NMR (600 MHz, $CDCl_3$) δ_H, ppm 7.81 (d, J = 8.4 Hz, 4H), 7.66 (d, J = 7.5 Hz, 4H), 7.56 (d, J = 8.6 Hz, 2H), 7.38 (s, 2H), 7.32 (d, J = 8.4 Hz, 4H), 7.15 (dd, J = 8.6, 2.6 Hz, 2H), 2.58 (s, 6H). MALDI-TOF MS; anticipated mass (Calcd for $C_{34}H_{24}B_1N_3F_2S_2I_2$): 841.33 m/z; observed mass: m/z = 716.64 $[M-I+2H]^+$ (Calcd for $C_{34}H_{26}B_1N_3F_2S_2I_1$: 716.44 amu), 696.59 $[M-I-F+H]^+$ (Calcd for $C_{34}H_{25}B_1N_3F_1S_2I_1$: 696.44 amu).

2.4.6. 3-(4-(Methylthio)phenyl)-1-(thiophen-3-yl)prop-2-en-1one

The chalcone was synthesised through a simple Aldol condensation reaction described in Section 2.4.1. [101, 102]. The dark yellow product was obtained in high yields.

Yield: 96% (983 mg). ^{1}H NMR (400 MHz, $CDCl_3$) δ_H, ppm 8.00 (d, *J* = 8.5 Hz, 1H), 7.64–7.58 (m, 3H), 7.54–7.50 (m, 2H), 7.32 (d, *J* = 5.0 Hz, 2H), 7.27 (d, *J* = 8.3 Hz, 4H), 7.16 (s, 1H), 7.06–7.02 (m, 2H), 2.45 (s, 6H).

2.4.7. 3-(4-(Methylthio)phenyl)-3-nitro-1-(thiophen-3-yl)propan-1-one

The nitro-derivative was obtained through a Michael addition reaction described in Section 2.4.2. [101, 102].

2.4.8. 1,7-(4-(methylthio)phenyl)-3,5-(thiophen-3-yl)-4a-diaza-s-indacene

The azadipyrromethene was obtained as described in Section 3.4.3 [101,102].

Yield: 88.6% (1.03 g). ^{1}H NMR (400 MHz, $CDCl_3$) δ_H, ppm 7.66 (s, 2H), 7.47 (d, *J* = 8.3 Hz, 2H), 7.42 (d, *J* = 5.0 Hz, 2H), 7.38 (dd, *J* = 8.2, 5.3 Hz, 5H), 7.20 (s, 4H), 6.30 (s, 2H), 2.55 (d, *J* = 1.9 Hz, 6H). MALDI-TOF MS; Anticipated mass (Calcd for $C_{30}H_{23}N_3S_4$): 553.79 amu; Observed mass: 555.88 $[M+2H]^+$.

*2.4.9. 4,4'-Difluoro-1,7-(4dimethylthio)phenyl)-5,7-(thiophen-3-yl)-4-bora-3a,4a-diaza-s-indacene (**2a**)*

The azadipyrromethene (543 mg, 0.903 mmol) was complexed using boron trifluoride diethyl etherate (1794 mg, 12.6 mmol) and DIPEA (1.17 mg, 9.03 mmol) under reflux in DCM (20 mL) for 12 h [101, 102]. The metallic blue product was isolated using silica chromatography.

Yield: 79% (1417 mg). ^{1}H NMR (400 MHz, $CDCl_3$) δ_H, ppm 7.31 (d, *J* = 3.7 Hz, 4H), 7.23 (s, 2H), 7.03 (d, *J* = 4.9 Hz, 4H), 6.97 (s, 4H), 6.86 (s, 2H), 2.15 (s, 6H). MALDI-TOF MS; anticipated mass (Calcd for $C_{30}H_{22}B_1N_3F_2S_4$): 601.59 amu; observed mass: m/z = 601.53 $[M]^+$.

*2.4.10. 4,4'-Difluoro-1,7-(4dimethylthio)phenyl)-5,7-(thiophen-3-yl))-2,6-diiodo-4-bora-3a,4a-diaza-s-indacene (**2**)*

2a (940 mg, 1.56 mmol) and NIS (880 mg, 3.91 mmol) in DCM (20 mL) were reacted in ambient conditions for 16 h [101]. The product was precipitated, washed with ethanol, and dried *in vacuo.*

Yield: 86% (1144 mg). ^{1}H NMR (400 MHz, $CDCl_3$) δ_H, ppm 7.68 (d, *J* = 3.7 Hz, 2H), 7.63 (d, *J* = 2.5 Hz, 4H), 7.60 (s, 2H), 7.40 (d, *J* = 5.0 Hz, 2H), 7.36 (d, *J* = 8.4 Hz, 4H), 2.53 (d, *J* = 1.5 Hz, 6H). MALDI-TOF MS; anticipated mass (Calcd for $C_{30}H_{20}B_1N_3F_2S_4I_2$): 853.39 amu; observed m/z = 727.50 $[M-I+H]^+$ (Calcd for $C_{30}H_{21}B_1N_3F_2S_4I_1$: 727.49 amu).

*2.4.11. **1**@**AuNPs** and **2**@**AuNPs** conjugates*

AuNPs were synthesised using the protocols described in the literature [103-105]. Excess AuNPs were added to a DMF (15 mL) solution of **1** or **2** (100 mg), and the mixture was agitated for 24 h at room temperature. After removing the supernatant, the conjugated AuNPs (**1**@**AuNPs** or **2**@**AuNPs**) solutions were centrifuged for 30 min and re-dispersed in aqueous solution. The products were dried in air and then stored.

Yield (**1**@**AuNPs**): 96.3 mg.

Yield (**2**@**AuNPs**): 93.5 mg.

2.4.12. 1-(4-Bromophenyl)-3-(4-hydroxyphenyl)prop-2-en-1-one

The chalcone was synthesised as described in Section 2.4.1. [101, 102].

Yield: 97% (988 mg). ^{1}H NMR (400 MHz, DMSO-d_6) δ_H, ppm 9.38 (s, 1H), 7.25 (d, *J* = 8.4 Hz, 2H), 7.07 (d, *J* = 8.4 Hz, 2H), 6.96 (s, 1H), 6.93 (d, *J* = 3.2 Hz, 3H), 6.91 (s, 1H), 6.88 (s, 2H).

2.4.13. 1-(4-bromophenyl)-3-(4-hydroxyphenyl)-3-nitropropan-1-one

The nitro-derivative was obtained in the manner described in Section 2.4.2. [101, 102].

2.4.14. 1,7-(4-(Bromophenyl)-3,5-(4-hydroxyphenyl)-4a-diaza-s-indacene

The azadipyrromethene was achieved through complexation on the nitro-derivative above, using the procedure described in Section 2.4.3. [101, 102].

Yield: 85% (540 mg). ^{1}H NMR (400 MHz, $CDCl_3$) δ_H, ppm 7.85 (d, *J* = 8.6 Hz, 4H), 7.67 (d, *J* = 8.3 Hz, 4H), 7.59 (d, *J* = 8.5 Hz, 5H), 7.25 (s, 1H), 6.87 (d, *J* = 8.6 Hz, 4H), 6.77 (s, 2H). MALDI-TOF MS; anticipated mass (Calcd for $C_{32}H_{21}N_3O_2Br_2$): 639.35 m/z; observed mass: 640.23 $[M+H]^+$.

*2.4.15. 4,4'-Difluoro-1,7-(4-(bromophenyl)-3,5-(4-hydroxyphenyl)-diaza-s-indacene (**3a**)*

The synthesis of the aza-BODIPY dye **3a** was achieved using the procedure described in Section 2.4.4. [101, 102].

Yield: 77% (600 mg). ^{1}H NMR (400 MHz, $CDCl_3$) δ_H, ppm 7.97 (d, *J* = 8.8 Hz, 4H), 7.88 (d, *J* = 8.7 Hz, 4H), 7.61 (s, 4H), 7.36 (s, 2H), 6.95 (d, *J* = 8.9 Hz, 4H), 6.86 (s, 2H). MALDI-TOF MS; anticipated mass (Calcd for $C_{32}H_{20}B_1N_3O_2F_2Br_2$): 687.15 amu;

observed mass: 688.31 $[M+H]^+$; 668.34 $[M-F]^+$ (Calcd for $C_{32}H_{20}B_1N_3O_2F_1Br_2$: 668.15).

*2.4.16. 4,4'-Difluoro-1,7-(4-(Bromophenyl)-3,5-(4-hydroxyphenyl)-2,6-diiodo-4a-diaza-s-indacene (**3**)*

3a (530 mg, 0.771 mmol) and NIS (173 mg, 1.93 mmol) in DCM (20 mL) were reacted in ambient conditions for 16 h [101]. The product was precipitated, washed with ethanol and dried *in vacuo.*

Yield: 79% (522 mg), ^{1}H NMR (400 MHz, $CDCl_3$) δ_H, ppm 8.01 (s, 2H), 7.93 (d, *J* = 8.7 Hz, 4H), 7.60 (d, *J* = 8.8 Hz, 8H), 7.18 (d, *J* = 5.6 Hz, 2H), 6.99 (d, *J* = 7.9 Hz, 2H). MALDI-TOF MS; anticipated mass (Calcd for $C_{32}H_{18}B_1N_3O_2F_2Br_2I_2$): 938.94 amu; observed mass: 925.66 $[M-OH-F+Na]^+$ (Calcd for $C_{32}H_{17}B_1N_3O_1F_1Na_1Br_2I_2$: 925.92 amu).

*3.4.17. Aza-BODIPY **3**@folic acid conjugate (**3-FA**)*

The aza-BODIPY@FA conjugates were prepared following previously reported procedures with minor modifications [69-72]. Briefly, FA (100 mg, 0.23 mmol) in dry DMF (3 mL) was activated NHS (9.78 mg, 0.085 mmol) and a coupling reagent, DCC (17.5 mg, 0.085 mmol) in DMF (2 mL) added. The reaction mixture was degassed, and TEA (0.2 mL) was added to catalyse the reaction. The reaction was stirred at ambient conditions for 48 h and monitored *via* TLC. After 48 h, aza-BODIPY **3** (21.8 mg, 0.057 mmol) in DMF (1 mL) was gradually added to the activated FA and then further stirred for 72 h. The γ-conjugated product (**3-FA**) was isolated *via* precipitation in diethyl ether. The conjugation was confirmed using FT-IR, X-ray photoelectron spectroscopy (XPS) and ^{1}H NMR.

Yield: 43% (33 mg). ^{1}H NMR (400 MHz, DMSO-d_6) δ_H, ppm 8.64 (s, 2H), 8.28 (s, 1H), 7.95 (s, 1H), 7.63 (d, *J* = 8.7 Hz, 4H), 6.92 (dd, *J* = 27.4, 21.4 Hz, 6H), 6.63 (d, *J* = 8.8 Hz, 4H), 4.49 (d, *J* = 5.9 Hz, 4H), 4.30 (dd, *J* = 13.6, 8.0 Hz, 2H), 3.41 (s, 1H), 3.40 (s, 2H), 3.38 (s, 2H), 3.36 (s, 1H), 3.18 (s, 1H), 2.74 (s, 4H).

2.4.18. 3-(4-Bromophenyl)-1-(4-hydroxyphenyl)prop-2-en-1-one

The chalcone was synthesised through a simple aldol condensation reaction, as described in Section 2.4.1. [101, 102].

Yield: 94% (899 mg). ^{1}H NMR (400 MHz, DMSO-d_6) δ_H, ppm 9.27 (s, 1H), 7.19 (d, *J* = 8.4 Hz, 2H), 6.91 (s, 1H), 6.88 (d, *J* = 7.9 Hz, 3H), 6.83 (s, 2H), 5.98 (d, *J* = 8.4 Hz, 2H).

2.4.19. 1-(4-bromophenyl)-3-(4-hydroxyphenyl)-4a-diaza-s-indacene

The nitro-derivative was obtained following the procedure described in Section 2.4.3. No purification was performed [101, 102].

2.4.20. 1-(4-bromophenyl)-3-(4-hydroxyphenyl)-4a-diaza-s-indacene

The azadipyrromethene was obtained from the nitro-derivative described above by following the procedure outlined in Section 2.4.4. [101, 102].

Yield: 82% (621 mg). ^{1}H NMR (400 MHz, DMSO-d_6) δ_H, ppm 9.88 (s, 2H), 7.64 (t, *J* = 8.0 Hz, 7H), 7.10 (d, *J* = 6.5 Hz, 3H), 6.91 (t, *J* = 8.3 Hz, 6H). MALDI-TOF MS; anticipated mass (Calcd for $C_{32}H_{21}N_3O_2Br_2$): 639.35 m/z; observed mass: 640.10 $[M+H]^+$.

*2.4.21. 4,4'-Difluoro-1-(4-bromophenyl)-3-(4-hydroxyphenyl)-4a-diaza-s-indacene (**4a**)*

The target aza-BODIPY **4a** was obtained through complexation of the azadipyrromethene with boron trifluoride diethyl etherate, following the procedure described in Section 2.4.5. [101, 102].

Yield: 78% (587 mg). ^{1}H NMR (400 MHz, $CDCl_3$) δ_H, ppm 8.02 (s, 2H), 7.98 (d, *J* = 8.7 Hz, 4H), 7.88 (d, *J* = 8.7 Hz, 4H), 7.61 (d, *J* = 8.7 Hz, 4H), 6.98 (d, *J* = 8.7 Hz, 4H), 6.88 (s, 2H). MALDI-TOF MS; anticipated mass (Calcd for $C_{32}H_{20}B_1N_3O_2F_2Br_2$): 687.15 amu; observed mass: 688.45 $[M+H]^+$.

*2.4.22. 4,4'-Difluoro-1-(4-bromophenyl)-3-(4-hydroxyphenyl)-2,6-diiodo-4a-diaza-s-indacene (**4**)*

4a (400 mg, 0.470 mmol) and NIS (264 mg, 1.17 mmol) in DCM (20 mL) were reacted in ambient conditions for 16 h [101, 102]. The product precipitated and was washed with ethanol and then dried *in vacuo.*

Yield: ^{1}H NMR (400 MHz, $CDCl_3$) δ_H, ppm 8.12 (d, *J* = 6.0 Hz, 2H), 8.01 (d, *J* = 5.8 Hz, 4H), 7.87 (d, *J* = 6.3 Hz, 4H), 7.77 (d, *J* = 5.8 Hz, 2H), 6.98 (d, *J* = 6.5 Hz, 4H). MALDI-TOF MS; anticipated mass (Calcd for $C_{32}H_{18}B_1N_3O_2F_2Br_2I_2$): 938.94 amu; observed m/z = 938.67 $[M]^+$.

*2.4.23. Aza-BODIPY **4**@folic acid conjugate (**4-FA**)*

The aza-BODIPY@FA conjugates were prepared following previously reported procedures with minor modifications [69-72]. Briefly, FA (100 mg, 0.23 mmol) in dry DMF (3 mL) was activated NHS (9.78 mg, 0.085 mmol) and a coupling reagent, DCC (17.5 mg, 0.085 mmol) in DMF (2 mL) added. The reaction mixture was degassed,

and TEA (0.2 mL) was added to catalyse the reaction. The reaction was stirred at ambient conditions for 48 h and monitored *via* TLC. After 48 h, aza-BODIPY **4** (21.8 mg, 0.057 mmol) in DMF (1 mL) was gradually added to the activated FA and then further stirred for 72 h. The γ-conjugated (**4-FA**) product was isolated *via* precipitation in diethyl ether. The conjugation was confirmed using FT-IR, XPS and ^{1}H NMR.

Yield: 45% (35.7 mg). ^{1}H NMR (400 MHz, DMSO-d_6) δ_H, ppm 8.64 (s, 2H), 8.01 (d, *J* = 6.9 Hz, 2H), 7.73 (d, *J* = 12.4 Hz, 1H), 7.64 (d, *J* = 8.4 Hz, 4H), 6.97 (d, *J* = 44.3 Hz, 6H), 6.64 (d, *J* = 8.6 Hz, 4H), 4.48 (d, *J* = 5.3 Hz, 4H), 4.33–4.27 (m, 2H), 3.37 (s, 1H), 3.36 (s, 1H), 3.17 (s, 1H), 2.28 (d, *J* = 7.3 Hz, 2H), 2.03–1.87 (m, 4H).

2.5. Synthesis of porphyrins

*2.5.1. 5,10,15,20-Tetrakis(4-pyridyl)porphyrin (**TPyP**)*

5,10,15,20-Tetrakis(4-pyridyl)porphyrin **(TPyP)** was prepared by following a previously reported literature procedure [106].

Yield: 76 % (352 mg). ^{1}H NMR (400 MHz, $CDCl_3$) δ_H, ppm 9.07 (d, *J* = 5.9 Hz, 8H), 8.87 (s, 8H), 8.18 (d, *J* = 5.9 Hz, 8H), −2.92 (s, 2H). MALDI-TOF MS; anticipated mass (Calcd for $C_{40}H_{26}N_8$): 618.70 amu; observed mass: m/z = 619.12 $[M]^+$.

*2.5.2. Trans-dihydroxo[meso-tetrakis(4-pyridyl)porphyrinato] tin(iv) trans-dihydroxy (**5**)*

A mixture of **TPyP** (100 mg, 0.07 mmol) and $SnCl_2$ (238 mg, 0.17 mmol) in pyridine (20 mL) was refluxed for 2 h and then cooled to room temperature [107]. Thereafter, 25% aqueous ammonia (10 mL) was added to the reaction mixture, and the reaction was stirred for 1 h [107]. The solvents were removed *in vacuo* and then purified through neutral alumina using chloroform/methanol (98:2 v/v) as an eluent.

Yield: 115 mg (92%). ^{1}H NMR (80 MHz, DMSO-d_6) δ_H, ppm 8.29 (s, 16H), 7.48 (d, J = 5.6 Hz, 8H), 0.40 (s, 2H). MALDI-TOF MS: anticipated mass (Calcd for $C_{40}H_{26}N_8O_2Sn_1$): 769.41 amu; observed mass: m/z = 768.37 $[M-H]^-$ (Calcd for $C_{40}H_{25}N_8O_1Sn_1$: 768.41 amu).

*2.5.3. Trans-dihydroxo[meso-tetrakis(4-pyridyl)porphyrinato] tin(iv) trans-folic acid (**5-FA**)*

Folic acid was activated following a previously reported procedure [69, 70]. Complex **5** (100 mg, 0.13 mmol) was dissolved in DMF (2 mL) and then gradually added to the activated folic acid solution. The reaction was monitored with TLC over a period of 3 days. The product was precipitated from solution using diethyl ether, and the pure conjugate was isolated through neutral alumina.

Yield: 119 mg (77%). ^{1}H NMR (400 MHz, DMSO-d_6) δ_H, ppm 9.17 (s, 2H), 9.09 (s, 2H), 8.66 (s, 4H), 8.14 (d, J = 7.7 Hz, 4H), 7.95 (s, 4H), 7.66 (d, J = 8.8 Hz, 8H), 6.65 (d, J = 8.8 Hz, 8H), 3.35 (s, 2H), 2.55 (d, J = 3.2 Hz, 4H), 2.32 (t, J = 7.5 Hz, 8H), 2.05 (dd, J = 9.0, 4.0 Hz, 4H), 1.96–1.88 (m, 4H).

*2.5.4. Trans-dihydroxo[meso-tetrakis(N-ethyl-pyridinium-4-yl)porphyrinato] tin(iv) trans-folic acid (**5-FAQ**)*

5 (44 mg, 0.037 mmol) and excess iodoethane (7 mL) in DMF (10 mL) were refluxed for 24 h under an inert atmosphere [108]. The reaction was cooled, and the product precipitated using excess diethyl ether. A dark purple solid was obtained.

Yield: 75% (36 mg). ^{1}H NMR (400 MHz, D_2O) δ_H, ppm 9.65 (s, 2H), 9.57 (s, 2H), 9.52 (s, 4H), 9.16 (d, J = 6.4 Hz, 8H), 8.73 (s, 2H), 8.04 (d, J = 11.2 Hz, 8H), 7.94 (s, 4H),

7.68 (d, *J* = 8.7 Hz, 8H), 3.70 (s, 8H), 3.36 (s, 12H), 2.68 (s, 4H), 2.60 (s, 4H), 2.01 (s, 4H), 1.55 (s, 4H), 1.34 (s, 4H).

*2.5.5. Trans-monohydroxo[meso-tetrakis (4-pyridyl)porphyrinato]indium (III) monohydroxy (**6**)*

A mixture of **TPyP** (155 mg, 0.25 mmol) and $InCl_3$ (0.38 mmol) was dissolved in acetic acid (25 mL) and refluxed for 16 h [106]. The reaction mixture was cooled to 0 °C, and the product precipitated from diethyl ether and dried *in vacuo*. Without further purification, the product was re-dissolved in tetrahydrofuran and reacted with an excess of potassium carbonate (1:50) in ultra-purified water for 6 h. The solvent was evaporated, and the product redissolved in an acetone/chloroform mixture and passed through anhydrous Na_2SO_4. The product was isolated using neutral alumina.

Yield: 149 mg (78%). ^{1}H NMR (400 MHz, DMSO-d_6) δ_H, ppm 7.98 (s, 8H), 7.91 (d, *J* = 4.9 Hz, 8H), 7.12 (d, *J* = 4.5 Hz, 8H), 1.98 (s, 1H). MALDI-TOF MS; anticipated mass (Calcd for $C_{40}H_{25}N_8O_1In_1$) 748.51 amu; observed mass: m/z = 731.50 $[M-OH]^+$ (Calcd for $C_{40}H_{24}N_8In_1$: 731.50 amu).

*2.5.6. Trans-monohydroxo[meso-tetrakis (4-pyridyl)porphyrinato]indium (III) trans-folic acid (**6-FA**)*

A similar procedure to the one above was used for the activation of FA [69, 70].

Yield: 75% (101 mg). ^{1}H NMR (400 MHz, DMSO-d_6) δ_H, ppm 8.15 (d, *J* = 5.2 Hz, 2H), 7.93 (s, 2H), 7.63 (d, *J* = 8.4 Hz, 8H), 6.93 (d, *J* = 5.6 Hz, 8H), 6.64 (d, *J* = 8.4 Hz, 8H), 3.16 (s, 2H), 2.41 (s, 4H), 2.03 (d, *J* = 7.2 Hz, 2H), 1.90 (s, 2H).

*2.5.7. Trans-monohydroxo[meso-tetrakis(N-ethyl-pyridinium-4-yl)porphyrinato] indium (III) trans-folic acid-monohydroxy (**6-FAQ**)*

A similar procedure to the one mentioned above was used for the quaternisation of **5-FA** [108].

Yield: 89% (60 mg). ^{1}H NMR (400 MHz, D_2O) δ_H, ppm 9.03 (s, 1H), 8.77 (d, *J* = 4.7 Hz, 2H), 8.64 (s, 1H), 7.95 (s, 8H), 7.85 (s, 8H), 7.59 (s, 8H), 4.60–4.56 (m, 8H), 3.71 (s, 1H), 3.63 (s, 12H), 3.56 (s, 2H), 2.59 (s, 4H), 2.27 (s, 2H), 2.11 (s, 2H).

2.6. Partition coefficients

The octanol-water partition coefficients (K_{OW}) estimate the hydrophilicity or hydrophobicity of neutral compounds [109, 110]. The lipophilicity of compounds usually correlates with the biological activity of the compounds, and it is expressed in the logarithm of a partition coefficient (Log P) [109, 110]. The lipophilicity of a pharmacological molecule is typically used to predict how it will behave inside the body. The water solubility of a molecule is inversely associated with its lipophilicity; higher lipophilicity raises the risk of metabolic clearance, while lower levels encourage renal clearance. For optimal oral and intestinal absorption, oral medication should have Log P values < 5, ideally between 1.35 and 1.8. The efficacy of a drug molecule will be hampered by low water solubility and high lipophilicity due to decreased bioavailability. The K_{OW} values of the aza-BODIPYs and porphyrins were obtained experimentally through the shake-flask method with the octanol-water system [109. 110].

2.7. Cell culture and *in vitro* studies on MCF−7 breast cancer cells

2.7.1. Cellular uptake

The ability of photosensitisers to effectively penetrate cancer cells determines their effectiveness. As a result, the quantitative analysis of the uptake of the dyes and conjugates studied by the MCF−7 cancer cells was examined. Incubation with 10 µM solutions of the compounds was used to evaluate uptake at various incubation times (6, 12, 24, and 48 h). After being put through identical experimental procedures, the absorbance of untreated (control) cells was also determined.

2.7.2. In vitro dark cytotoxicity

The *in vitro* studies and cell culturing procedures described in the literature were followed exactly [53, 54]. Prior to *in vitro* photodynamic therapy research, *in vitro* cytotoxicity tests employing human breast cancer cells (MCF−7 cells) were carried out in the dark. DMEM with 4.5 g/L glucose, L-glutamine, Phenol red, 10% (v/v) heat-inactivated FCS, and 100 units/mL each of penicillin, streptomycin, and amphotericin B were used to cultivate the MCF−7 cells. The cells were cultivated in Porvair® 75 cm^2 vented flasks and then incubated at 37 °C with 5% CO_2 in a humid environment. Routine subculturing was conducted with traditional trypsinisation. Viable trypsinised cells were counted with a hemacytometer and the trypan blue dye exclusion assay (0.4%). 10,000 cells per well of 96-well tissue culture plates (Porvair®) supplemented DMEM containing Phenol red were planted. To help the cells adhere to the wells, they were incubated at 37°C under a 5% CO_2 atmosphere for 24 h. Following two 100 µL DPBS washes, 100 µL of supplemented DMEM-containing compounds were administered at a series of doses (100, 50, 25, 12.5, 6.25, 3.13, 0 µM). Placebo cells were only cultured in DMEM that had been supplemented. Following a 24-h treatment

period, the wells were twice rinsed with 100 L DPBS, then re-incubated for another 24 h period with DMEM supplemented with Phenol red. The number of viable cells in the monolayers of drug-treated cells and in the control were measured using the WST-1 assay. The quantification was performed using a Synergy 2 multi-mode microplate reader (BioTek®) at 450 nm in line with the instructions of the manufacturer. Eq. (10) was used to calculate the percentage of viable cells:

$$\% \text{ Cell viability} = \frac{\text{Absorbance sample at 450 nm}}{\text{Absorbance of control at 450 nm}} \times 100 \quad \text{..... (10)}$$

Where Absorbance of control at 450 nm is the value for the placebo cells containing supplemented DMEM with phenol red only, and Absorbance sample at 450 nm is the value for the cells containing the dyes. The WST−1 assay was used to assess the cytotoxicity of the compounds on MCF−7 cancer cells.

2.7.3. In vitro photodynamic therapy

The PDT-treated MCF−7 cells were grown and seeded into 96-well plates in accordance with the instructions in the preceding section. Compounds were produced in stock quantities in 5% DMSO, and the volume was filled with more DMEM. The volume was filled with supplemented DMEM after the stock concentrations of water-soluble compounds were prepared in Millipore water. Placebo cells were only cultured in DMEM that had been supplemented. Following a 24 h treatment period, the wells were twice rinsed with 100 L DPBS, supplemented with DMEM and Phenol red, and the plates were then re-incubated for another 24 h period. Phenol red-free supplemented DMEM was poured into the plates after they had been washed with 100 L PBS rather than Phenol red-supplemented DMEM. Using Thorlabs M660L4 and M730L4 LEDs to illuminate a batch of plates for 20 min resulted in different irradiance values at each wavelength. After illumination, phenol red-free supplemented DMEM

was replaced with phenol red-supplemented DMEM. The cells were then washed with PBS. After 24 h of re-incubation with supplemented DMEM containing Phenol red, the number of surviving cells was determined using the WST−1 test. The percentage of values obtained for the placebo cells using the formula in Eq. 10 above was used to express cell survival. The WST−1 assay was used to assess the cytotoxicity of the compounds on MCF−7 cancer cells.

2.7.4. Statistical analysis

The tests were carried out in triplicate (n = 3). The data were statistically examined using analysis of variance (ANOVA), and the results presented average ± standard deviation of IC_{50} and Log_{10} CFU/mL values. For the independent experiments, a P-value of 0.05 was attained and deemed statistically significant.

2.8. Antimicrobial studies

The PACT studies were conducted against *S. aureus* following literature procedures [34, 36, 38]. To create a bacterial colony, *S. aureus* was cultivated on agar plates by following the instructions of the manufacturer [90]. To promote bacterial development, this colony was inoculated into the nutrient broth and then placed overnight on a rotary shaker (200 rpm) in an incubator set at 37°C. To reach a mid-logarithmic phase ($OD_{620\ nm} \approx 0.6$), aliquots of the bacteria culture were added to freshly made broth (4 mL) and cultured for an additional 24 h at 37°C. The broth culture was separated for 15 min at 3000 rpm to extract the bacteria at its mid-logarithmic phase. To create the working stock solution of *S. aureus*, the bacteria extract was diluted to 1/1000 (v/v) of *S. aureus*/PBS after being washed three times with PBS to eliminate the nutritional broth.

PACT trials were conducted using a previously described method [34]. *S. aureus* suspensions were incubated for 30 min. in each experiment at 37°C in an oven with a shaker. In a 24-well plate, 3 mL of the incubated *S. aureus* culture was exposed to radiation at the major spectral band of the compounds' absorption maxima. A 24-well plate was used to plate the remaining 3 mL of the *S. aureus* solution, which was stored in the dark. 100 µL samples were put into agar plates after 3 h of radiation spaced 45 min apart, and they were then incubated for 24 h at 37°C. The same procedure was used for the 24-well plates that were kept in the dark. A Scan® 500 automatic colour colony counter was used to measure the number of CFU/mL of bacteria.

Chapter 3:

Characterisation of aza-BODIPYs and porphyrins

3.1. Syntheses and characterisation of aza-BODIPYs and porphyrins

The synthesis and characterisation of several new aza-BODIPY dyes and porphyrin-based compounds are described in this chapter. When necessary, ^{1}H NMR, UV-visible absorption spectroscopy, mass spectrometry, and other techniques were used to characterise these dyes. Analysis was also carried out on the photochemical and photophysical characteristics.

3.1.1. Synthesis of aza-BODIPY dyes

The synthesis of the aza-BODIPY dyes is shown in **Scheme 1**. The aza-BODIPY dyes were synthesised through a couple of steps. First, the chalcones were obtained through the Aldol condensation of respective aldehydes and ketones in basic (NaOH) ethanoic media at ambient conditions [101, 102]. The yellow product was isolated through recrystallisation in methanol and obtained in 92−96% yields. The nitro-derivatives were obtained through the Michael addition reaction in basic ethanoic media under reflux [101, 102]. The product was extracted using DCM, and no further characterisation was carried out. The azadipyrromethenes were synthesised by cyclising the nitro-derivatives in excess ammonium acetate in butanol under reflux [101, 102]. The resultant blue products were isolated using column chromatography and dried *in vacuo*.

The azadipyrromethenes were then complexed with $BF_3{\cdot}OEt_2$ at ambient conditions to obtain respective aza-BODIPY dyes [101, 102]. TEA was used as a catalyst. Metallic blue crystalline products were isolated through column chromatography or precipitated from the reaction vessel. The aza-BODIPY dyes were modified to enhance the rate of ISC. This was obtained through the electrophilic substitution of the protons at the pyrrolic (2,6-) positions of the core using NIS under ambient conditions

[101]. The target products (metallic blue) were isolated through column chromatography.

Four series of aza-BODIPY dyes were synthesised in this work. Their structures are shown in **Figures 12-14**.

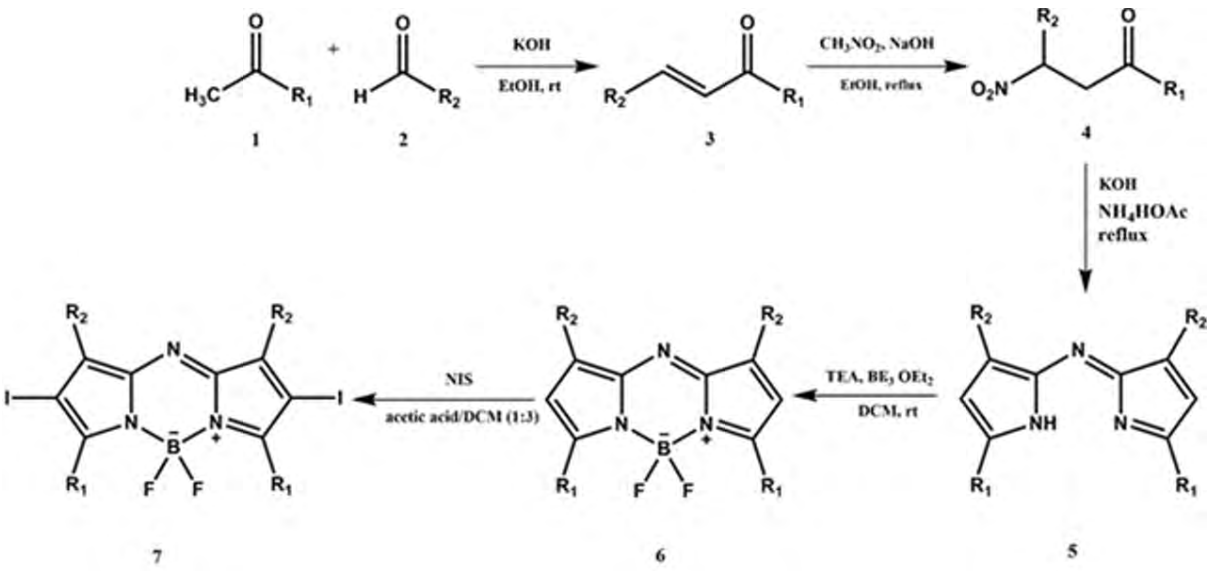

Scheme 1. The reaction scheme for aza-BODIPY synthesis.

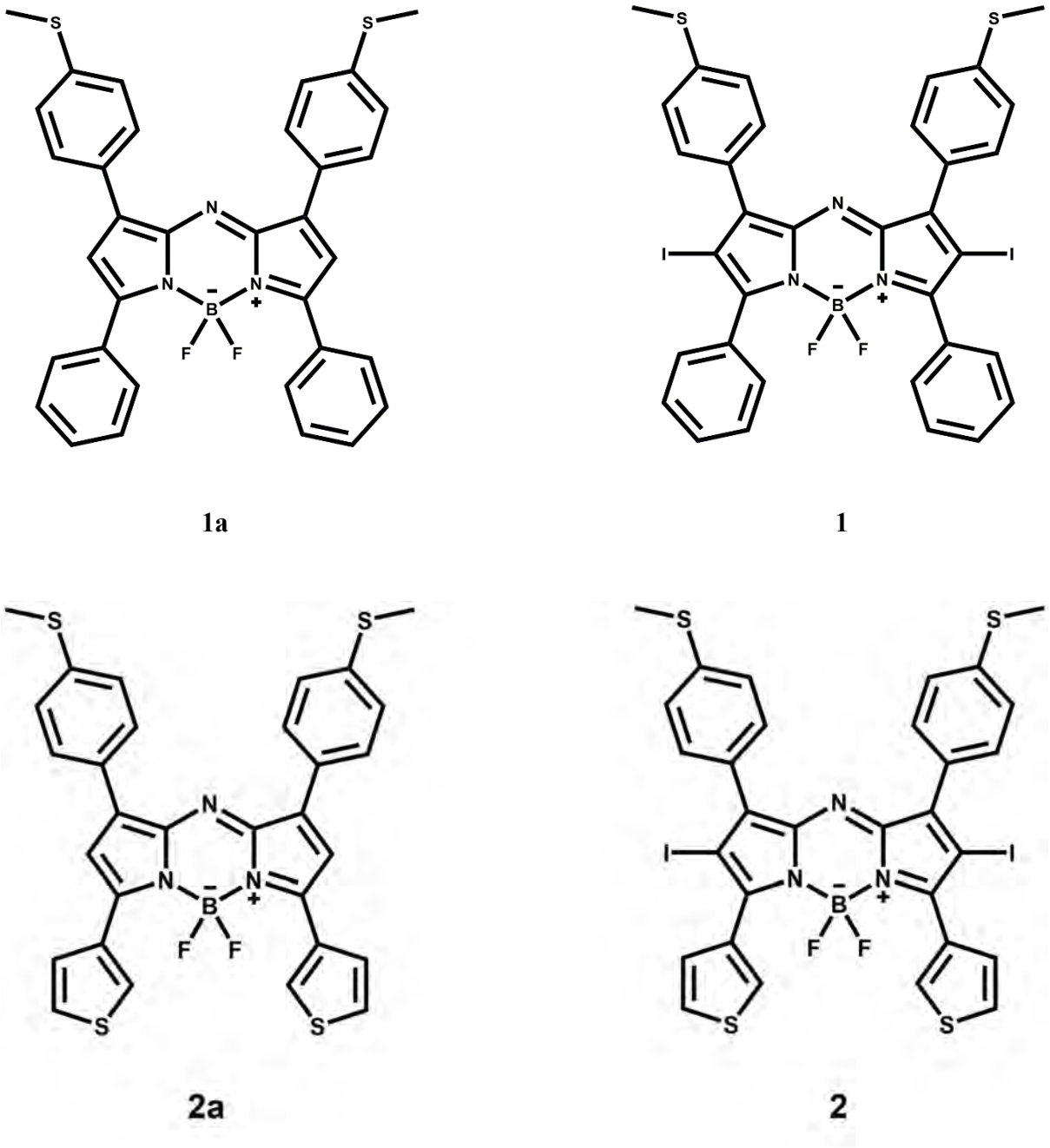

Figure 12. The structures of **1a** and **1** (TOP) and **2a** and **2** (BOTTOM).

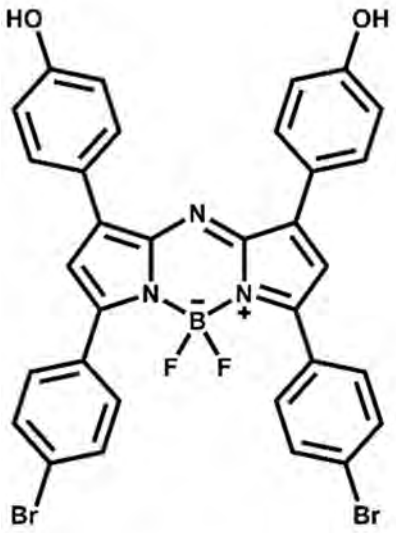

3a

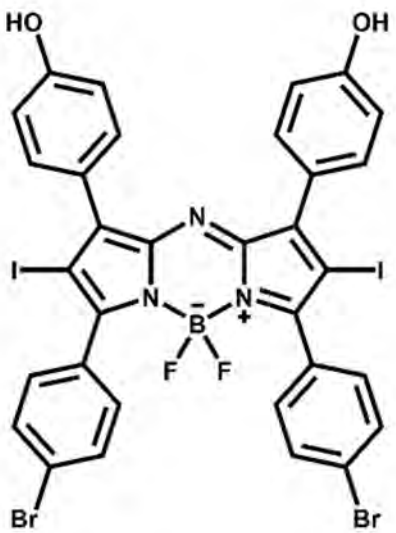

3

Figure 13. The structures of **3a** and **3**.

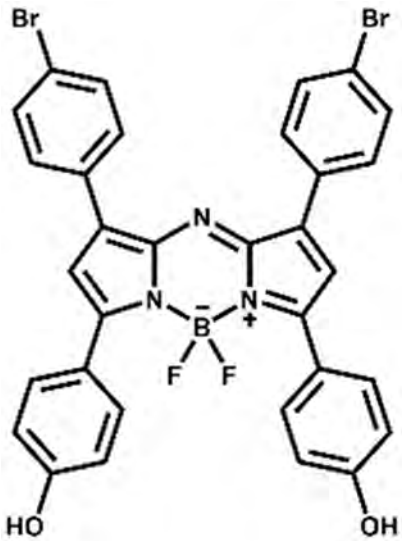

4a

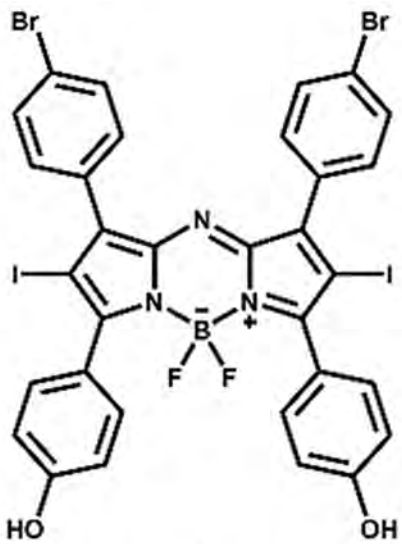

4

Figure 14. The structures of **4a** and **4**.

3.1.2. Characterisation

3.1.2.1. Aza-BODIPY dyes

The structures of the synthesised aza-BODIPY dyes were confirmed using ^{1}H NMR spectroscopy and MALDI-TOF MS. The anticipated masses were observed on mass spectra of all the aza-BODIPYs. The respective ^{1}H NMR observations are given below. The assignment of peaks was carried out through colour/letter-coding, as observed in the respective ^{1}H NMR spectra described below.

Aza-BODIPY **1a**: ^{1}H NMR spectroscopy was used to elucidate the structure of **1a**, **Figure 15**. All the anticipated protons were observed and assigned as follows: the singlet at 2.16 ppm was assigned to six methyl protons of the 4-methylthio substituents at the 1,7-positions of the molecule. Another singlet corresponding to two hydrogens was observed at 6.86 ppm and was assigned to the 2,6-positions of the aza-BODIPY core. The eighteen aromatic protons appeared between 6.44 and 7.80 ppm. The mass spectrum of **1a** is provided in **Figure 16**. The anticipated mass was 589.54 m/z. The observed peak at 589.83 m/z can be readily assigned as the $[M]^{+}$ peak.

Aza-BODIPY **2a**: all the anticipated protons were observed in **Figure 17**. The singlet at 2.16 ppm was assigned to six methyl protons of the 4-methylthio substituents at the 1,7-positions of the molecule. The singlet at 6.86 ppm was assigned to the two pyrrolic protons. The fourteen aromatic protons were observed between 6.97 and 7.31 ppm. **Figure 18** shows the mass spectrum of **2a**. The anticipated mass for the parent peak was 601.59 m/z, while the observed peak at 601.53 m/z can be readily assigned as the $[M]^{+}$ peak.

Aza-BODIPY **3a**: all the twenty anticipated protons were observed, **Figure 19**. The two pyrollic protons appeared at 6.87 ppm. The aromatic protons appeared between 6.59 and 7.98 ppm. **Figure 20** shows the mass spectrum of **3a**. The anticipated mass for the parent peak was 687.15 m/z, while the observed peak at 688.31 m/z can be readily assigned as the $[M+H]^+$ peak. A secondary peak at 668.34 m/z corresponds to a $[M-F]^+$ peak with an anticipated mass of 668.15 m/z.

Aza-BODIPY **4a**: the twenty anticipated protons were readily identified, **Figure 21**. The two pyrrolic protons were observed at 6.88 ppm. The aromatic protons were observed between 6.97 and 7.99 ppm. The peak for the two 4-hydroxyl protons appears at 8.02 ppm. The anticipated mass for the parent peak of **4a** was 687.15 m/z, while the observed peak at 688.45 m/z can be readily assigned as the $[M+H]^+$ peak, **Figure 22**.

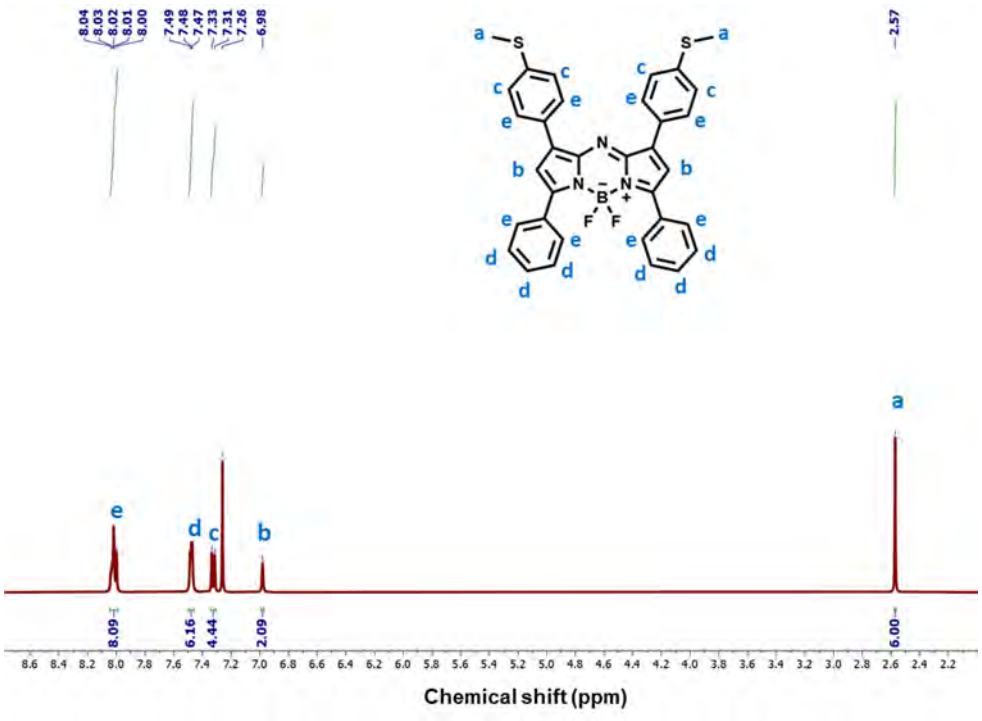

Figure 15. ^{1}H NMR spectrum of **1a**. Solvent: $CDCl_3$.

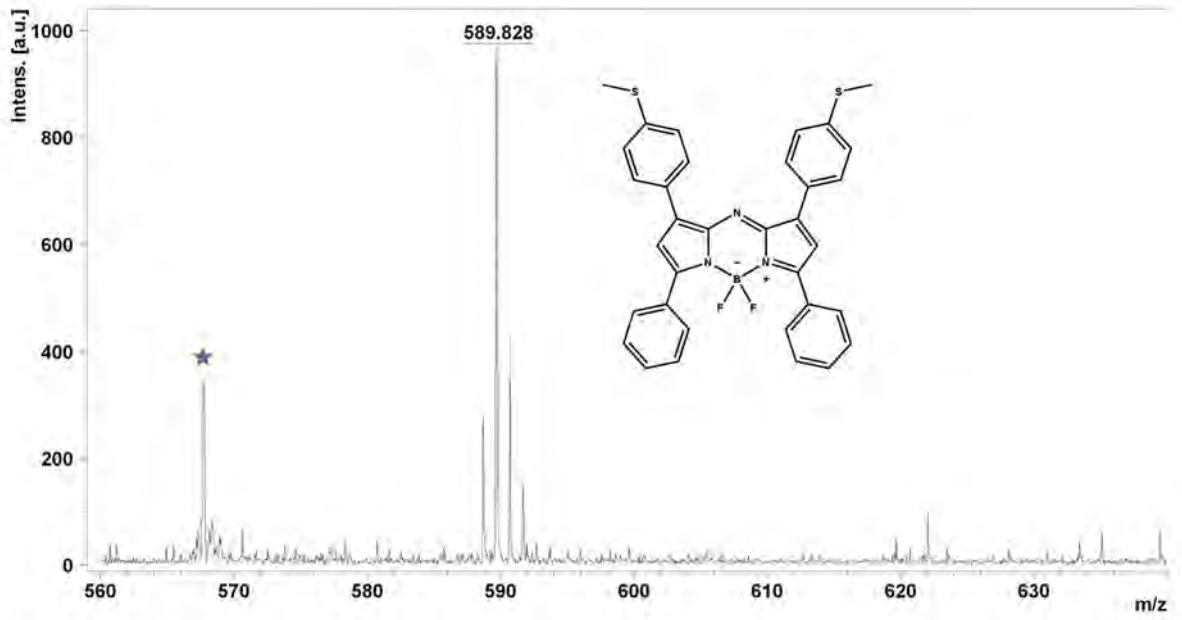

Figure 16. MALDI-TOF mass spectrum of aza-BODIPY **1a**. Anticipated mass (Calcd for $C_{34}H_{26}B_1N_3F_2S_2$): 589.54 m/z; observed m/z = 589.83 $[M]^+$. The starred peak is matrix related.

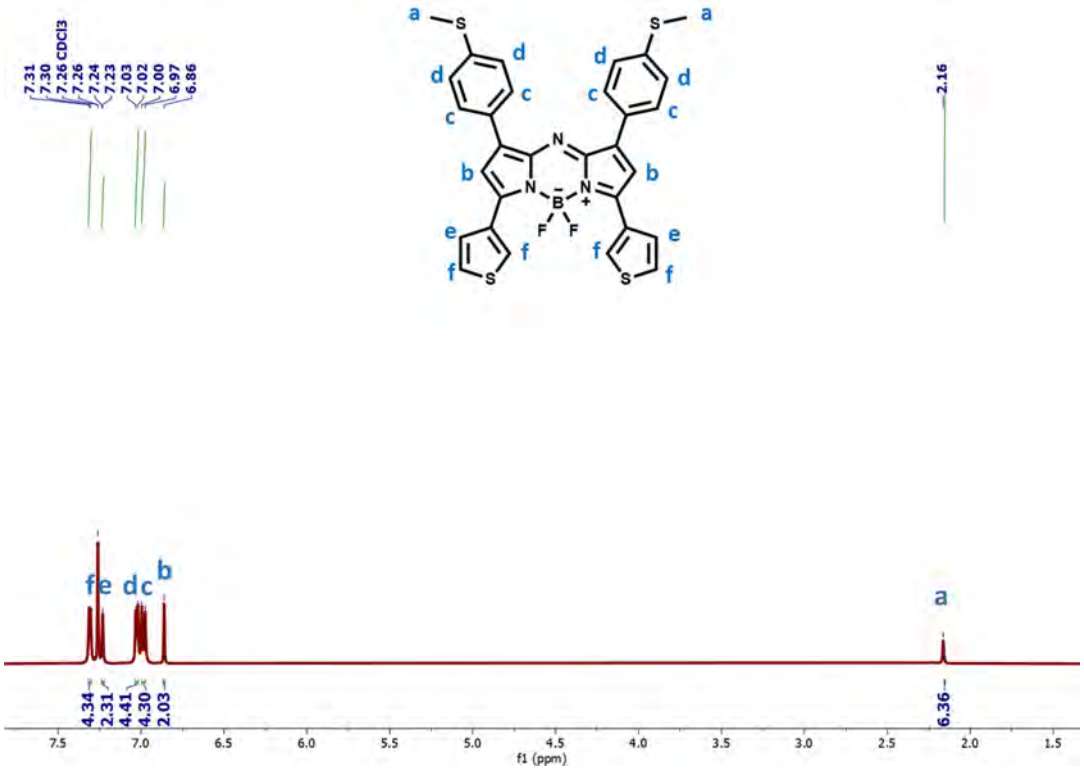

Figure 17. ^{1}H NMR spectrum of **2a**. Solvent: $CDCl_3$.

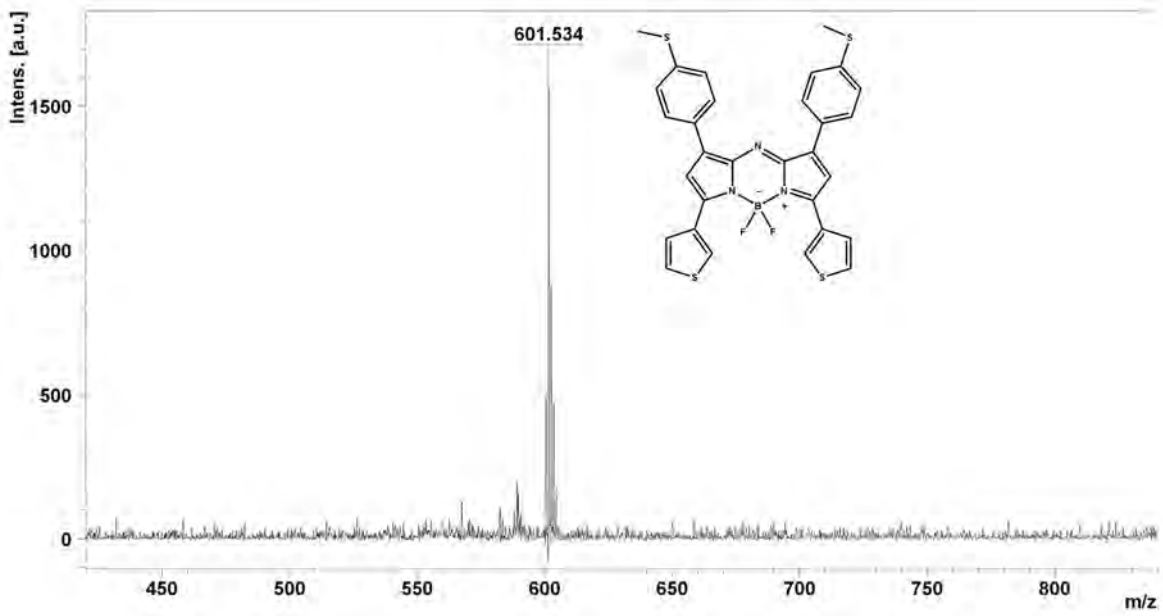

Figure 18. MALDI-TOF mass spectrum of aza-BODIPY **2a**. Anticipated mass (Calcd for $C_{30}H_{22}B_1N_3F_2S_4$): 601.59 m/z; observed m/z = 601.53 $[M]^+$.

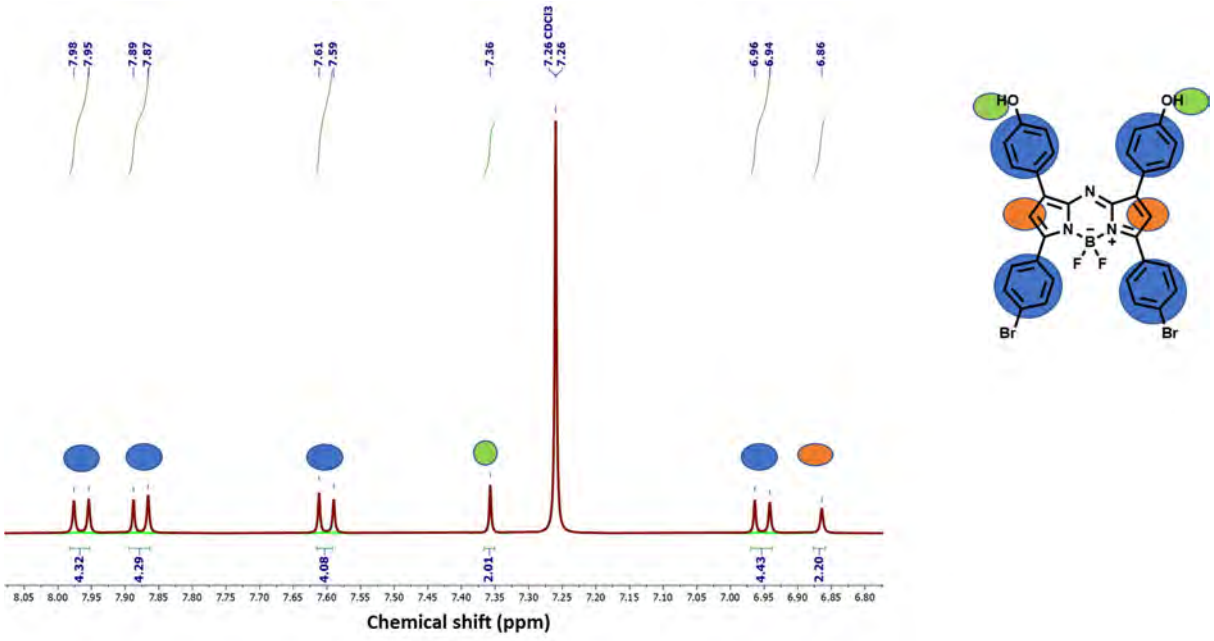

Figure 19. ^1H NMR spectrum of **3a**. Solvent: $CDCl_3$.

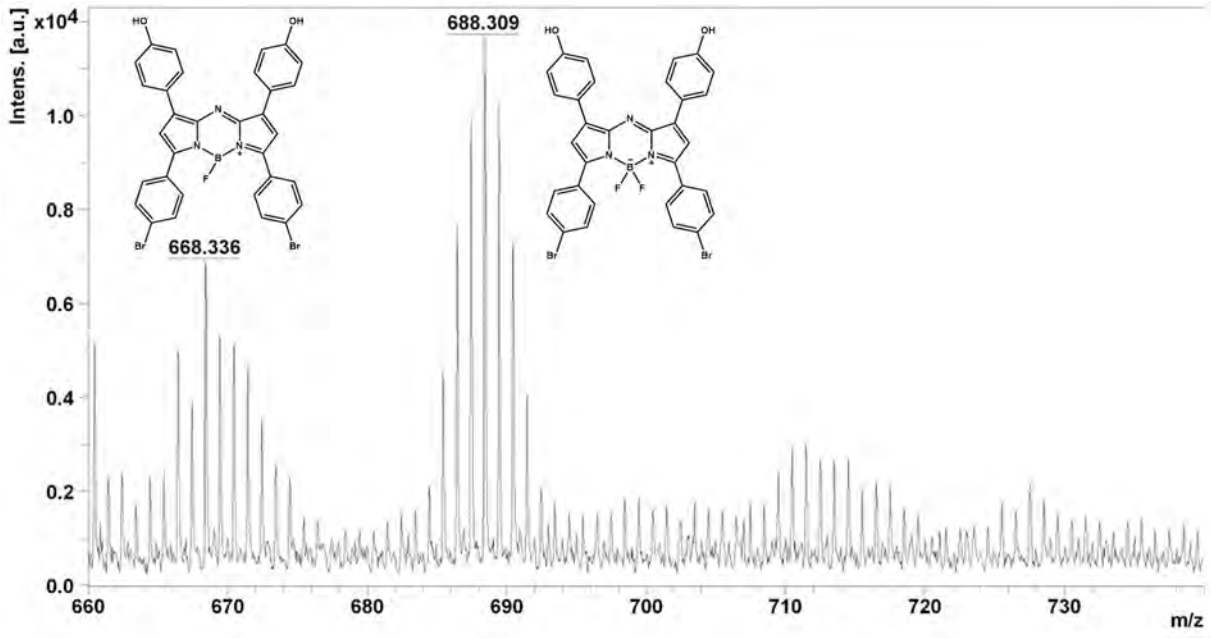

Figure 20. MALDI-TOF mass spectrum of aza-BODIPY **3a**. Anticipated mass (Calcd for $C_{32}H_{20}B_1N_3O_2F_2Br_2$): 687.15 m/z; observed m/z = 688.31 $[M+H]^+$; 668.34 $[M-F]^+$ (Calcd for $C_{32}H_{20}B_1N_3O_2F_1Br_2$: 668.15).

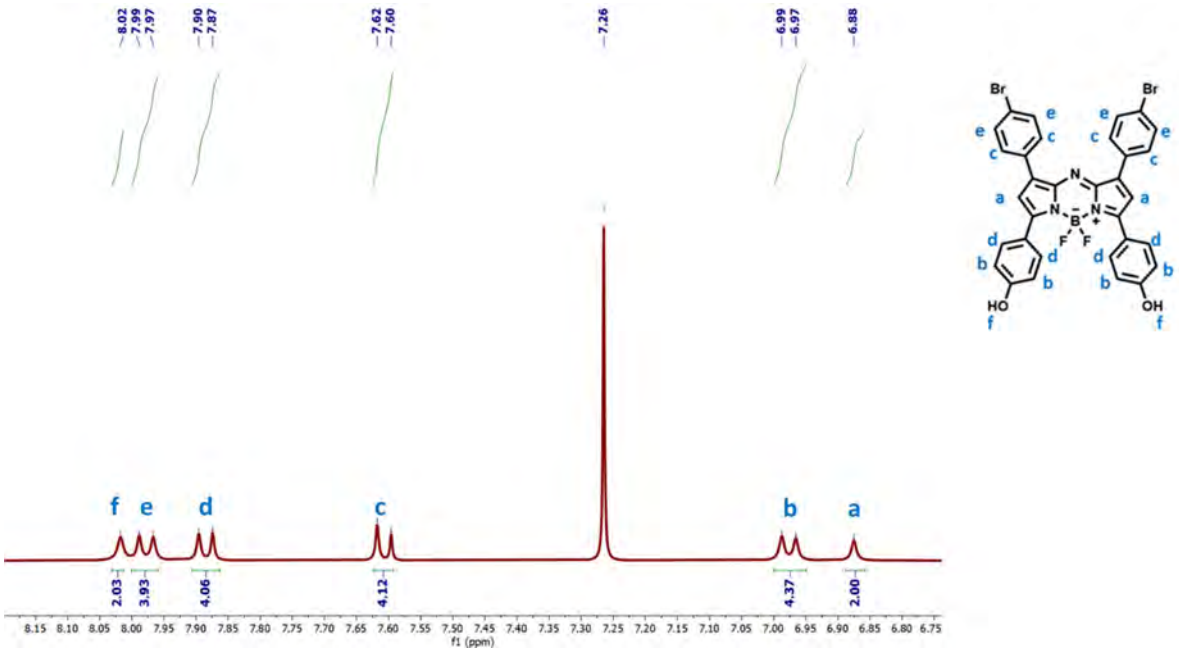

Figure 21. ^1H NMR spectrum of **4a**. Solvent: $CDCl_3$.

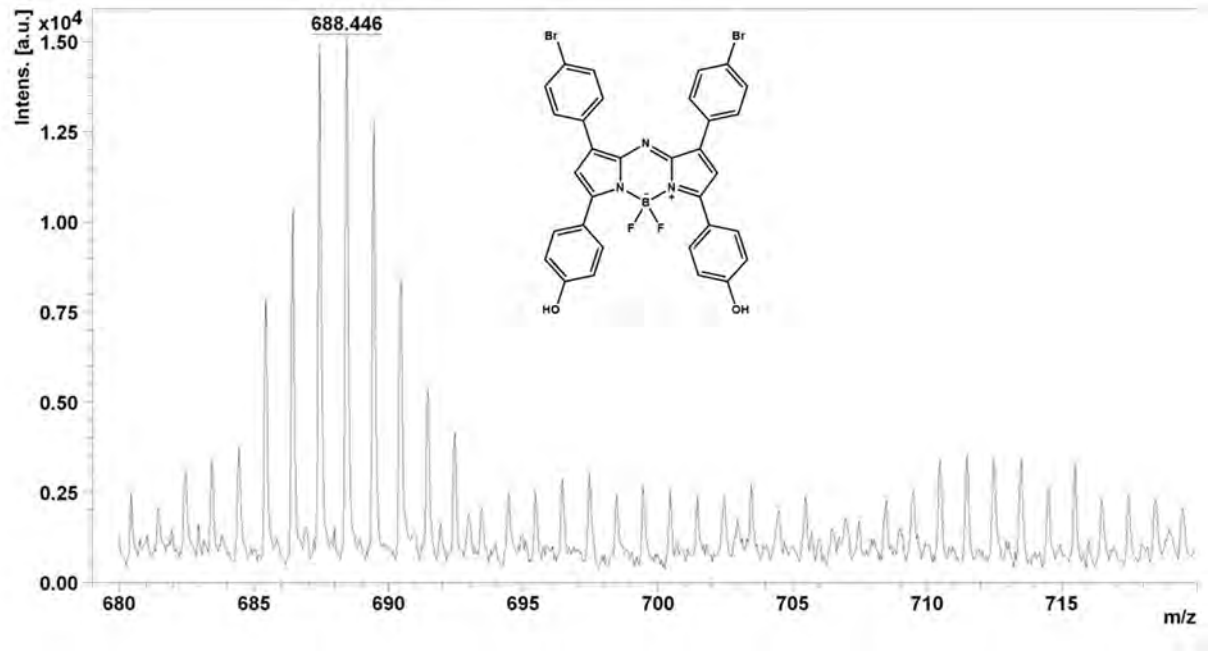

Figure 22. MALDI-TOF mass spectrum of aza-BODIPY **4a**. Anticipated mass (Calcd for $C_{32}H_{20}B_1N_3O_2F_2Br_2$): 687.15 m/z; observed m/z = 688.45 $[M+H]^+$.

^{1}H NMR spectroscopy was used to confirm the structures of the diiodinated aza-BODIPY dyes. MALDI-TOF MS was further used to confirm the iodination of the dyes, **Figure 23-30**. The crucial confirmation of diiodination was the disappearance of the peak for the two pyrrolic protons in the ^{1}H NMR spectra. The assignment of peaks was carried out through colour-coding as seen in the respective ^{1}H NMR spectra.

Aza-BODIPY **1**: the compound has an anticipated mass of 841.33 m/z, while the most intense peak was observed at 716.64 m/z, which can be assigned as a $[M-I+2H]^+$ peak with a calculated mass of 716.44 m/z, **Figure 24**. A secondary peak observed at 696.59 m/z can be assigned as a $[M-I-F+H]^+$ peak with a calculated mass of 696.44 m/z. Since iodine is a good leaving group, it is not unusual that a mono-iodinated

derivative was observed on mass spectrometry. The calculated isotopic distribution patterns for $[M-I]^+$ and $[M-I-F]^+$ peaks are provided as insets in **Figure 24**. Since the ^1H NMR spectrum is consistent with the disappearance of the two pyrrolic protons, **Figure 23**, so the structure of **1** can be concluded to be a di-iodinated derivative.

Aza-BODIPY **2**: the ^1H NMR spectrum of diiodinated compound **2** is also consistent with the absence of 2,6-position pyrrole protons, **Figure 25**. MS was used to further confirm the structure of the compound. The MS data contains a relatively weak parent peak at 853.41 m/z, **Figure 26**, which is consistent with the anticipated mass of 853.39 m/z. A more intense peak is observed at 727.50 m/z that can be readily assigned as a $[M-I+H]^+$ peak with a calculated mass of 727.49 m/z.

Aza-BODIPY **3**: the ^1H NMR spectrum of the diiodinated compound **3** is consistent with the disappearance of the 2,6-position pyrrole protons, **Figure 27**. The anticipated mass for the parent peak of **3** is 938.94 m/z. The observed peak at 925.66 m/z can be assigned as a $[M-OH-F+Na]^+$ peak with a calculated mass of 925.92 m/z, **Figure 28**.

Aza-BODIPY **4**: the ^1H NMR spectrum of the diiodinated compound **4** is consistent with the disappearance of the 2,6-position pyrrole protons, **Figure 29**. No peak is observed for the two OH protons. This may be due to exchange since $CDCl_3$ contains a trace of DCl. It is also possible that the peak coincides with the solvent residual at 7.26 ppm. Attempts were made to measure the spectrum in DMSO-d_6, but issues were encountered with the solubility of the dye. The anticipated mass for the parent peak of **4** is 938.94 m/z. The observed peak at 938.67 m/z can be readily assigned as the $[M]^+$ peak, **Figure 30**.

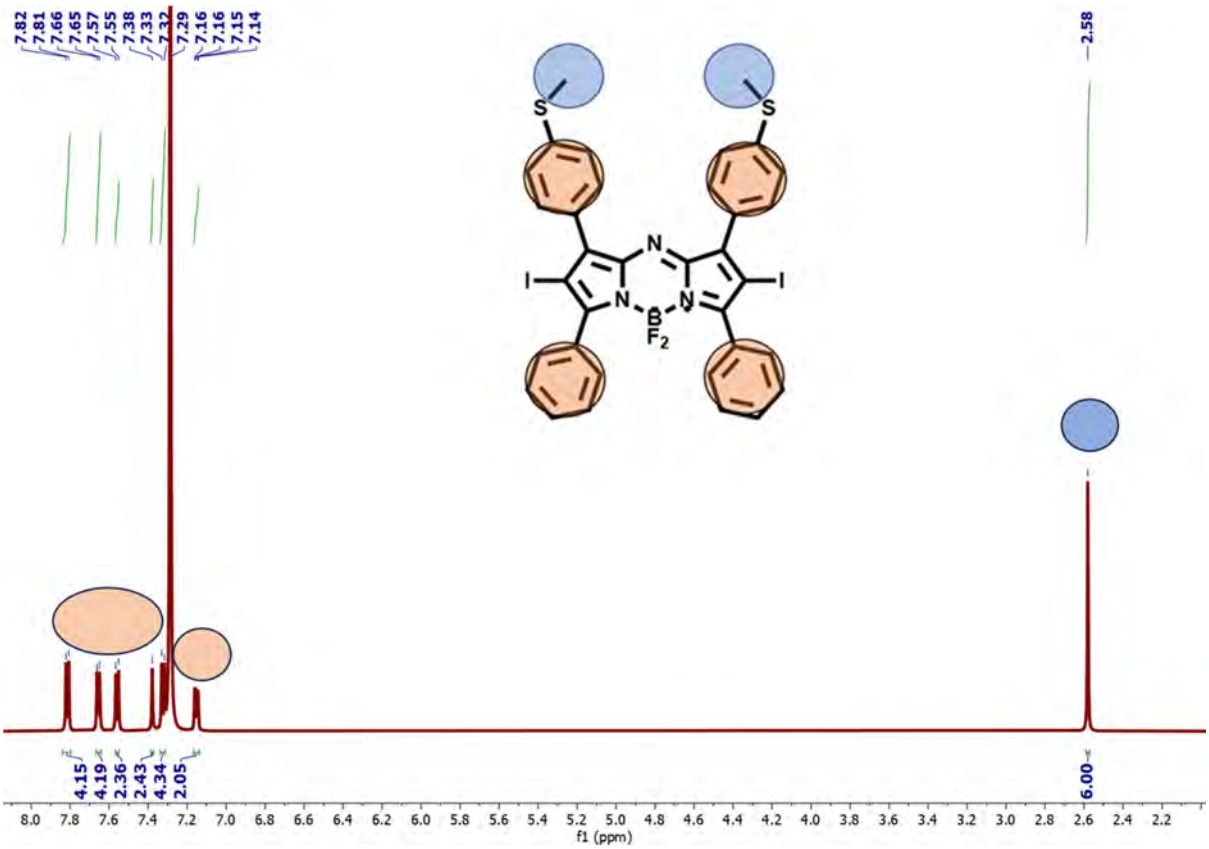

Figure 23. ^{1}H NMR spectrum of **1**. Solvent: $CDCl_3$.

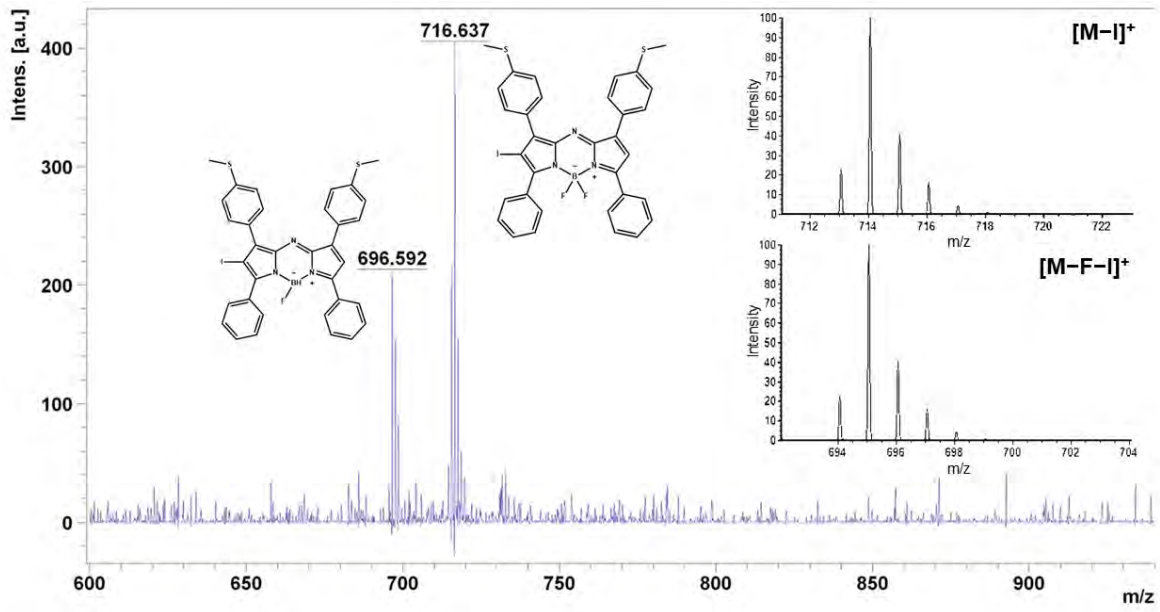

Figure 24. MALDI-TOF mass spectrum of aza-BODIPY **1**. Anticipated mass (Calcd for $C_{34}H_{24}B_1N_3F_2S_2I_2$): 841.33 m/z; observed m/z = 716.64 $[M-I+2H]^+$ (Calcd for $C_{34}H_{26}B_1N_3F_2S_2I_1$: 716.44 m/z), 696.59 $[M-I-F+H]^+$ (Calcd for $C_{34}H_{25}B_1N_3F_1S_2I_1$:

696.44 m/z). Calculated isotopic distribution patterns for $[M-I]^+$ and $[M-F-I]^+$ species provide evidence for multiple protonation in the context of the observed peak at 716.64 m/z in contrast to the 696.59 m/z peak.

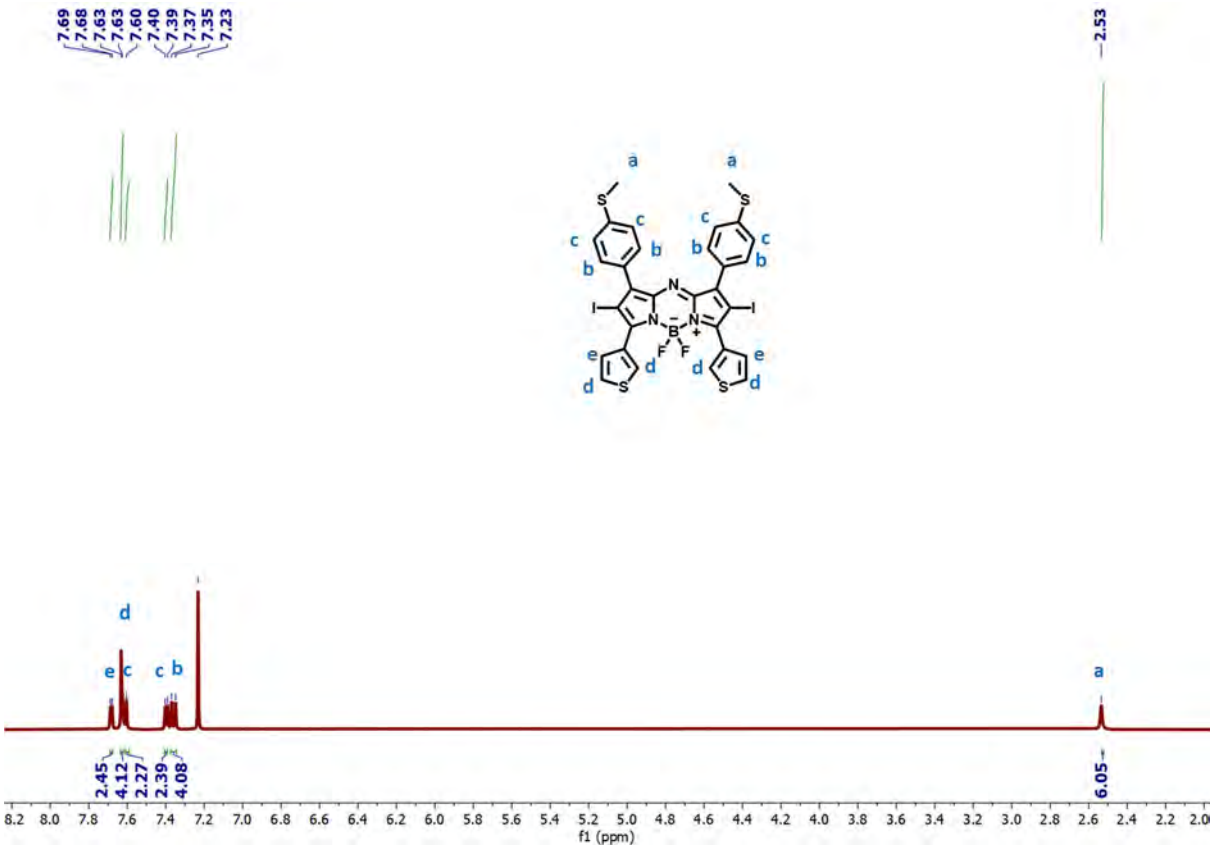

Figure 25. ^{1}H NMR spectrum of aza-BODIPY **2**. Solvent: $CDCl_3$.

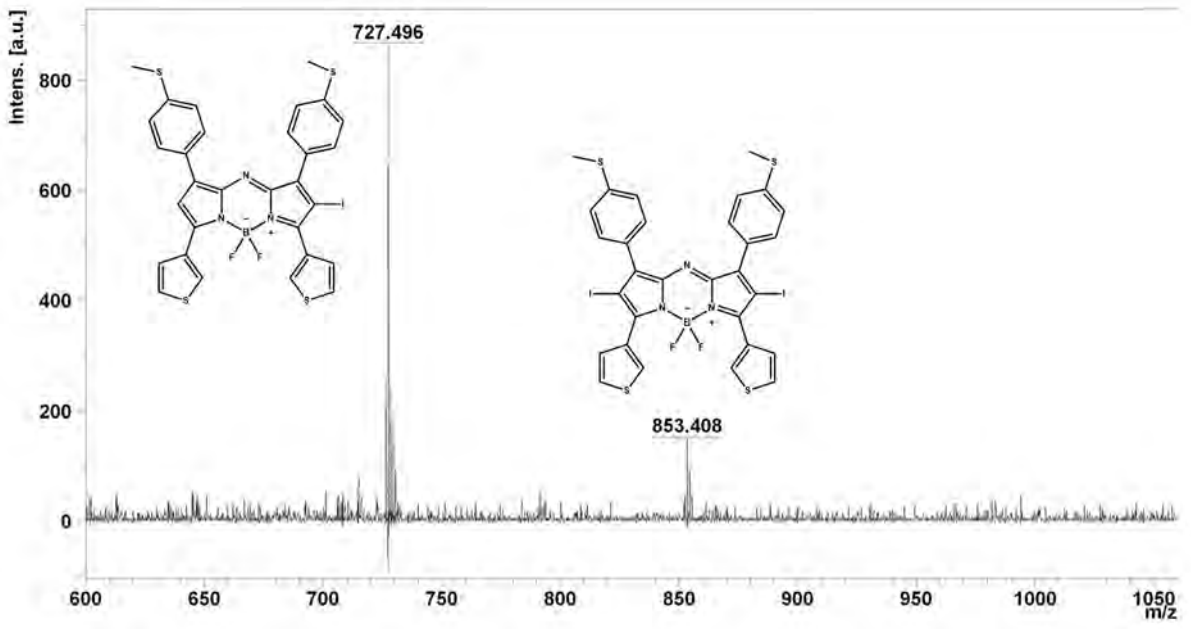

Figure 26. MALDI-TOF mass spectrum of aza-BODIPY **2**. Anticipated mass (Calcd for $C_{30}H_{20}B_1N_3F_2S_4I_2$): 853.39 m/z; observed m/z = 853.41 $[M]^+$, 727.50 $[M-I+H]^+$ (Calcd for $C_{30}H_{21}B_1N_3F_2S_4I_1$: 727.49 m/z).

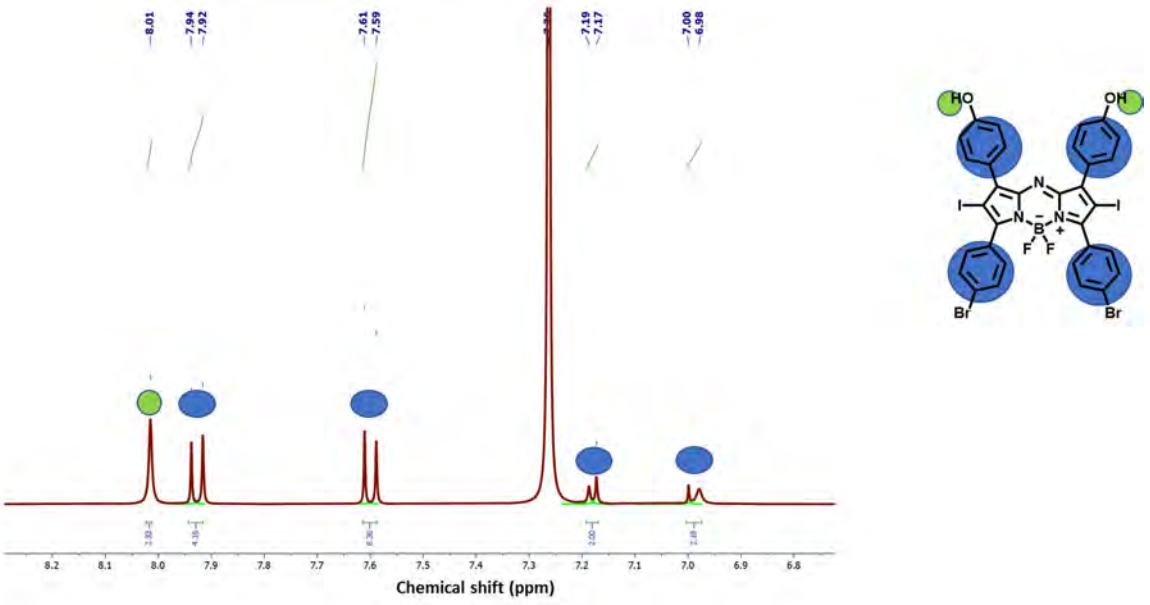

Figure 27. ^{1}H NMR spectrum of aza-BODIPY **3**.

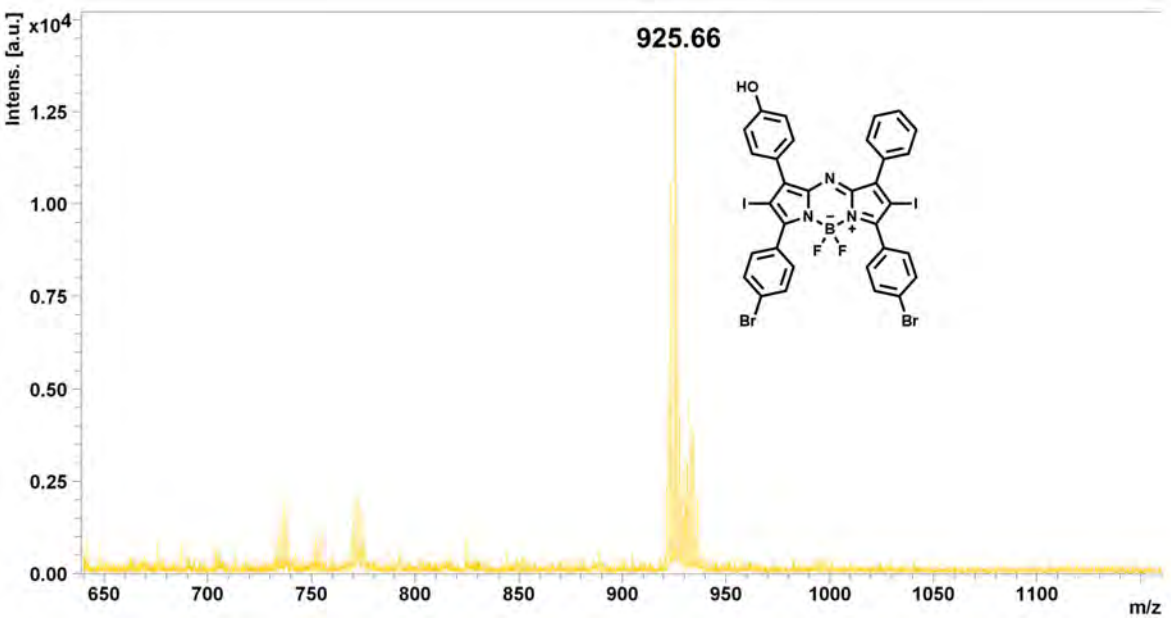

Figure 28. MALDI-TOF mass spectrum of aza-BODIPY **3**. Anticipated mass (Calcd for $C_{32}H_{18}B_1N_3O_2F_2Br_2I_2$): 938.94 m/z; Observed m/z = 925.66 $[M-OH-F+Na]^+$ (Calcd for $C_{32}H_{17}B_1N_3O_1F_1Na_1Br_2I_2$: 925.92 m/z).

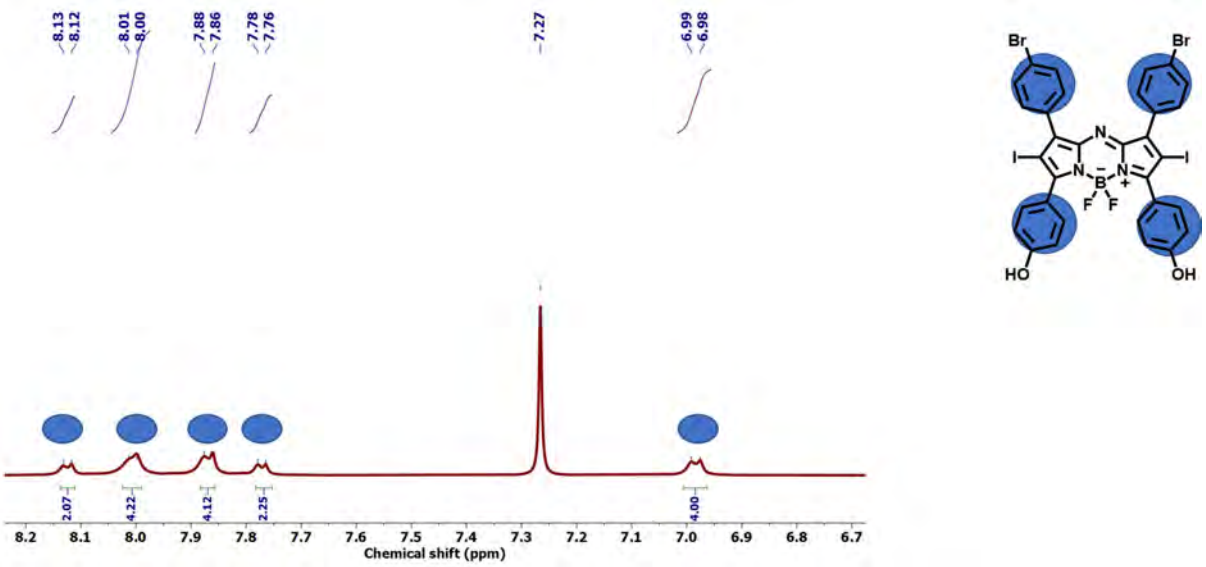

Figure 29. ^1H NMR spectrum of aza-BODIPY **4**. Solvent: $CDCl_3$

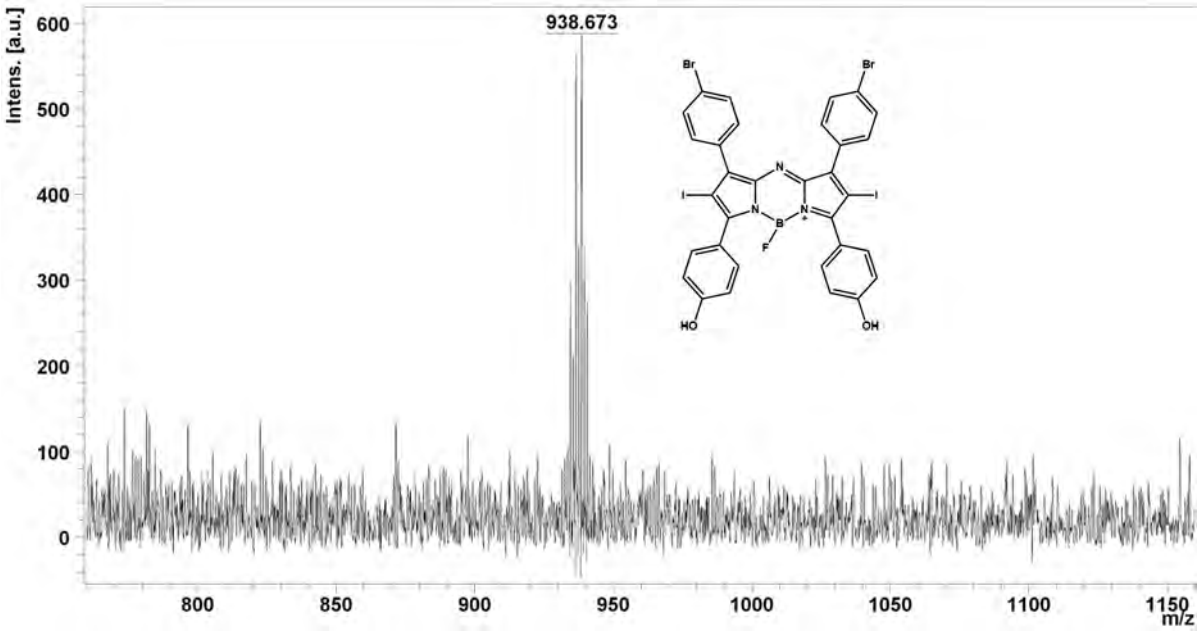

Figure 30. MALDI-TOF mass spectrum of aza-BODIPY **4**. Anticipated mass (Calcd for $C_{32}H_{18}B_1N_3O_2F_2Br_2I_2$): 938.94 m/z; observed m/z = 938.67 $[M]^+$.

3.1.2.2. Optical spectroscopy

The primary absorption bands, which result from the $S_0 \rightarrow S_1$ transition, lie in the 650 −800 nm region, as observed in the UV-visible absorption spectra. These bands are characteristic of monomeric aza-BODIPY dyes. A weaker band arising from a $S_0 \rightarrow S_n$ transition was observed below 400 nm. The different aryl groups at the 3,5-positions of the core structure have a significant effect on the wavelengths of the main absorption bands of the aza-BODIPY dyes.

The electronic absorption spectra of the azadipyrromethenes and aza-BODIPY dyes before and after iodination were recorded in a polar solvent, DMSO, and, where necessary, a non-polar solvent (toluene). The absorption maxima (λ_{max}), molar absorption coefficients (Ɛ), fluorescence quantum yields (Φ_f), and triplet lifetimes (τ_T)

are tabulated in **Table 2**. The absorption spectra are shown in **Figure 31**. The increasing red shift of the absorbance maxima following complexation with boron trifluoride was a commonly observed trend. For both aza-BODIPY dyes, intense absorption bands were observed at 681 and 743 nm for **1a** and **2a**, respectively. Iodination of aza-BODIPY dyes caused the absorption maxima to blue shift to 663 and 730 nm, respectively, as would normally be anticipated [101]. The main spectra bands of aza-BODIPY **2a** and **2** were more red-shifted due to the presence of the electron-donating thiophene substituents at the proximal (3,5) positions of the aza-BODIPY core. The high molar absorptivity observed for both dyes before and after iodination was consistent with literature values observed for similar dyes [101, 102].

Upon the iodination of the aza-BODIPY dyes, there is a hypochromic (blue shift) of the absorption maxima. All the aza-BODIPYs exhibited a blue shift in the absorption maxima in toluene compared to their spectra in DMSO. Of the two aza-BODIPY series studied, Series 4 (**4a** and **4**) exhibited the most red-shifted absorption band, demonstrating that the electron-donating nature of the hydroxyl groups was most marked when the groups were attached at the 3,5-positions of the pyrrole rings relative to the electron-withdrawing bromo groups attached at the 1,7-positions [101, 102].

Table 2 summarises the spectroscopic data for aza-BODIPY dyes in water (polarity index = 10.2), DMSO (polarity index = 7.2), and toluene (polarity index = 2.4) [111]. Since polar solvents are used in the context of the intended applications, the study concentrated on them; hence, the spectroscopic, photophysical, and photochemical properties of non-polar solvents were not thoroughly examined. In general, during the investigations in the latter two solvents, no spectroscopic changes consistent with

aggregation were observed. With increasing solvent polarity, there were slight bathochromic changes in the absorption maxima.

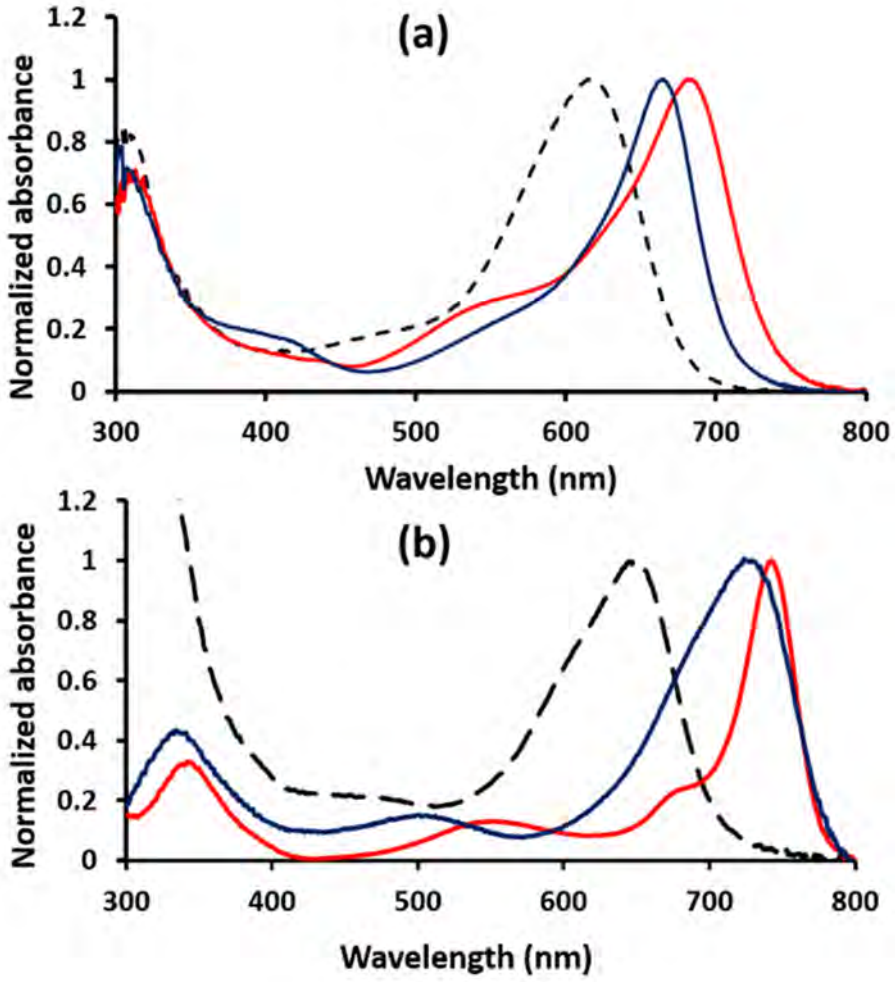

Figure 31. Ground-state absorption spectra of azadipyrromethenes (black), aza-BODIPYs (red), and diiodo-aza-BODIPYs (blue). (a) Series 1 (**1a** and **1** and the azadipyrromethene), and (b) Series 2 (**2b**, **2** and the respective azadipyrromethene). Solvent: DMSO.

The absorption maxima versus concentration graphs depicted in **Figure 32** (as an example) were used to calculate the log molar extinction coefficients (log Ɛ) values.

The chosen dyes did not exhibit aggregation effects at concentrations below 3.8×10^{-6} mol. L^{-1} since there was a linear behaviour in accordance with Beer-Lambert's law [112]. The compounds have high log ε values in DMSO, ranging from 4.14–5.80. These values are consistent with those reported previously for comparable dyes [101, 102]. Where applicable, the molar absorption coefficients in toluene were significantly lower than in DMSO because of solvent polarity, **Table 2**.

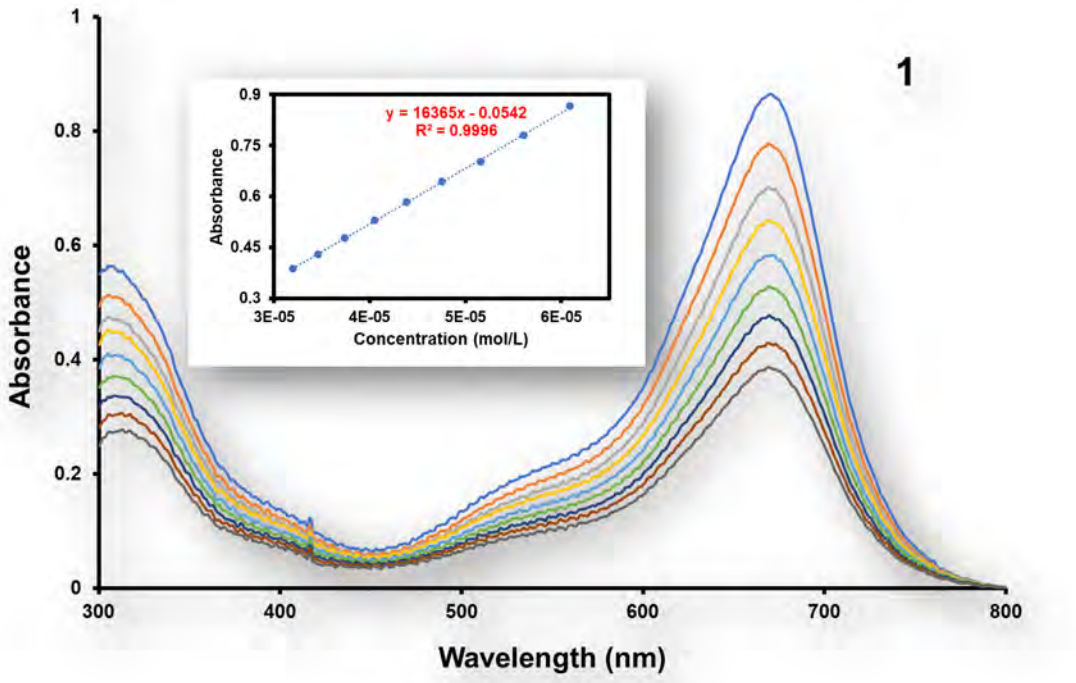

Figure 32. UV-visible absorption spectra and absorption maxima *vs* concentration plot of **1** for log Ɛ determination. Solvent = DMSO.

3.1.2.3. Photophysicochemical Studies of BODIPY dyes

The photophysical characteristics of the dyes and standards were measured in two different solvents (DMSO and toluene) using diluted solutions (0.05–0.10 absorbance). The aza-BODIPYs were excited at the range of 600–700 nm. All the dyes barely exhibited fluorescence under ultraviolet light. The fluorescence was even

lower when they were iodinated. As such, the emission was very weak at the measured concentration, so weak emission bands with maxima between 700 and 900 nm were obtained. The decline is due to the presence of heavy atoms (iodine atoms), which quench the fluorescence while increasing the ISC [101, 102].

A similar approach was used to determine the fluorescence quantum yield (Φ_F) values of the dyes. Methylene blue was used as a standard for aza-BODIPY dyes. **Table 2** lists the calculated Φ_F values for various dyes. Due to their rigid core structure and little ISC, unmodified aza-BODIPY dyes typically have excellent fluorescence quantum yields and very low quantum yields for the triplet state [101, 102]. However, the Φ_F values of aza-BODIPYs in Series 1 and 2 (**Table 2**) are lower than expected. This is attributed to the methylthio substituents, which serve as electron donors, while the aza-BODIPY core is an accepter. Likewise, the Series 3 and 4 derivatives also had lower than anticipated Φ_F values. Hydroxyl groups are present, and these groups tend to quench the photophysics of molecules in polar solvents such as DMSO. The Φ_F value was relatively high in toluene, a non-polar solvent, prior to iodination.

Using a TCSPC instrument, the fluorescence lifetime (τ_F) values were calculated. Since emission happens from the lowest excited state according to Kasha's rule [46], the τ_F value does not depend on the excitation and emission wavelengths. As an illustration, the fluorescence decay curve of aza-BODIPY **2a** is shown in **Figure 33**. **Table 2** provides a summary of the τ_F values obtained for the PS dyes used in this work. The values for the aza-BODIPY dyes, each with a single exponential decay curve, are comparable to those previously reported for similar aza-BODIPY dyes [101, 102]. Some τ_F values could not be determined since the lifetime values are very low (**Table 2**).

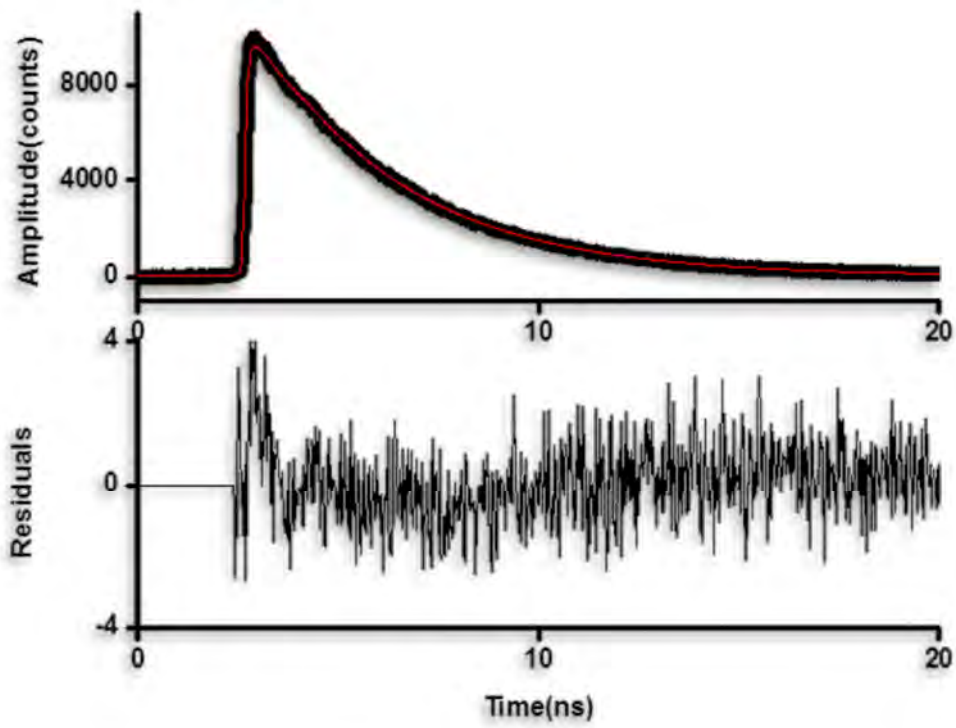

Figure 33. Fluorescence decay curve and residuals of aza-BODIPY **2a**. Solvent = DMSO. The fluorescence intensity decay curve is shown by a solid black exponential line. The red exponential line shows the line of best fit. The lower panel provides the residual difference between the experimental and theoretical values.

3.1.2.4. Photochemical studies

The singlet oxygen generation experiments were conducted using the comparative technique by using 1,3-diphenylisobenzofuran (DPBF) as a $^1O_2$ scavenger in the presence of an aza-BODIPY or a standard. After the irradiation at particular intervals, the decline in the DPBF absorption band at 410 nm was observed, and the photosensitiser's value was compared to the standard. **Figure 34** shows the degradation of DPBF in the presence of **3** as an example.

The obtained Φ_Δ values for **1a** and **2a** were 0.08 and 0.03, respectively. Iodination resulted in the increase of Φ_Δ to 0.83 and 0.17 for **1** and **2**, respectively. According to the literature [113, 114], the thienyl substituents at the aza-BODIPYs' periphery do not directly contribute to the ISC. As a result, the Φ_Δ value depends on the effectiveness of the ISC when heavy atoms are substituted at the 2,6-positions of the aza-BODIPY core [113, 114].

For Series 3, the Φ_Δ increased from Φ_Δ = 0.06 (**3a**) to Φ_Δ = 0.32 (**3**) in toluene. For Series 4, the Φ_Δ increased from Φ_Δ = 0.02 (**4a**) to Φ_Δ = 0.29 (**4**) in toluene. The Φ_Δ values in DMSO were lower due to the presence of polar hydroxy groups in the structure of the compounds, **Table 2**.

Since no discernible deterioration in the intensity of the primary aza-BODIPY spectral band during the irradiations was observed, all of the PS dyes were found to be highly photostable in this context.

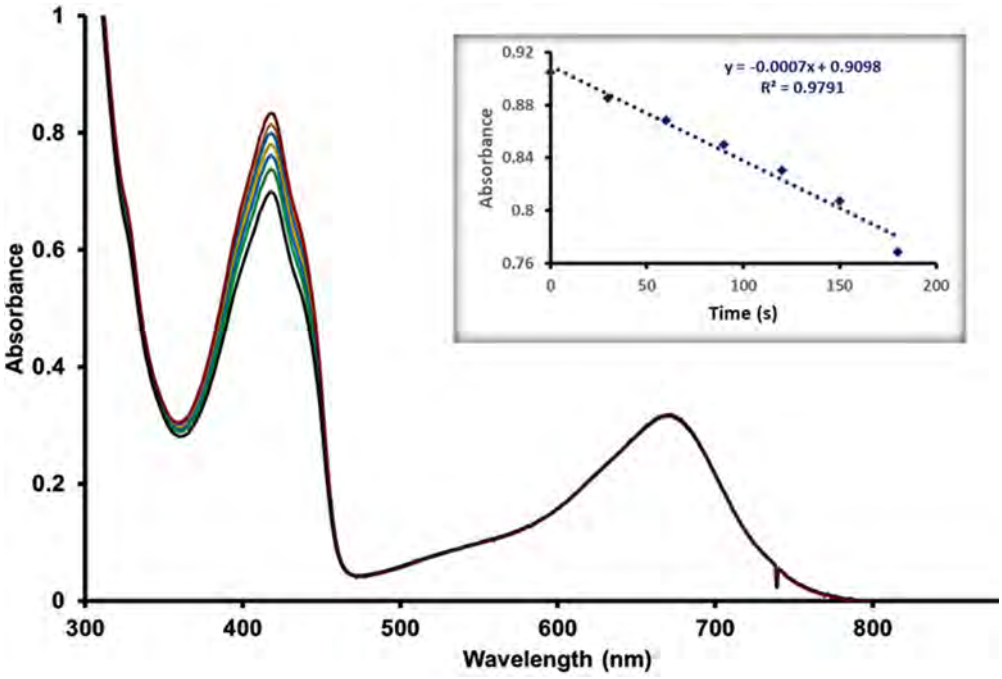

Figure 34. UV-visible absorption spectra showing the photodegradation of DPBF in the presence of BODIPY **3** at 30 s intervals. Solvent = DMSO.

Table 2. Summary of photophysical and photochemical data for aza-BODIPYs studied in DMSO and/or toluene.

	Solvent	λ_{abs} [nm]	ε [M^{-1} cm^{-1}]	Φ_F	τ_F (μS)	Φ_Δ	τ_T (μs)
1a	DMSO	681	1672	<0.01	[a]n.d.	0.08	-
1	DMSO	663	18 441	<0.01	[a]n.d.	0.83	13.2
2a	DMSO	743	4 837	<0.01	[a]n.d.	0.03	-
2	DMSO	730	20 396	<0.01	[a]n.d.	0.17	10.2
3a	DMSO	685	5 943	0.10	3.67	0.05	-
	Toluene	680	2 972	0.08	2.88	0.06	-

3	DMSO	669	16 365	<0.01	[a]n.d.	0.14	13.6 ± 0.12
	Toluene	670	5 828	<0.01	[a]n.d.	0.32	-
4a	DMSO	722	7 669	0.09	1.97	0.01	-
	Toluene	697	5 154	0.07	1.64	0.02	-
4	DMSO	720	17 800	<0.01	[a]n.d.	0.04	19.4 ± 0.67
	Toluene	695	10 407	<0.01	[a]n.d.	0.29	-

[a]n.d. suggests that the value is too low to be detected.

3.1.2.5. Photostability

The cultured media solutions of aza-BODIPYs in Series 1–4 were irradiated with suitable Thorlabs LEDs at 5-min intervals for 30 min (cultured media) to assess their photostability in an organic (DMSO) and aqueous media. After each illumination, the UV-visible absorption spectra were successively measured. All of the compounds' absorption bands remained mostly unaltered throughout time, with no new bands appearing. According to the observations, the dyes exhibited high photostability and underwent no photo-transformation in both organic and aqueous conditions during the research period. The plot of **1** is shown below (**Figure 35**) as an example.

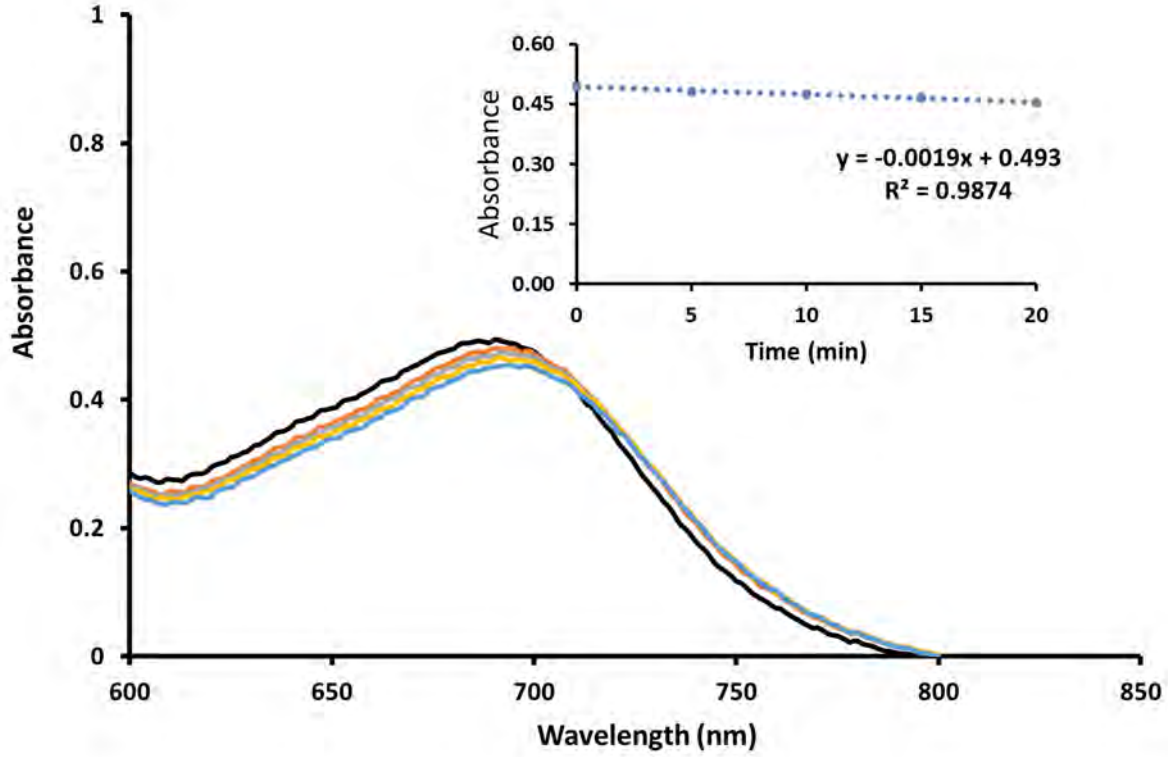

Figure 35. Stability plots for **1** over 20 min irradiation time. Solvent 1% DMSO culture media.

3.1.1.6. Partition coefficients

The hydrophilicity or hydrophobicity of neutral substances is calculated using the octanol-water partition coefficients (K_{OW}) [109, 110]. The biological activity of a substance is typically correlated with its lipophilicity, which is expressed as the logarithm of a partition coefficient (Log P) [109, 110]. Experimentally, utilising the shake-flask method with the octanol-water system, the K_{OW} value of the aza-BODIPYs in Series 1−4 were estimated [109, 110]. The outcomes are shown in **Table 3**. The results show that aza-BODIPYs **1** and **2** have comparable lipophilicity. Aza-BODIPYs **3** is more lipophilic than **4**. This is because **4** has 4-hydroxyphenyl groups at the 1,7-positions, and this increased the hydrophilicity compared to **3**, which has 4-

bromophenyl groups at the 1,7-positions. Due to its low Log P_{OW} value, **4** was discovered to be the most hydrophilic compound, followed by **3**, **2**, and then **1**.

Table 3. The octanol-water partition coefficients of aza-BODIPY dyes.

	K_{ow}	**Log P_{ow}**
1	1.48	0.17
2	1.44	0.16
3	1.39	0.14
4	0.20	−0.70

3.2. Synthesis and characterisation of porphyrin dyes

This section describes the characterisation of Sn(IV) and In(III) tetrapyridylporphyrins (**Figure 36**). The dyes were characterised by ^{1}H NMR, mass spectrometry and UV-visible absorption spectroscopy. The photophysicochemical properties were also analyzed.

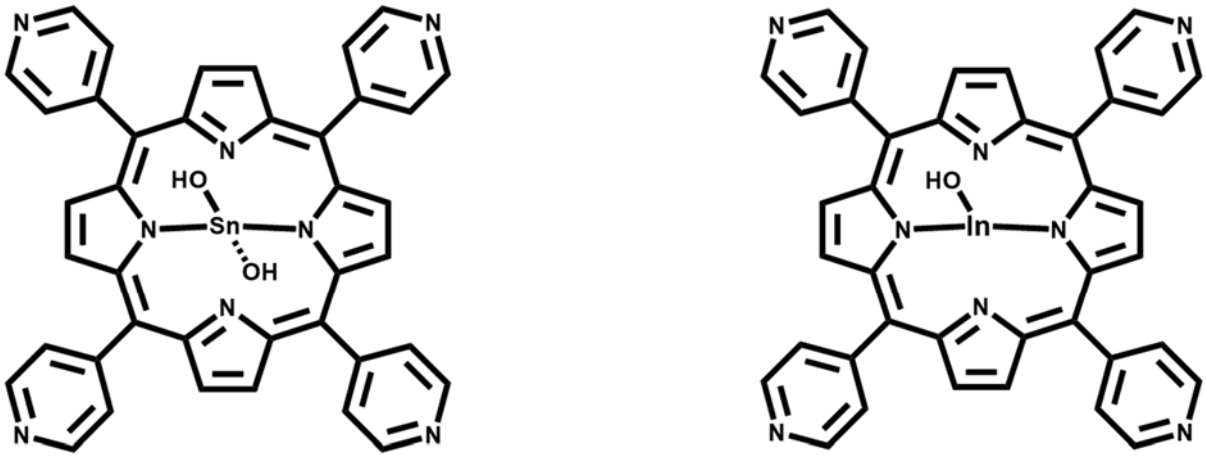

5 6

Figure 36. The structures of porphyrins **5** and **6**.

3.2.1. Synthesis of porphyrins

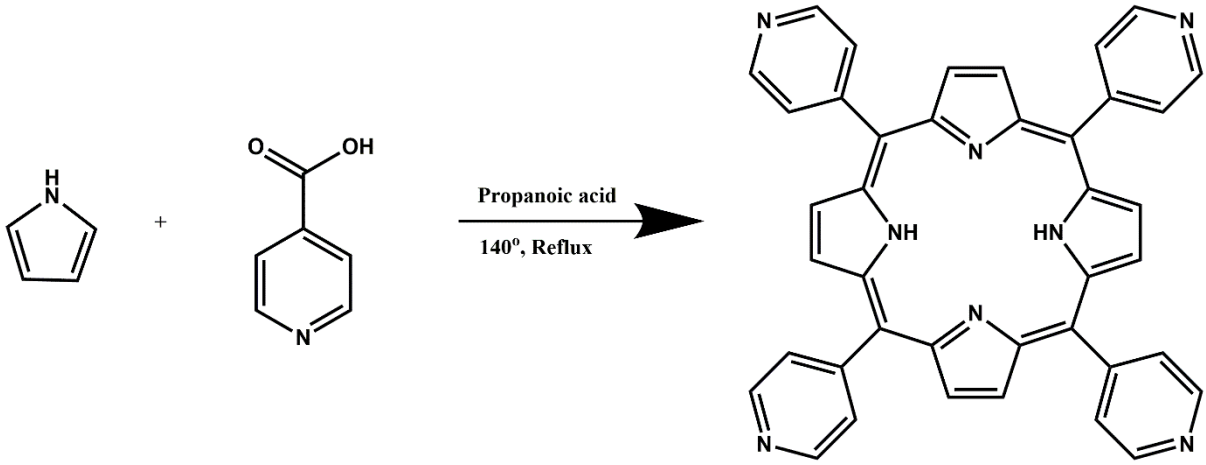

Scheme 2. The synthetic procedure for a generic free-base porphyrin [115].

Meso-substituted porphyrins are widely studied because of their simple synthesis and propensity for synthetic elaboration. Condensation of pyrrole and aldehydes with acid catalysts is a straightforward way of creating these compounds (**Scheme 2**) [115]. An essential and effective pre-requisite for the synthesis of *meso*-substituted porphyrins is the utilisation of acid catalysis. The carbonyl group of the aldehydes is protonated

by the acid catalyst, which causes pyrrole to attack it in an aromatic electrophilic substitution, resulting in the production of the tetrapyrrolic chain [115].

Sn(IV) porphyrins have many favourable properties due to the unique features provided by the highly charged main group metal centre [116]. The large Sn(IV) ion can fit inside the porphyrin core without affecting the macrocyclic ligand's planarity [116]. The complexes have *trans*-diaxial anionic (or occasionally neutral) ligands and are diamagnetic. The unique oxophilicity of the Sn(IV) centre confers a strong predilection for the coordination of carboxylates and aryloxides, and several researchers have lately taken advantage of these features to create complex multi-porphyrin arrays [116]. Similarly, the large In(III) ion also fits in the porphyrin core without affecting the planarity of the ligand [117]. The In(III) complexes have a single axial ligand, providing space for coordination with other ligands.

3.2.2. ^{1}H NMR spectroscopy and MALDI-TOF MS data

The structure of free base porphyrin has been extensively characterised. The structure of the metalated porphyrins was reported instead. The anticipated protons can be readily identified in the ^{1}H NMR spectrum. All 24 anticipated protons could be assigned to peaks in the ^{1}H NMR spectrum (**Figure 37**). The peak for the 16 aromatic protons of the 4-pyridyl rings was observed at 8.29 ppm. The eight β-protons were observed as a doublet between 7.44 and 7.51 ppm. The two hydrogens of the hydroxyl groups in the porphyrin cavity were observed at 0.40 ppm. The structure of **5** was further confirmed using MALDI-TOF MS, **Figure 38**. The observed parent peak at 768.37 m/z can be assigned as a $[M-H]^-$ peak with a calculated mass of 768.41 m/z.

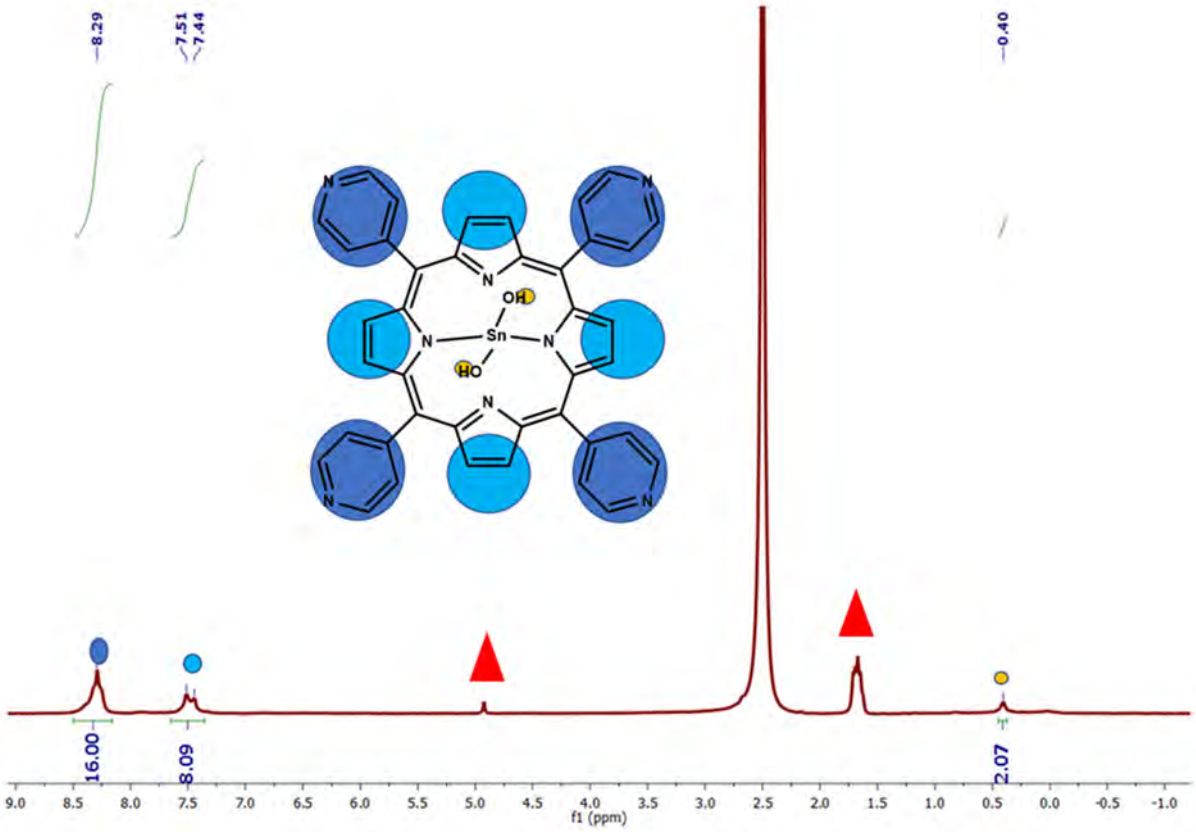

Figure 37. ^{1}H NMR spectrum of complex **5**. Solvent = $CDCl_3$. The red triangle denotes the solvent peaks.

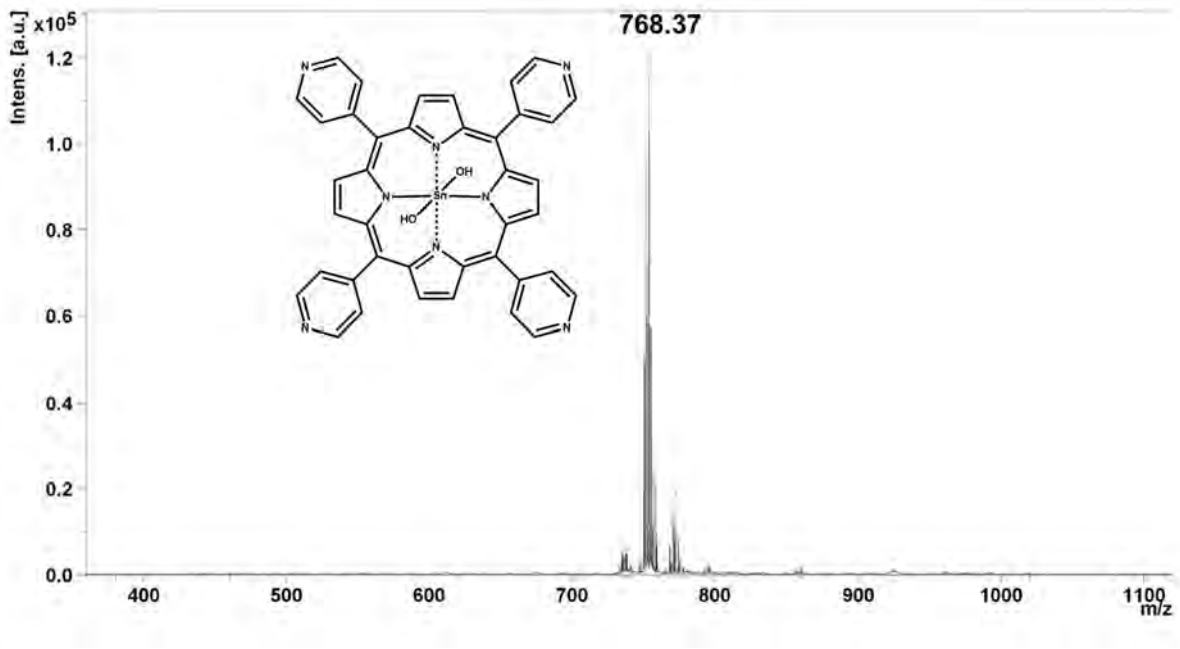

Figure 38. MALDI-TOF mass spectrum of **5**. Anticipated mass (Calcd for $C_{40}H_{26}N_8O_2Sn_1$): 769.41 m/z; observed mass m/z = 768.37 $[M-H]^-$ (Calcd for $C_{40}H_{25}N_8O_1Sn_1$: 768.41 m/z).

A similar characterisation of **6** was conducted. The singlet signal at 7.98 ppm was assigned to the eight protons (highlighted in dark blue) of the 4-phenylpyridyl substituents. The doublet signal denoted by green shading, which resonates between 7.90−7.91 ppm, was assigned to the other eight protons of the 4-pyridyl substituents. The doublet signal at 7.11−7.13 pm was assigned to the pyrrolic protons (β-protons) of the porphyrin structure. The hydroxyl proton in the porphyrin cavity was observed at 1.98 ppm, **Figure 39**. The structure of **6** with an anticipated mass of 748.51 m/z was further confirmed using MALDI-TOF MS, **Figure 40**. The observed parent peak at 731.50 m/z can be assigned as a $[M-OH]^+$ peak with a calculated mass of 731.50 m/z.

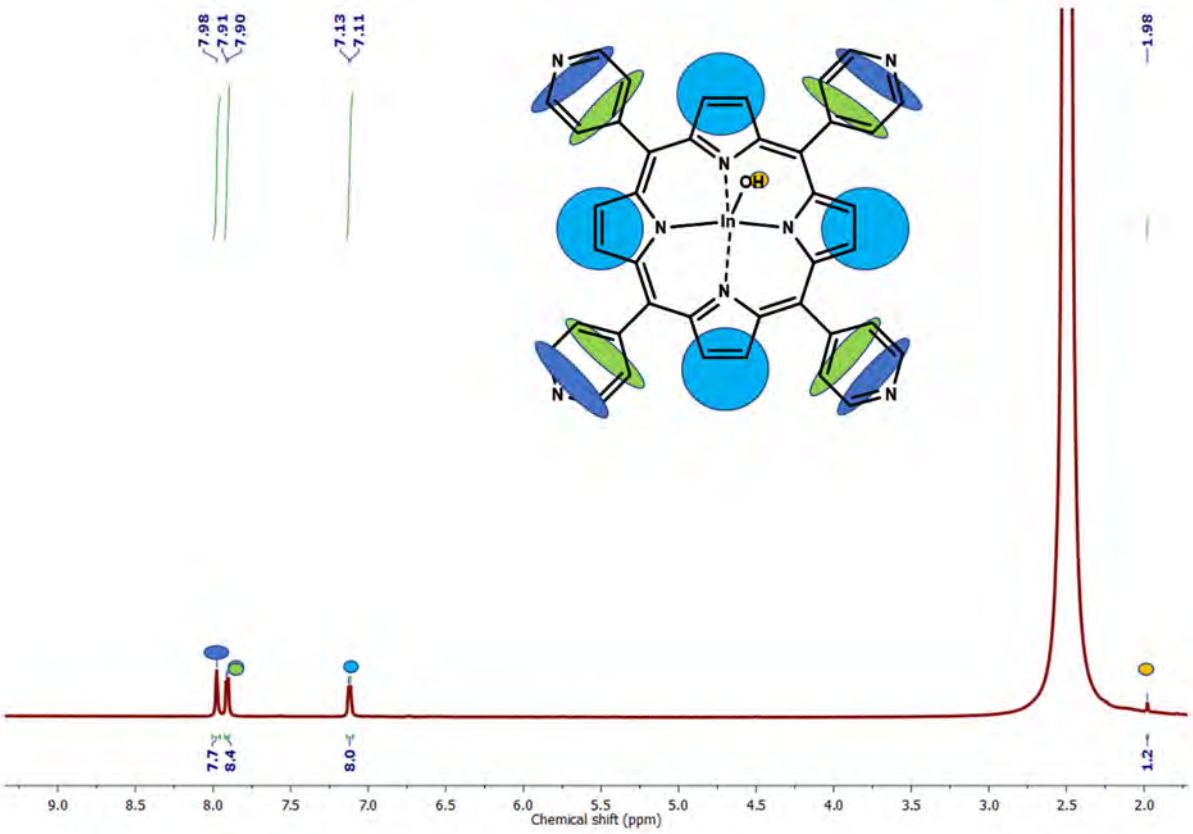

Figure 39. ^{1}H NMR spectrum of **6**. Solvent = DMSO-d_6.

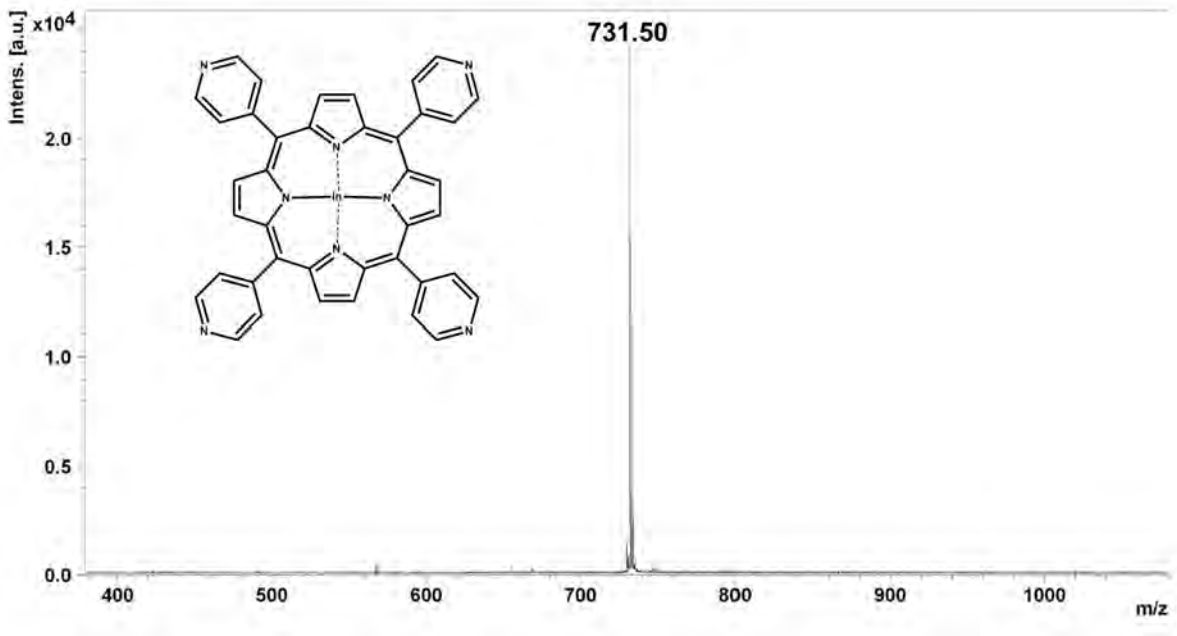

Figure 40. MALDI-TOF mass spectrum of **6**. Anticipated mass (Calcd for $C_{40}H_{25}N_8O_1In_1$) 748.51 m/z; observed m/z = 731.50 $[M-OH]^+$ (Calcd for $C_{40}H_{24}N_8In_1$: 731.50 m/z).

3.3.3. Optical spectroscopy of porphyrins

The UV-visible absorption spectra of **TPyP** (the free base porphyrin) and **5** showed the distinctive bands of porphyrins (**Figure 41**). The intense B (Soret) band corresponding to $S_0 \rightarrow S_2$ transitions was observed at 417 nm for **TPyP** [49, 50, 98]. The metalation with Sn(IV) caused a spectral shift to 426 nm. In the **TPyP** spectrum, the Q-bands are located at 510, 553, 592, and 642 nm. After metalation, two Q-bands at 560 and 600 nm were observed for compound **5**. Two Q-bands vanished, which indicated that the free base porphyrin was successfully metalated. Similar trends were observed after metalation with In(III) to obtain complex **6**. The summary of the bands is provided in **Table 4.**

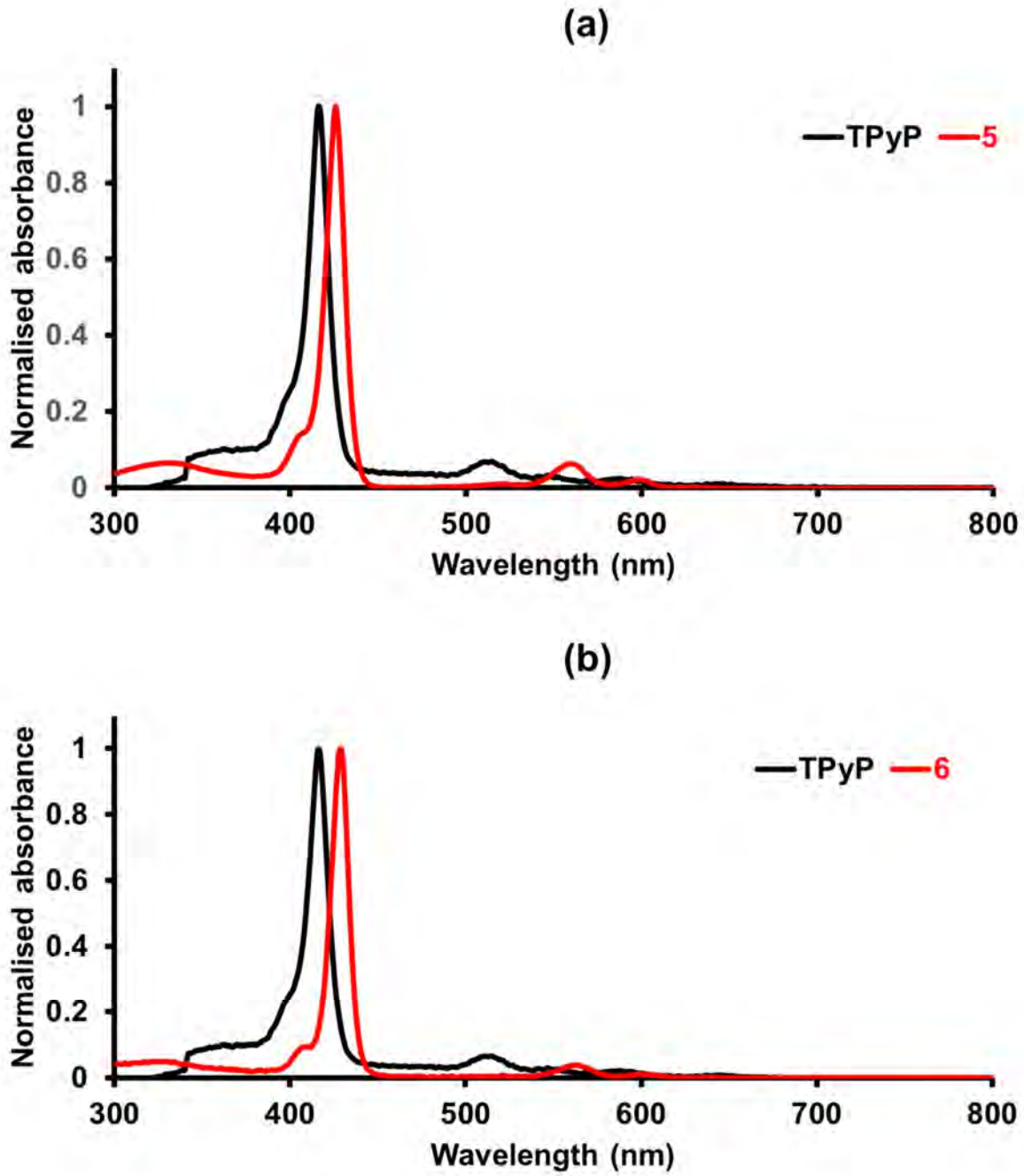

Figure 41. UV-visible absorption spectra of TPyP, **5** (top) and **6** (bottom). Solvent: DMSO. An optical glass cuvette was used for the TPyP measurement resulting in a cut-off at *ca.* 350 nm.

3.3.4. Photopysicochemical properties of porphyrins

The electronic characteristics of the porphyrins in the excited state were investigated through steady-state fluorescence. The normalised emission spectrum of **5** is displayed in **Figure 42.** Upon excitation close to the Soret band, all the porphyrins exhibited two distinct emission bands at around 600 and 652 nm. These emission bands match those reported for Sn(IV) and In(III) porphyrin complexes and correlate to the $S_0 \rightarrow S_1$ transitions [116, 117]. **Table 4** provides a list of all the emission wavelengths of the examined complexes. Due to heightened ISC facilitated by the heavy central metal ion, the fluorescence quantum yields were discovered to be less than or equal to 0.01 for all complexes.

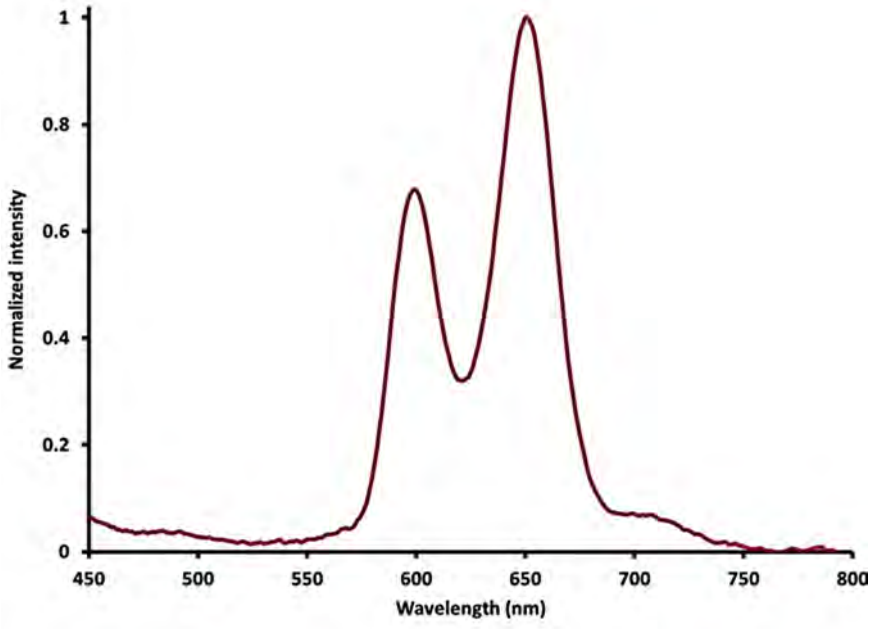

Figure 42. Normalised emission spectrum of complex **5**. Solvent = DMSO.

3.3.5. Singlet oxygen quantum yields

Using DMA as a $^1O_2$ scavenger and H_2TPP as a reference, the efficiency of the Sn(IV) and In(III) complexes in generating $^1O_2$ quantum yields was assessed. Over the course

of 180 s, the deterioration of DMA was observed at 30 s irradiation intervals. **Table 4** contains the values obtained for each complex. After the free-base porphyrins were metalated, as predicted, the Φ_Δ increased. The increase in the Φ_Δ is due to the presence of heavy metals, which increase the rate of ISC to the triplet state.

Table 4. Photophysical properties of Sn(IV) and In(III) porphyrins in DMSO.

PS	λ_{abs} / nm	λ_{em} / nm	Φ_F	Φ_Δ
TPyP	B (417), Q (511, 588, 613, 642)	649, 710	0.01	0.10
1	B (426), Q (559, 599)	600, 652	<0.01	0.45
2	B (424), Q (558, 596)	602, 554	<0.01	0.39

3.4. Concluding remarks

New aza-BODIPY dyes that absorb between 600 and 700 nm were synthesised and studied. Iodine atoms were added to the aza-BODIPY structures as heavy atoms, and this increased the generation of singlet oxygen. The primary absorption bands of the aza-BODIPY dyes were shifted through facile substitution of electron-donating aryl groups at the 1,7- or 3,5-positions. In comparison, the aza-BODIPYs in Series 2 are more red-shifted than those in Series 1. This is due to the presence of electron-donating thienyl groups at the 3,5-positions of the dyes compared to the phenyl groups at the same positions in Series 1. Similarly, the presence of electron-withdrawing bromine atoms at the 3,5-positions relative to electron-donating hydroxyl groups at the 1,7-positions rendered the aza-BODIPYs in Series 4 more red-shifted compared to aza-BODIPYs in Series 3 with the opposite substitution at the 1,7- and 3,5-positions respectively.

Additionally, new tetrapyridylporphyrins adducts were synthesised and studied, which will be described in more detail in Chapter 5. The major modification to these well-studied Sn(IV) and In(III) tetrapyridylporphyrins was achieved through axial ligation with folic acid. Compared to the free base tetrapyridylporphyrin, the metallated porphyrin analogues have red-shifted lowest energy Q bands and relatively high singlet oxygen values.

These aza-BODIPYs and porphyrin dyes can potentially be used as PS dyes in PACT and PDT due to their ability to generate singlet oxygen and high photostability.

Chapter 4 : Pluronic® F-127/L121 micelles encapsulation complexes

4.1. Pluronic® F-127/L121 micelles encapsulation complexes

Targeted drug delivery is preferred due to a variety of advantages, including minimum drug degradation and loss, minimum side effects and increased drug availability at the tumour site. The use of mixed micelles is preferred due to their increased drug solubility, loading efficiency and stability. To increase the effectiveness and biocompatibility of drug molecules in physiological conditions, it is essential to use nanocarriers in drug delivery. Successful conjugation of nanoparticles to PS dyes such as phthalocyanines and porphyrins has been achieved [38-40]. PS dyes can be transported using polymeric nanocarriers such as liposomes and Pluronics. Solubilisation using Pluronic® F-127/L-121 micelles was investigated because hydrophobicity restricts the biocompatibility and effectiveness of aza-BODIPYs in physiological conditions. The FDA has approved the use of solubilising agents as drug delivery agents because they are aqueously soluble and biocompatible in biological settings [118].

Briefly, Pluronic® is a triblock copolymer with hydrophilic polyethylene oxide (PEO) end units and a hydrophobic polypropylene oxide (PPO) centre unit [119, 120]. Because the PPO unit of the copolymer is more soluble at higher temperatures, micelles form more easily as the temperature rises [119, 120]. When a hydrophobic drug molecule is present in the solution, the Pluronics encapsulate the drug molecule, making it water-soluble. With mixed micelles, the micelles form in a similar manner and form more water-soluble complexes [121-125]. A thin-film method (temperature-dependent method) was used in this investigation to create encapsulation complexes with hydrophobic aza-BODIPY dyes.

For applications in physiological conditions, specifically PDT, two aza-BODIPY dyes, **1** and **2** (**Figure 43**), were encapsulated in Pluronic® F-127/L-121 mixed micelles to increase their solubility in water. TEM was used to demonstrate the formation of aza-BODIPY-Pluronic® micelles. The mixed micelles were then characterised using UV-visible absorption spectroscopy.

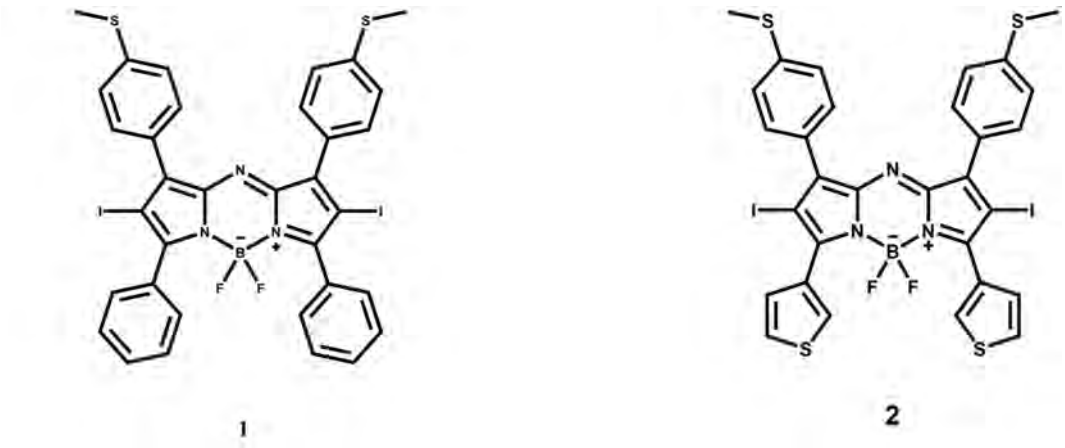

Figure 43. Aza-BODIPYs used for the preparation of encapsulation complexes with Pluronic® F-127/L-121.

4.2. Preparation of the Pluronic® F-127/L-121 micelles encapsulated aza-BODIPYs

To incorporate dyes into Pluronic® F-127/L-121 micelles, a previously described thin-film hydration approach was utilised, with a few changes [126, 127]. Each dye was added to DCM (5 mL) along with the same proportion of Pluronic® F-127 and L-121(1/40: w/w), and the mixture was then sonicated for 15 min. After that, the solution was desiccated for 12 h after being dried *in vacuo* for 1 h at 50 °C. The resulting solid was swirled for an additional 2 h after being hydrated with Millipore water (5 mL) and sonicated for 15 min. A 0.2 µm filter was used to remove unloaded dye molecules from the solution. The fluid was then freeze-dried for two days to create solid inclusions. Using a similar procedure, micelles without encapsulated aza-BODIPY dyes were prepared.

4.3. Characterisation of Pluronic® F-127/L-121 mixed micelles

4.3.1. Transmission electron microscopy

Figure 44 shows the TEM micrographs of Pluronic® F-127/L-121 mixed micelles before (a), after (b) aza-BODIPY **1** was encapsulated in the micelles (**1@M**) and after (c) aza-BODIPY **2** was encapsulated in the micelles (**2@M**). The plain Pluronic® F-127/L-121 mixed micelles were near spherical with an average size of 20.6 nm. The encapsulation complexes exhibited a similar morphology with an increased size range of 52−55 nm. The presence of the dyes in the core of the mixed micelles resulted in an increase in size. The encapsulation complexes appear more dispersed compared to the plain mixed micelles.

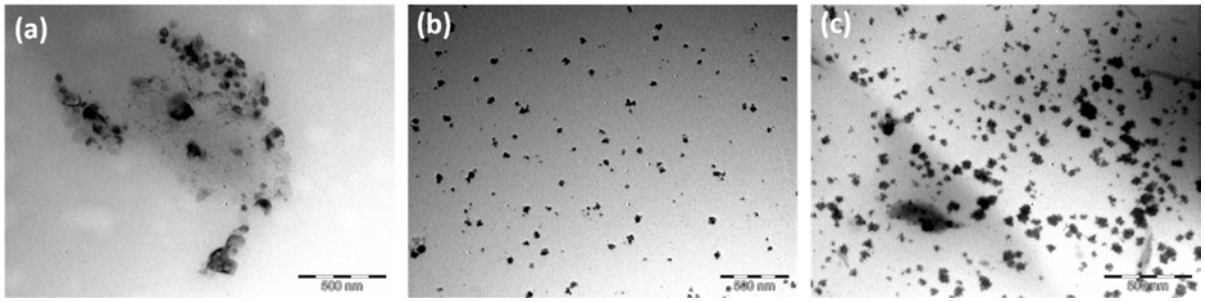

Figure 44. TEM micrographs for Pluronic® F-127/L-121 (a), **1@M** (b) and **2@M** (c) micelles. The Pluronic® F-127/L-121 mixed micelles are relatively spherical with an average size of 20.6 nm, while the encapsulation complexes have similar morphology with a size range of 52−55 nm.

4.3.2. Determination of aza-BODIPY stability in mixed micelles

Following the 24 h storage of the micelles in the desiccator, the mixed micelles appeared decolourised. A stability study was conducted using UV-visible absorption spectroscopy to determine how the mixed micelles encapsulation complexes behaved in water over a period of 16 h. **1@M** was dissolved in deionised water, and the

absorbance was determined. The first set of data was collected over a period of 210 min at 30 min intervals and then left for a further 210 min. After this, data was collected over a further 210 min at 30 min intervals. **Figure 45** shows the results obtained.

After the first 210 min, a gradual decrease in the absorbance of the dye was observed. A significant decrease in the absorbance value was observed after a further 210 min. The absorbance value gradually decreased again after a further 210 min, with the dye being completely degraded after 24 h. Similar results were observed for **2@M**, where the dye completely degraded after 24 h.

Due to the degradation of the dyes in Pluronic® F-127/L-121 mixed micelles, further studies related to the photophysicochemical properties of **1@M** and **2@M** and their PDT activities were not conducted.

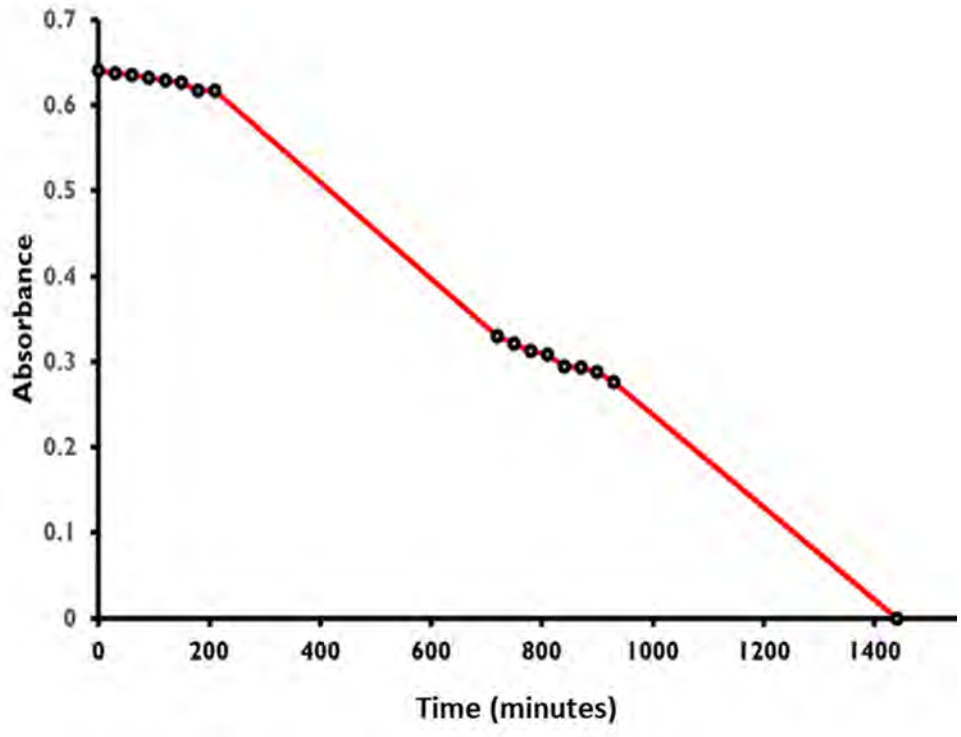

Figure 45. Stability studies of **1@M** in deionised water.

4.4. Concluding remarks

Following the work carried out during earlier MSc research where Pluronic© F-127 and Pluronic© F-127-folic acid conjugates were used as nano-carriers for encapsulating BODIPY dyes, the initial portion of the PhD project aimed to use mixed Pluronic© F-127 and L-121 to encapsulate aza-BODIPY dyes. The encapsulation was not successful due to the degradation of the aza-BODIPY dye when encapsulated. The reason why this was the case was not experimentally investigated due to time constraints. The study was swiftly re-directed towards conjugation to AuNPs and later conjugation of suitable aza-BODIPY dyes and porphyrins to folic acid.

Chapter 5: Gold nanoparticles and folic acid conjugates

5.1. Aza-BODIPY-AuNPs conjugates

Two aza-BODIPY dyes, **1** and **2** (**Figure 46**), were conjugated to AuNPs to enhance their biocompatibility and possibly their solubility in physiological environments for application in PDT. The formation of aza-BODIPY@AuNPs conjugates was confirmed by UV-visible absorption spectroscopy, EDS, TEM, XRD and DLS.

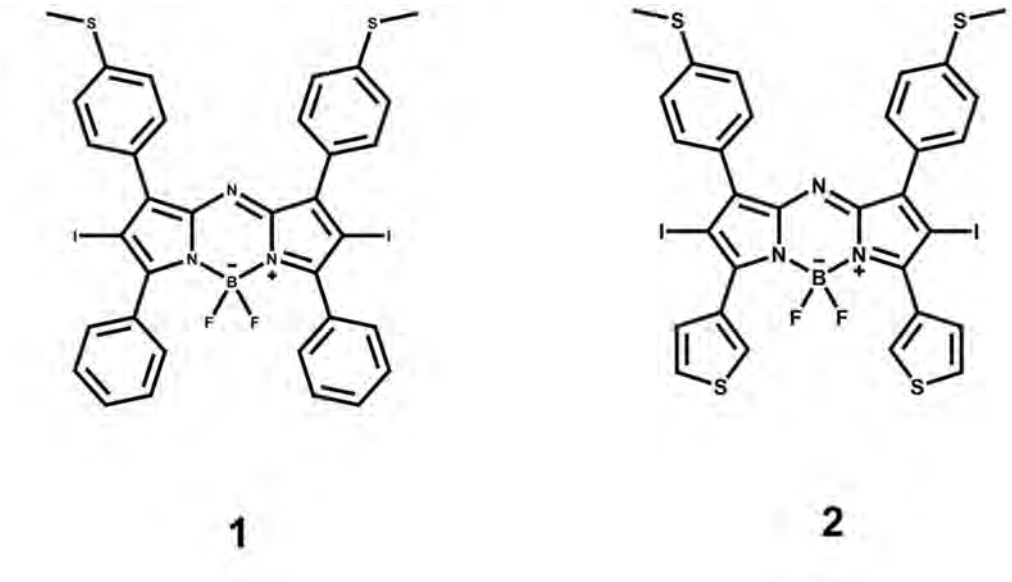

Figure 46. Aza-BODIPYs used for the preparation of aza-BODIPY@**AuNPs** conjugates.

5.1.1. Characterisation of aza-BODIPY-AuNP conjugates

5.1.1.1. UV-visible absorption spectroscopy

The aza-BODIPYs were conjugated to AuNPs to form biocompatible nanocomposites. The absorption band maximum in the UV-visible absorption spectrum of the colloidal solution of AuNPs lies at 524 nm [55-58], as illustrated in **Figures 47(a)** and **47(b)**. (a) represents the spectra of **1** and its conjugate, while (b) represents **2** and its conjugate. Because there is just one surface plasmon band, it can be concluded that the synthesised nanoparticles are nearly spherical [55-58]. Their maximum absorption

value is comparable with literature data. Upon conjugation to aza-BODIPY dyes, there was a slight blue shift of the absorption maxima. The weak bands of the PSs at around 350 nm were enhanced due to the incorporation of the AuNPs, **Figure 47**.

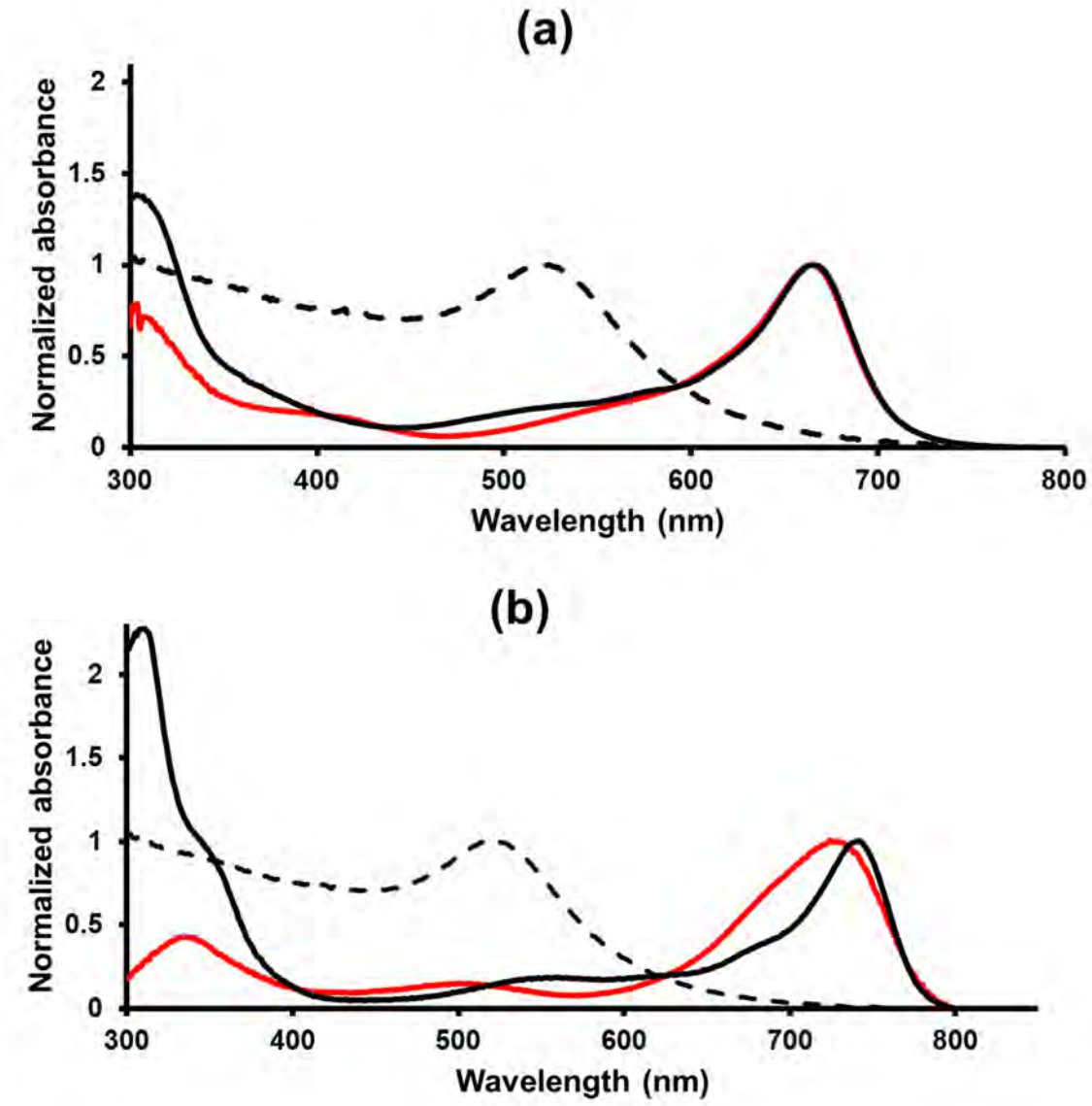

Figure 47. Normalised ground-state absorption spectra of (a) AuNPs (dotted line), **1** (red line) and **1@AuNPs** (black line), (b) AuNPs (dotted line), **2** (red line) and **2@AuNPs** (black line). Solvent: DCM.

5.1.1.2. Transmission electron microscopy images

It is crucial to determine the sizes of nanoparticles in drug delivery because nanoparticles with sizes below 30 nm are preferred over larger ones [127]. This is because small nanoparticles can easily bypass the reticular endothelial system and thus can be more efficient in penetrating the target cells [127]. TEM was used to determine the sizes of the AuNPs and their conjugates. The TEM micrographs for unconjugated AuNPs (a), **1@AuNPs** (b) and **2@AuNPs** (c) are shown in **Figure 48**. The AuNPs are relatively spherical with an average size of 2 nm, while the conjugates afforded similar morphology with a size range of 6−10 nm for both **1** and **2** conjugates.

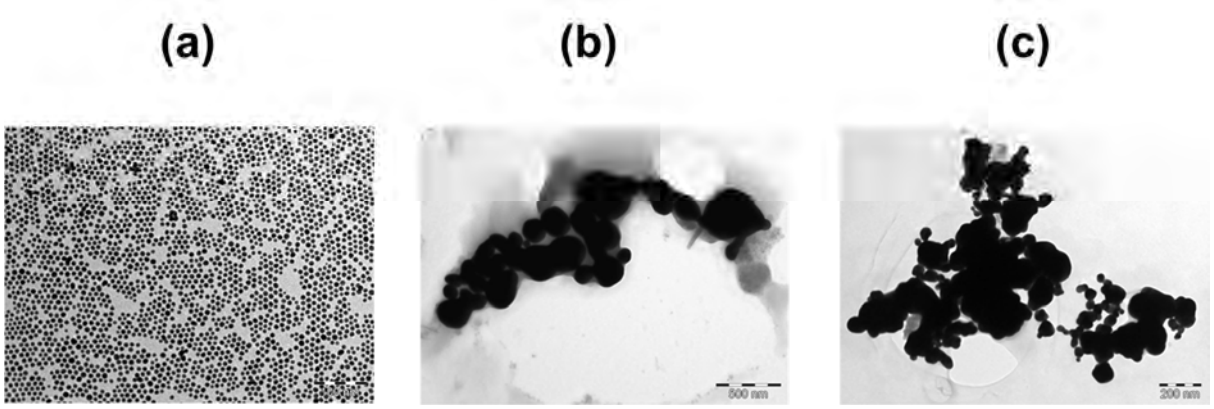

Figure 48. TEM micrographs for (a) **AuNPs**, (b) **1@AuNPs** and (c) **2@AuNPs**. The **AuNPs** are relatively spherical with an average size range of 2 nm, while the conjugates exhibit similar morphology with a size range of 6−10 nm.

5.1.1.3. Dynamic light scattering

DLS was used to determine the hydraulic diameters of the AuNPs and their conjugates to aza-BODIPY dyes. The values obtained were 20.1, 7.63 and 8.12 nm for AuNPs (a), **1@AuNPs** (b) and **2@AuNPs** (c), respectively, as shown in **Figure 49**.

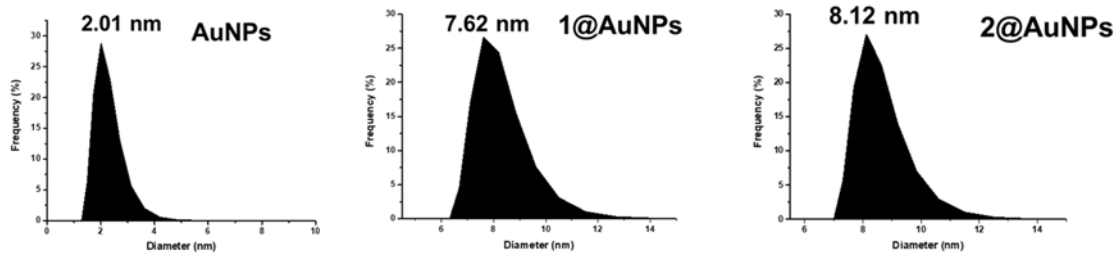

Figure 49. Dynamic light scattering of (a) AuNPs, (b) **1@AuNPs** and (c) **2@AuNPs**. Solvent = DCM.

5.1.1.4. X-ray diffraction

XRD analysis was used for structural characterisation. The typical XRD pattern for AuNPs is shown in **Figure 50**. The XRD pattern observed corresponds to AuNPs and shows Bragg reflections, which are readily visible in the face-centred cubic gold nanostructures [55-58]. The diffraction peak at 38° belongs to the 111 plane of the face-centred-cubic structure (**Figure 50**). Other gold planes, such as 200, 220, and 311, have much weaker diffraction peaks [55-58]. The nanoparticles were not entirely crystalline. There is an amorphous peak at 20°. Complete crystallinity was observed after conjugation to the aza-BODIPY dyes.

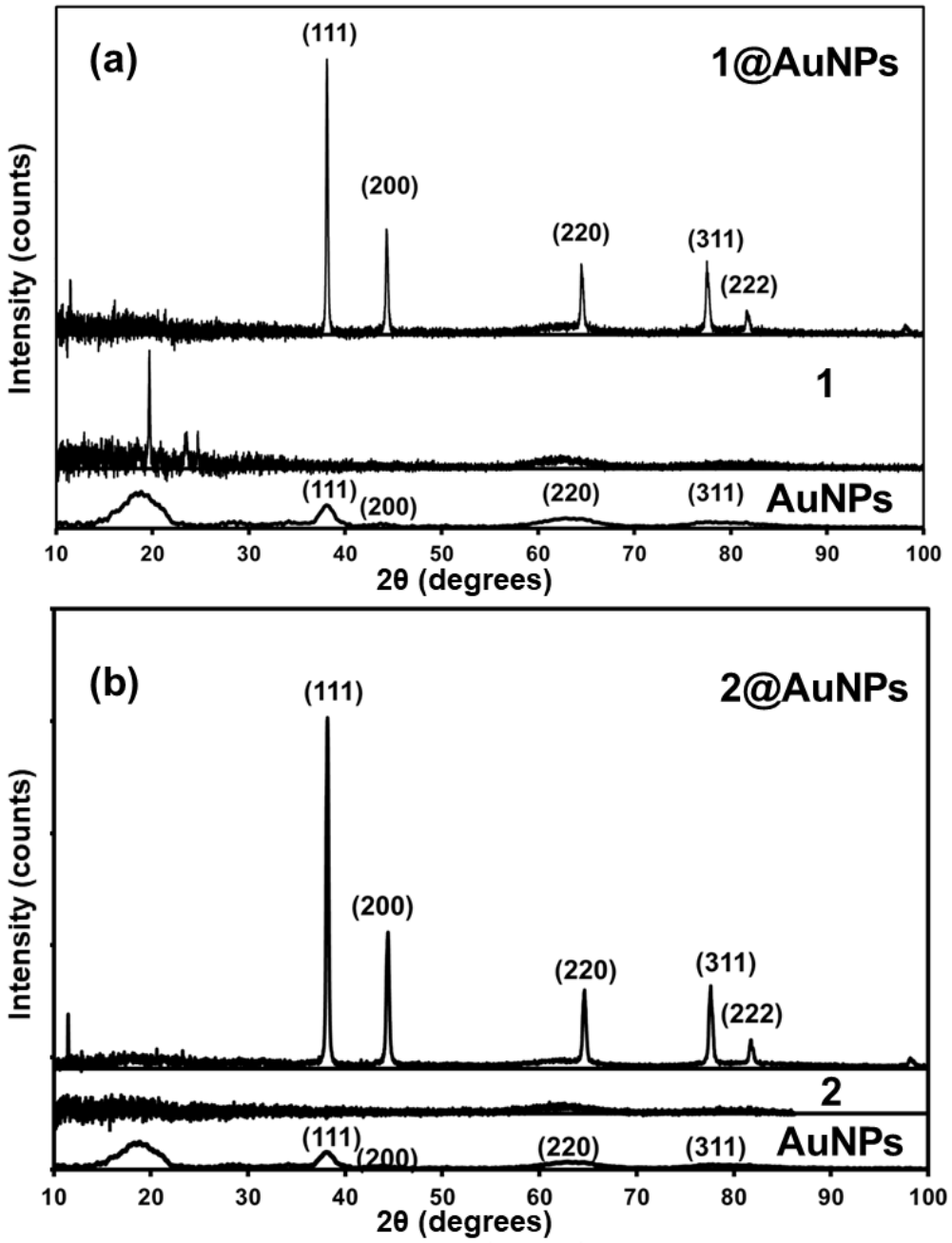

Figure 50. XRD diffractograms of (a) AuNPs, **1** and **1@AuNPs** and (b) AuNPs, **2** and **2@AuNPs**.

5.1.1.5. Energy-dispersive X-ray spectroscopy

The elemental composition of the unconjugated AuNPs and their conjugates was determined using EDS. Before conjugation to the respective aza-BODIPYs, the AuNP spectrum exhibited gold peaks, while the spectra of aza-BODIPYs contain nitrogen,

iodine, carbon and sulfur peaks. All these elements are present in the dye structures. Upon conjugation to aza-BODIPYs **1** and **2**, a combination of the elements in the AuNPs and aza-BODIPYs was observed, **Figure 51**.

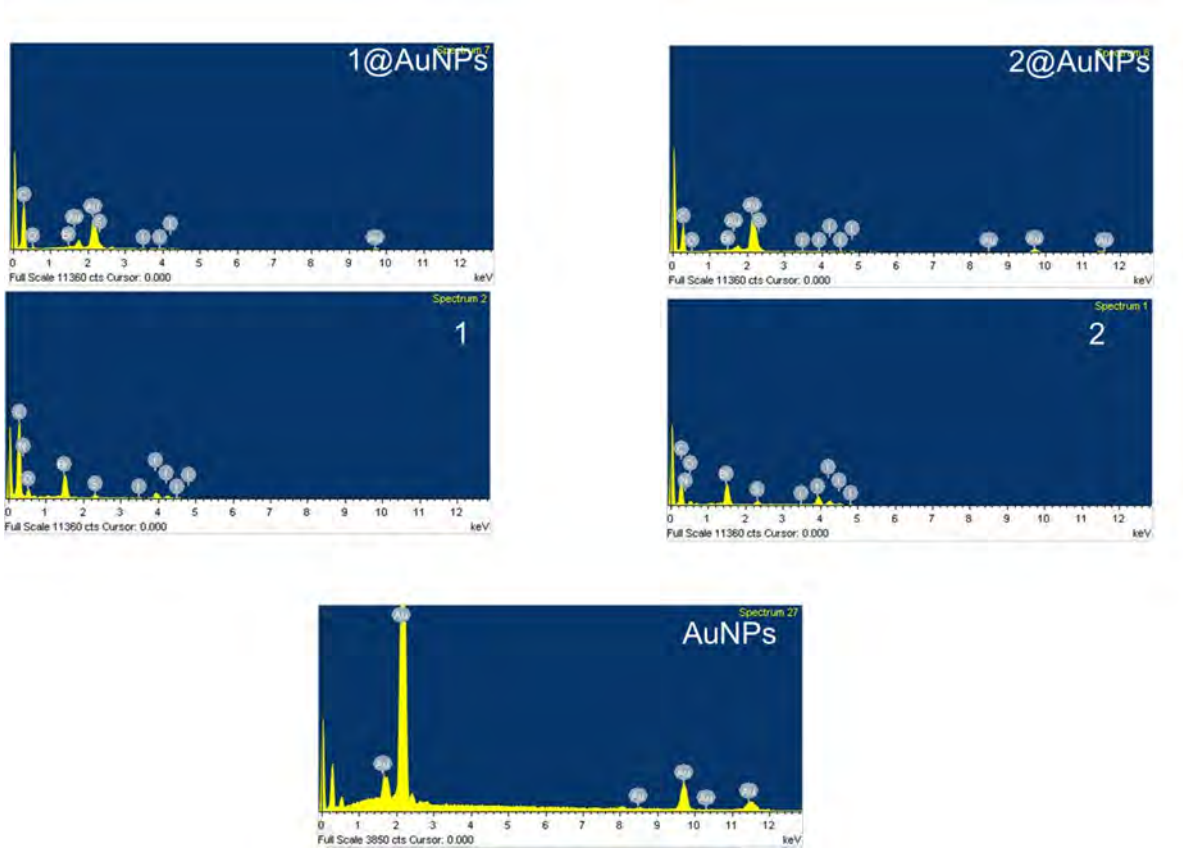

Figure 51. EDS spectra of AuNPs, **1**, **1@AuNPs**, **2** and **2@AuNPs**.

5.1.1.6. Partition coefficients

The partition coefficients of the conjugates were obtained through the octanol-water system, as described in Chapter 3. The results show that aza-BODIPYs **1** and **2** have comparable hydrophilicity, while the respective conjugates are more hydrophilic than the dyes alone. **2@AuNPs** has a higher degree of hydrophilicity than **1@AuNPs.** **Table 5** provides a summary of these results.

Table 5. The octanol-water partition coefficients of aza-BODIPY dyes and their AuNP conjugates.

	K_{ow}	**Log P_{ow}**
1	1.48	0.17
1@AuNPs	1.34	0.13
2	1.44	0.16
2@AuNPs	1.29	0.11

5.1.1.7. Singlet oxygen quantum yields and triplet lifetimes

The $^1O_2$ quantum yields were quantified in DMSO using DPBF as a $^1O_2$ scavenger and methylene blue as a standard. The unconjugated aza-BODIPYs had lower Φ_Δ than the conjugates, with **1** having Φ_Δ = 0.83 and **2** with Φ_Δ = 0.17. The conjugates had 0.88 and 0.26 for **1@AuNPs** and **2@AuNPs**, respectively. The increment in the $^1O_2$ quantum yields is attributed to the external heavy atom effect contributed by the AuNPs. The triplet state quantum yields were determined in DMSO. As expected, the triplet quantum yields of both dyes after conjugation slightly decreased. The values are listed in the table below (**Table 6**).

Table 6. Singlet oxygen and triplet quantum yields.

	Φ_Δ (± 0.01)	**τ_T (± 0.01) (μs)**
1	0.83	13.2

1@AuNPs	0.88	10.3
2	0.17	10.2
2@AuNPs	0.26	8.62

5.2. Aza-BODIPY-folic acid conjugates

The conjugation of aza-BODIPYs with FA was achieved through the esterification of the hydroxyl groups of the dyes and the γ-carboxylic acid groups of the FA to obtain **3-FA** and **4-FA**, respectively. It has been reported that FA conjugates achieved through γ-carboxylic acid groups of FA retain their affinity towards the folate receptors [69, 70]. As such, selective activation of the γ-carboxylic acid groups adapted in this work has been reported to yield 55−90% of the γ-conjugates. The conjugates formed were easily separated through precipitation in diethyl ether.

Two aza-BODIPY dyes, **3** and **4** (**Figure 52**), were conjugated to folic acid, a targeting ligand, to enhance their binding to the cancer cells due to the cancer cells having folic receptors on their surface. The presence of folic acid in the dye structures enhances their biocompatibility and solubility in physiological environments for application in PDT. The formation of aza-BODIPY-folic acid conjugates was confirmed by UV-visible absorption and NMR spectroscopy, and XPS. The conjugates could not be ionised when mass spectroscopy was used.

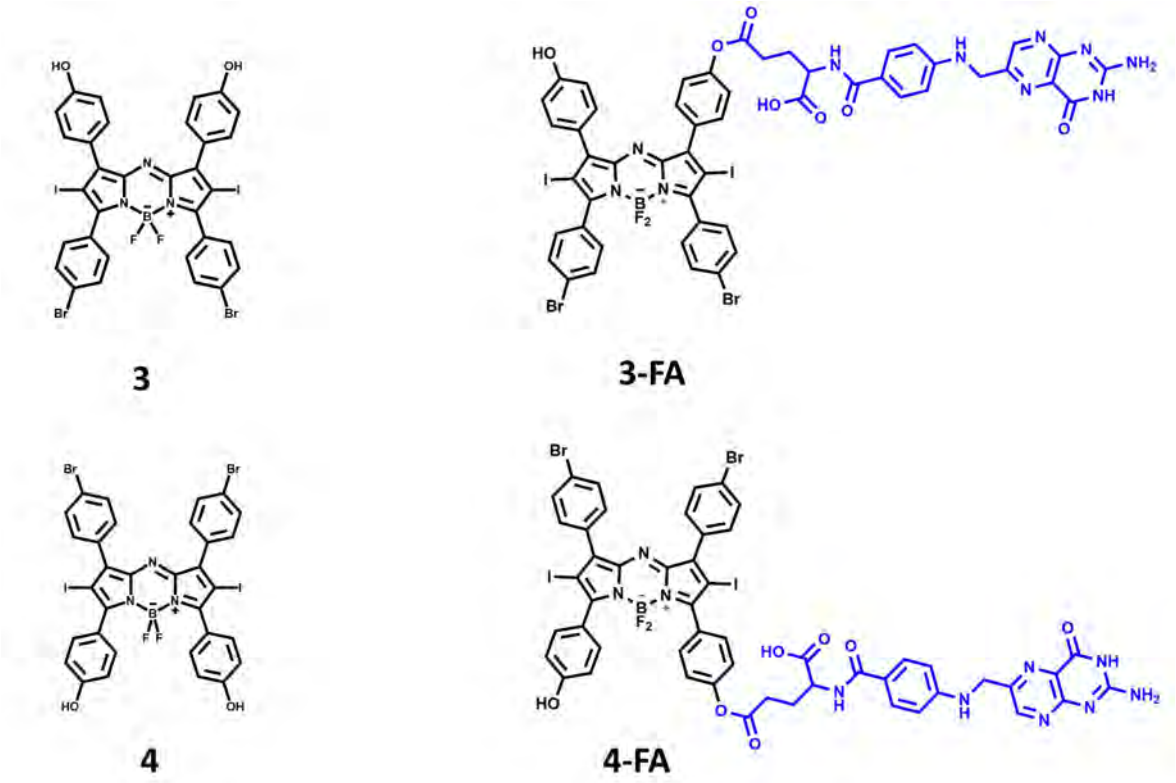

Figure 52. Aza-BODIPY dyes and their respective aza-BODIPY-folic acid conjugates.

5.2.1. Characterisation of aza-BODIPY-folic acid conjugates

5.2.1.1. UV-visible absorption spectroscopy

Folic acid was conjugated to aza-BODIPYs **3** and **4**. The UV-visible absorption spectra of the respective dyes and their conjugates are shown in **Figure 53**. The absorption spectra of the dyes in DMSO are illustrated in **Figure 53**. Broad bands ranging from around 550 to 750 nm, corresponding to $S_0 \rightarrow S_1$ transitions, were observed in the UV-visible absorption spectra of the dyes. The absorption maxima observed for the two series of dyes were as follows, Series 3: 669 nm for **3** and 630 nm for **3-FA**. Series 4: 719 nm for **4** and 643 nm for **4-FA**, as illustrated in **Figure 53 (a & b)**. A large blue shift was observed of the major aza-BODIPY spectral bands upon conjugation to FA. This may be related to aggregation. Most importantly, the aza-BODIPY@FA

conjugates were soluble in water, and broad absorption maxima were observed between 600 and 750 nm for both **3-FA** and **4-FA** in the phototherapeutic window.

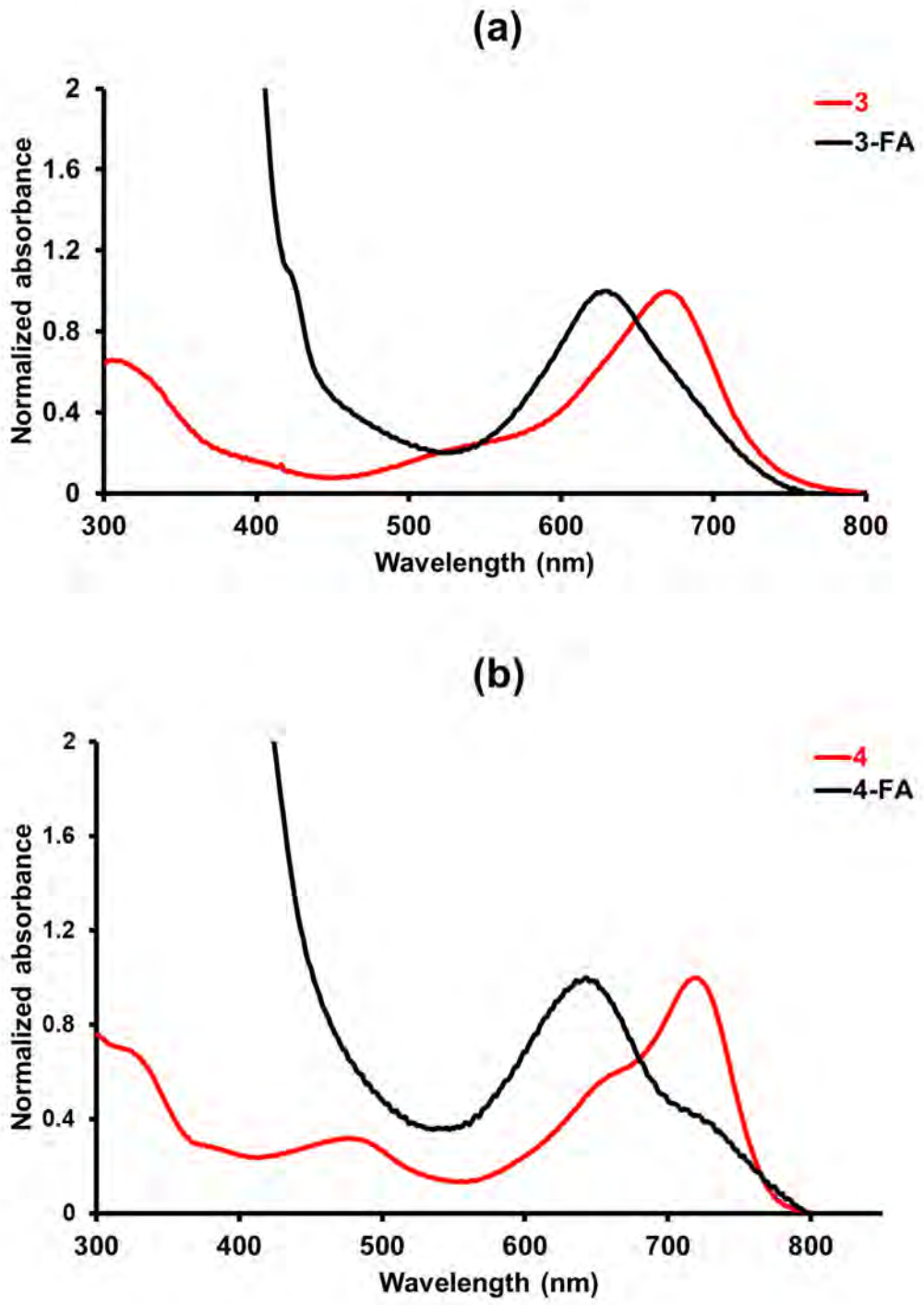

Figure 53. (a) Normalised ground-state absorption spectra of **3** and **3-FA**. (b) Normalised ground-absorption spectra **4** and **4-FA**. Solvent = DMSO.

5.2.1.2. ^{1}H NMR spectrum of aza-BODIPY-folic acid conjugates

The ^{1}H NMR spectra of the parent and conjugated dyes were obtained. **Figure 54** shows the ^{1}H NMR spectrum of the **3-FA**. The elucidation of the conjugates was difficult since the NMR spectrum of FA is complicated [128, 129]. The conjugation of the aza-BODIPYs to FA was confirmed by additional peaks in the ^{1}H NMR spectra attributed to the FA protons. There was a disappearance of one hydroxyl proton, suggesting a conjugation at one of the hydroxyl groups. A similar trend was observed for **4-FA** conjugate, **Figure 55**. A single conjugation of the folic acid was obtained, possibly due to the bulkiness of the folic acid, which could have caused some steric hindrance.

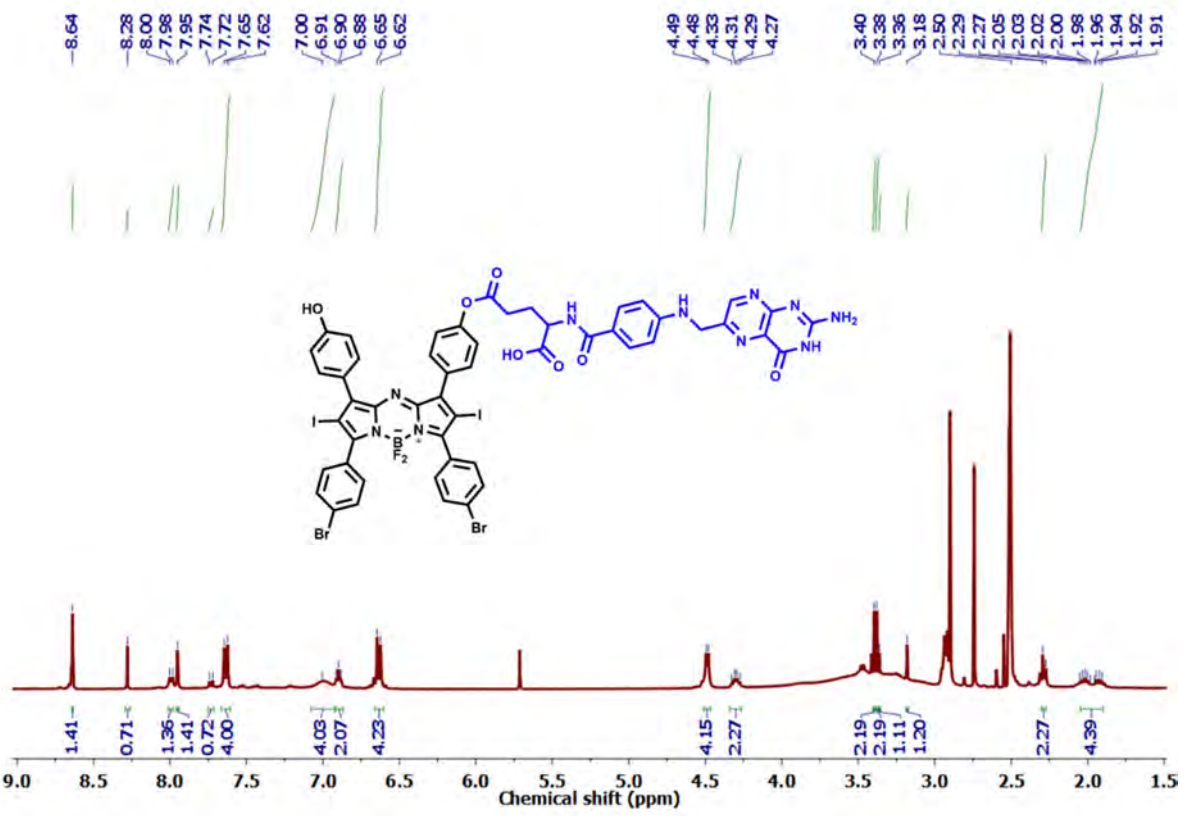

Figure 54. ^{1}H NMR spectrum of **3-FA**. Solvent: DMSO-d_6.

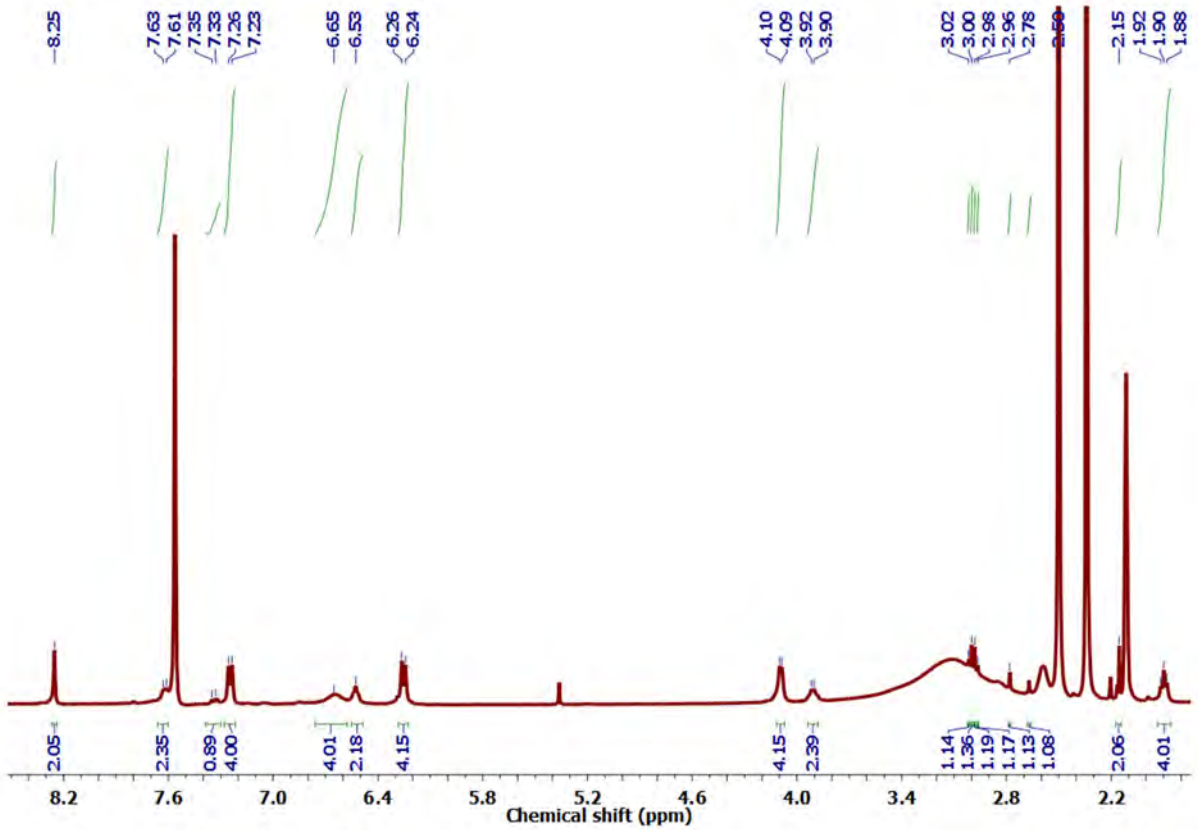

Figure 55. ^{1}H NMR spectrum of **4-FA**. Solvent: DMSO-d_6.

5.2.1.3. Partition coefficients

The partition coefficients of the folic acid conjugates were obtained through the previously described octanol-water system method in Chapter 3. The results show that the presence of the sulfur group in aza-BODIPY **4** increased the hydrophilicity of the dye (Log P_{OW} = -0.10), compared to the more lipophilic derivative, **3** (Log P_{OW} = 1.04). The two folic acid conjugates were found to be less hydrophilic, with **3-FA** being more hydrophobic (higher Log P_{OW}) than **3-FA**. **Table 7** provides a summary of these results.

Table 7. The octanol-water partition coefficients of aza-BODIPY dyes and their folic acid conjugates.

	K_{ow}	Log P_{ow}
3	1.39	0.14
3-FA	11.41	1.06
4	0.20	-0.70
4-FA	2.53	0.40

5.2.1.4. Singlet oxygen quantum yields and triplet state lifetimes

The $^1O_2$ quantum yields were quantified in DMSO using DPBF as a $^1O_2$ scavenger and methylene blue as a standard. The unconjugated aza-BODIPYs had lower Φ_Δ than the conjugates, with **3** having Φ_Δ = 0.14 and **4** with Φ_Δ = 0.04. The conjugates had 0.09 and 0.09 for **3-FA** and **4-FA**, respectively. The values are listed in the table below (**Table 8**). Aggregation effects are the most likely explanation for the relatively low Φ_Δ values since the conjugates were water-soluble and exhibited broad spectral bands in DMSO and in water.

Table 8. Singlet oxygen and triplet state lifetimes.

	Φ_Δ (± 0.01)	τ_T (μs)
3	0.14	13.6 ± 0.12
3-FA	0.09	19.7 ± 0.32
4	0.04	19.4 ± 0.67

4-FA	0.02	16.1 ± 0.86

5.3. Porphyrin-folic acid conjugates

Folic acid was specifically selected for conjugation to Sn(IV) and In(III) metallated tetrapyridylporphyrins for the reasons mentioned in Section 5.2. above. To the best of our knowledge, the axial ligation of these adducts with folic acid has not been explored previously. Thus, this approach was explored to determine whether it provides better targeting of the cancerous site, biocompatibility, and prevention of aggregation as folic acid is bulky and, to some extent, improved solubility in physiological environments. To further enhance the water-solubility of these conjugates, the FA conjugates were quaternised to afford readily water-soluble dyes. UV-visible absorption spectroscopy, ^{1}H NMR and XPS were used to characterise the conjugates. The porphyrins and their folic acid conjugates before and after quaternisation are shown in **Figure 56**.

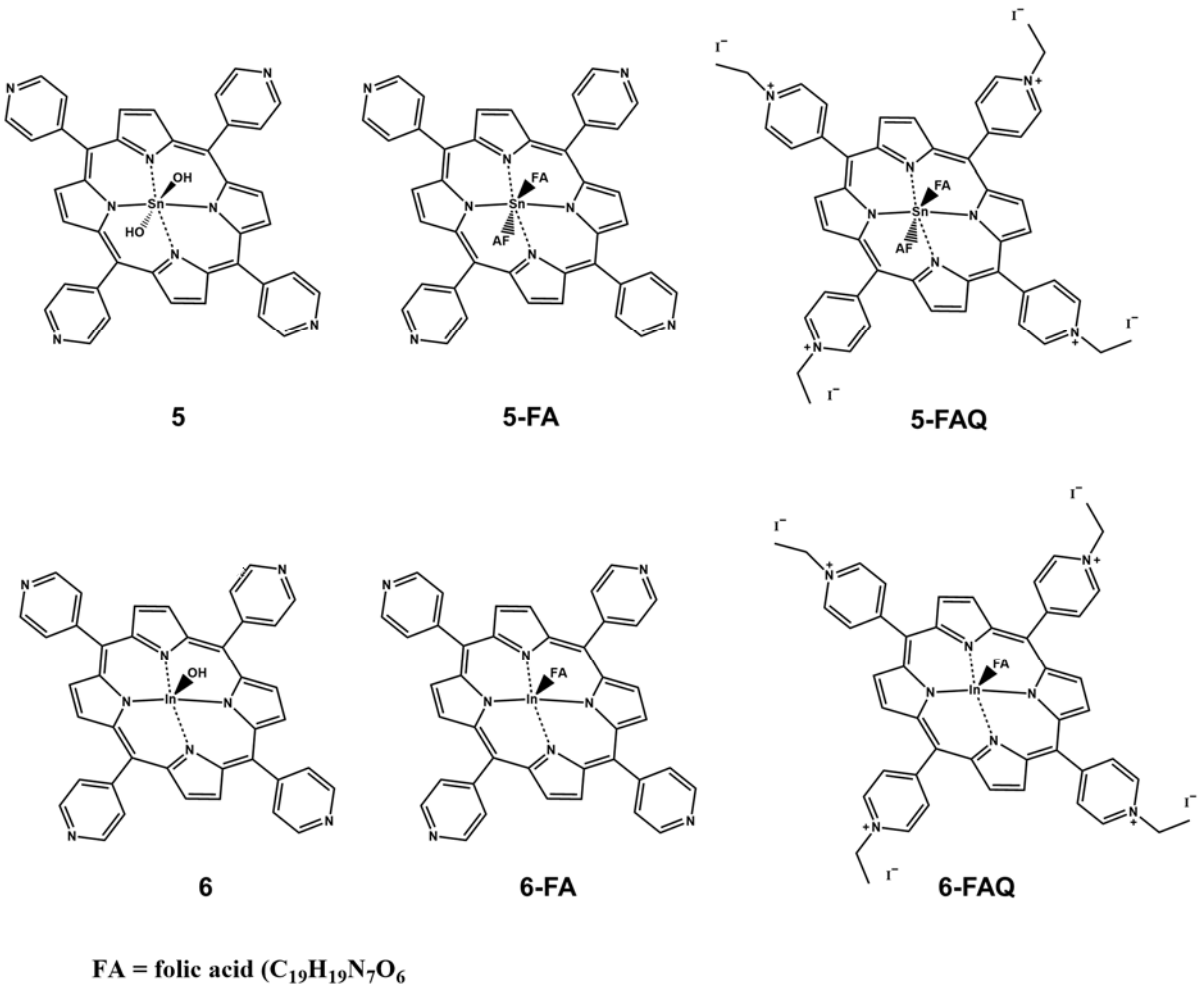

Figure 56. Porphyrins, porphyrin-folic acid conjugates and quaternised porphyrin-folic acid conjugates.

5.3.1. Characterisation of porphyrin-folic acid conjugates

*5.3.1.1. UV-visible absorption spectroscopy of **5-FA***

As anticipated, an intense Soret (or B) and two Q bands were observed in the UV-visible absorption spectra of the porphyrins for reasons outlined in Chapter 3. As shown in **Figure 57**, the absorption spectrum of FA-incorporated Sn(IV) complex (**5-FA**) is the same as that of parent complexes **5**, with a slight blue shift of the B and Q bands. The same trends were observed for In(III) porphyrins complexes.

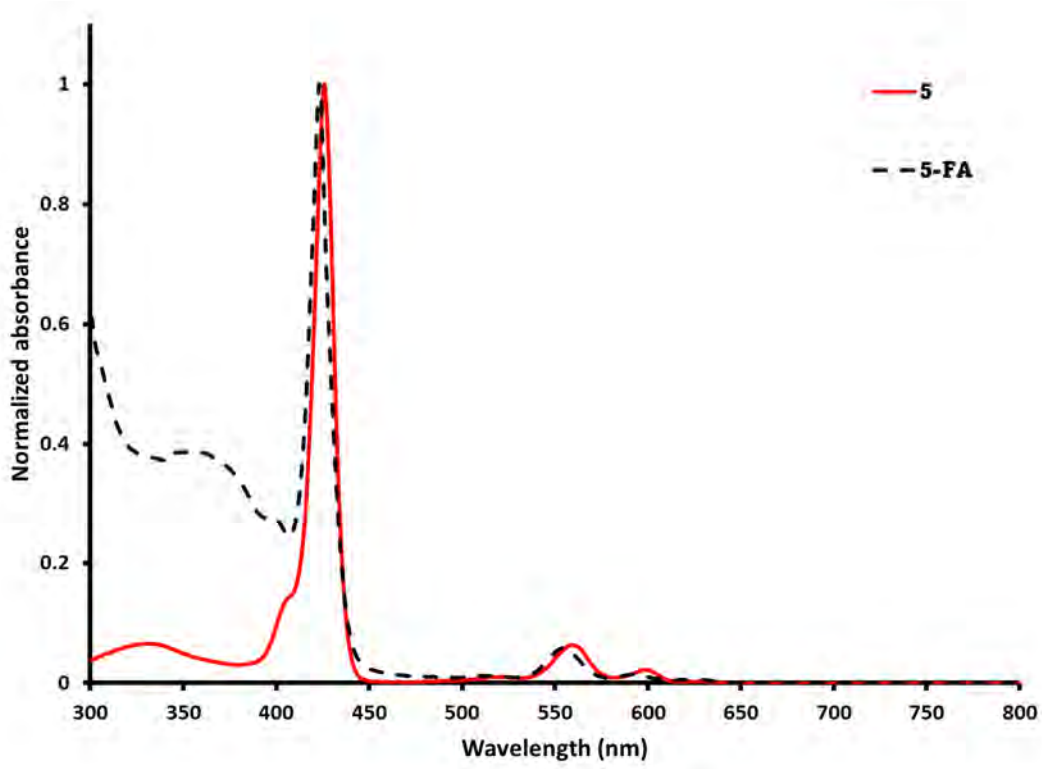

Figure 57. Normalised absorption ground-state spectra of **5** and **5-FA**. Solvent = DMSO.

*5.3.1.2. UV-visible absorption spectroscopy of **5-FAQ***

After quaternisation with ethyl iodide, **5-FAQ** and **6-FAQ** also preserved the parent absorption profiles with a slight red shift of the B and Q bands. The results are summarised in **Table 7**, and the UV-visible absorption spectra of **5**, **5-FA** and **5-FAQ** are shown in **Figure 58**.

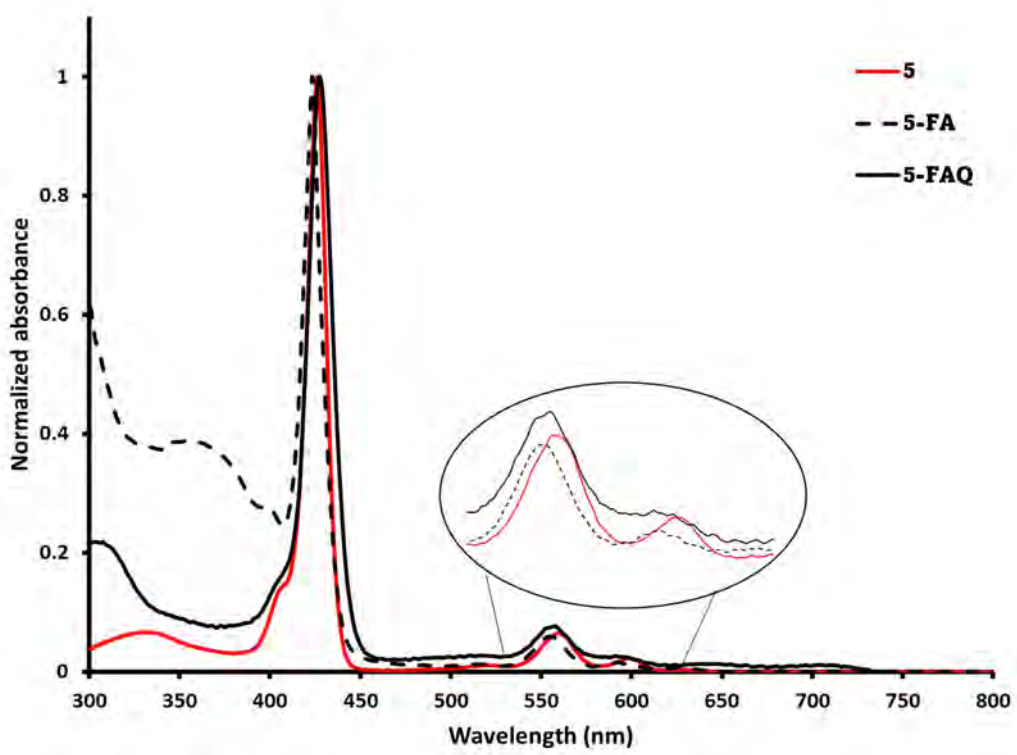

Figure 58. Normalised absorption ground-state spectra of **5**, **5-FA** and **5-FAQ**. Solvent = DMSO.

5.3.1.3. ^{1}H NMR spectra of porphyrin-folic acid conjugates

The ^{1}H NMR spectra of the parent and conjugated dyes were obtained. **Figure 59** shows the ^{1}H NMR spectrum of the **5-FA**. The appearance of additional peaks in the ^{1}H NMR spectrum of the porphyrin-FA conjugate confirmed the successful conjugation in qualitative terms. The extra protons are attributed to the FA protons. Two FA ligands were believed to be present for the Sn(IV) metallated porphyrin complex based on the integrated peak values. Since the In(III) metalated porphyrin has a single hydroxyl axial proton, a single FA axial ligand was confirmed by integrating the ^{1}H NMR spectrum of **6-FA**, **Figure 60**. There was a disappearance of the hydroxyl proton, suggesting that conjugation at the hydroxyl group of the complex was successful.

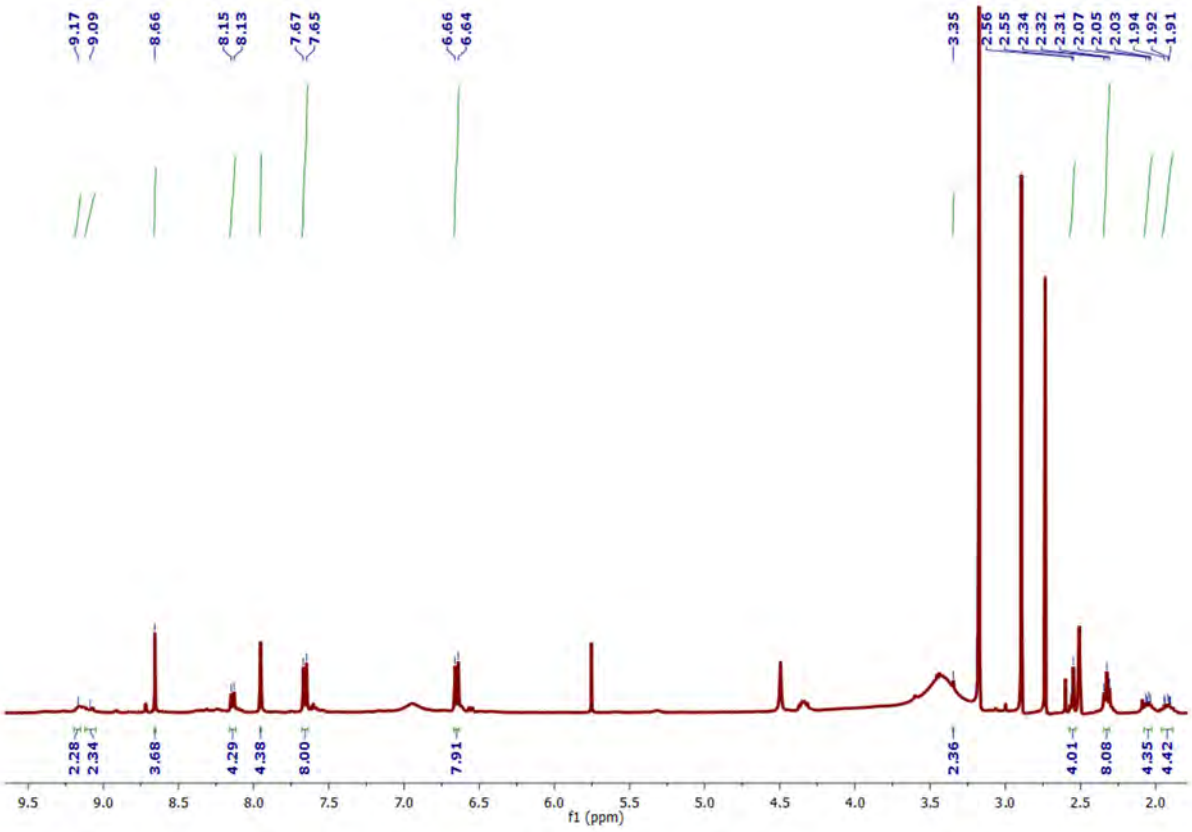

Figure 59. ^{1}H NMR spectrum of **5-FA**. Solvent = $CDCl_3$.

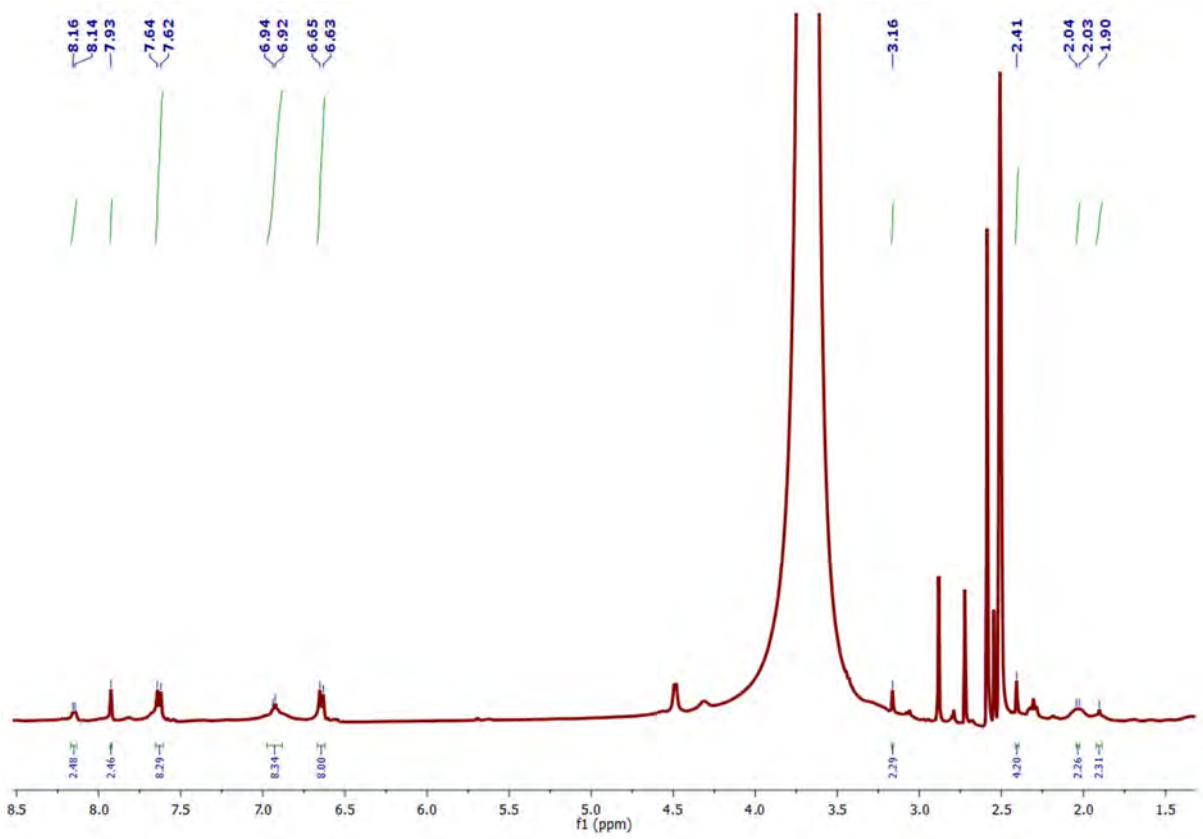

Figure 60. ^{1}H NMR spectrum of **6-FA**. Solvent = $CDCl_3$.

5.3.1.4. ^{1}H NMR spectra of quaternised porphyrin-folic acid conjugates

The ^{1}H NMR spectra of the quaternised folic acid-conjugated porphyrins were very difficult to integrate, **Figures 61** and **62**, but provided direct spectroscopic evidence in proof of principle terms that quaternisation had occurred through the presence of further additional peaks. Both the Sn(IV) and In(III) porphyrins were confirmed to be tetra-quaternised in this context.

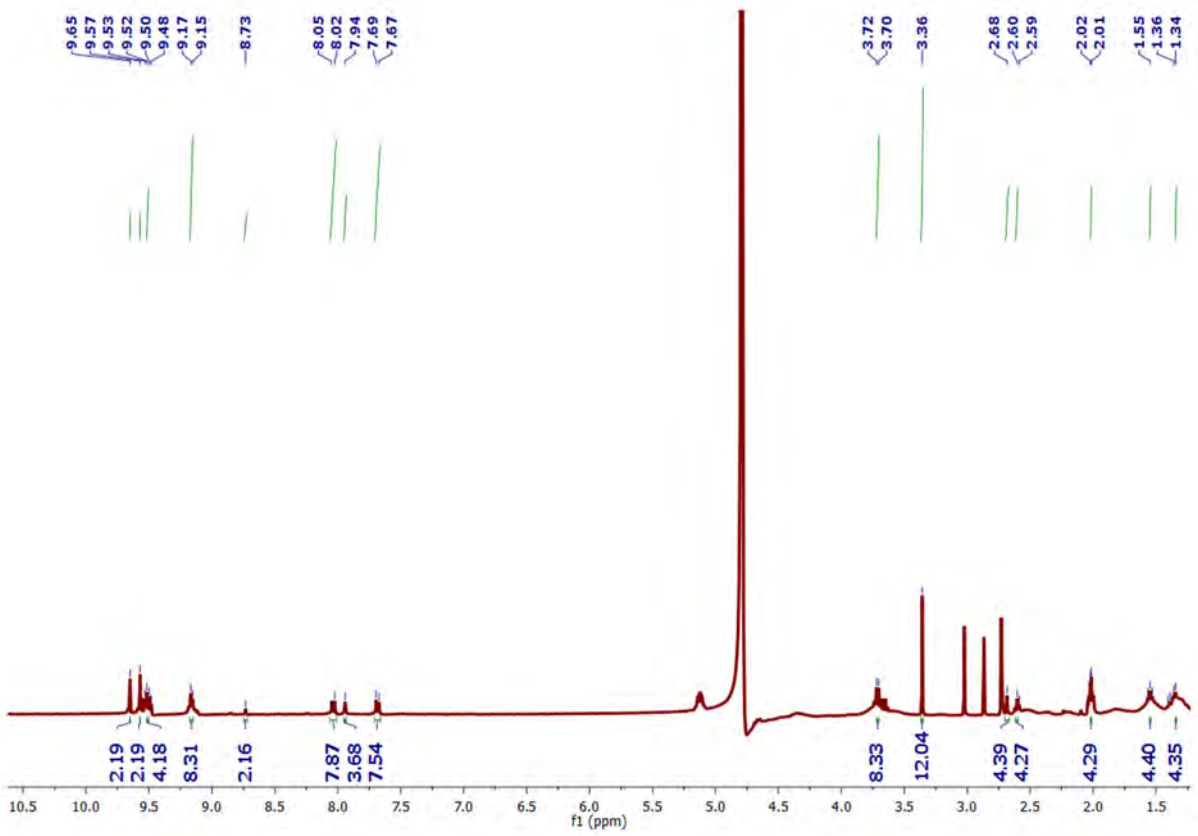

Figure 61. ^{1}H NMR spectrum of (a) **5-FAQ**, solvent = D_2O. and (b) **6-FAQ**, solvent DMSO-d_6.

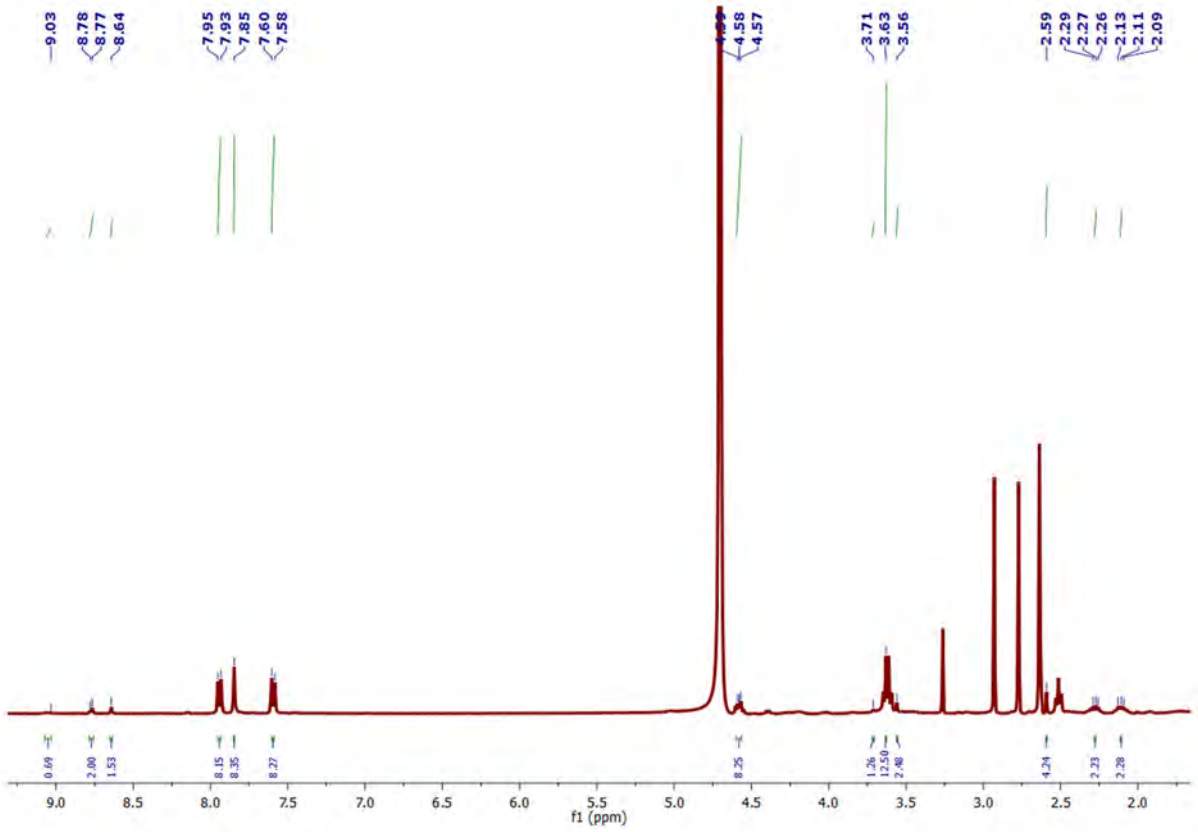

Figure 62. ^{1}H NMR spectrum of **6-FAQ**. solvent D_2O.

5.3.1.5. X-ray photoelectron spectroscopy

XPS was used to confirm the conjugation of porphyrin complexes to folic acid. High-resolution XPS was used to prove that **5** was successfully linked to folic acid *via* ester bonds. The N 1s peak was deconvoluted with two subpeaks which match (1) the pyridinic nitrogen overlapping the N-H and (2) the pyrrolic nitrogen overlapping the N-H_2 peaks at 398 and 399 eV, respectively [131, 132], **Figure 63**. The intensities of the conjugate N 1s peaks (**Figure 63 (a)**) are much lower than the intensity of the folic acid and the porphyrin alone. The C 1s peaks of the conjugate were observed at 284 eV (C=O) and 287 eV (C-N/C-NH_2) [131, 132]. There was a pronounced increase in the intensity of the C-N peak of the conjugate, suggesting the linkage of the porphyrin and folic acid. The O 1s of the porphyrin and folic acid (**Figure 63 (b) and (c)**),

respectively, have two deconvoluted peaks at 530 and 532 Ev [131, 132]. Upon conjugation, the peaks were overlapping and broad, with the maximum binding energy at 531 eV (**Figure 63 (a)**). In general, the morphology of the peaks in the conjugate differs from the morphology of the folic acid and porphyrin alone. This helps to further confirm their successful conjugation.

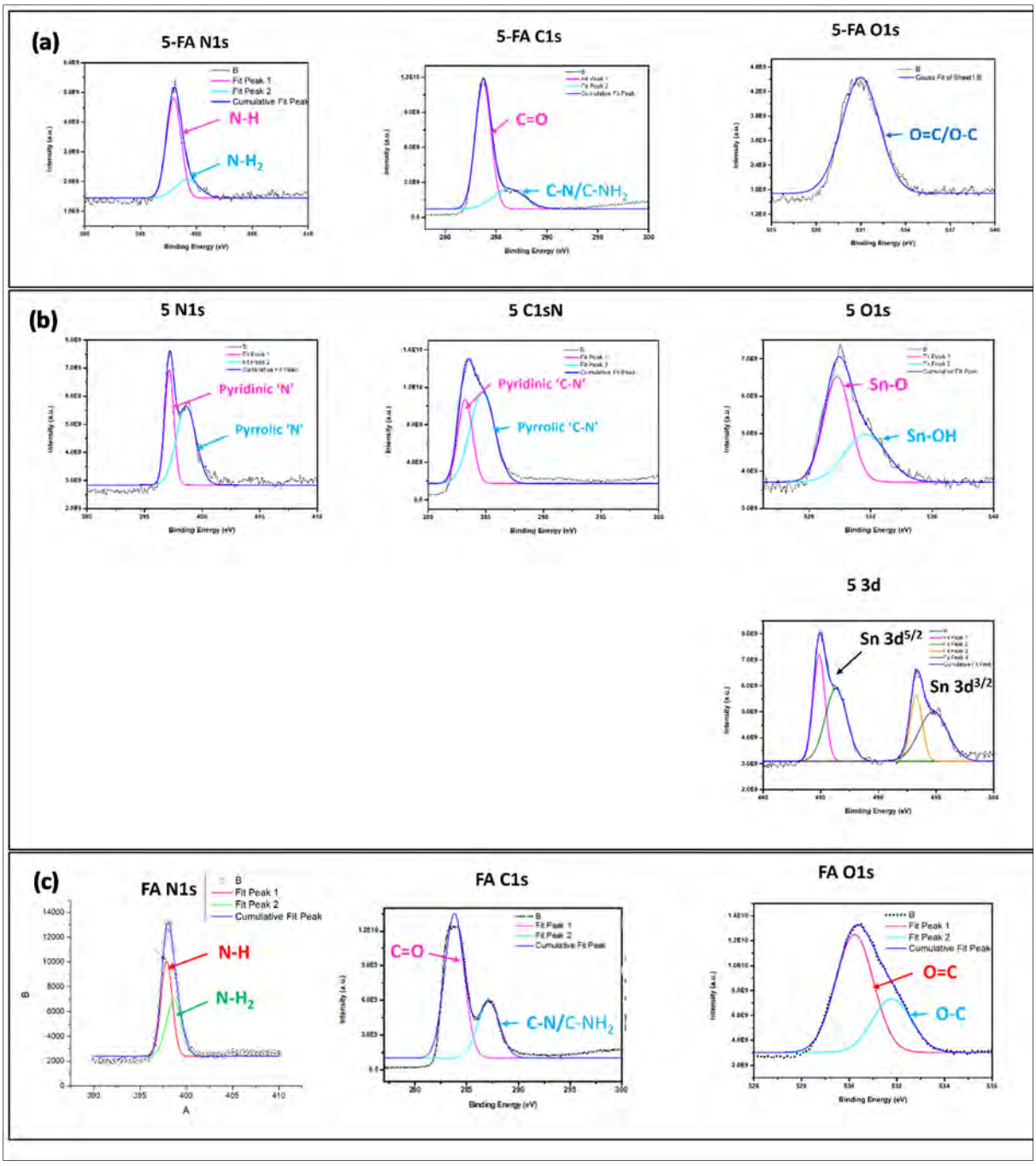

Figure 63. High-resolution XPS of (a) **5-FA**, (b) **5** and (c) FA.

5.3.1.6. Partition coefficients

The octanol-water system technique was used to obtain the Log P_{OW} values of the porphyrins and the conjugates [109, 110]. The results show that the unconjugated porphyrins had the lowest solubility in water and, thus, the highest lipophilicity. The values obtained for **5** and **6** were recorded as Log P_{OW} = −0.10 and 1.04, respectively. The two quaternised folic acid conjugates were found to be the least lipophilic, with a preference for residing in the aqueous phase and are, thus, the most hydrophilic of the complexes. **Table 9** provides a summary of these results.

Table 9. The octanol-water partition coefficients of porphyrins and their folic acid conjugates.

	K_{ow}	**Log P_{ow}**
5	11.4	1.06
5-FA	1.39	0.14
5-FAQ	1.10	−0.70
6	2.53	0.40
6-FA	0.20	−0.70
6-FAQ	0.02	−1.70

5.3.1.7. Singlet oxygen quantum yields and triplet quantum yields

The $^1O_2$ quantum yields of the porphyrins and their conjugates were determined in DMSO, using DMA as a $^1O_2$ scavenger and H_2TPP as a standard. **Figure 64** shows the degradation of the DMA peaks at 10 s intervals over a period of 70 s, using **5** as an example.

The general trend observed was that the $^1O_2$ quantum yields increased upon conjugating the porphyrins to folic acid. After the quaternisation of the conjugates with ethyl iodide, the singlet oxygen decreased. This is due to the increased polarity of the dyes. The summary of the results is given in **Table 10**.

The triplet lifetime quantum yields of the porphyrins and their conjugates were studied. The results are given in **Table 10**. There is a gradual decrease in the quantum yields upon conjugation of the porphyrins with folic acid. This could be attributed to the solubilisation imparted by the folic acid ligand on the porphyrin and, thus, the decrease in the triplet lifetimes.

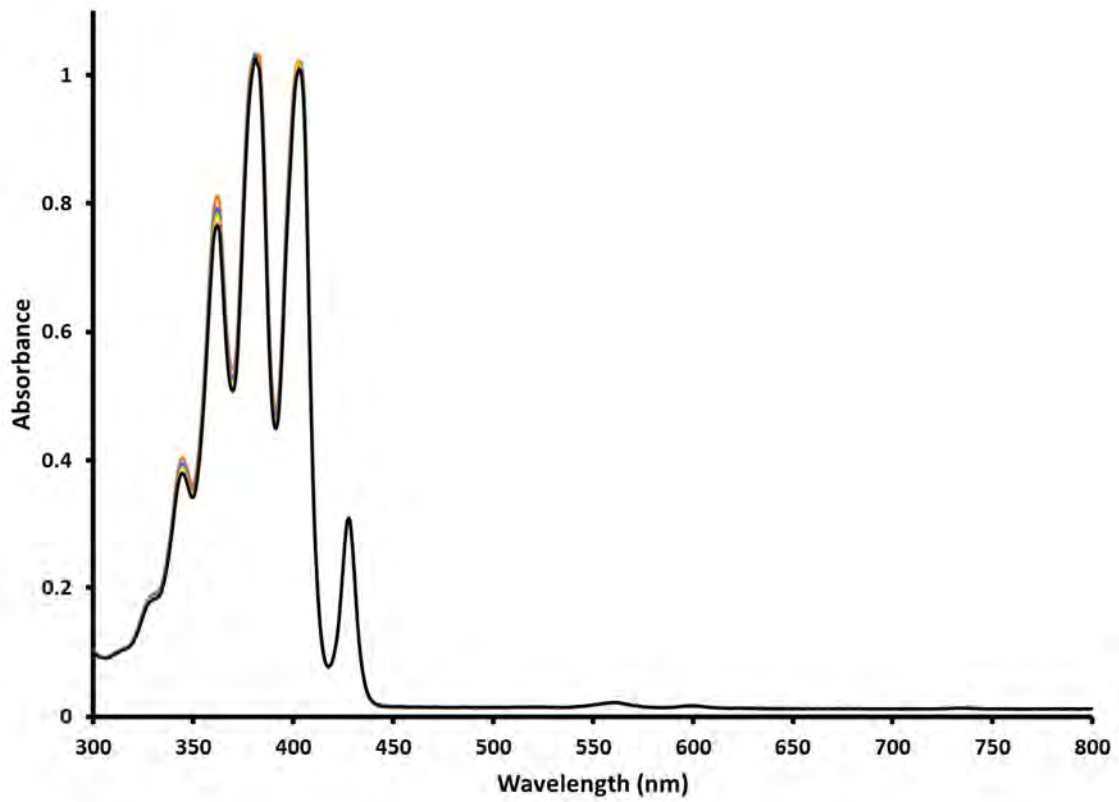

Figure 64. UV-visible absorption spectra were recorded to determine the Φ_Δ value of **5** in the presence of DMA as a scavenger. Solvent = DMSO.

Table 10. Singlet oxygen and triplet quantum yields.

	Φ_Δ (±0.01)	τ_T (± 0.01) (μs)
5	0.45	50.3±0.13
5-FA	0.49	39.8±0.11
5-FAQ	0.14	35.9±0.27
6	0.30	15.3±0.14
6-FA	0.38	9.52±0.10

6-FAQ	0.11	7.55±0.10

5.4. Concluding remarks

The synthesis of new porphyrin and aza-BODIPY adducts using facile procedures was successful. The **1@AuNPs** and **2@AuNPs** conjugates yielded relatively high $^1O_2$ quantum yields due in part to the external heavy atom effect, making the dyes potentially suitable for use in PDT and PACT. Secondly, a set of aza-BODIPY dyes was conjugated to folic acid to form water-soluble aza-BODIPY-folic acid conjugates **3-FA** and **4-FA**. Aqueous solubility is crucial in physiological applications such as PDT. The relatively low $^1O_2$ quantum yields and blue shifted major aza-BODIPY spectral bands may be consistent with significant aggregation effects, however. This topic will be explored further in Chapter 9. Thirdly, two porphyrin dyes were conjugated to folic acid. In contrast with **3-FA** and **4-FA**, these conjugates were not water-soluble. Thus, it was decided to introduce ethyl iodide to achieve water-soluble porphyrin-folic acid conjugates through quaternisation. The **5-FAQ** and **6-FAQ** conjugates produced appreciable $^1O_2$ quantum yields and were hence carried forward into the PDT studies.

Chapter 6: Photodynamic therapy

6.1. Cellular uptake studies

This chapter describes the cellular uptake and the photodynamic effect of aza-BODIPY dyes, porphyrins and their AuNPs or folic acid conjugates against MCF-7 cancer cells. The uptake of photosensitisers by cancer cells is one of the factors that determines the photodynamic effect of photosensitisers. According to the literature, highly lipophilic compounds can increase cellular absorption because they easily penetrate the lipid bilayer in cells [133, 134]. The cellular uptake of all the dyes and their complexes was studied over a period of 48 h. Triton-X100 was used as a permeabilisation agent to determine the uptake of the respective compounds by the cells.

The absorbance of MCF-7 cancer cells with 10 μM concentration of the compounds at various incubation durations was measured. The absorbance of the cells alone (i.e. the control) remained constant throughout the investigation. According to the experiments, both dyes and their conjugates effectively accumulated in the cells after a 24-h period, and the relative cellular absorption reduced after 24 h. For these reasons, the 24-h incubation was used in the subsequent PDT research.

*6.1.1. Cellular uptake of aza-BODIPYs **1** and **2** and their **1@AuNPs** and **2@AuNPs** conjugates.*

Figure 65 displays the cellular uptake of the two aza-BODIPYs, **1** and **2**, and their **1@AuNPs** and **2@AuNPs** conjugates. The cellular uptake of **2** and **2@AuNPs** was found to be relatively higher compared to that of **1** and **1@AuNPs**. This could be attributed to the hydrophilicity of the molecule, as observed with the partition coefficients in the previous chapter, making these two compounds more bioavailable compared to **1** and **1@AuNPs**.

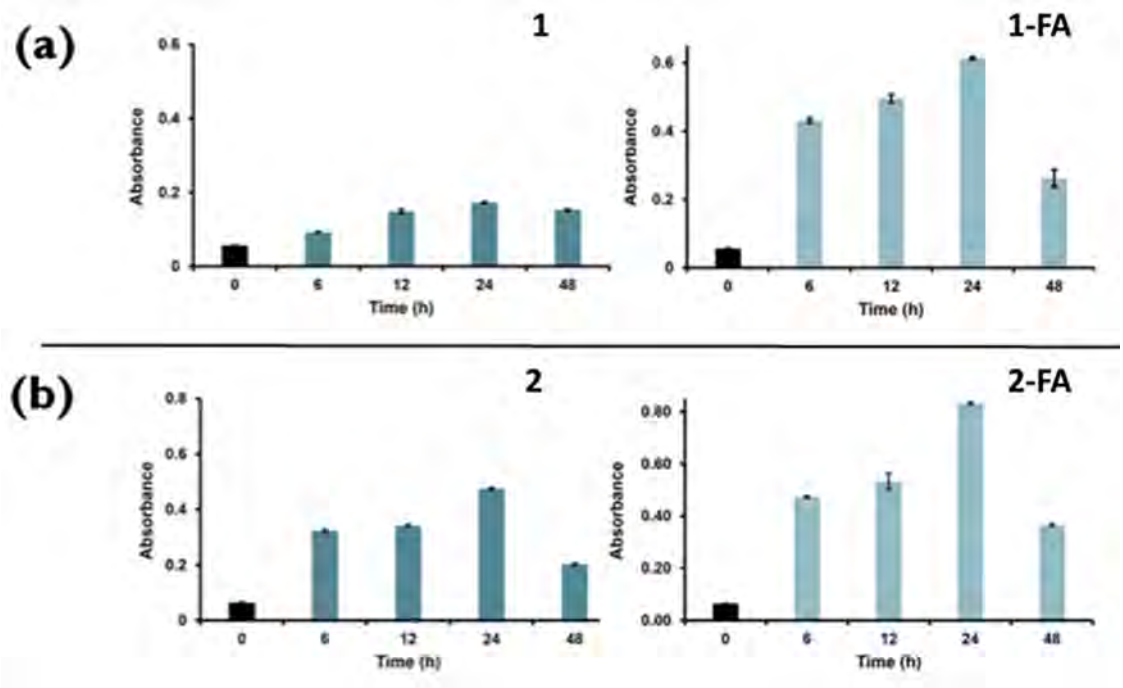

Figure 65. Bar graph showing the cellular uptake of (a) **1** and **1@AuNPs** and (b) **2** and **2@AuNPs** by MCF-7 cancer cells over a 48 h period. The data represent mean ± SD.

*6.1.2. Cellular uptake of aza-BODIPYs **3** and **4** and their folic acid conjugates **3-FA** and **4-FA***

The two conjugates, **3-FA** and **4-FA**, were found to have a relatively higher total cellular absorption than the parent aza-BODIPYs (**Figure 66**). The cellular uptake is very pronounced in the conjugates due to the presence of a targeting ligand, folic acid. The enhanced lipophilicity of the dyes, which allows them to easily penetrate the lipophilic cellular membranes of the cancer cells, contributes to the increased uptake.

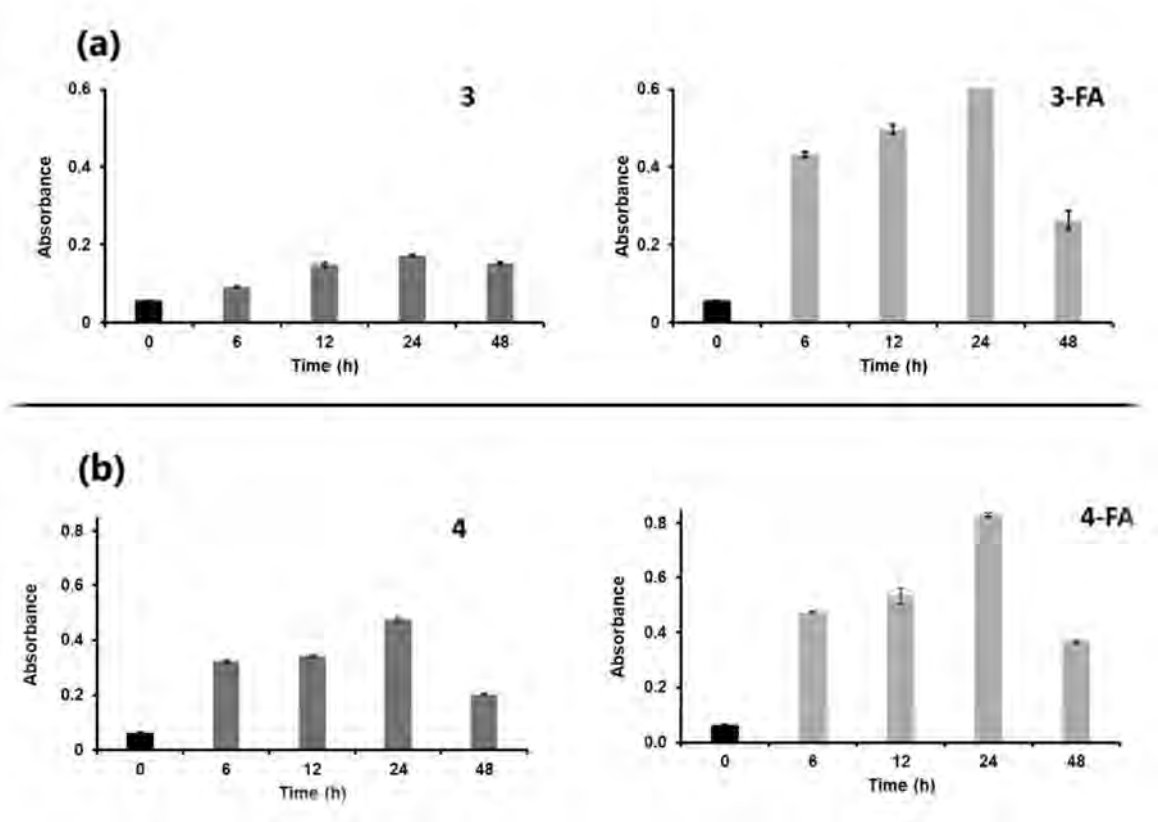

Figure 66. Bar graph showing the cellular uptake of (a) **3** and **3-FA** and (b) **4** and **4-FA** by MCF-7 cancer cells over a 48 h period. Data represent mean ± SD.

*6.1.3. Cellular uptake of porphyrins **5** and **6**, their folic acid conjugates **5-FA** and **6-FA** and their quaternised conjugates, **5-FAQ** and **6-FAQ***

The two conjugates, **5-FA** and **6-FA**, were found to have a relatively higher total cellular absorption than the parent porphyrins (**5** and **6**) and the positively charged/quaternised counterparts (**5-FAQ** and **6-FAQ**), respectively (**Figure 67**). The pronounced cellular uptake is due to the presence of a targeting ligand, folic acid. The positively charged compounds (**5-FAQ** and **6-FAQ**) exhibited less accumulation in the cell, however. This could be due to their high hydrophilicity, which tampers their ability to penetrate the cellular membranes. These *in vitro* observations agree with the results obtained for the partition coefficients in Chapter 4.

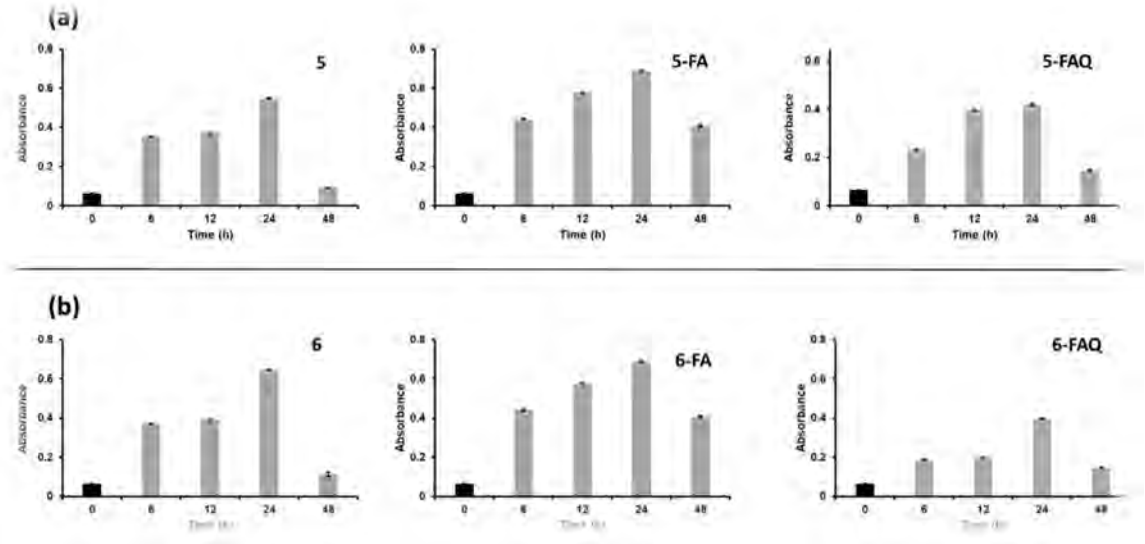

Figure 67. Bar graph showing the cellular uptake of (a) **5**, **5-FA** and **5-FAQ** and (b) **6**, **6-FA** and **6-FAQ** by MCF-7 cancer cells over a 48 h period. Data represent mean ± SD.

6.2. *In vitro* photodynamic therapy

The assessment of the efficacy of the dye molecules and their water-soluble conjugates in the context of photodynamic treatment is covered in this section. Using MCF-7 cells from human breast adenocarcinomas, *in vitro* investigations were carried out. The percentage of viable cells in cells treated with aza-BODIPY or porphyrin dyes and their conjugates was calculated using the WST-1 assay. The dark cytotoxicity of the compounds was also assessed. The half maximum inhibitory concentration (IC_{50}) value, a measurement of a compound's efficacy in inhibiting a certain biological behaviour, was calculated to assess the PDT activity. The concentration of dyes or their conjugates needed to inhibit the proliferation of MCF-7 cells by 50% was measured using these IC_{50} values.

In addition, the PDT activity of aza-BODIPY dyes synthesised for this study and other previously reported complexes will be directly compared against the photoinhibition of MCF−7 cancer cells. The effect of different substituents on the dyes and the $^1O_2$ quantum yields produced by the dyes will be highlighted. **Figure 68** shows the structures of the studied dyes.

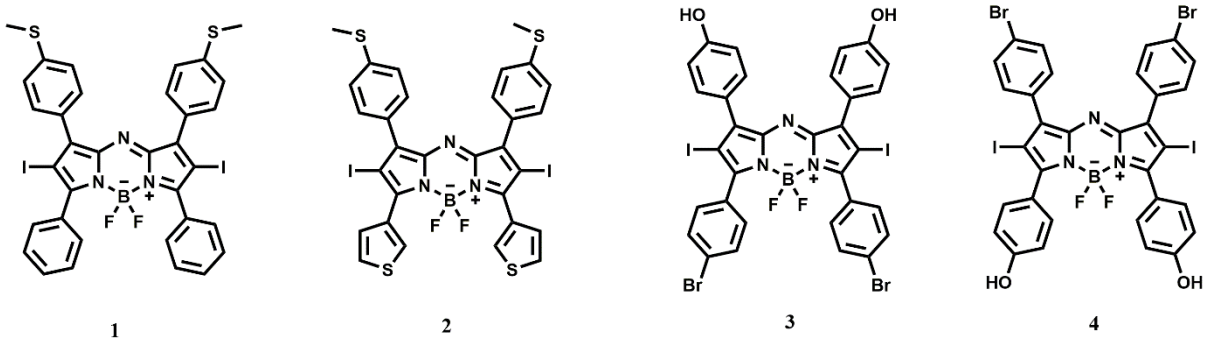

Figure 68. Structures of aza-BODIPY dyes studied for PDT.

6.3. *In vitro* photodynamic studies

6.3.1. Dark and light cytotoxicity studies for aza-BODIPYs and their AuNPs conjugates.

The control samples showed insignificant cell growth inhibition. Dark cytotoxicity was observed over a concentration range of 1.56−100 µM for all the samples. There was insignificant cytotoxicity at lower concentrations and a gradual increase in dark cytotoxicity with increasing concentration. Distinctively, the dyes alone were more toxic than the AuNPs conjugates in the dark (**Figure 69**). The conjugation to AuNPs, therefore, improved the dark cytotoxicity of the dyes. The IC_{50} values are recorded in **Table 11**.

For light studies, the MCF-7 cells were irradiated for 20 min over a concentration range of 1.56−100 μM, using the illumination chamber of a Modulight® 7710-680 Medical Laser fitted with a Thorlabs M660L4 LED (280 mW.cm^{-2}) for **1** and **1@AuNPs** and a Thorlabs M730L4 (160 mW.cm^{-2}) for **2** and **2@AuNPs** to provide doses at the well-plate of 2.0 and 1.1 J.cm^{-2}, respectively.

The IC_{50} values of the dyes alone (**1** and **2**) are 11.0 ± 0.78 and 12.8 ± 0.96 μM, respectively. Upon conjugation to AuNPs, there was a decrease in the IC_{50} to 3.60 ± 0.78 to 10.0 ± 0.05 μM for **1@AuNPs** and **2@AuNPs**, respectively. The results show that the AuNPs conjugates were more efficient in inhibiting cancer cell growth because they killed 50% of the cells at lower concentrations than the respective dyes alone. In general, **1** and its conjugate **1@AuNPs** were more efficient because they produced higher $^1O_2$ quantum yields than **2** and **2@AuNPs**, respectively. The dark cytotoxicity and PDT results are shown in **Figure 69** and summarised in **Table 11**.

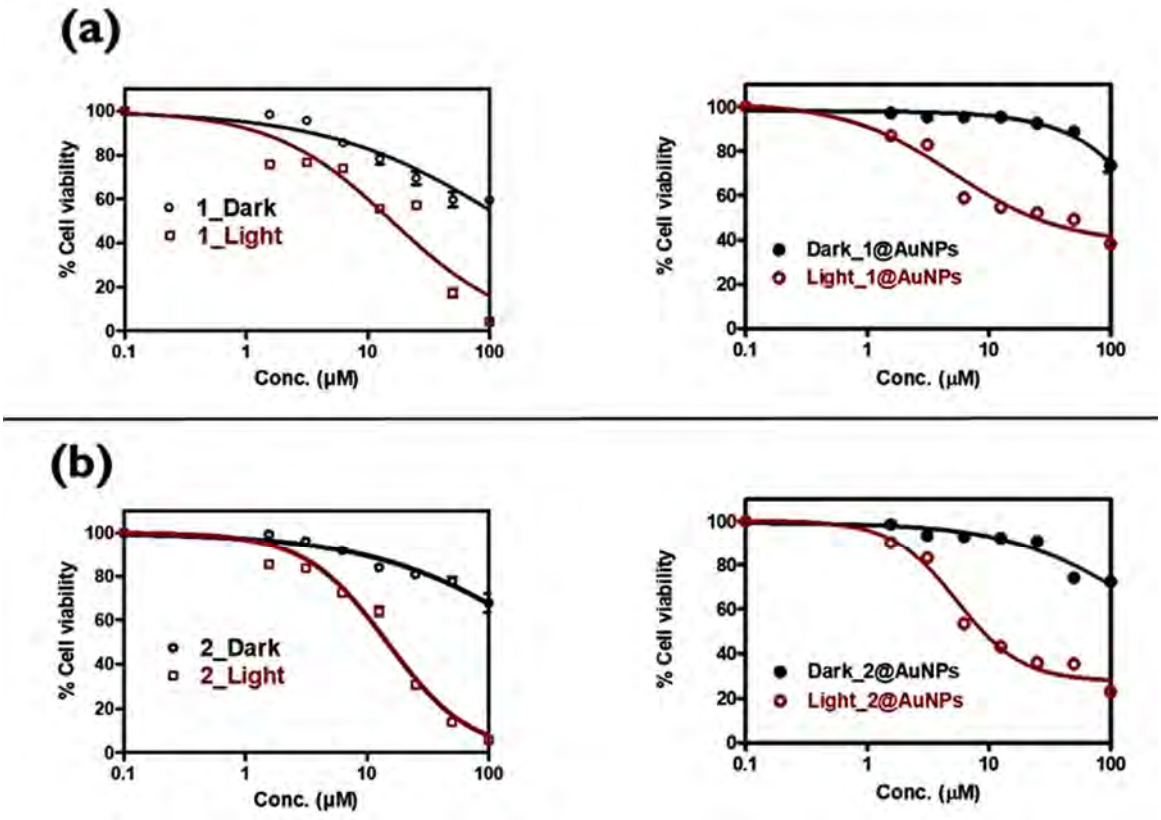

Figure 69. Cell viability plots highlighting the cytotoxic effect of aza-BODIPYs **1** and **2**, and respective conjugates **1@AuNPs** and **2@AuNPs** on MCF-7 cancer cells in the dark (black symbols) and after 20 min irradiation (red symbols).

Table 11. A summary of the IC_{50} values for the aza-BODIPYs and their gold nanoparticle conjugates.

	IC_{50} (Dark)	**IC_{50} (Light)**
1	26.0 ± 0.64	11.0 ± 0.78
1@AuNPs	> 50	3.60 ± 0.07
2	32.6 ± 0.37	12.8 ± 0.96
2@AuNPs	> 50	10.0 ± 0.05

6.3.2. Dark and light cytotoxicity studies for aza-BODIPYs and their folic acid conjugates

The approach used for the *in vitro* studies that was outlined in Section 5.1.1. was followed for aza-BODIPYs **3**, **4** and their folic acid conjugates **3-FA** and **4-FA**. A Modulight® 7710-680 Medical Laser fitted with a Thorlabs M660L4 LED (280 $mW.cm^{-2}$) was used for **3** and **3-FA** and with a Thorlabs M730L4 (160 $mW.cm^{-2}$) was used for **4** and **4-FA** providing doses at the well-plate of 2.0 and 1.1 $J.cm^{-2}$, respectively.

Minimal dark cytotoxicity was observed for all compounds at lower concentrations. There was a gradual increase in dark cytotoxicity at higher concentrations.

Fortunately, the conjugates had improved cytotoxicity compared to the dyes alone, **Figure 70**. The efficiency of the dyes in eradicating cancer cells increased significantly after conjugation to folic acid from 11.3 ± 1.05 (**3**) and 13.0 ± 1.11 (**4**) to 0.91 ± 0.04 (**3-FA**) and 7.48 ± 0.87 (**4-FA**) μM, respectively. The targeting ability of folic acid rendered the conjugates more efficient and biocompatible, thus making it easier for the cancer cells to internalise the conjugates. **Table 12** summarises the results obtained.

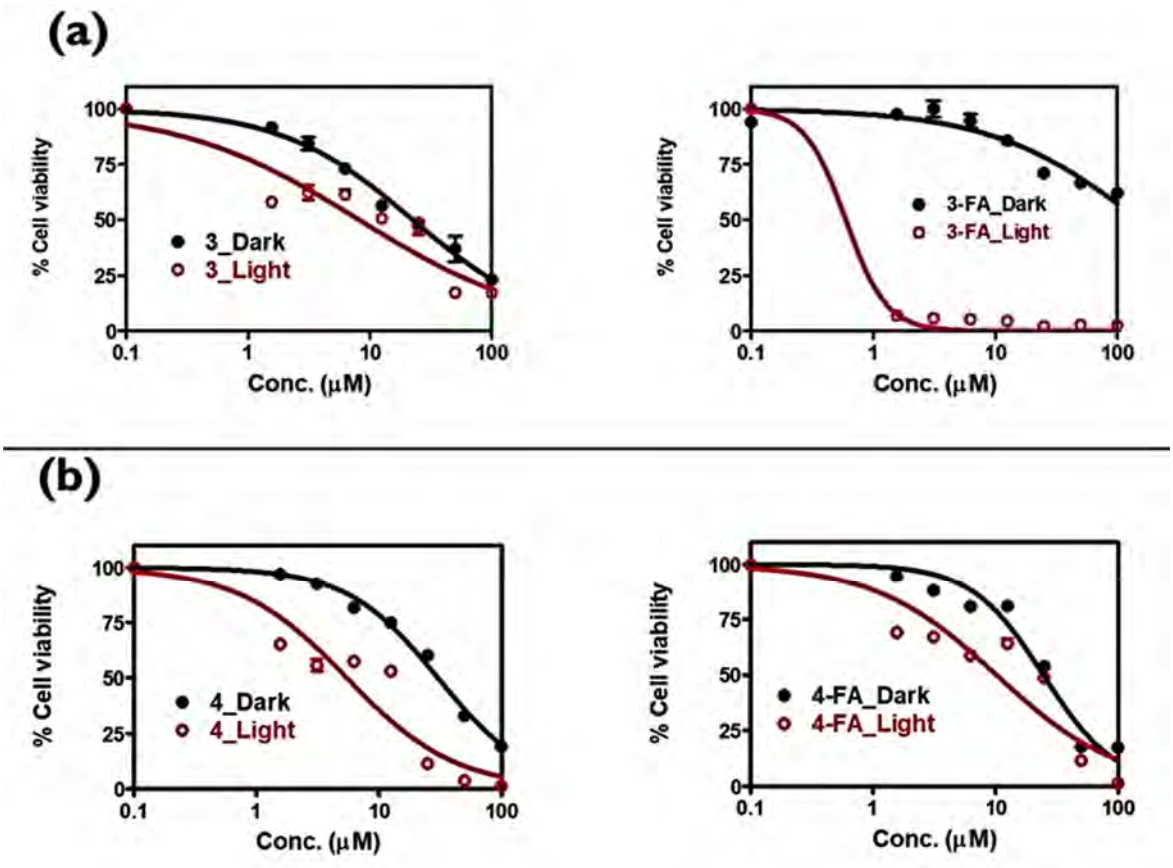

Figure 70. Cell viability plots highlighting the cytotoxic effect of aza-BODIPYs **3** and **4**, and the **3-FA** and **4-FA** conjugates on MCF-7 cancer cells in the dark (black symbols) and after 20 min irradiation (red symbols).

Table 12. A summary of the IC_{50} values for the aza-BODIPYs and their folic acid conjugates.

	IC_{50} (Dark)	**IC_{50} (Light)**
3	> 50	11.3 ± 1.05
3-FA	> 50	0.91 ± 0.04
4	> 50	13.0 ± 1.11
4-FA	> 50	7.48 ± 0.87

6.3.3. The comparison of studied aza-BODIPY dyes with previous studies

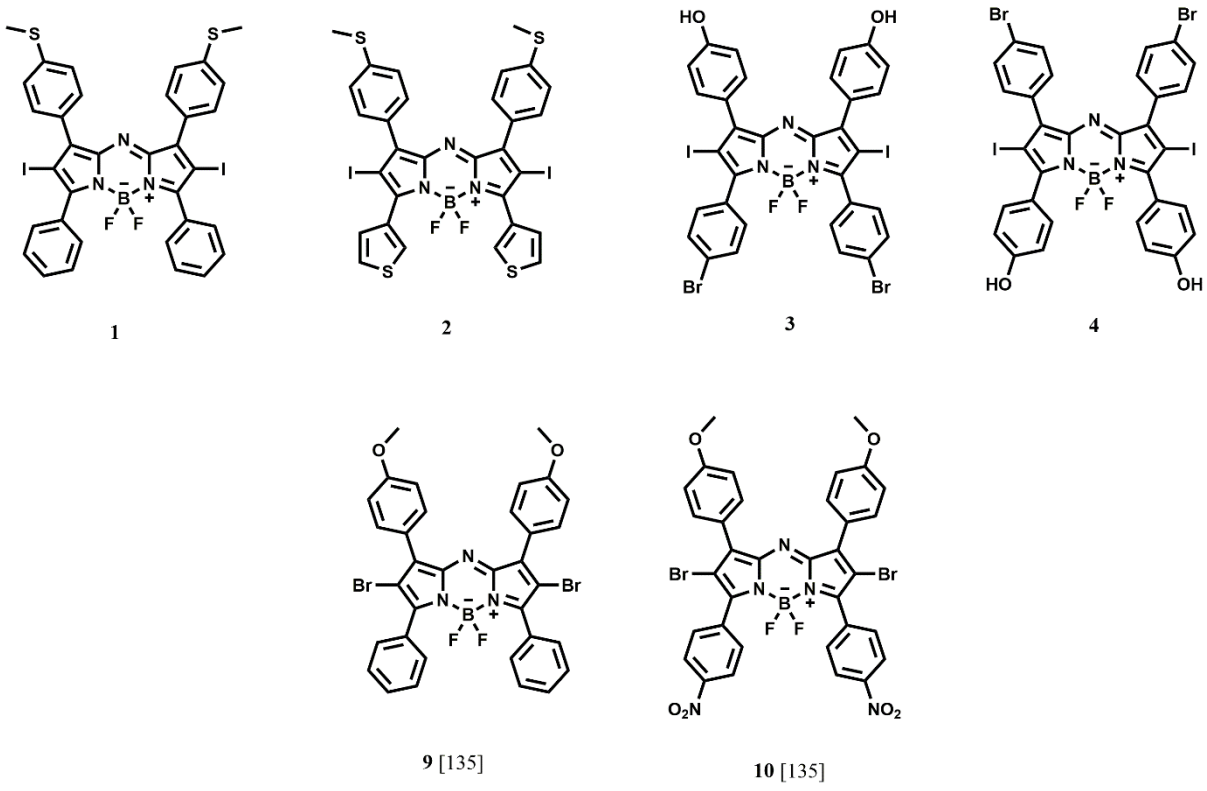

Figure 71. Structures of aza-BODIPY dyes studied and compared for PDT.

The comparison of the PDT activities of the structurally analogous aza-BODIPY dyes synthesised for this study with previously reported aza-BODIPY dyes (**Figure 71**) will be discussed in this section [135]. The primary focus will be on the effect of different substituents on the PS dyes and the $^1O_2$ quantum yields produced by the dyes.

Aza-BODIPY **3** had the best effect in inhibiting the growth of MCF-7 cancer cells with IC_{50} = 11.3 ± 1.05 μM. This is due to its higher $^1O_2$ quantum yield. **4** and **9** had similar effects against MCF-7 cancer cells despite having different substituents. This was also attributed to the amount of singlet oxygen generated by these dyes. **10** only had a moderate $^1O_2$ quantum yield and thus exhibited the least activity against the MCF-7 cancer cells.

Table 13. PDT results and the effect of different substituents on aza-BODIPY dyes against MCF-7 cancer cells.

	Substituents		**IC_{50} (μM)**	**Reference**
	Proximal	**Distal**	**(Light)**	
3	4-bromophenyl	4-hydroxyphenyl	11.3 ± 1.05	-
4	4-hydroxyphenyl	4-bromophenyl	13.0 ± 1.11	-
9	4-nitrophenyl	4-methoxyphenyl	13.4 ± 1.1	[135]
10	Phenyl	4-methoxy	42.5 ± 1.8	[135]

6.3.4. Dark and light cytotoxicity studies for porphyrins and their folic acid conjugates

The approach used for the *in vitro* studies that was outlined in Section 5.1.1. was followed for porphyrins **5** and **6**, their folic acid conjugates **5-FA** and **6-FA** and the respective cationic conjugates **5-FAQ** and **6-FAQ**. The illumination chamber of a Modulight® 7710-680 Medical Laser fitted with a Thorlabs M625L4 LED (240 $mW.cm^{-2}$) was used for all six compounds to provide a dose at the well-plate of 1.7 $J.cm^{-2}$.

Minimal dark cytotoxicity was observed for all compounds at lower concentrations. At higher concentrations, a gradual increase in dark cytotoxicity was observed to varying degrees. The conjugates had improved cytotoxicity compared to the dyes alone, **Figure 72**. There was a significant increase in the cytotoxicity of the porphyrins upon conjugation with folic acid, **Table 14**.

For the light studies of the Sn (IV) complexes, there was an increase in the efficacy from IC_{50} = 48.2 ± 0.04 µM (**5**) to 29.6 ± 0.02 µM (**5-FA**). After quaternisation, a drastic decrease in the inhibition of cancer cell growth was observed, with the IC_{50} value being way over 50 µM, **Figure 72 (a)**. This reduction in killing the cancer cells is due to the high water solubility of the cationic porphyrin, **5-FAQ**, which limits the complex's ability to penetrate the cellular membranes. These results are consistent with the cellular uptake and the partition coefficient results.

Similar trends to Sn (IV) complexes were found for the In (III) complexes after irradiation for 20 min. The inhibition of cancer cell growth increased from IC_{50} = 43.9 ± 0.06 µM (**6**) to 13.3 ± 1.13 µM (**6-FA**). Upon quaternisation, there was a drastic reduction in the ability of the conjugate (**6-FAQ**) to inhibit cancer cell growth. The IC_{50} value of **6-FA** was far greater than 50 µM, probably due to the high water solubility,

which limits the complex's ability to penetrate the cellular membranes. In a similar manner, these results are consistent with the cellular uptake and partition coefficient results and demonstrate the importance of these parameters.

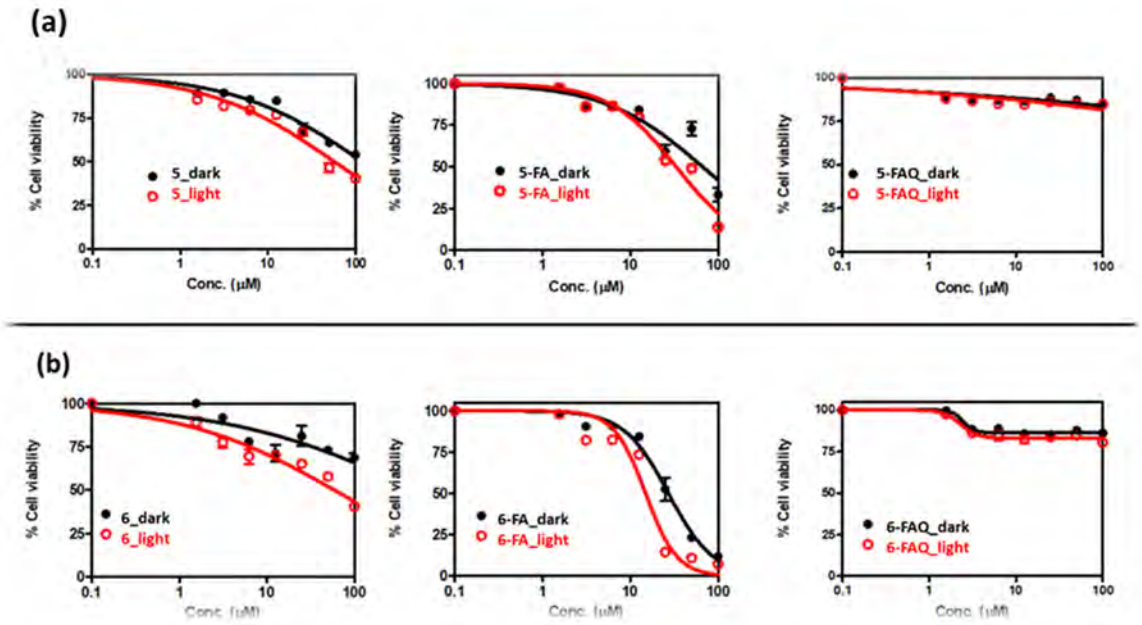

Figure 72. Cell viability plots highlighting the cytotoxic effect of porphyrins **5** and **6**, their respective conjugates **5-FA** and **6-FA** and their quaternised conjugates **5-FAQ** and **6-FAQ** on MCF-7 cancer cells in the dark (black symbols) and after 20 min irradiation (red symbols).

6.3.5. The comparison of studied porphyrins with previous studies

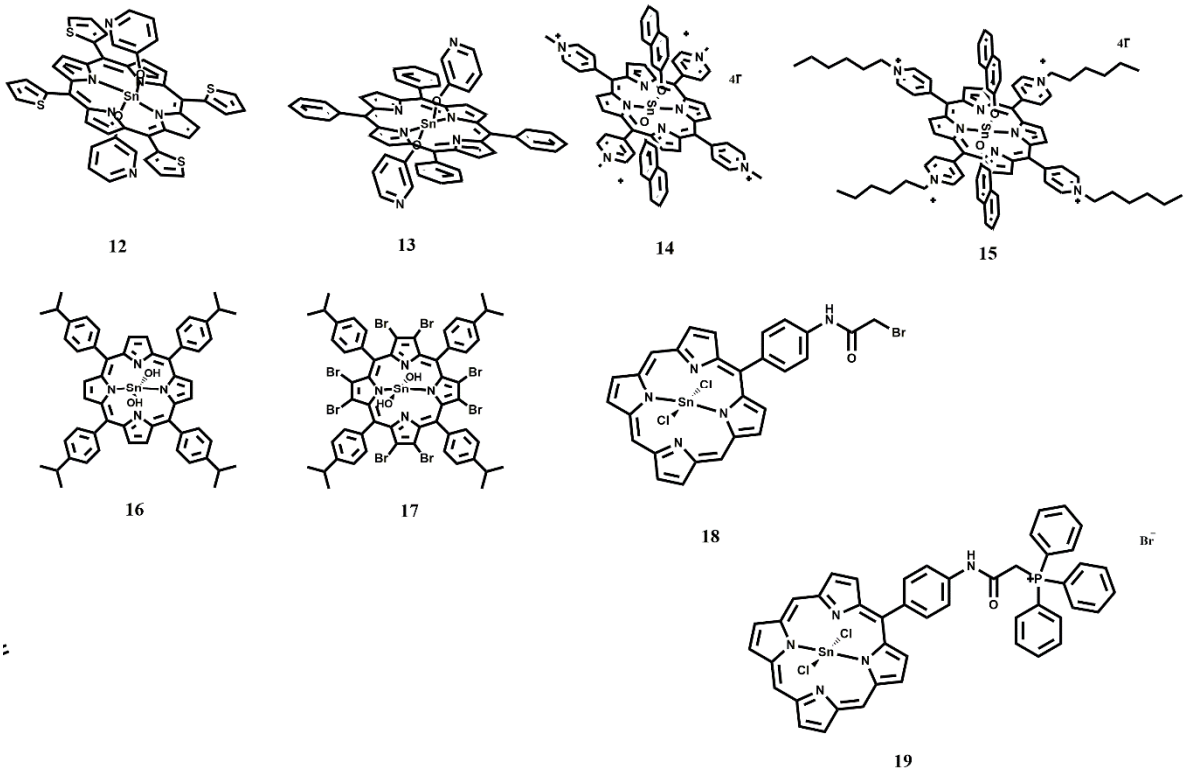

Figure 73. Structures of porphyrins previously reported by Mack and coworkers [136].

This section highlights the PDT activities of the porphyrins synthesised in this work and of similar compounds previously reported by Mack and coworkers using a similar experimental approach [136]. The work on tin(IV) porphyrins in this thesis was an extension of this earlier work so that the potential utility of folic acid conjugation to other structural modification strategies could be assessed. The structures of the porphyrins studied by Mack and coworkers are provided in **Figure 73**. A comparison of the efficacy of the compounds against MCF-7 cancer cells was carried out. **Table 14** demonstrates that significantly lower IC_{50} values have been obtained using other strategies to modify the structures of Sn(IV) porphyrins. As discussed in Section 6.2.4., the quaternised Sn(IV)-tetrapyridylporphyrins with folic acid axial ligands were successfully tested against MCF-7 cancer cells. Notably, the presence of folic acid as

a targeting ligand was proven to increase the PDT activity of the compounds. When a comparison of the PDT activities of **5-FA** and **5-FAQ** with those of **11-18** is made, it is clear that all the compounds reported previously by Mack and coworkers had significantly higher activity against MCF-7 cancer cells. The IC_{50} value for the **6-FA** complex with an In(III) ion was more comparable, however.

A triphenylphosphonium (TPP) targeting ligand was attached to **18**, while **17** had no TPP attached to it. Since both compounds had the same $^1O_2$ quantum yield (0.73 in DMF), the activity against MCF-7 cancer cells was solely attributed to the presence of the cationic TPP moiety, which was found to be more lipophilic and easily taken up by the cancer cells. It was no surprise that the activity of **18** was three-fold that of **17**. Although **11** and **12** had no targeting ligand, the presence of sulfur atoms on **11** (Sn(IV) tetrathien-2-ylporphyrin) increased the $^1O_2$ quantum yield of the compound compared to the nitrogen atom of the 3-tetrapyridyl moiety on **12**. Further studies were conducted, where cationic Sn(IV)-tetrapyridylporphyrins quaternised with methyl and hexyl alkyl chains, **13** and **14**, respectively, were tested against MCF-7 cancer cells. The hexyl alkyl chains rendered **14** more lipophilic and had better PDT activity (four-fold) than **13**, which had a shorter alkyl chain. To further increase the singlet oxygen production of porphyrins, Mack and coworkers also explored the addition of eight bromine atoms at the β-positions of porphyrins as observed for **16**. **15** was used as a control compound in this context. The presence of these heavy atoms resulted in an increase in the PDT activity of **16**, with a 4-fold increment compared to the activity of **15**.

Table 14. A summary of the IC_{50} values for the porphyrins and their folic acid conjugates.

	IC_{50} (Dark)	**IC_{50} (Light)**	**Reference**
5	> 50	48.2 ± 0.04	-
5-FA	> 50	29.6 ± 0.02	-
5-FAQ	> 50	> 50	-
6	> 50	43.9 ± 0.06	-
6-FA	26.1 ± 1.40	13.3 ± 1.13	-
6-FAQ	> 50	> 50	-
11	> 50	5.60	[136]
12	> 50	18.7	[136]
13	> 50	14.3	[136]
14	> 50	8.50	[136]
15	> 50	38.9	[136]
16	> 50	10.7	[136]
17	> 50	9.80	[136]
18	> 50	2.90	[136]

6.4. Concluding remarks

2,6-Diiodinated-1,3,5,7-aryl-aza-BODIPY dyes, Sn(IV) and In(III) porphyrins with moderately high $^1O_2$ quantum yields were conjugated to AuNPs (**1** and **2**) and folic acid (**3**, **4**, **5** and **6**). The aza-BODIPY dyes and their respective conjugates are new, while only the porphyrin conjugates are new in this work. All the compounds and their related conjugates were tested for their dark cytotoxicity and photodynamic activity against the human breast adenocarcinoma MCF-7 cell line. When applied alone or in combination with either AuNPs or folic acid, all the compounds, except **6-FA**, exhibited minimal dark cytotoxicity against the human breast adenocarcinoma MCF-7 cell line and, with the exception of **5-FAQ** and **6-FAQ**, exhibited significant PDT activity.

Upon conjugation of aza-BODIPYs **1** and **2** to AuNPs, a very significant increase in PDT activity was observed. Lower dark cytotoxicity at higher concentrations was also observed. Enhanced PDT activity was also observed upon the conjugation of porphyrins (**5** and **6**) and aza-BODIPYs (**2** and **3**) to folic acid. The PDT activity of the cationic porphyrins (**5-FAQ** and **6-FAQ**) was very low due to their high water solubility. The comparative study of the aza-BODIPYs shows that the relative magnitudes of the $^1O_2$ quantum yields produced by the dyes contributed to their activity against MCF-7 cancer cells than the substituents on the dyes. Overall, the AuNPs and folic acid aza-BODIPY conjugates studied in this work demonstrated potential to be used as PDT agents against breast cancer cells and merit further in-depth study, while the results for the **5-FAQ** and **6-FAQ** porphyrin complexes demonstrate that care has to be taken not to enhance the hydrophilicity of the dyes in a manner that hinders cellular uptake by limiting their lipophilicity.

Comparison with earlier studies by Mack and coworkers [136] suggests that folic acid conjugation of porphyrins through axial ligation to form **5-FA** and **6-FA** is not as effective a structural modification strategy for Sn(IV) porphyrin complexes as some of the others that have been explored previously using a similar experimental approach. Sn(IV) dyes have been studied in this context since their *trans*-axial ligation hinders aggregation effects that can alter their photophysicochemical properties, and the heavy central ion introduces a heavy atom effect that enhances singlet oxygen generation. Although the results in this regard with folic acid conjugation can be viewed as negative, they have helped to form a clearer picture of how readily synthesized porphyrin dyes can be readily structurally modified to enhance their potential utility for use in PDT.

Chapter 7: Photodynamic antimicrobial chemotherapy

7.1. PACT studies on *Staphylococcus aureus*

This chapter describes the results obtained during PACT studies against *S. aureus* with aza-BODIPYs **1**, **2**, **3** and **4**, and porphyrins **18a**, **18**, **19a** and **19**. This work is an extension of a larger project where the porphyrins were tested against MCF-7 cancer cells [98]. A direct comparison of the PACT activities of structurally analogous aza-BODIPY dyes synthesised for this work and those reported previously at Rhodes University was made. The structures of the aza-BODIPYs and porphyrins studied against *S. aureus* and the ones previously reported are shown in **Figure 74**. The porphyrins studied and those previously reported by Mack and coworkers [136] are shown in **Figure 75**.

The antimicrobial activity of neutral aza-BODIPY dyes was tested against a Gram-(+) bacteria, *S. aureus*, following previously reported procedures with minor modifications [34, 38]. An aliquot of *S. aureus* was suspended in freshly prepared broth (5 mL) and incubated at 37 °C until the mid-logarithmic phase was achieved (absorbance = 0.6−0.8 at 620 nm). The bacteria were concentrated through centrifugation (4000 rpm for 10 min), and the broth was removed. The bacteria pellet was washed twice with PBS and suspended in fresh PBS (4 mL), and the bacteria culture was diluted to 1/100 to make a stock solution of 10^{-2} dilution. A series of concentrations with dilution factors 10^{-3}, 10^{-4}, 10^{-5}, 10^{-6} and 10^{-7}. For each dilution, 100 µL was aseptically inoculated on agar plates (triplicates) and then incubated for 24 h, after which the respective bacteria colonies were counted. The concentration with a 10^{-6} dilution factor was chosen as the working concentration for the studies since it had an average of 157 colonies. The dye stock solutions were prepared at 1000 µM, and a series of concentrations (0.313, 0.625, 1.25, 2.5, 10, 5 and 10 µM) were prepared for the concentration optimisation

study. 1.25 μM was the optimum concentration, with only one colony survival after 60 min irradiation (log CFU = 7.75). The actual studies were then carried out using *S. aureus* at 10^{-6} dilution factor and 1.25 μM concentration in triplicates. 100 μL of the control and dark toxicity samples with and without the dyes were inoculated at appropriate times and kept in the incubator at 37 °C in the dark. The bacteria inactivation studies were carried out by irradiation with the respective LEDs at 15 min intervals for 60 min. At each study time, 100 μL of each sample was inoculated on the agar plate and then incubated for 24 h. The number of colony survivals was determined thereafter.

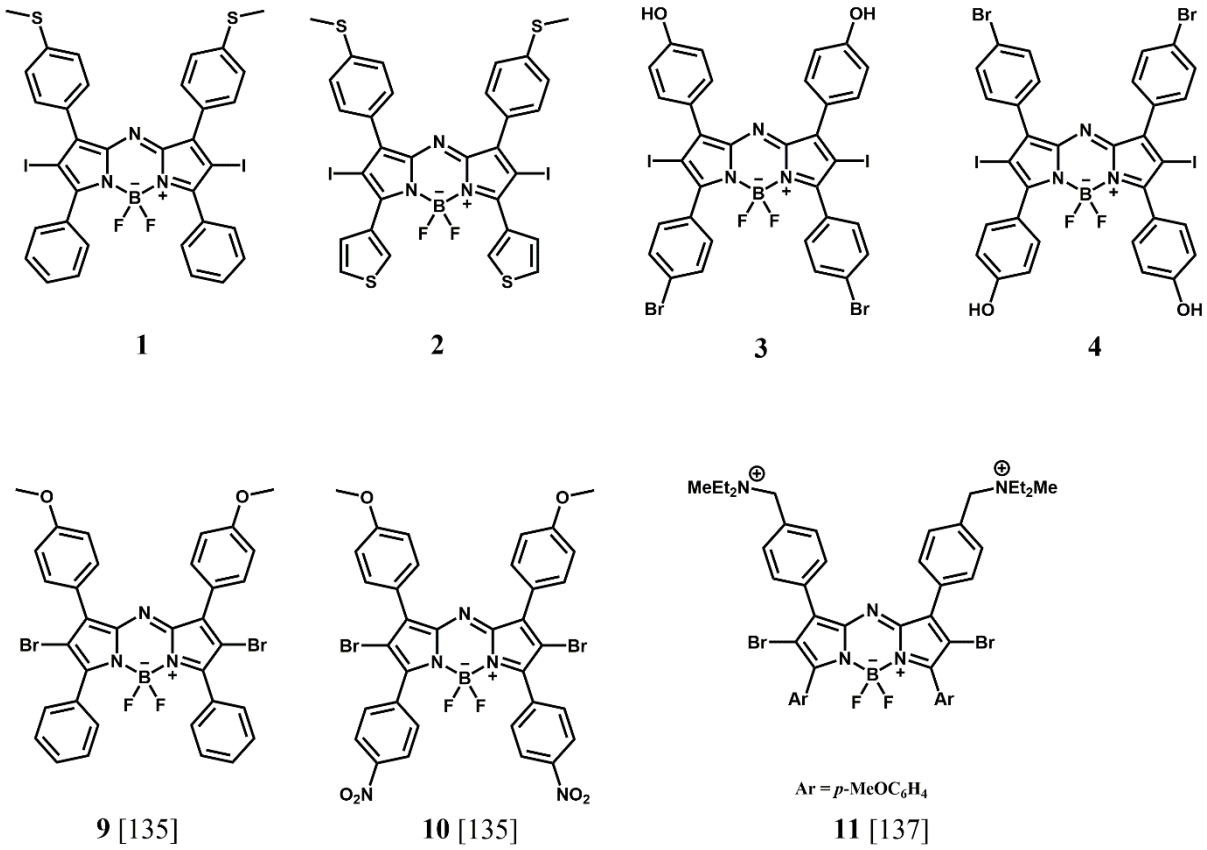

Figure 74. Aza-BODIPYs studied for the photo-inactivation of *S. aureus.*

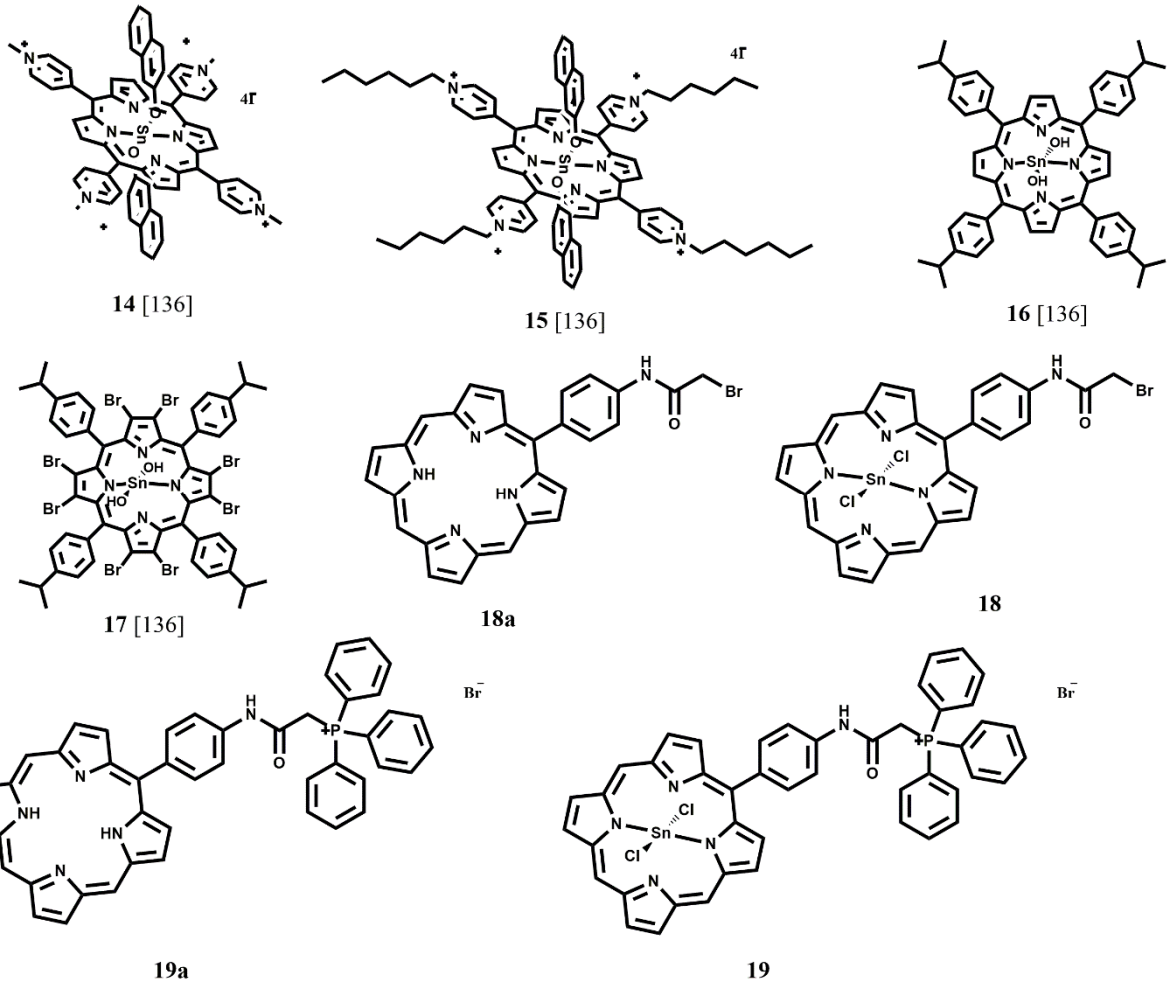

Figure 75. Sn(IV) porphyrins studied and previously reported [136] for the photo-inactivation of *S. aureus* along with non-metalated control compounds.

7.1.1. Optimisation studies for aza-BODIPY dyes in Series 1

To find the ideal concentration for the photoinactivation of aza-BODIPY dyes in series 1 (**1** and **2**), aza-BODIPY **1** was used for optimisation. Aza-BODIPY **1** was chosen after conducting concentration studies for both dyes, where **2** was relatively inactive over the studied concentration range. Aza-BODIPYs **1** and **2** were found to be minimally cytotoxic in the dark over a concentration range of 0.313−10.0 μM. A Thorlabs M660L4 LED (280 mW.cm^{-2}) was used to irradiate **1** over a concentration range of 0.313−10.0 μM. 1.25 μM was found to be the optimum concentration with

only one colony survival after 60 min irradiation time (log CFU = 7.75, p-value > 0.05) and a dose at the well-plate of 6.0 J.cm^{-2}, as shown in **Figure 76**. Precipitation of the dye occurred at higher concentrations. This was postulated to be the reason for the higher cell survival.

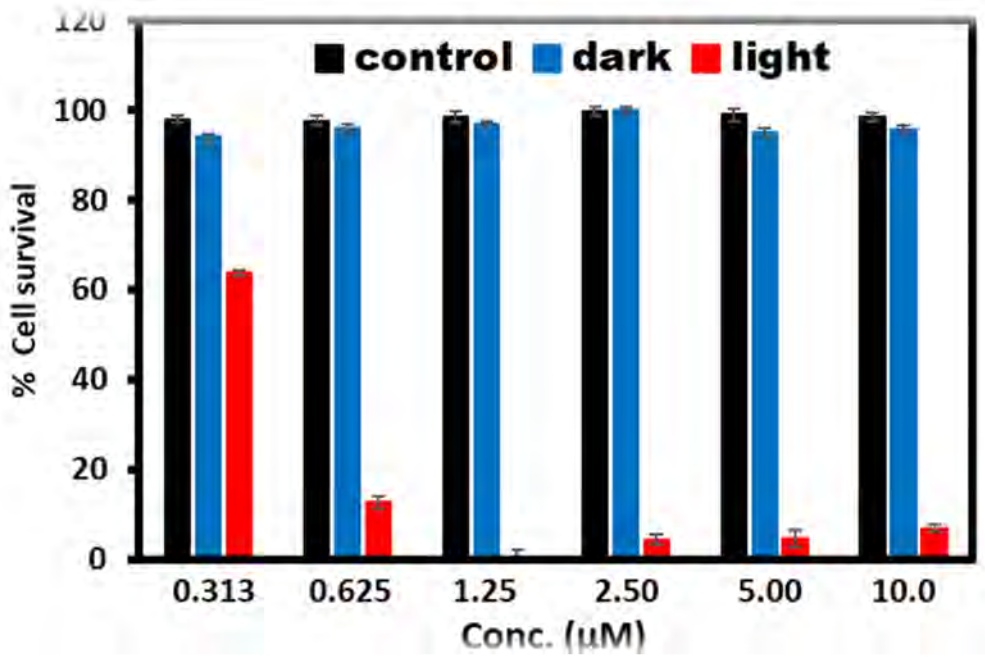

Figure 76. Bar chart showing optimisation of aza-BODIPY **1** at a concentration range of 0.313−10 μM over a 60 min period. The graph shows the *S. aureus* colonies before and after treatment, with **1** as an example. The values represent mean ± SD.

7.1.2. PACT studies for Series 1

The PACT studies for **1** and **2** were carried out according to the optimisation concentration obtained (1.25 μM). A Thorlabs M660L4 LED (280 mW.cm^{-2}) mounted on the illumination chamber of a Modulight® 7710-680 medical laser system was used for the irradiation of **1**, while a Thorlabs M730L4 LED (160 mW.cm^{-2}) was used for **2** over a period of 60 min providing a dose of the well-plate of 6.0 and 3.4 J.cm^{-2}, respectively. The results are shown in **Figure 77**. Aza-BODIPY **1** was very efficient in

photo-inactivating the bacteria after the 60 min irradiation time relative to the control, with zero colonies remaining at the end of the treatment. The PACT activity recorded was log CFU = 7.82 (p-value > 0.05). Aza-BODIPY **2** was ineffective in killing the bacteria, with a log reduction of log CFU = 1.37 (p-value > 0.05). The higher activity of **1** was attributed to its higher $^1O_2$ quantum yield compared to that of **2**. The summary of the PACT results is given in **Table 15**.

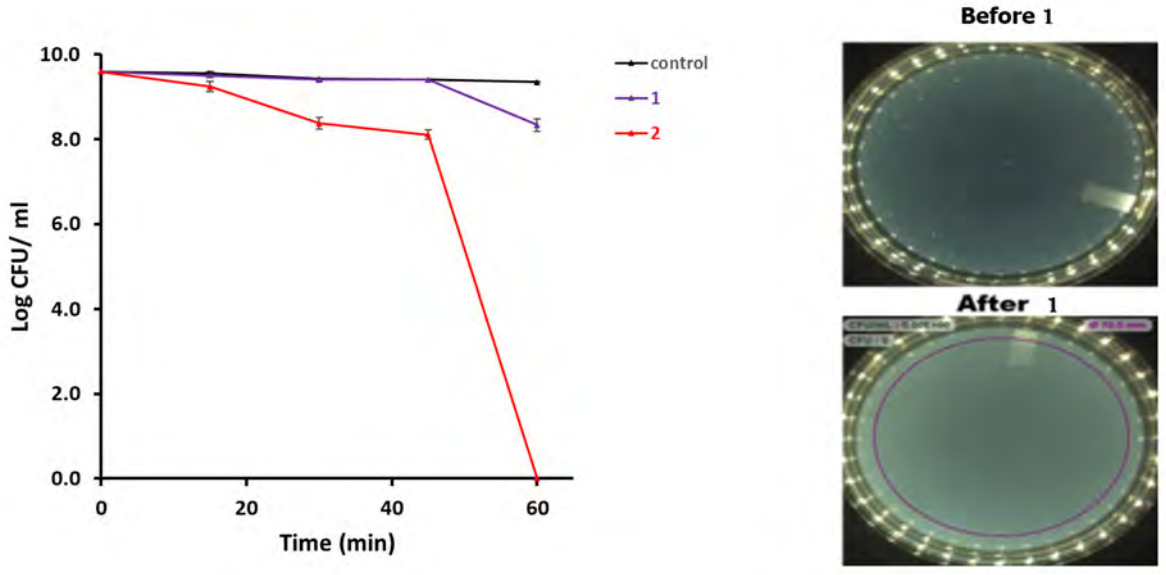

Figure 77. Log_{10} reduction plot showing the inhibition of *S. aureus* at 1.25 µM over 60 min period. Control (black line), treatment with **1** (red line) and treatment with **2** (purple line). The images show the *S. aureus* colonies before and after treatment with aza-BODIPY **1** as an example. The values represent mean ± SD.

7.1.3. PACT studies for Series 2

The PACT studies for **3** and **4** were also carried out according to the optimisation concentration obtained (1.25 µM) for Series 1 above. This was done to allow comparison of the molecules' activity. A Thorlabs M660L4 LED (280 $mW.cm^{-2}$) mounted on the illumination chamber of a Modulight® 7710-680 medical laser system was used for the irradiation of **3**, while a Thorlabs M730L4 (160 $mW.cm^{-2}$) was used

for **4** over a period of 60 min to provide a dose of 6.0 and 3.4 J.cm^{-2}. The results obtained are shown in **Figure 78**. Aza-BODIPY **3** was more efficient in photo-inactivating the bacteria compared to **4** after the 60 min irradiation time relative to the control. However, there were sixteen colonies remaining at the end of the treatment for **3**, while forty colonies remained for **4**. The log reductions recorded were log CFU = 1.20 (p-value > 0.05) for **3** and log CFU = 0.20 (p-value > 0.05) for **4**. The higher activity of **3** compared to **4** was attributed to the higher $^1O_2$ quantum yield produced by the former dye molecule. The summary of the PACT results is given in **Table 15**.

In comparing the activity of the dyes in Series 1 (Section 7.1.2.) to the ones in Series 2, the dyes in Series 1 had higher activity. Aza-BODIPY **1** is the most efficient of the dyes in the photoinactivation of *S. aureus* at 1.25 µM due to its high $^1O_2$ quantum yield.

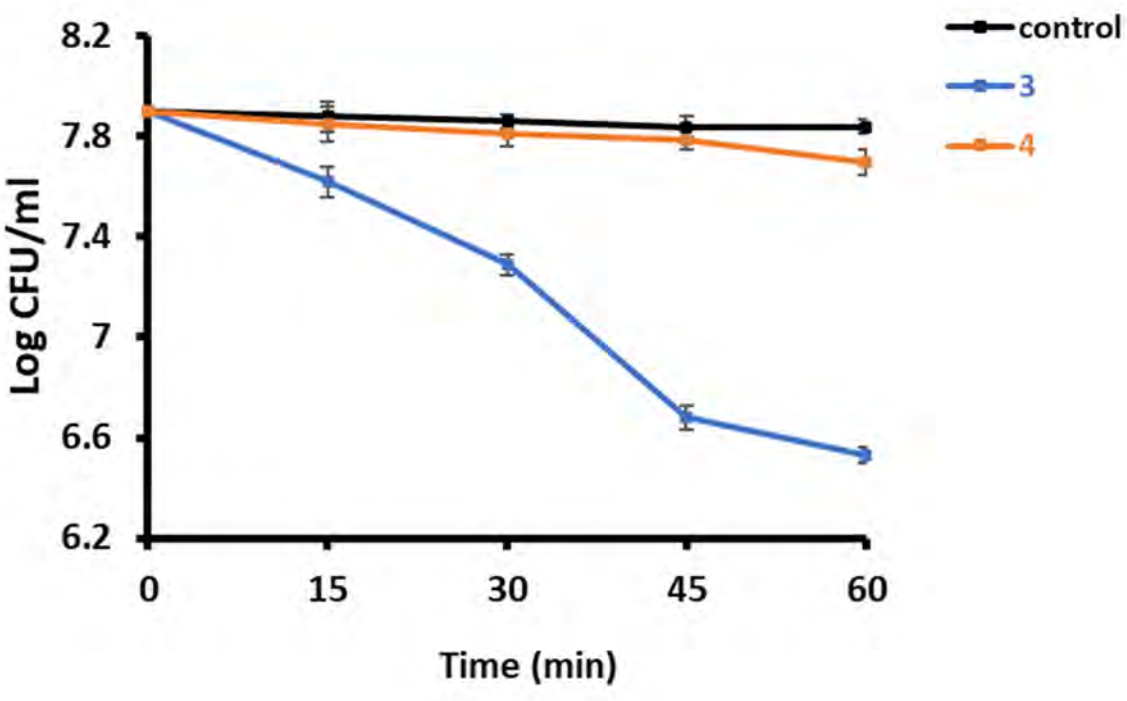

Figure 78. Log_{10} reduction plot showing the inhibition of *S. aureus* at 1.25 µM over 60 min period. The values represent mean ± SD.

7.1.4. The comparison of the of the PACT activity of studied PS dyes with previous studies

This section describes the comparison of the PACT activities of the structurally analogous aza-BODIPY dyes synthesised for this study with previously reported aza-BODIPY dyes (**Figure 74**) [135, 137]. The main focus will be on the effect of different substituents on the PS dyes and the $^1O_2$ quantum yields produced by the dyes. Looking at **Table 15**, it was concluded that **1** is superior to all the analogues due to its high $^1O_2$ quantum yield, thus the highest Log_{10} reduction value obtained against *S. aureus.* There is no clear trend in the activity of the dyes where the substituents are concerned. For example, a balance between hydrophilicity and lipophilicity is preferred in biological studies so that the amphiphilic molecules can permeate the cellular membranes of bacteria easily. **3** and **4** have hydrophilic hydroxyl substituents, but they have less antimicrobial activity than entirely hydrophobic analogues, **1** and **2**. However, **9** and **10** [135] exhibited inferior activity compared to **1** and **2** as anticipated. The presence of cationic ammonium salts in **11** [137] is expected to impart sufficient hydrophilicity in the molecules, thus encouraging microbial cellular uptake. Despite this, **11** was found to be less photoactive than **1** against *S. aureus,* but different experimental conditions were used in contrast with **9** and **10** from the MSc thesis of Nadine Dubazana at Rhodes University where 90 min irradiation with a Thorlabs M660L4 LED (280 $mW.cm^{-2}$) mounted on the illumination kit of a Modulight® 7710-680 to provide a dose of 9.0 $J.cm^{-2}$.

Table 15. PACT results and the effect of different substituents per studied concentration against *S. aureus*.

	Substituents		Conc. (μM)	Log_{10} reduction or % inactivation	Ref.
	Proximal	**Distal**			
1	phenyl	4-methylthiophenyl	1.25	7.82	-
2	thien-3-yl	4-methylthiophenyl	1.25	1.37	-
3	4-bromophenyl	4-hydroxyphenyl	1.25	1.20	-
4	4-hydroxyphenyl	4-bromophenyl	1.25	0.20	-
9	4-nitrophenyl	4-methoxyphenyl	1.24	92%	[135]
10	phenyl	4-methoxy	1.40	82%	[135]
11	4-diethylmethyl ammoniomethylphenyl-4-methoxyphenyl	4-ethylmethyl ethanaminium	1.28	3.00	[137]

7.1.5. Optimisation studies for porphyrins

To find the ideal concentration for the photoinactivation of porphyrins, **18** was chosen for optimisation purposes after preliminary concentration studies were conducted for all the porphyrins (**18a**, **18**, **19a** and **19**). All the porphyrins were relatively inactive in inhibiting the growth of *S. aureus* when irradiating at the Q-bands using a Thorlabs M595L4. The B-band was therefore chosen to carry out the studies where **18** was

found to be the most active, thus chosen for concentration optimisation over a concentration range of 0.313−10.0 µM, **Figure 79**. 5.00 µM was found to be the optimum concentration with only 30 % colony survival after 60 min irradiation time (log CFU = 7.12, p-value > 0.05), as shown in **Figure 79.** Although relatively low PACT activity was observed in this context, 5 µM was selected primarily to facilitate comparisons with earlier studies by Mack and coworkers [136] under similar experimental conditions.

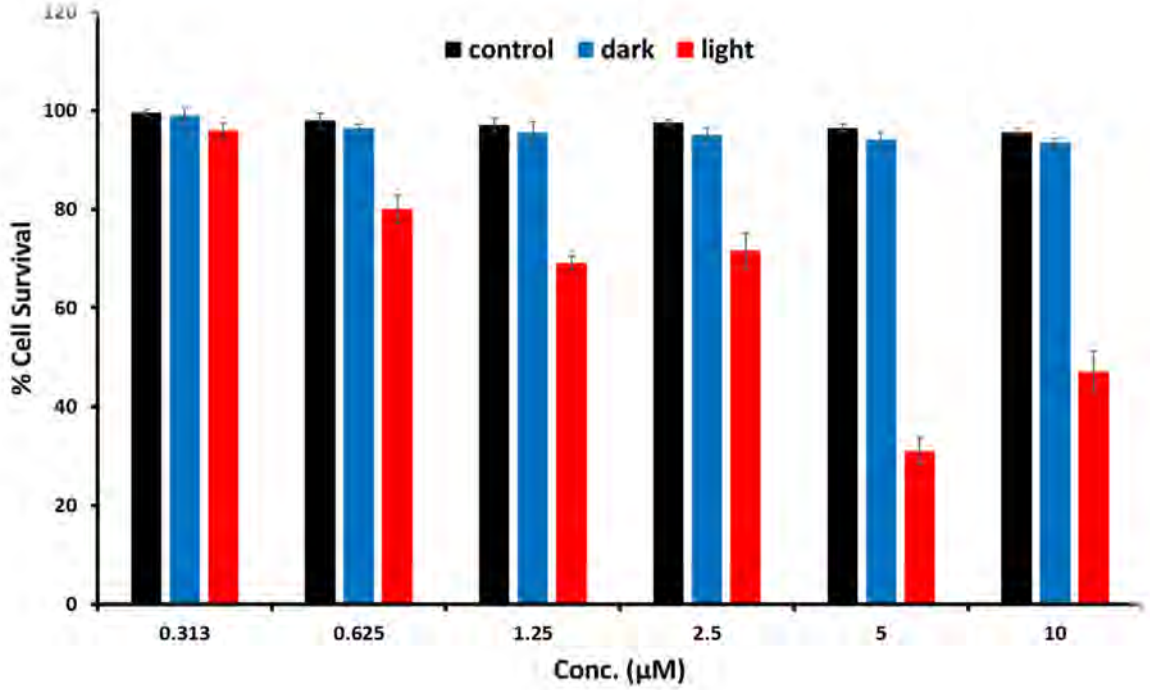

Figure 79. Bar chart showing optimisation of porphyrins at a concentration range of 0.313−10 µM over a 45 min period. The graph shows the *S. aureus* colonies before and after treatment with **18** at 5.00 µM. The values represent mean ± SD.

7.1.6. PACT studies for porphyrins

The PACT studies of the porphyrins were carried out following the optimum concentration of 5.00 µM. Relative to the control, **19** was more efficient in the

photoinactivation of *S. aureus*. The Log_{10} reduction values were as follows: 0.35, 1.80, 0.25 and 2.13 (p-value > 0.05) for **18a**, **18**, **19a** and **19**, respectively. The cationic porphyrin, **19** with a triphenyl phosphonium moiety, was expected to be more active. This is observed in the Log_{10} reduction values, **Figure 80**. The summary of the PACT results is provided in **Table 15**.

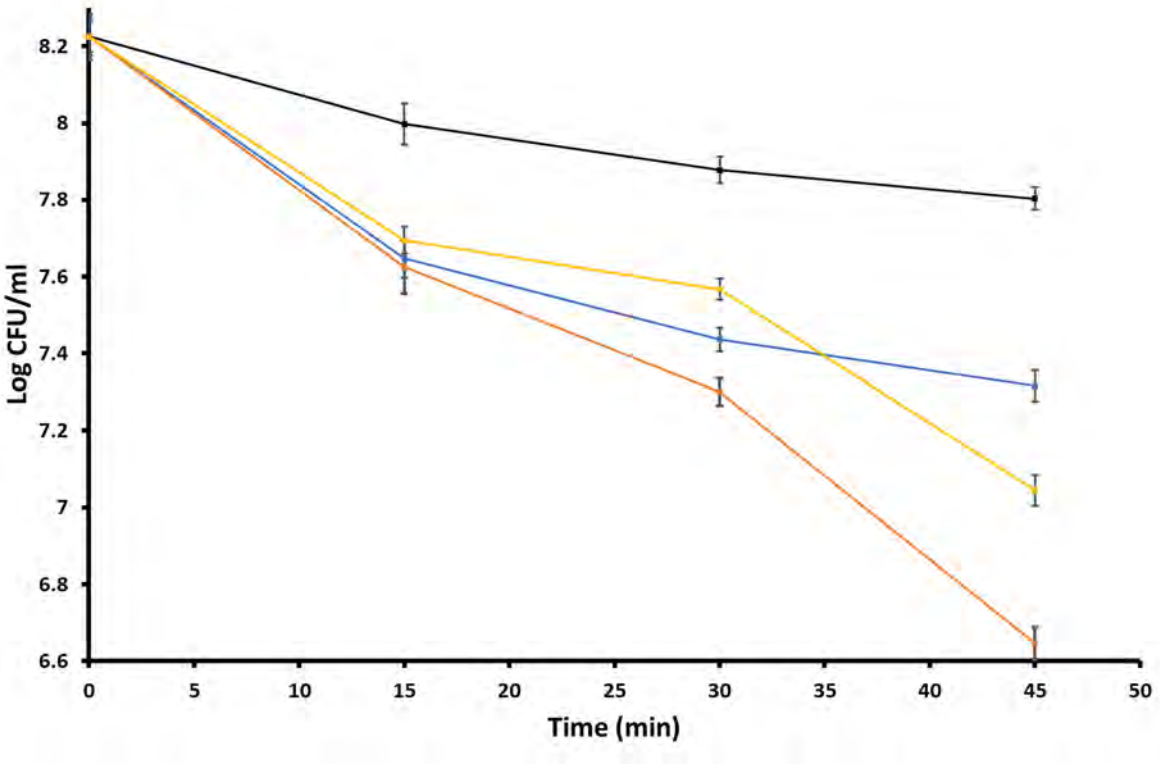

Figure 80. Log_{10} reduction plot showing the inhibition of *S. aureus* at 5 µM over 45 min period.**18a** (blue line), **18** (yellow line), **19a** (black line) and **19** (orange line). The values represent mean ± SD.

7.1.7. The comparison of studied porphyrins with previous studies

This section provides a direct comparison of the PACT activity of four porphyrins previously studied by Mack and coworkers [136] and four synthesised previously by Babu *et al*. [98] and studied in this work against *S. aureus*. The structures of the porphyrins are shown in **Figure 75**, and the Log_{10} reduction values are summarised

in **Table 16**. From the results, it is evident that **15** performed better than all the porphyrins due to the presence of hexyl alkyl chains, which made the porphyrin lipophilic and, hence, more easily taken up by bacteria cells. Likewise, **19a** and **19** were expected to have relatively high activity (high Log_{10} reduction values) since they have mitochondrial targeting triphenylphosphonium moiety. The low activity of the quaternised (cationic) porphyrin **14** can be attributed to its hydrophilicity, which makes it difficult for it to be taken up by the bacteria cells. The hydrophobic porphyrins, **16**, **17**, **18a** and **18** could not be solubilised easily in aqueous media, so 5% DMSO was used for solubilisation. Despite this, **17** had the second highest activity.

Table 16. PACT results summary for free base and Sn(IV) porphyrins in this study or previously reported by Mack and coworkers [136].

	Φ_Δ[a]	Conc. (μM)	Log_{10} reduction	Thorlabs LED (dose)	Reference
14	0.86	0.5	2.02 (90 min)	M595L4 (8.1 J.cm^{-2})	[136]
15	0.84	0.5	9.69 (90 min)	M595L4 (8.1 J.cm^{-2})	[136]
16	0.64	5	0.85 (60 min)	M660L4 (6.0 J.cm^{-2})	[136]
17	0.78	5	5.74 (60 min)	M660L4 (6.0 J.cm^{-2})	[136]
18a	-	5	0.35 (45 min)	M595L4 (4.0 J.cm^{-2})	-
18	0.74	5	1.80 (45 min)	M595L4 (4.0 J.cm^{-2})	-
19a	-	5	0.25 (45 min)	M595L4 (4.0 J.cm^{-2})	-

19	0.73	5	2.13 (45 min)	M595L4 (4.0 J.cm^{-2})	-

[a] – singlet oxygen quantum yield in dimethylformamide.

7.2. Concluding remarks

The PACT activity of selected aza-BODIPY dyes was determined against *S. aureus*. Aza-BODIPY **1** was found to be the most active, with a Log_{10} reduction of 7.82 at a concentration of 1.25 µM. There is no obvious reason why the PACT activity of **1** would be significantly higher than those of **2-4** in terms of Φ_{Δ} values, so the reasons for this merit further in-depth study. The PACT activities of four porphyrins reported previously by Babu *et al.* [98] were also studied. The activity data demonstrates that there is significant PACT activity for the Sn(IV) complexes, with **19** exhibiting better activity across the studied concentration range. The comparative studies with earlier studies carried out by Mack and coworkers under similar experimental conditions highlight that although it can be challenging to prepare porphyrin complexes that are suitable for this application, the lipophilicity properties can be very important where *in vitro* studies are concerned [136].

Chapter 8: Non-linear Optics

8.1. Non-linear optical properties

This chapter discusses the nonlinear optical limiting properties of aza-BODIPY and porphyrin dyes in organic solvent solutions. For the objective of examining how structure influences optical limiting properties, the aza-BODIPY dyes were specifically chosen. It is hypothesised that the presence of electron-donating groups will enhance the NLO properties based on research on aza-BODIPYs and other compounds [138-144]. The total effect of electron-donating substituents at the 3,5- and 1,7-positions on the hyperpolarisability and NLO properties is evaluated in this work using eight new aza-BODIPY dyes. **Figure 81** depicts the structures of the dyes that were researched.

The primary goal of the NLO research was to examine and contrast the optical limiting characteristics of the various dyes both before and after halogenation. Firstly, the NLO characteristics of **1a** and **1** (both of which have phenyl groups in the 3,5-positions) will be compared to those of **2a** and **2** (with thien-3-yl groups at the 3,5-positions). Similar to this, the effect of the structural differences between **3a** and **3**, and **4a** and **4** will be examined with regard to the NLO properties. While **3a** and **3** have 4-hydroxyphenyl groups at the 1,7-positions relative to 4-bromophenyl groups at the 3,5-positions, **4a** and **4** have 4-hydroxyphenyl groups at the 3,5-positions relative to 4-bromophenyl groups at the 1,7-positions. Iodine atoms are present in the structures of **1**, **2**, **3**, and **4** compared to their absence in **1a**, **2a**, **3a**, and **4**, respectively. The structures of the studied dyes are shown in **Figure 81**.

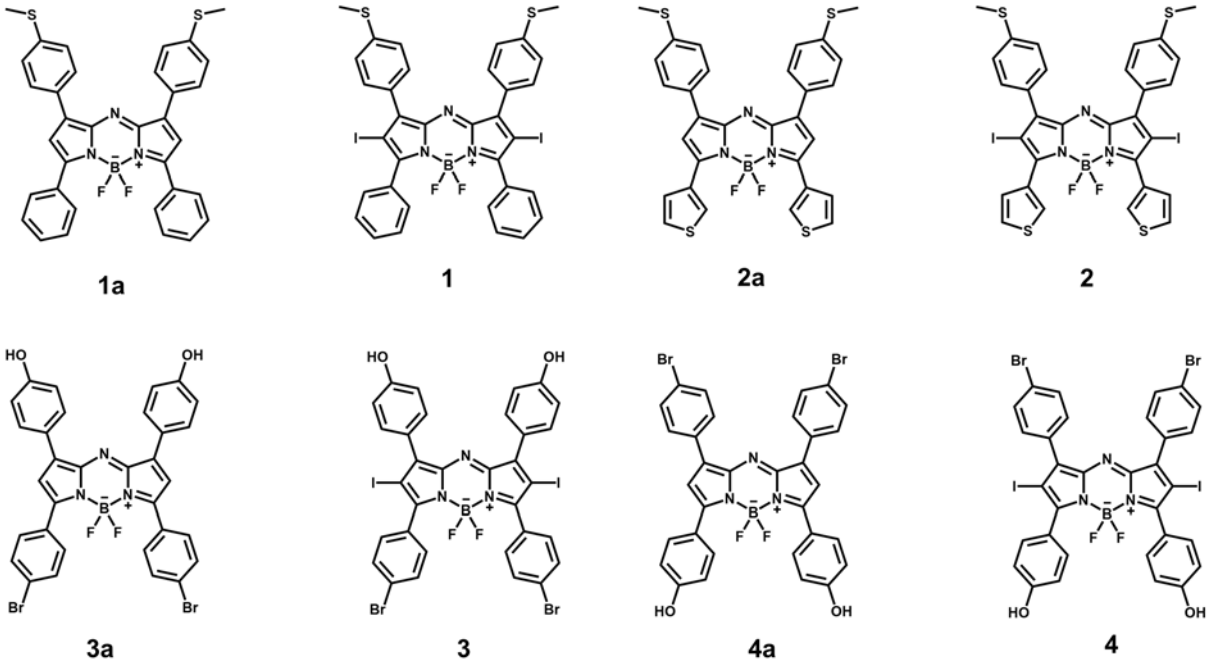

Figure 81. Structures of aza-BODIPYs used in NLO.

8.2. Mechanisms and parameters of optical limiting

The OL properties of various dyes were characterised using the open-aperture Z-scan method [144]. Nonlinear refraction, scattering, or absorption are all possible sources of OL. This study concentrated on NLA, where the transmittance was assessed using an open-aperture Z-scan at 532 nm as a function of material position utilising approximately 10-ns pulses with a constant input irradiance (*ca.* 42 μJ). Since an optical limiter cannot be characterised by a single parameter, the effectiveness of an optical limiter was measured using a variety of optical limiting characteristics. **Table 17** provides a summary of these factors. The parameters studied in this work are the β_{eff}, $Im[\chi^3]$, γ, and I_{lim} values of the dyes. The β_{eff} value is a crucial factor in determining if a material is suitable for optical limiting. It gauges nonlinear absorptivity to a certain extent and is reliant on the population of molecules in the excited state [146-148], while the second-order hyperpolarisability assesses the interaction of the incident photon

with the permanent dipole moments of the aza-BODIPY dyes [148-150]. This parameter often depends on nPA processes, which can be sequential or simultaneous [149-151].

High absorbance should occur in optical limiting materials when incident light intensity rises. The Im[$\chi^{(3)}$] value gauges how quickly an OL material reacts to a disturbance brought on by intense laser pulses [146-151]. An essential factor in OL measurements is the I_{im} fluence. I_{lim} is defined as the input fluence at which the nonlinear transmittance is half that of the linear transmittance [152]. An RSA response is typically observed for optical limiting upon nanosecond pulse stimulation [153-155]. RSA typically occurs in a molecular system when the excited state absorption cross-section is larger than that of the ground state [153-155]. It is consistent with a decline in transmittance as the sample gets closer to the zero point in Z-scan measurements. RSA can be produced by procedures such as ESA and the TPA-assisted ESA, **Figure 82** [156]**.** RSA can happen through ESA in the singlet manifold [157] or in the triplet manifold depending on several variables, such as the laser pulse duration and intensity, or occasionally the media in which the sample is dissolved.

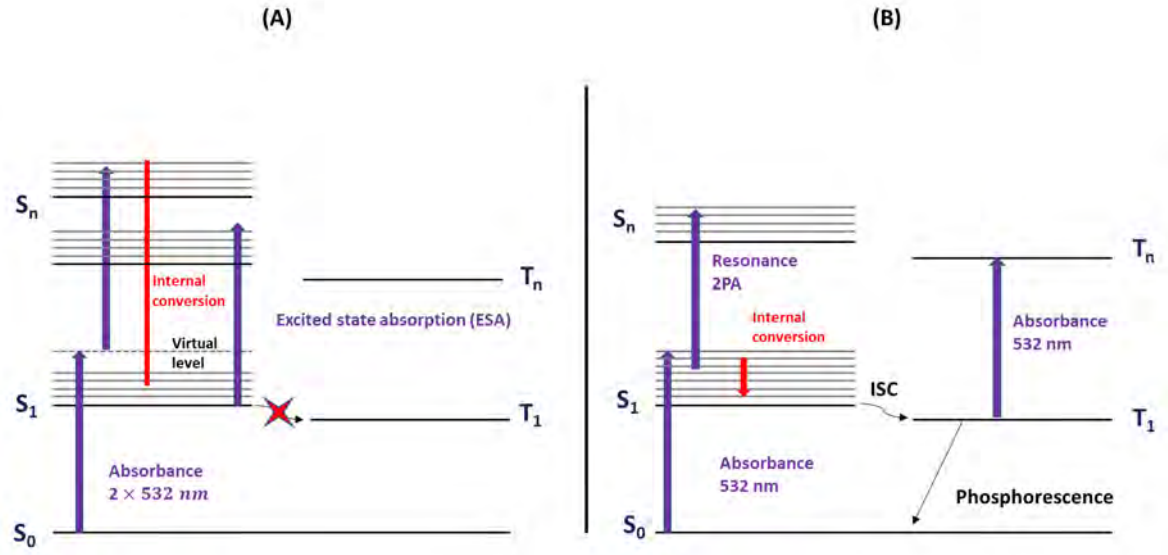

Figure 82. An explanation of the RSA's underlying process that highlights the two types of ESA.

Hanack *et al.* [157] reported that RSA, depending only on the singlet manifold, typically results from high beam intensity and brief pulse duration in the context of phthalocyanines. The ESA is comparable to that of $S_1 \rightarrow S_n$ in this scenario (**Figure 82(A)**). The ESA, however, becomes equivalent to that of $T_1 \rightarrow T_n$ when it occurs in the triplet manifold (**Figure 82(B)**) [157]. In general, intersystem crossover to the triplet manifold occurs at insignificant rates for non-halogenated aza-BODIPY dyes. As a result, ESA in the singlet manifold is predicted to be the major mechanism behind their observed RSA. The triplet manifold can be populated through halogenation. Therefore, it is reasonable to assume that the latter mechanism will also play a big role in this study.

When TPA populates the excited state involved with ESA rather than typical linear one-photon absorption, this is known as TPA-assisted ESA [158]. If the β_{eff} value remains constant regardless of the on-axis input intensity, TPA can be shown to have a dominant role [159, 160]. Only an effective β_{eff} can be calculated because

nanosecond laser pulses rather than femtosecond laser pulses are being used in this research, making it unlikely that the RSA responses seen during Z-scan measurements as the focal point is approached are caused solely by the TPA effect [163]. Since this work serves as a preliminary study using the set of aza-BODIPY dyes studied here, one solvent was used to determine the OL characteristics of the aza-BODIPY dyes. DCM was the solvent of choice since all the dyes could be readily solubilised in it and exhibited no signs of aggregation at the concentration used.

8.3. Nonlinear optical limiting properties of 1a, 1, 2a and 2

The optical limiting properties of **1a**, **1**, **2a** and **2** were evaluated in DCM. All the dyes had their absorption maxima close to the NIR region, distant from 532 nm, where the z-scan measurements were conducted. The UV-visible absorption spectra of the four dyes are shown in **Figure 83**. At 532 nm, there is a significant ground state absorption for all the studied dyes. As a result, the dyes have a non-zero absorption coefficient (α).

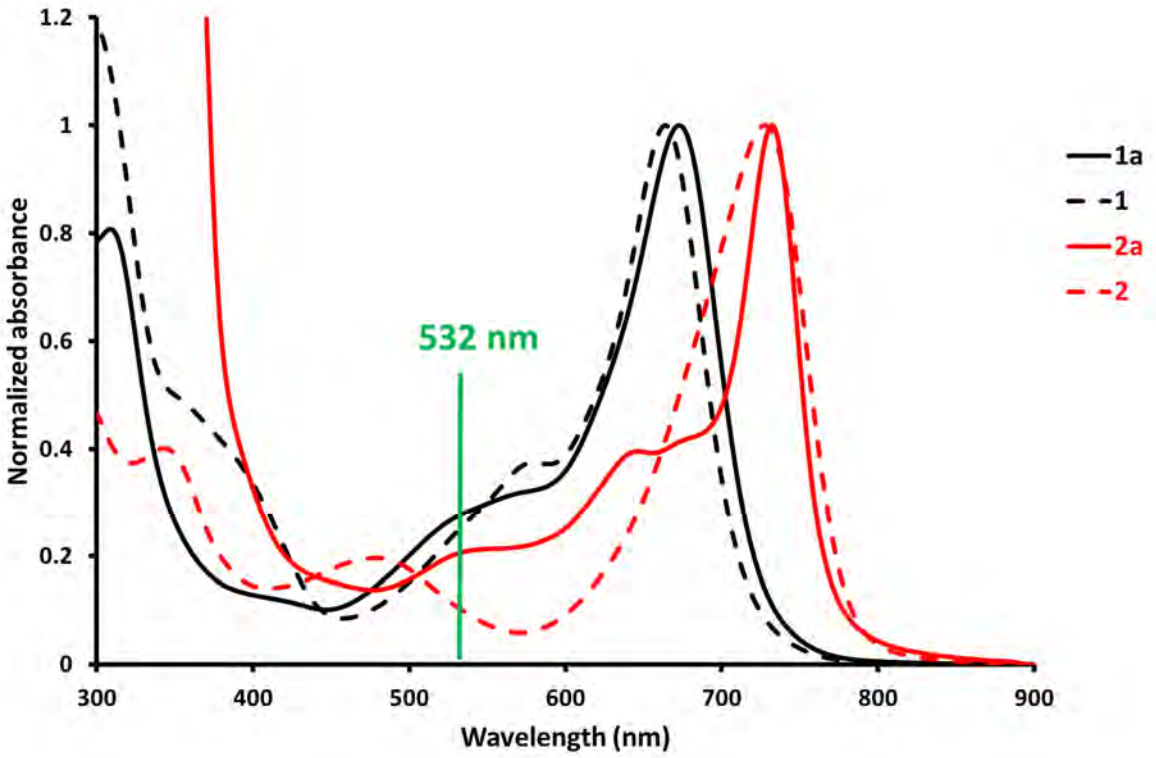

Figure 83. Normalised ground-state absorption spectra of **1a**, **1**, **2a** and **2**. The NLO wavelength, 532 nm, used for measurements is highlighted.

Figure 84 shows the open-aperture Z-scan data for dyes **1a**, **1**, **2a** and **2** with a fixed solution absorbance for the main spectral band of 1.8 in a 2 mm cuvette and input laser pulse energy (*ca.* 42 μJ), with an emphasis on the substituent effect. The data show significant NLA behaviour having RSA signatures discernible in the forms of the Z-scan profile [156]. As a result, given that aza-BODIPYs **1**, **2a** and **2** were able to lower the intensity of the visible light below 50%, they can be effective optical limiting materials. Although aza-BODIPY **1a** did not lower the transmittance to below 50%, it nevertheless has strong optical limiting characteristics.

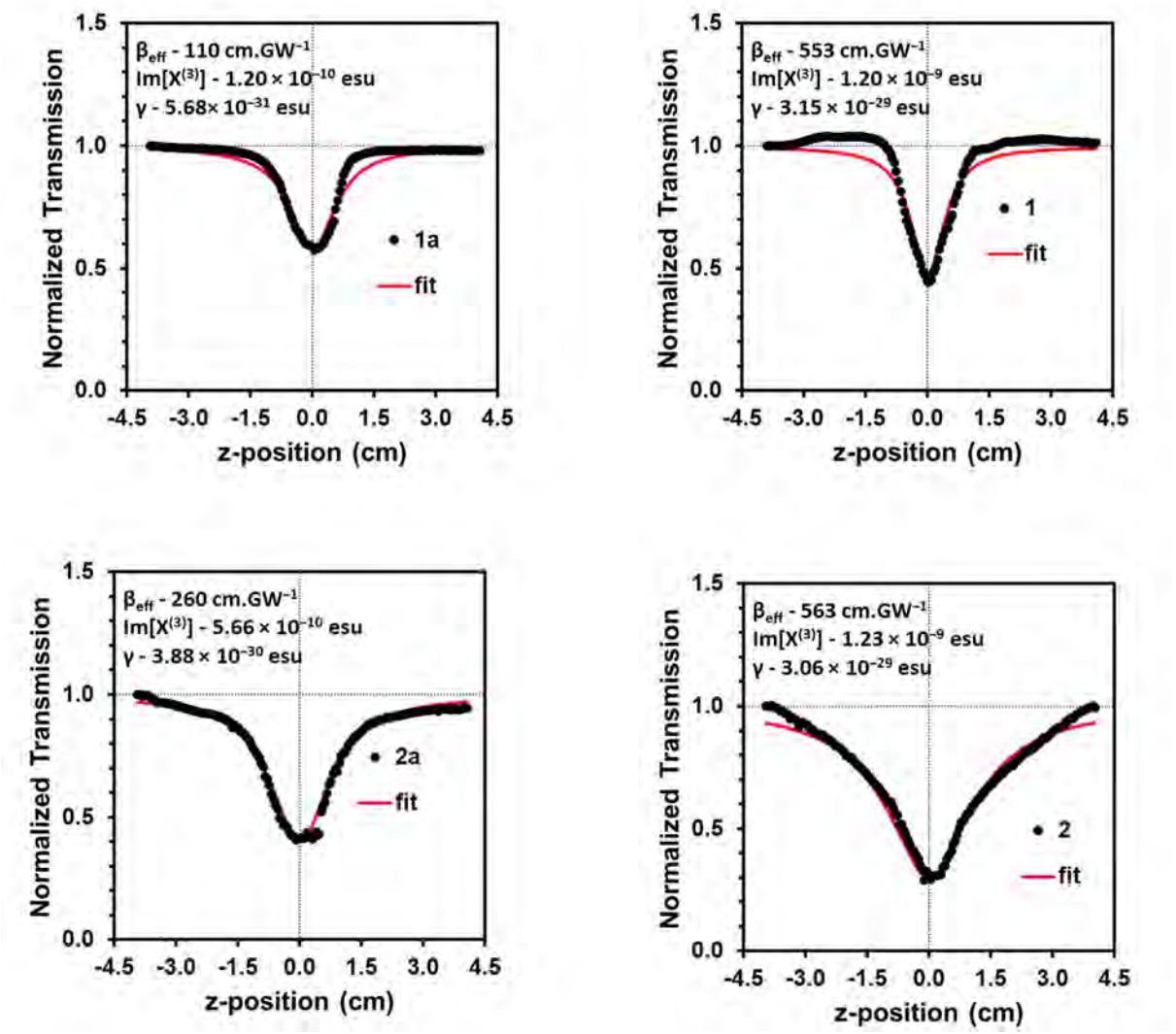

Figure 84. Open-aperture Z-scan curves for aza-BODIPYs **1a**, **1**, **2a** and **2** in DCM,

The estimated parameters in **Table 17** and the open-aperture Z-scan curves displayed in **Figure 84** demonstrate the importance of the structural alterations on the NLO response of the aza-BODIPY dyes. The non-iodinated derivatives, **1a** and **2a**, showed lower transmittance reductions and β_{eff} values compared to the iodinated counterparts, **1** and **2**, **Figures 85** and **86**. Overall, **2a** and **2** performed better than **1a** and **1**, possibly because their main absorption band lies further from 532 nm, and they have less linear 1PA absorbance at this wavelength. The reasons for this will be explored further in Chapter 9 and are related to the effect of introducing strongly electron-donating aryl groups to the structure. The red-shifted maximum absorbance is due to the presence

of thien-3-yl substituents at the 3,5-positions of **2a** and **2**. Fitting the data to the TPA function yielded β_{eff} values between 10^{-8} and 10^{-7} esu, which fall within the range previously reported for other organic compounds appropriate for OL applications.

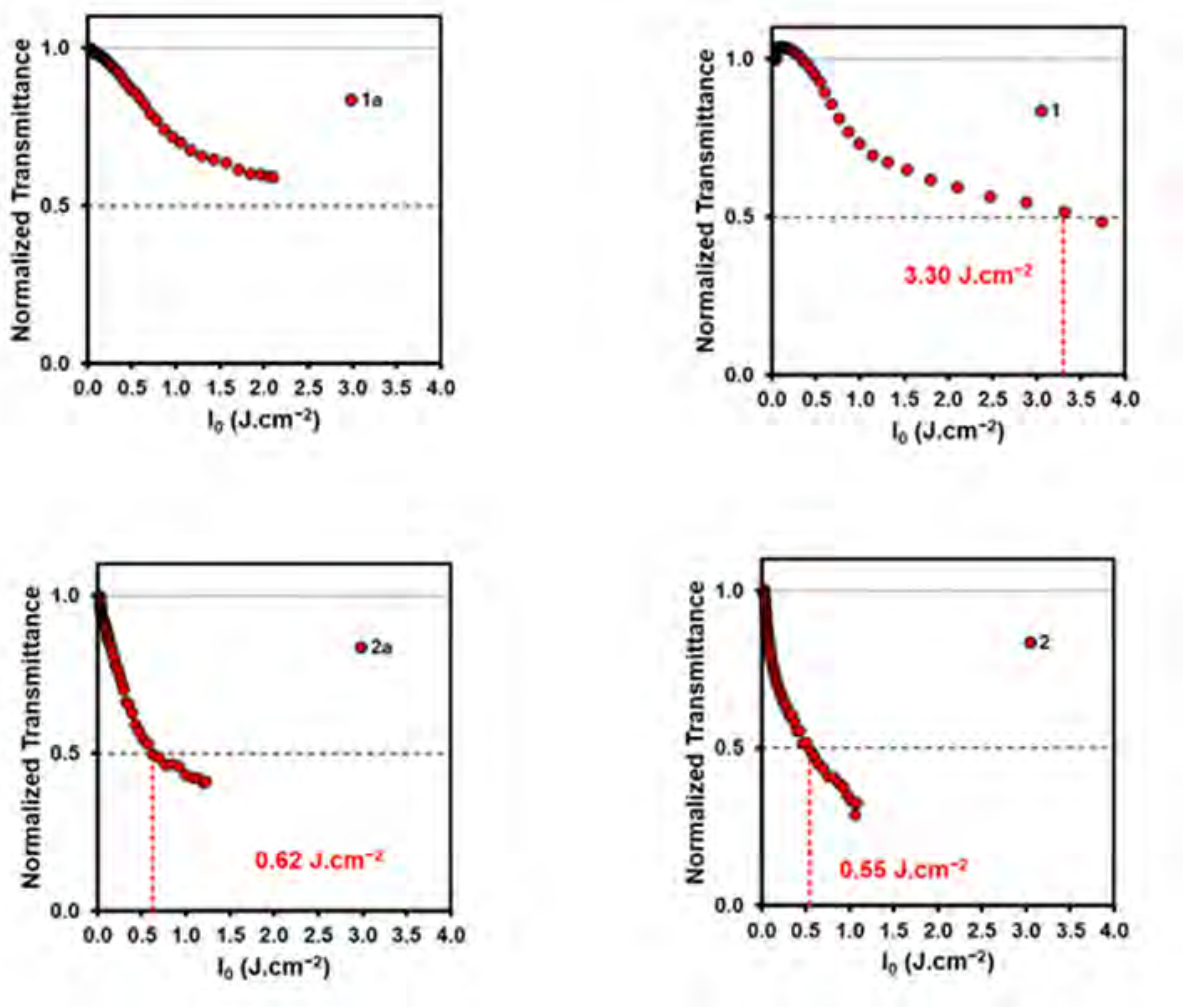

Figure 85. Transmittance versus input fluence (I_0) curves for **1a**, **1**, **2a** and **2** in DCM. The I_{lim} values were extracted at the point where the curve crosses the dashed line, which represents the 50% transmittance.

The limiting threshold, the input fluence at which the transmittance is 50% of the linear transmittance value, is an important indicator of how well-suited optical limiting materials are for applications since low OL thresholds are crucial. A recommendation [163] for exposure limits to various lasers has been released by the International

Commission on Non-Ionizing Radiation Protection. Equation 13 may be used to establish the exposure limit because this study employs 10 ns pulses at 532 nm.

$$\text{Exposure limit} = 2.7C_A t^{0.75}\ \text{J.cm}^{-2} \quad (13)$$

Where t is the exposure time, C_A is a correction factor (= 1 for 400–700 nm). The exposure limit for a 0.25 s exposure time to the second harmonic of Nd:YAG lasers is 0.95 J.cm^{-2}, which corresponds to the typical human blink reflex to a rapid flood of light [234]. Plotting transmittance against input fluence will yield the I_{lim} value (**Figure 85**). The I_{lim} values determined in DCM were found to be 3.30, 0.62 and 0.55 J.cm^{-2} for **1**, **2a** and **2**, respectively. The I_{lim} value for **1a** could not be determined. The I_{lim} values for **1** and **2** are well below the calculated exposure limit (0.95 J.cm^{-2}). This shows that these dyes are more likely candidates than **1a** and **2a** to be used in OL applications.

The third-order susceptibility (Im[$\chi^{(3)}$]) and second-order hyperpolarisability (γ) values often vary linearly with β_{eff}, meaning that the materials with the highest β_{eff} values also have the highest Im[$\chi^{(3)}$] and γ values [152-161]. Im[$\chi^{(3)}$] and γ values are crucial NLO metrics that assess how hyperpolarisable a material is in response to light irradiation [152-161]. These two variables are largely influenced by the active molecule's shape. For NLO applications, materials with high Im[$\chi^{(3)}$] and γ values are preferable [151-162]. The general observation for this Series of dyes is that **1** had the highest β_{eff} and γ values (**Table 15**). Although the Im[$\chi^{(3)}$] value of **2** was higher than that of **1**, the γ value was found to be less than that of **1**. This could be due to **1** being more hyperpolarisable than **2**. The Im[$\chi^{(3)}$] of **1** was higher than that of **1a** and **2a** but lower than that of **2. 1a** has the least Im[$\chi^{(3)}$] and γ values, **Table 17**. It can be concluded that **1** was the most hyperpolarisable dye due to the presence of the inductively

electron-withdrawing phenyl substituents at 3,5-positions, which have been reported to enhance the optical properties of optical limiting materials [138-141]. The presence of iodine atoms proved to enhance the optical properties of the studied aza-BODIPY dyes.

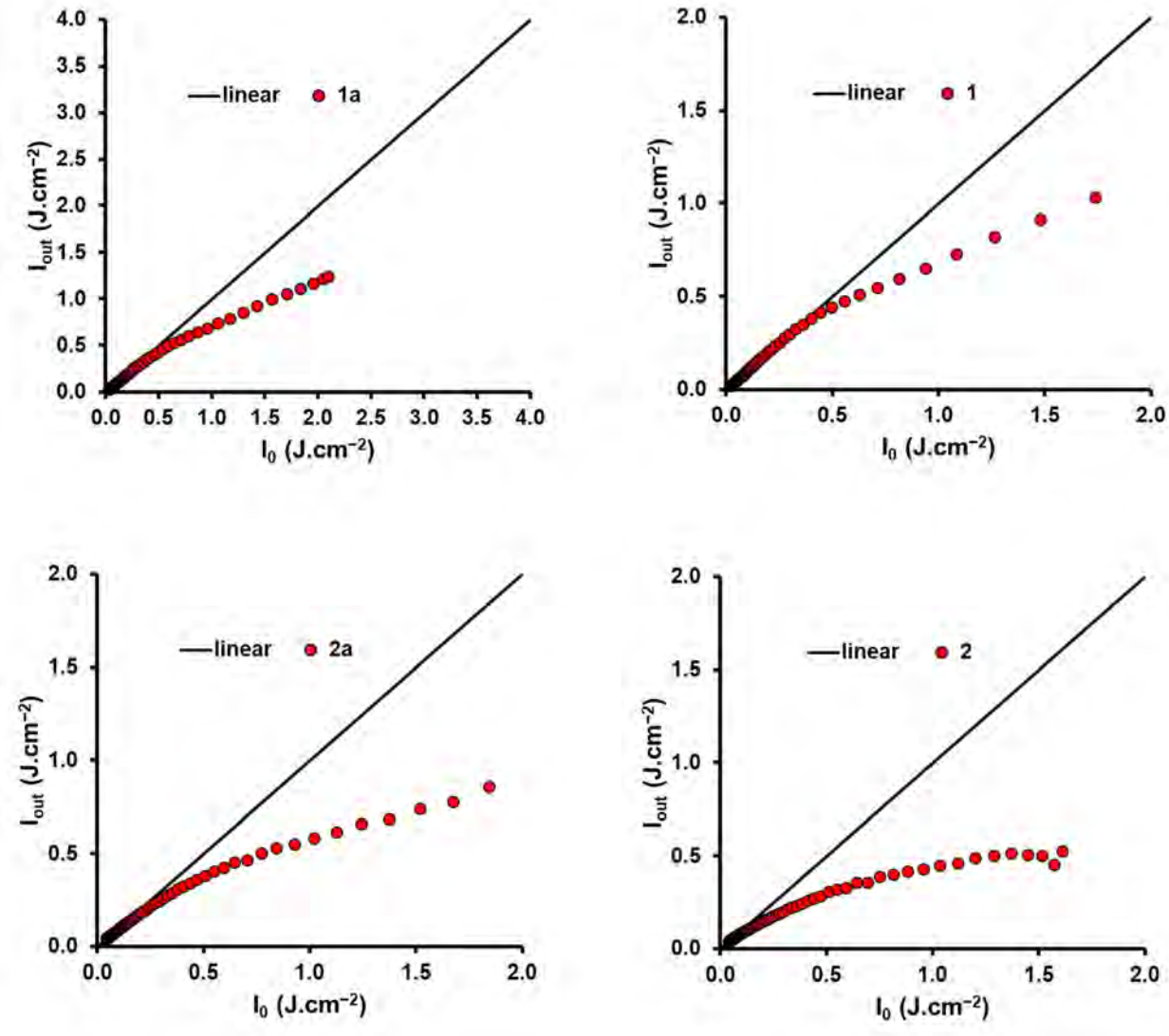

Figure 86. Output fluence (I_{out}) versus input fluence (I_0) curves for **1a**, **1**, **2a** and **2** in DCM.

All compounds studied have non-zero linear absorption values at 532 nm, proving that TPA can occur concurrently with the single photon absorption to the S_1 state. This suggests that various processes affect these compounds' OL characteristics in different ways. As such, for the non-iodinated derivatives, **1a** and **2a**, linear single-photon absorption populates the excited states to enable ESA from the S_1 state. For the heavy atom-containing derivatives **1** and **2**, the heavy iodine atoms facilitate the intersystem crossover. Thus, the observed RSA responses are caused by a combination of 2PA and ESA, **Figure 82**.

8.4. Nonlinear optical limiting properties of 3a, 3, 4a and 4

The optical limiting characteristics of **3a**, **3**, **4a** and **4** were measured in DCM. Their absorption maxima lie far from 532 nm, where z-scan measurements are taken. **Figure 87** displays the UV-visible absorption spectra of the four dyes. All the dyes under investigation exhibit significant ground state absorption at 532 nm. The dyes consequently have an absorption coefficient (α) that is not zero.

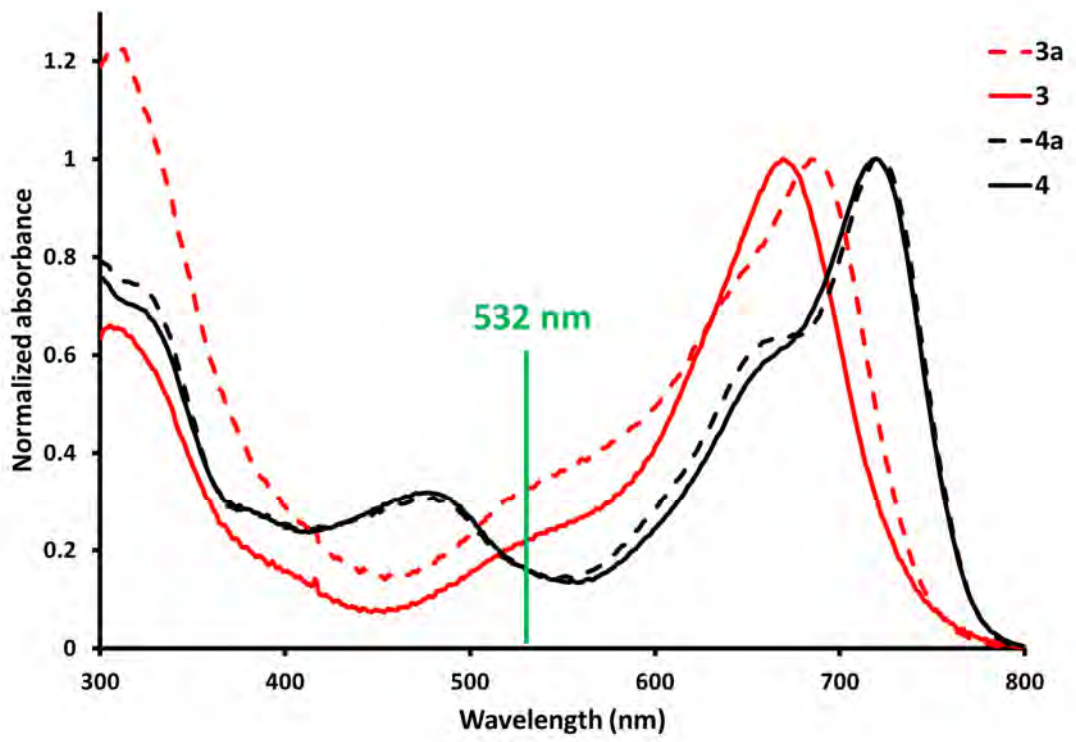

Figure 87. Normalised ground-state absorption spectra of **3a**, **3**, **4a** and **4**. The NLO wavelength, 532 nm, used for measurements is highlighted.

With a focus on the substituent effect, **Figure 88** displays the open-aperture Z-scan data for the dyes **3a**, **3**, **4a**, and **4** with a fixed solution absorbance and input laser pulse intensity. The data demonstrate considerable NLA behaviour with RSA signatures visible in the Z-scan profile forms. For a material to be an effective optical limiter, its transmittance must be reduced by at least 50% [163]. Because aza-BODIPYs **3**, **4a**, and **4** may reduce the intensity of visible light below 50%, they can function as efficient optical limiting materials. Despite not lowering the transmittance to below 50%, aza-BODIPY **3a** displays some optical limiting properties.

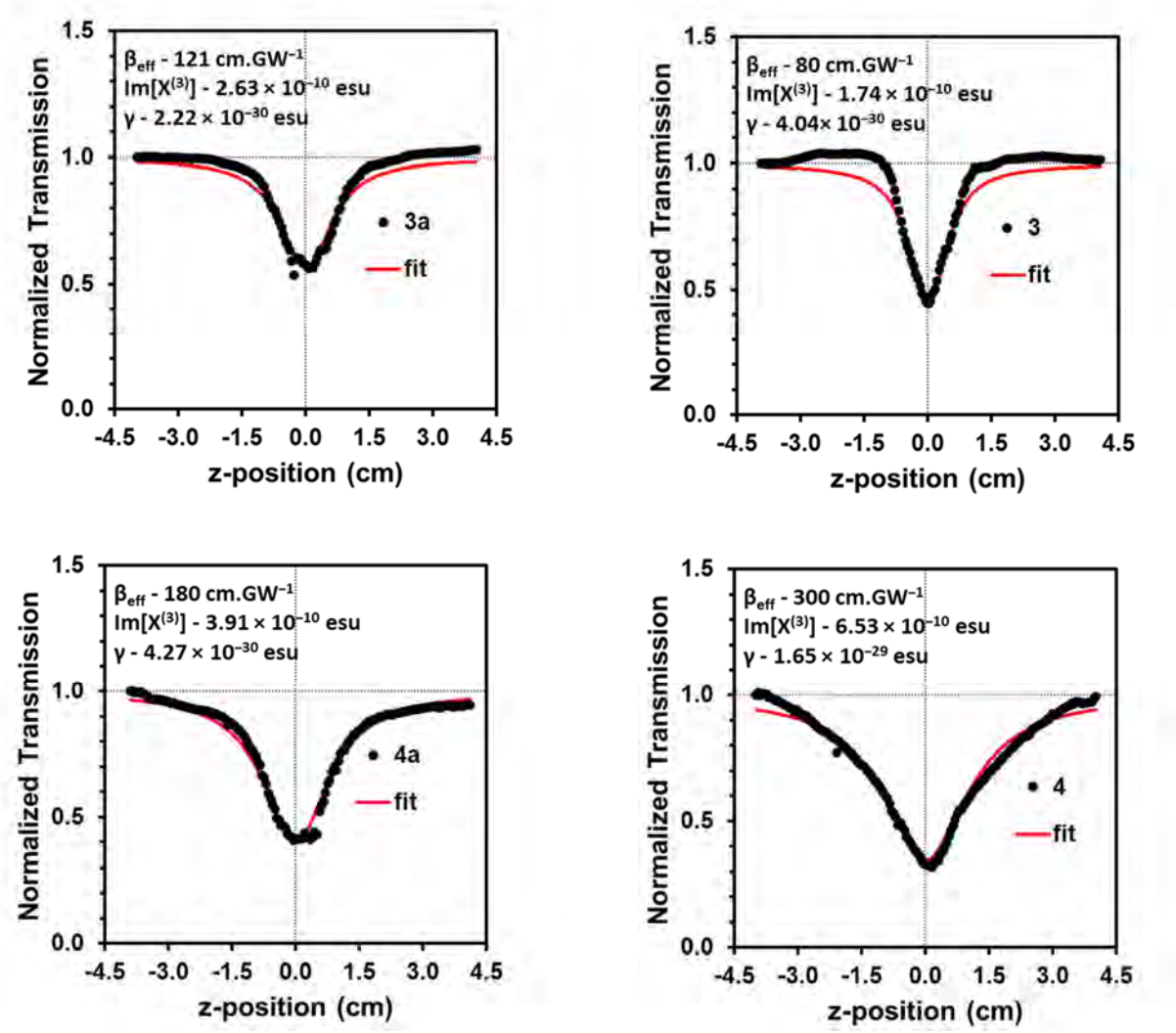

Figure 88. Open-aperture Z-scan curves for aza-BODIPYs **3a**, **3**, **4a** and **4** in DCM.

The calculated parameters in **Table 17** and the open-aperture Z-scan curves shown in **Figure 88** show how crucial the structural changes are to the aza-BODIPY dyes' NLO response. In comparison, **3a** has a higher β_{eff} value than the iodinated counterpart **3**. In contrast, the iodinated derivative, **4**, has a higher β_{eff} value than the parent derivative, **4a**. The iodinated derivatives generally have higher transmittance reductions than the parent compounds (**Figures 89** and **90**).

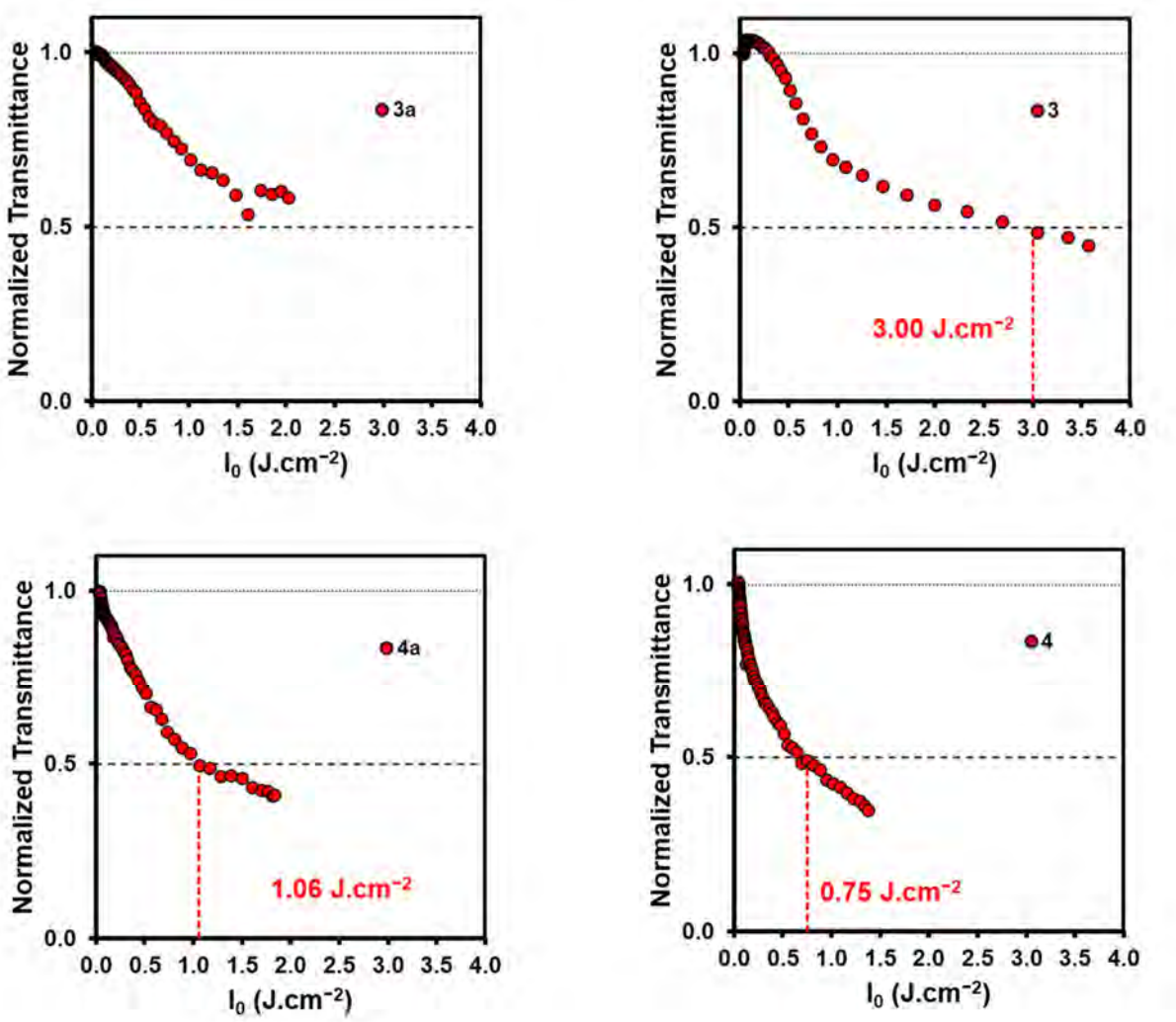

Figure 89. Transmittance versus input fluence (I_0) curves for **3a**, **3**, **4a** and **4** in DCM. The I_{lim} values were extracted at the point where the curve crosses the black dashed line, which represents the 50% transmittance.

Due to their ability to absorb away from 532 nm, **4a** and **4** performed better overall than **3a** and **3**, since this results in a lower α value for linear 1PA absorbance. The presence of 4-hydroxyphenyl substituents at the 3,5-positions of 4**a** and **4** resulted in the red-shifted maximum absorbance. After the data were fitted to the TPA function, β_{eff} values between 10^{-8} and 10^{-7} esu were obtained, within the range of values previously reported for other organic compounds suitable for OL applications [138-163].

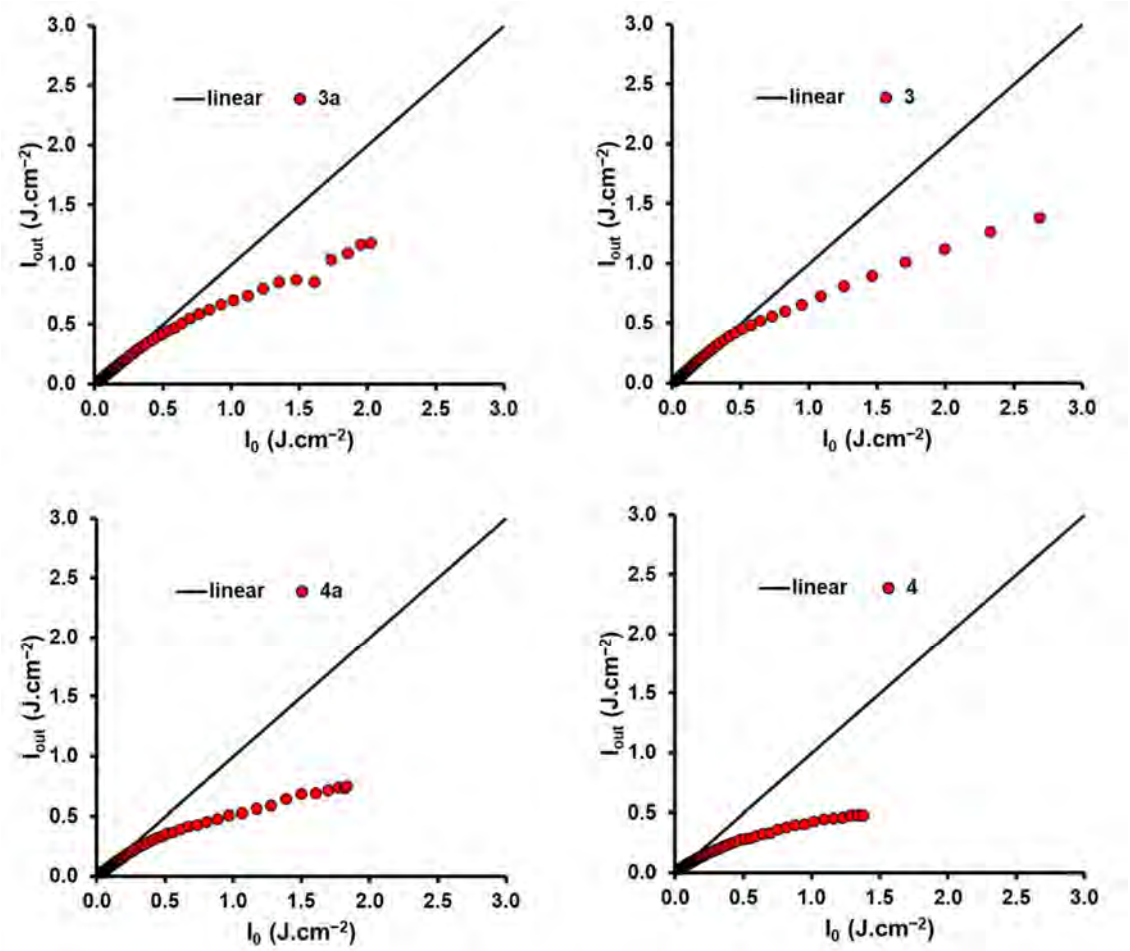

Figure 90. Output fluence (I_{out}) versus input fluence (I_0) curves for **3a**, **3**, **4a** and **4** in DCM.

Since low OL thresholds are essential, the I_{lim}, which is the input fluence at which the transmittance is 50% of the linear transmittance value, is a significant indicator of how well-suited optical limiting materials are for NLO applications. The International Commission on Non-Ionizing Radiation Protection has published a recommendation [164] for exposure limits to various lasers. The exposure limit may be determined using Equation 13 because this investigation uses 10 ns pulses at 532 nm.

Each of the investigated dyes exhibits non-zero linear absorption values at 532 nm, demonstrating the ease with which the S_1 state can be populated through single photon absorption and the occurrence of TPA. This implies that multiple processes

can contribute to the OL properties of these molecules. As a result, linear single-photon absorption populates the excited states for the non-iodinated derivatives **3a** and **4a** to enable ESA from the S_1 state. The observed RSA responses are the result of a combination of 2PA and ESA in the case of the heavy atom-containing derivatives **3** and **4**, as shown in **Figure 82**.

Table 17. A summary of optical limiting properties of aza-BODIPY dyes obtained with 10 ns pulses at 532 nm in DCM.

	α (cm^{-1})	**β_{eff} ($cm.GW^{-1}$)**	**I_{lim} ($J.cm^{-2}$)**	**Im[$\chi^{(3)}$] (esu)**	**γ (esu)**
1a	7.29	110	-	2.39×10^{-10}	5.68×10^{-31}
1	5.58	553	3.30	1.20×10^{-9}	3.15×10^{-29}
2a	1.19	260	0.62	5.66×10^{-10}	3.88×10^{-30}
2	2.95	563	0.55	1.23×10^{-9}	3.06×10^{-29}
3a	7.29	121	-	2.63×10^{-10}	2.22×10^{-30}
3	1.99	80	3.00	1.74×10^{-10}	4.04×10^{-30}
4a	1.38	180	1.06	3.91×10^{-10}	4.27×10^{-30}
4	0.28	300	0.75	6.53×10^{-10}	1.65×10^{-29}

8.5. Comparison of the studied aza-BODIPY dyes with previously reported ones

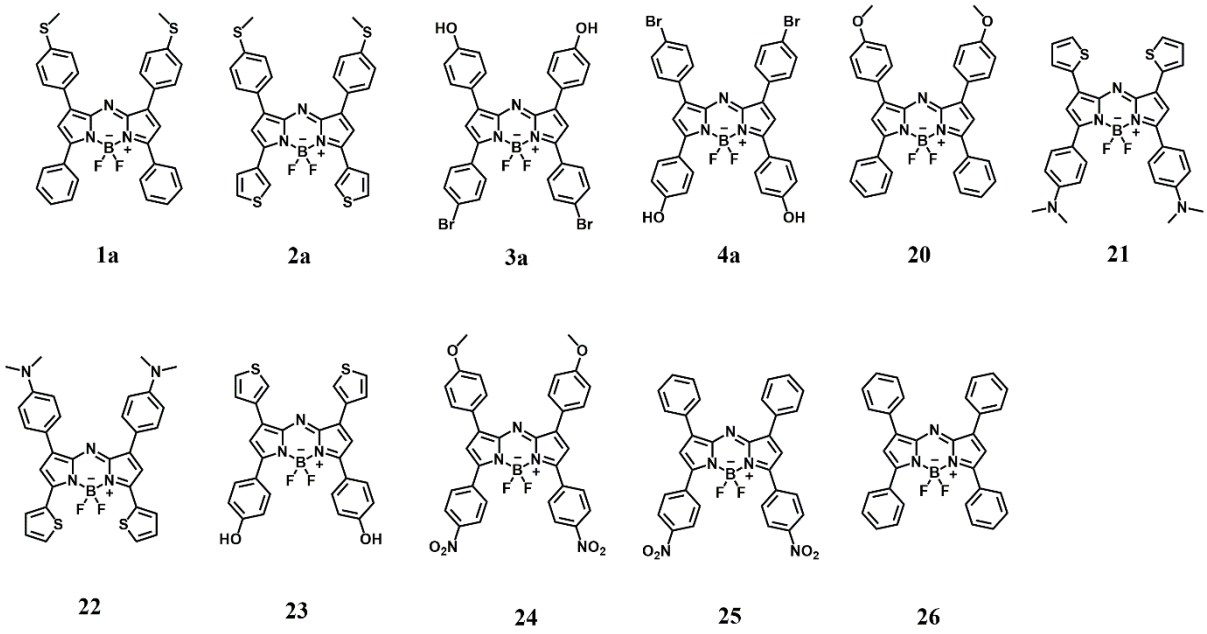

Figure 91. Structures of studied aza-BODIPY dyes and the ones from previous studies [156].

The NLO properties of studied aza-BODIPY dyes synthesised in this work were compared to the properties of the dyes previously reported by Kubheka [156], **Figure 91**. Despite different solvents being used to study the dyes, the OL properties can be indirectly compared. All the dyes in this section are non-halogenated. Therefore, ESA in the singlet manifold ($S_1 \rightarrow S_n$) is anticipated to be the main mechanism behind the observed RSA. The α value for all the dyes is non-zero, meaning that the dyes have a significant absorbance at 532 nm. This means that a linear single-photon absorption populates the excited states to enable ESA in the S_1 state.

To enable an easy comparison of the OL properties of the dyes, the dyes will be grouped according to their substituents. Five groups were established (**Figure 91**): (a) **26**, **1a** and **20**, (b) **2a** and **22**, (c) **4a** and **21**, (d) **21** and **23**, and (e) **24** and **25**. A summary of the NLO parameters is provided in **Table 18**. The most important from the

standpoint of providing a comparison is the γ value since the concentration of the dye solution is taken into consideration.

(a) The γ value **26** was found to be higher than those of **1a** and **20** (**Table 18**) despite having the lowest calculated dipole moment (**Figure 92**). **26** has no thiomethyl or methoxy groups at the *para*-positions of 1,7-position phenyl rings.

(b) **2a** is more hyperpolarisable than **22** (**Table 18**) despite having a lower calculated dipole moment (**Figure 92**). It has a 4-methylthiophenyl group at the para-positions of the 1,7-position aryl rings rather than the 4-dimethylaminophenyl rings of **22**.

(c) **4a** is more hyperpolarisable than **21** (**Table 18**) since it has a larger γ value despite having a lower calculated dipole moment (**Figure 92**). It has 4-hydroxyphenyl rings at the 3,5-positions rather than the 4-dimethylaminophenyl rings of **21**.

(d) **23** is more hyperpolarisable (**Table 18**) despite having a lower calculated dipole moment (**Figure 92**. It has 4-hydroxyphenyl groups at the 3,5-positions rather than the 4-dimethylaminophenyl rings of **21**.

(e) **25** was more hyperpolarisable than **24** despite having a lower calculated dipole moment (**Figure 92**). **24** has 4-methoxyphenyl rings at the 1,7-positions rather than phenyl rings. This series differs from group (a) by having 4-nitrophenyl rings at the 3,5-positions. This results in significantly larger calculated dipole moments, but this does not significantly enhance the γ values relative to that of the parent 1,3,5,7-tetraphenyl dye **26**.

Counterintuitively, it can be concluded from these trends that maximising the calculated ground state dipole moment is not an approach that can readily be used

when rationally designing an azaBODIPY dye for the optical limiting application. It is noteworthy that there is also no clear trend between the γ values of **1a**, **2a**, **3a** and **4a** and the calculated dipole moments (**Figure 92**). Iodinated dyes **1**, **2**, **3** and **4** were found to have higher γ values despite having lower calculated dipole moments (**Figure 92**). If a simultaneous 2PA effect were the main mechanism responsible for the observed optical limiting response, the dipole moment of the dye would be expected to determine the β and γ values, see Equations 10−12. If this were the case, the ESP maps and calculated dipole moments described in Section 8.6 would be useful for rationally designing dyes for this application.

In the context of the nanosecond timescale, however, only an effective nonlinear absorption coefficient, β_{eff}, is obtained when a two-photon analysis is applied to the RSA response, since ESA in the singlet and/or triplet manifold shapes the optical limiting properties. Since this depends on the relative cross-sections associated with the ESA from the S_1 and T_1 states on the one hand and from the S_0 ground state on the other, minimising the extent of linear 1PA absorbance at 532 nm and hence minimising the α value by shifting the main aza-BODIPY spectral band as far to the red as possible is likely to be important. This means that molecular modelling can still provide an important insight through TD-DFT calculations of the UV-visible absorption spectra. This will be explored further in Chapter 9.

Table 18. A summary of optical limiting properties of aza-BODIPY dyes obtained with 10 ns pulses at 532 nm.

	α (cm^{-1})	**β_{eff} ($cm.GW^{-1}$)**	**I_{lim} ($J.cm^{-2}$)**	**Im[$\chi^{(3)}$] (esu)**	**γ (esu)**	**Reference**
1a	7.29	110	-	2.39×10^{-10}	5.68×10^{-31}	-

2a	1.19	260	1.37	5.66×10^{-10}	3.88×10^{-30}	-
3a	7.29	121	-	2.63×10^{-10}	2.22×10^{-30}	-
4a	1.38	180	1.06	3.91×10^{-10}	4.27×10^{-30}	-
20	2.6	32.4	-	3.20×10^{-11}	2.70×10^{-31}	[153]
21	3.2	140	1.5	3.0×10^{-10}	1.50×10^{-31}	[153]
22	1.4	76.0	1.3	1.70×10^{-10}	1.50×10^{-32}	[153]
23	1.9	48.0	-	2.60×10^{-10}	1.70×10^{-31}	[153]
24	1.0	14.0	-	3.10×10^{-11}	3.90×10^{-31}	[153]
25	1.2	6.00	-	1.50×10^{-11}	4.90×10^{-31}	[153]
26	1.0	46.0	3.3	8.90×10^{-11}	2.70×10^{-30}	[153]

8.6. Molecular Electrostatic Potential maps for the aza-BODIPY dyes studied for application in NLO

The charge distributions on aza-BODIPY dyes studied for NLO application are described in this section. Electrostatic potential maps (**Figure 92**) can be used to visualize different charge distributions across the structures of the aza-BODIPY dyes [165, 166]. To further understand the hyperpolarisability of the molecules in the context of NLO, the understanding of charge distribution can be achieved through understanding the dipole moments of molecules. This is because large dipole moments were expected to enhance the hyperpolarisability of the dye molecules. On the electrostatic potential (ESP) maps, the red area represents the negative region of

the ESP map where the electron-rich region of the molecule attracts a positive charge. In contrast, the blue area represents the positive region where the electron-deficient region of the structure repels a positive charge (**Figure 92**).

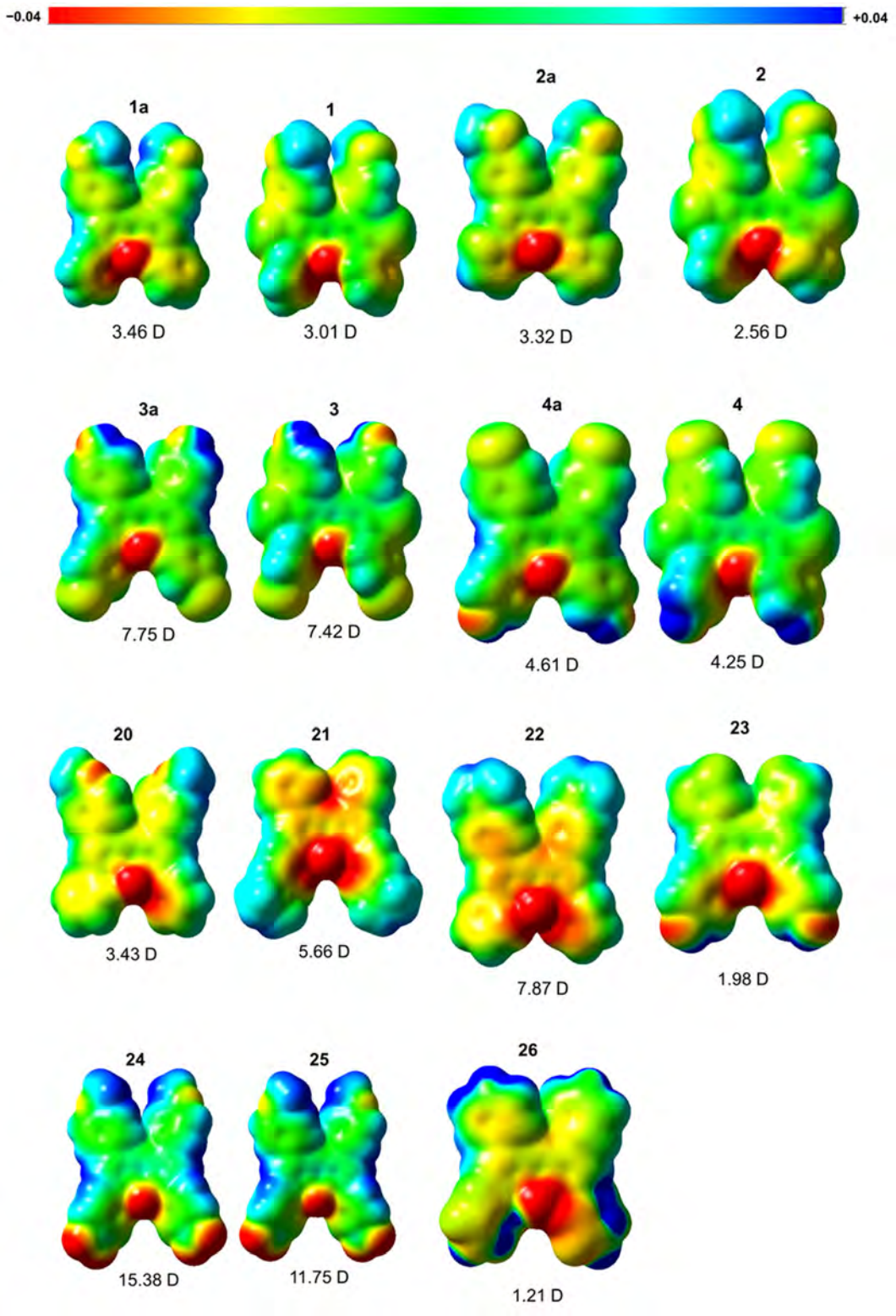

Figure 92. Molecular electrostatic potential maps for the aza-BODIPY dyes studied for NLO applications. The mapping was performed using GaussView. The mapping corresponds to the attractive and repulsive force exerted on a point positive charge. A

red surface colour highlights negative regions of electrostatic potential in which electron-rich portions of the structure attract a positive point charge. Blue surfaces highlight positive regions where electron-deficient areas of the structure repel a positive point charge.

The BF_2 centre of all the aza-BODIPY dyes contains an intense red colour due to the electron-withdrawing nature of the fluorine atoms. At the 1,7-positions, **1**, **1a**, **2** and **2a**, all have an intense blue colour (positively charged) since the respective substituents are electron deficient. The same applies to the substituents at the 3,5-positions. For **3** and **3a** at the 1,7-positions, there is an intense red colour due to the electronegative oxygen atom of the 4-hydroxyphenyl group. The 3,5-positions have a blue colour since the substituents are electron-deficient. Conversely, **4** and **4a** have an intense red colour at the 3,5-positions relative to the 1,7-positions. The red colour on the oxygen atom suggests that there is an increase in the negative charge centre on the electron negative oxygen atom.

20 has its negative charge centred at the oxygen of the 4-methoxyphenyl substituent, thus the intense red colour at the 1,7-positions. The negative charge centre of **21** is observed at the electronegative nitrogen atom of the 4-dimethylaminophenyl substituent at the 3,5-positions, which is characterised by the intense red colour. In comparison with **21**, there is a slightly red colour along the 1,7-positions thien-2-yl region and an intense red colour on the sulfur atom of the thien-2-yl substituent. This shows that the negative charge is centred on the substituent at the 1,7-positions of **21.** For **22**, the most electronegative atom is the nitrogen of the 4-dimethylaminophenyl group at the 1,7-positions, thus the reddish colour along the position. **23** has its negative charge centre at the 3,5-positions since there is an electronegative oxygen atom of the 4-hydroxyphenyl substituent. The intense red colour signifies the negative

charge centre of **23**. **24** and **25** both have their negative charge centre at the aniline centre due to the two atoms (nitrogen and oxygen), which are more electronegative than oxygen on the 4-methoxyphenyl substituent of **24** and the benzene ring of **25**.

8.7. Nonlinear optical limiting properties of porphyrins

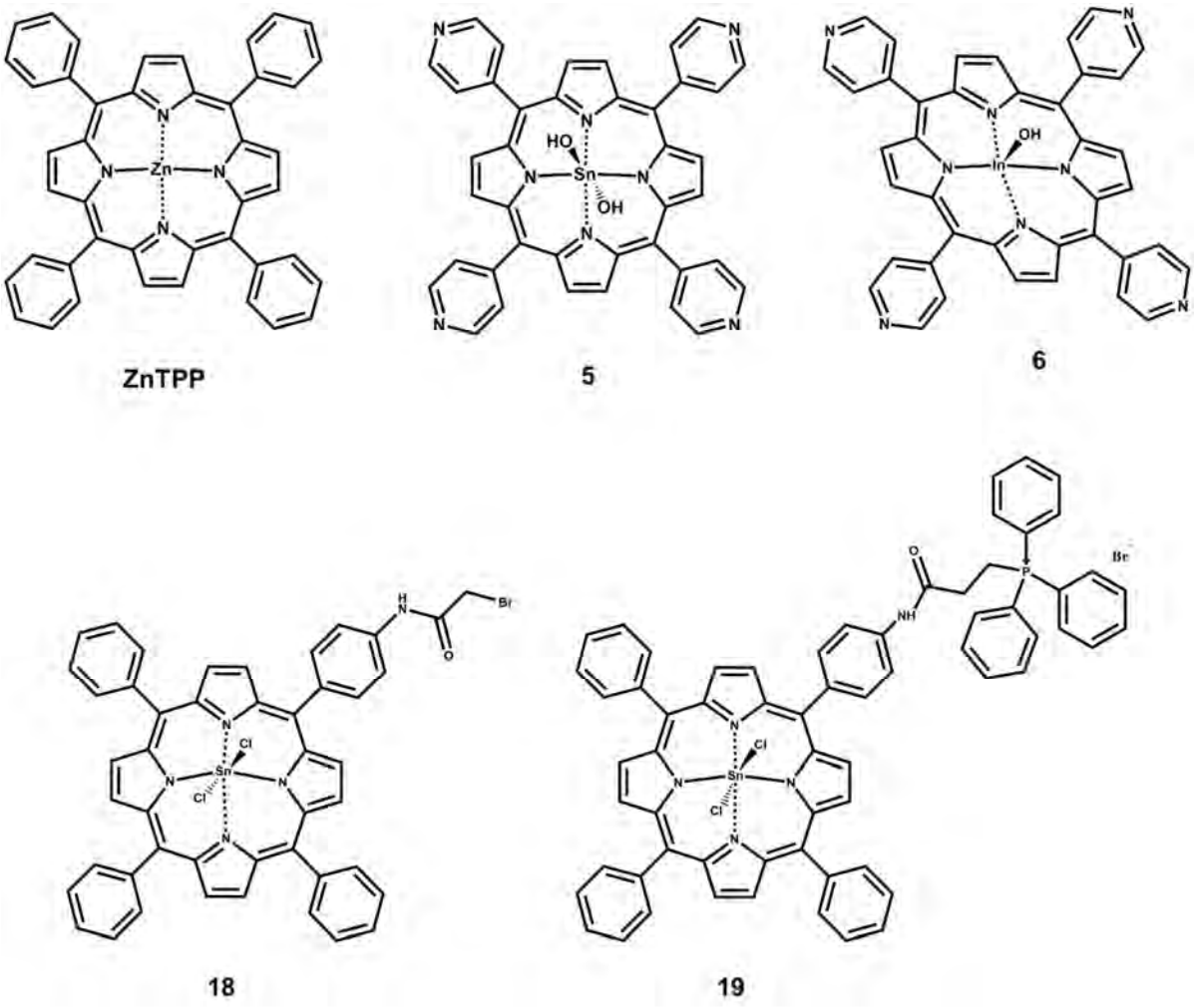

Figure 93. Structures of porphyrins used in NLO.

Among the numerous examples documented in the literature [167, 168], 2D architectures based on π-delocalised macrocycles, like metal porphyrins and porphyrins [169-171], have garnered significant interest because of their good solubility, thermal and chemical stability. Moreover, porphyrins' architectural flexibility

permits a wide range of substituents to be attached to the axial position of a metal porphyrin or at the meso or β-pyrrolic positions of the porphyrin ring [171-173].

Heterocyclic rings can be electron-rich or electron-poor systems. In particular, pyrrole, due to its six π electrons and five π orbitals, belongs to the first category. Therefore, the porphyrin ligand, having four pyrrolic rings, is an electron-rich system in which electron-rich (β-pyrrolic) or electron-poor (*meso*) carbon atoms can be recognised [171-173]. The focus of this work was to examine the NLO properties of structurally analogous porphyrins from this study relative to Zn(II) tetraphenylporphyrin (**ZnTPP**) to determine the extent to which the optical limiting properties are modified.

The optical limiting properties of the porphyrins, **ZnTPP**, **5**, **6**, **18** and **19** (**Figure 93**) were evaluated in DMSO. The intense Soret bands of these dyes lie between 428−430 nm, while the weaker forbidden Q-bands lie between 590 and 620 nm. These main bands do not lie close to 532 nm, where the z-scan measurements were conducted. The UV-visible spectra of the five compounds are shown in **Figure 94**. At 532 nm, all the studied compounds have minimal ground state absorption (between 0.01 and 0.02). As a result, the compounds have been assigned a non-zero absorption coefficient (α = 0.12 for all the compounds).

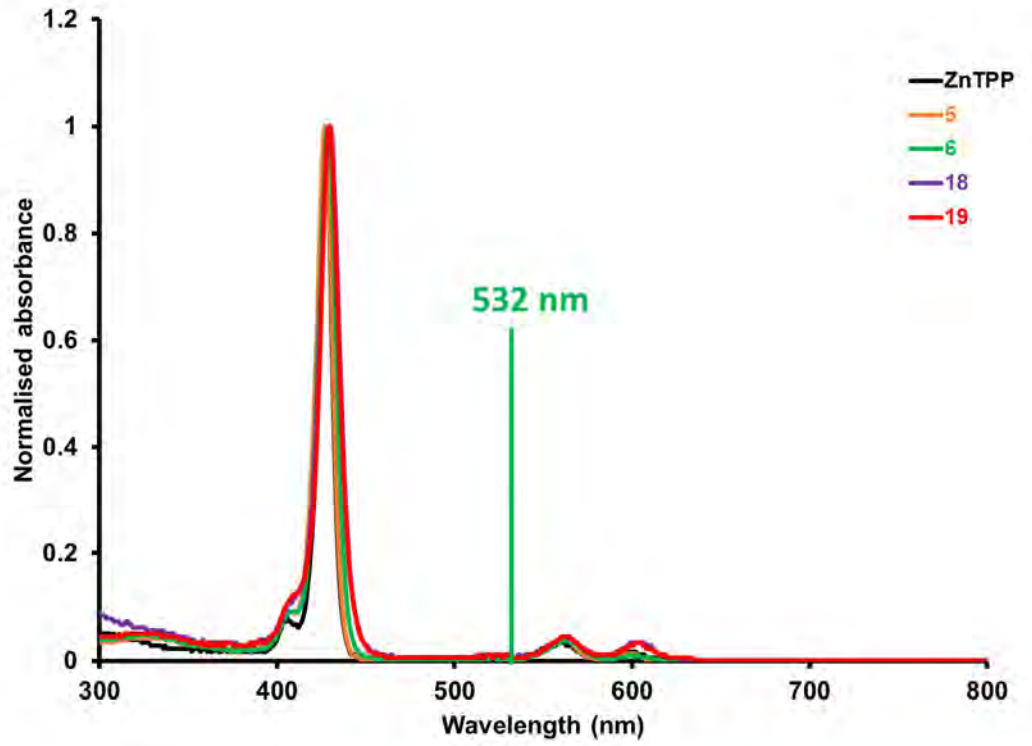

Figure 94. Normalised ground-state absorption spectra of **ZnTPP**, **5**, **6**, **18** and **19**. The NLO wavelength, 532 nm, used for measurements is highlighted.

With a fixed solution absorbance of 1.8 at the B band maxima and input laser pulse energy of 35 µM, **Figure 95** displays the open-aperture Z-scan data for dyes **ZnTPP**, **5**, **6**, **18**, and **19**. The focus will be on the substituents at the *meso*-positions. This is because it has been shown experimentally and theoretically that the nature of the metal in porphyrin complexes has no bearing on the second-order NLO response; rather, the metal's capacity to coordinate in the free axial position [174]. As a result, the metal only influences the NLO response indirectly in solvents that permit aggregation processes. This is why, when considering the second-order NLO response of chromophores such as porphyrins, which can assemble in non-donor solvents with low polarity such as dichloromethane and chloroform, the nature of the solvent must also be carefully taken into account [174].

The data exhibit notable NLA behaviour with RSA signatures that may be seen in the *Z*-scan profile. **ZnTPP** was used as a reference. According to **ZnTPP**'s open-aperture profile (**Figure 95**), the compound reduced visible light intensity by less than 20%. Compared to **ZnTPP**, **18** exhibited a higher reduction in visible light intensity than the other compounds, **5**, **6** and **19**. The superiority of **18** could be influenced by the electron-withdrawing 2-bromo-*N*-phenylacetamide functional group on compound **18**. The electron-donating tetrapyridyl substituents of **6** relative to the In(III) central metal ion rendered the compound more hyperpolarisable than the other compounds. Despite not reducing the transmittance to less than 50%, each compound possesses certain optical limiting properties. Overall, **18** exhibited the highest attenuation of the visible light intensity, with **6** being the most hyperpolarisable (highest γ values), **Table 19**. None of the dyes decreased the transmission of visible light intensity to below 50% (**Figure 95**). Thus, we could not obtain the I_{lim} value in **Figures 96** and **97**. The summary of the results is provided in **Table 19**.

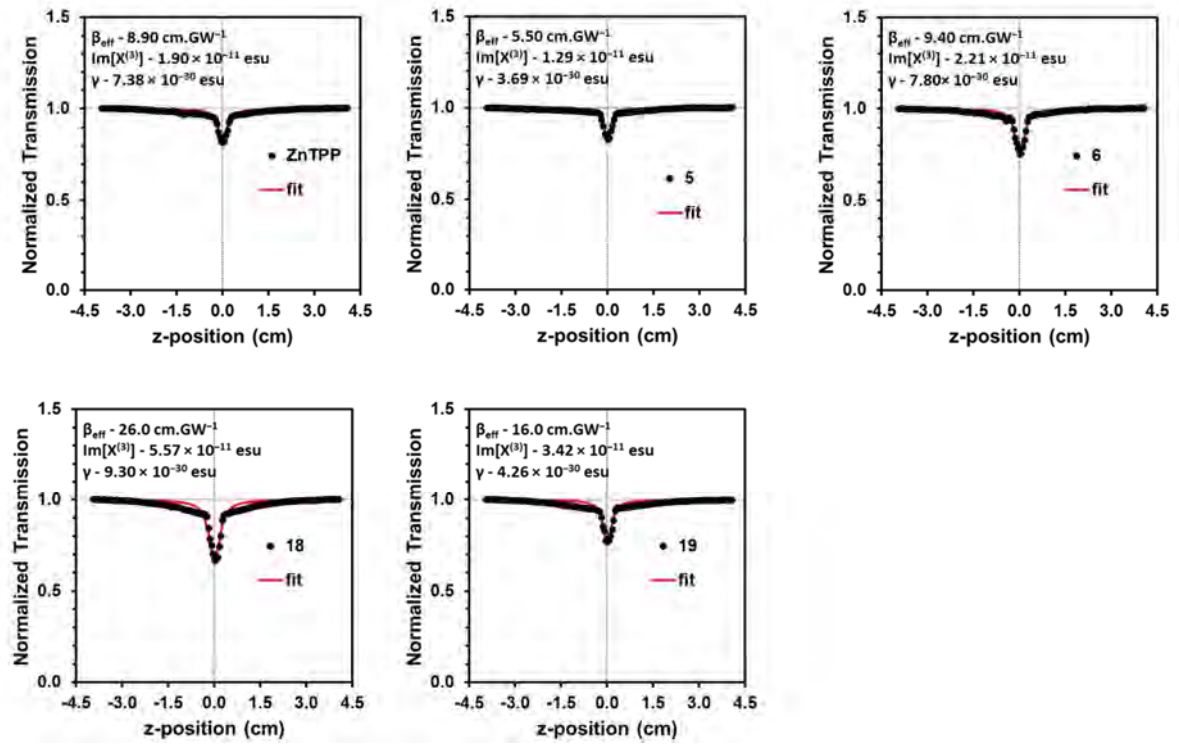

Figure 95. Open-aperture Z-scan curves for porphyrins **ZnTPP**, **5**, **6**, **18** and **19** in DMSO.

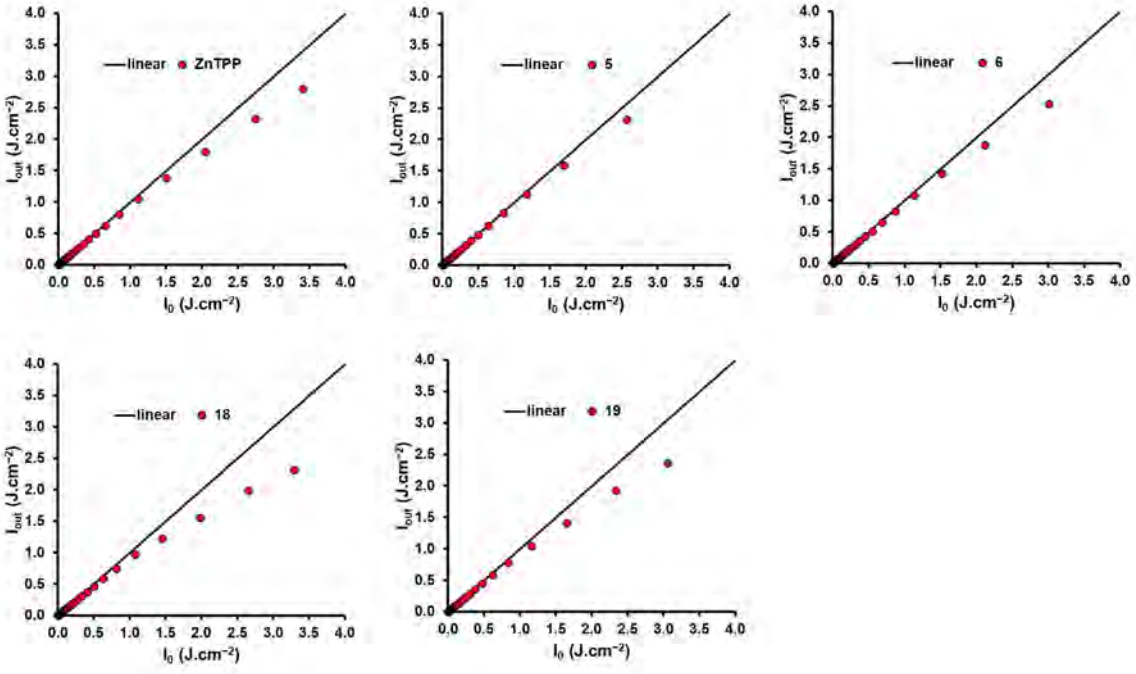

Figure 96. Output fluence (I_{out}) versus input fluence (I_0) curves for **ZnTPP**, **5**, **6**, **18** and **19** DMSO.

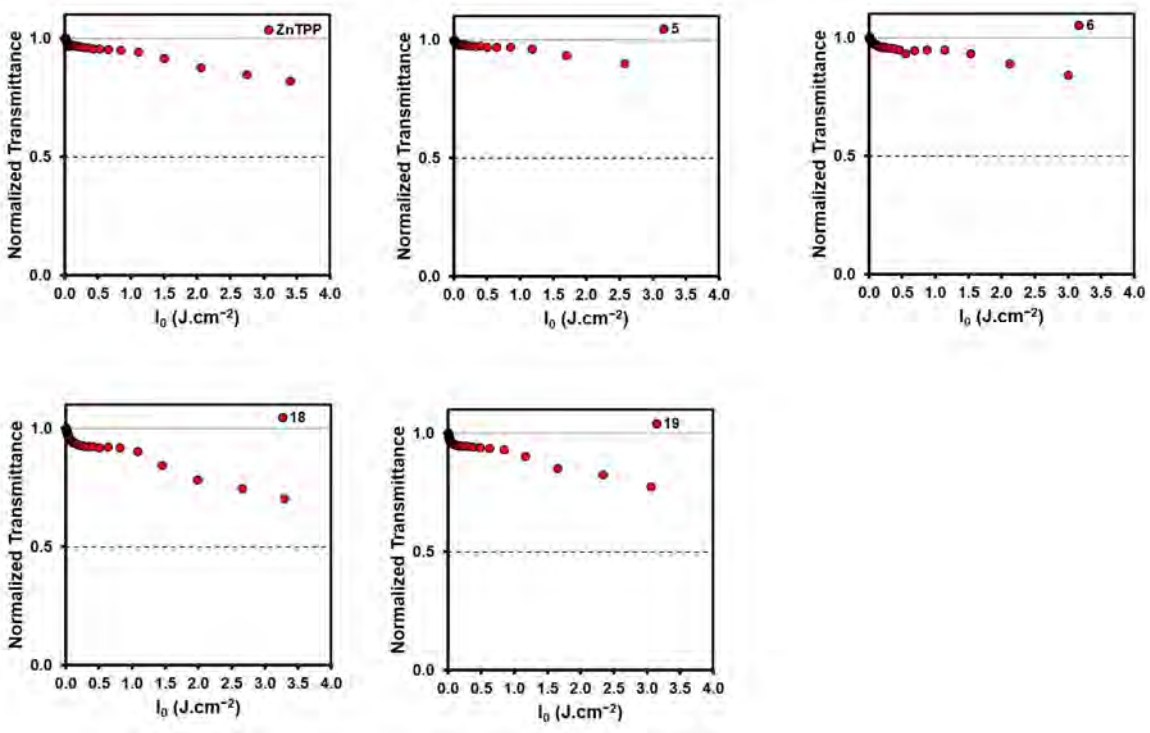

Figure 97. Transmittance *versus* input fluence (I_0) curves for **ZnTPP**, **5**, **6**, **18** and **19** DMSO. The I_{lim} values were extracted at the point where the curve crosses the dashed line, which represents the 50% transmittance.

Table 19. A summary of optical limiting properties of porphyrins obtained with 10 ns pulses at 532 nm in DMSO.

	α (cm^{-1})	**β_{eff} (cm.GW^{-1})**	**I_{lim} (J.cm^{-2})**	**Im[$\chi^{(3)}$] (esu)**	**γ (esu)**
ZnTPP	0.12	8.90	-	1.91×10^{-11}	7.38×10^{-30}
5	0.12	5.50	-	1.29×10^{-11}	3.69×10^{-30}
6	0.12	9.40	-	2.21×10^{-11}	7.80×10^{-30}
18	0.12	26.0	-	5.57×10^{-11}	9.30×10^{-30}
19	0.12	3.42	-	3.42×10^{-11}	4.26×10^{-30}

8.8. Concluding remarks

All the investigated aza-BODIPY dyes displayed strong NLA behaviour with Z-scan data sets that contained RSA profiles. In organic solutions with a fixed absorbance of 1.8 for the main spectral band in a 2 mm cuvette, aza-BODIPYs **1**, **2a**, **2**, **3**, **4a** and **4** lowered the transmitted intensity of the powerful laser beam to less than 50%. Although **1a** and **3a** did not reduce the laser beam to less than 50% at the concentrations studied, they still possess significant OL properties. This study demonstrates that effective strategies to generally improve the OL characteristics of aza-BODIPY dyes at 532 nm include substituting iodine atoms at the 2,6-positions. Higher γ values were obtained for iodinated dyes **1**, **2**, **3** and **4** than for the analogous non-iodinated dyes **1a**, **2a**, **3a** and **4a**. This is not the trend that has typically been observed with BODIPY dyes [97]. The particularly high γ value of **1** merits further in-depth nanosecond and femtosecond laser flash photolysis studies so that the ESA properties of the iodinated and non-iodinated dyes can be analysed.

A comparative study was carried out involving four non-iodinated aza-BODIPY dyes, **1a**, **2a**, **3a** and **4a** and seven non-iodinated aza-BODIPY dyes, **20**-**26**, that were reported previously in a PhD thesis by Gugu Kubheka at Rhodes University [156]. It was concluded on this basis that the observed optical limiting on the nanosecond timescale is related primarily to ESA from the S_1 and T_1 states, since no clear trends could be identified through comparison with ESP maps and calculated dipole moments. The results of the study suggest that an emphasis should be placed on minimising the linear absorption coefficient, α, at 532 nm by red shifting the main aza-

BODIPY spectral band as far as possible into the NIR region. The ultimate goal would be to embed the dyes in polymer thin films for practical applications [97, 143].

Although the porphyrins prepared in this study exhibited significant RSA responses, they do not appear to be efficient materials for further use in optical limiting at 532 nm on the nanosecond timescale relative to the aza-BODIPYs.

Chapter 9: Molecular Modelling

9.1. Molecular Modelling

In recent times, time-dependent density function theory has become the most suitable approach to performing theoretical calculations for various molecules. This approach can accurately predict numerous properties of various molecules, including aza-BODIPY dyes. This chapter explores the optical properties of aza-BODIPY dyes as predicted using molecular modelling, also referred to as theoretical calculations. The properties that were predicted for this work are the electronic structures and the spectroscopic trends of aza-BODIPY dyes. The structure-property relationships of aza-BODIPYs towards determining the suitability of aza-BODIPYs with different substituents for application in PDT, PACT and NLO are crucial. The emphasis of the calculations is on the effects of halogenation (specifically iodination) and the strategic introduction of EDGs on the properties of the dyes used for PDT, PACT and NLO studies. Where PDT is concerned, the goal was to red shift the main spectral bands deep into the phototherapeutic window where there is minimal interference from biological molecules. The red shift is achieved by introducing substituents that can narrow the HOMO−LUMO gap. **Figure 98** shows the structures of the aza-BODIPY dyes studied. The parent aza-BODIPY (**core**) and tetraphenyl-substituted aza-BODIPY (**4-Ph**) structures were used as model complexes to determine the effects of substituents at the 1,7- and 3,5-positions of the dyes.

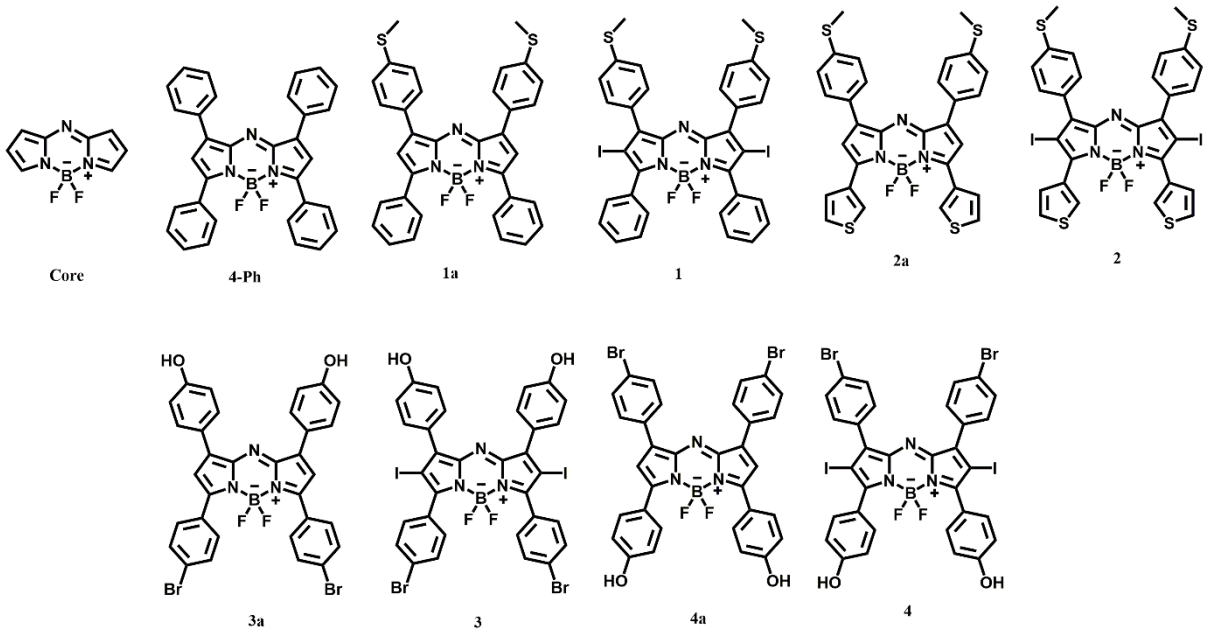

Figure 98. Structures of aza-BODIPY dyes used in the TD-DFT calculations.

9.2. The HOMO and LUMO of typical aza-BODIPYs

The electronic structure of the parent unsubstituted aza-BODIPYs is similar to that of BODIPY dyes. Principally, the HOMO of a typical aza-BODIPY, as shown in **Figure 99**, resembles half of Gouterman's a_{1u} orbital of a simple porphyrin, where the electron density of a porphyrin is mostly located at the pyrrolic α- and β-carbons [175] (**Figure 99**). The LUMO of a typical aza-BODIPY resembles Gouterman's a_{2u} orbital, which has its electron density concentrated at the pyrrolic nitrogen atom [175, 176]. The LUMO of aza-BODIPYs is significantly stabilised relative to that of BODIPYs because there is a highly electronegative nitrogen in place of a *meso*-carbon, and there is a large MO coefficient at this position. Consequently, the HOMO−LUMO energy gap of aza-BODIPYs is significantly narrower than that of BODIPYs. This results in a large red shift of the main spectral bands of aza-BODIPYs. This is an important property for biological studies such as PDT, where deeper-lying malignant tissues are targeted.

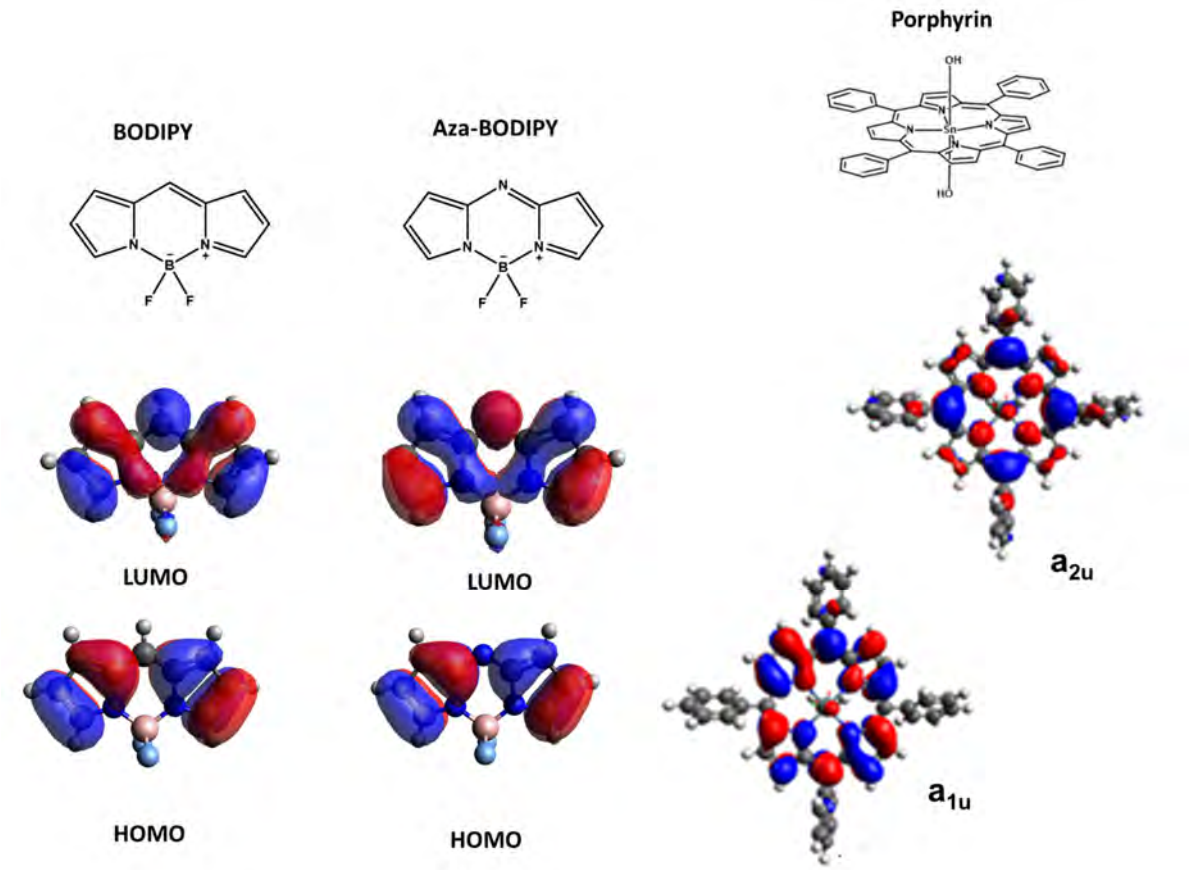

Figure 99. HOMOs and LUMOs of typical BODIPY and aza-BODIPY compared to Gouterman's a_{1u} and a_{2u} orbitals of a porphyrin.

9.3. Theoretical calculations

The Gaussian 09 software package was used to carry out the calculations [99]. Firstly, the geometry of the molecules was optimised using the Beck, three-parameter, Lee-Yang-Parr (B3LYP) functional and the default Gaussian09 SDD basis sets. Secondly, the TD-DFT calculations were performed using the Coulomb-attenuated B3LYP (CAM-B3LYP) functional and SDD basis sets to predict the UV-visible absorption properties. The reason for using the SDD basis sets is that they can be used to predict trends for molecules with heavy iodine atoms, unlike 6-31G(d) basis sets. The CAM-B3LYP functional was used because it provides a long-range adjustment by

integrating increasing fractions of semi-empirical Hartree-Fock (HF) exchange parameters.

9.4. Effects of halogenation and substitution at the 1,7- and 3,5-positions on aza-BODIPY dyes in Series 1 and 2

9.4.1. Effect of halogenation at 2,6-positions

This section describes the effect of introducing iodine atoms at the 2,6-positions of aza-BODIPYs **1** and **2**. The TD-DFT calculations demonstrate that the main spectral bands of **4-Ph**, **1a**, **1**, **2a** and **2** are in the NIR (red shifted), **Figure 100**. This is due to the $S_0 \rightarrow S_1$ transition arising from the one-electron transition from the HOMO to the LUMO [177-180]. These transitions are strongly permitted ($f > 0.75$), **Table 20.** In the visible region of the spectrum, smaller and weaker transitions are observed, **Figure 100**. These weaker bands are due to the $S_0 \rightarrow S_2$ (oscillator strengths predicted ($f < 0.15$)). Similar weaker bands were observed experimentally.

In theoretical calculations, the 2,6-positions of the aza-BODIPYs are known to have lower partial positive charges [43]. This makes them vulnerable to electrophilic substitution with iodine atoms due to their electronegativity. The presence of these halogen atoms at the 2,6-positions results in a net inductive effect [181]. After the halogenation of **1a** to form **1**, a slight blue shift in the main spectral band is predicted (**Figure 100**). The HOMOs of aza-BODIPYs typically possess larger MO coefficients than the LUMOs, **Figure 101**. As such, the presence of iodine atoms results in a relative stabilisation of the HOMO, **Figure 102**. The blue shift hence results from the

widening of the HOMO−LUMO energy gap, as observed in the MO energy plot, **Figure 102**. Similar trends are observed after the iodination of **2a** to form **2**, **Figures 100-102**.

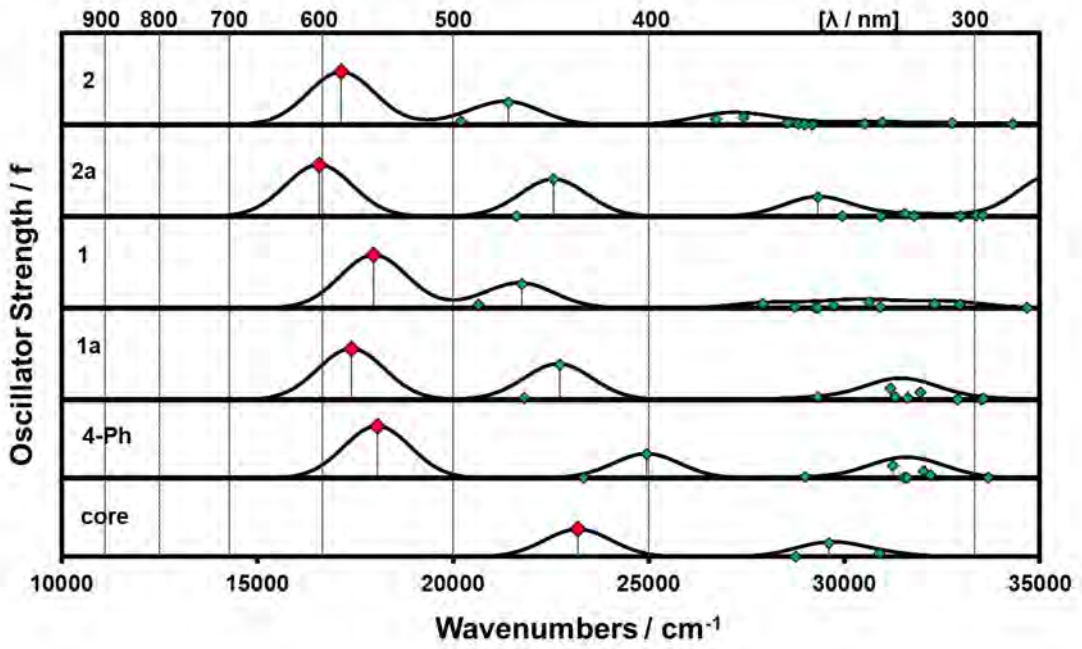

Figure 100. Calculated TD-DFT spectra of the B3LYP/SDD optimised geometries of aza-BODIPYs (**core**, **4-Ph**, **1a** and **2a**) and diiodinated derivatives (**1** and **2**) at the CAM-B3LYP/SDD level of theory. The main aza-BODIPY spectral bands are highlighted with red diamonds. Spectra were simulated by using the Chemcraft program with bandwidths fixed at 2000 cm^{-1}.

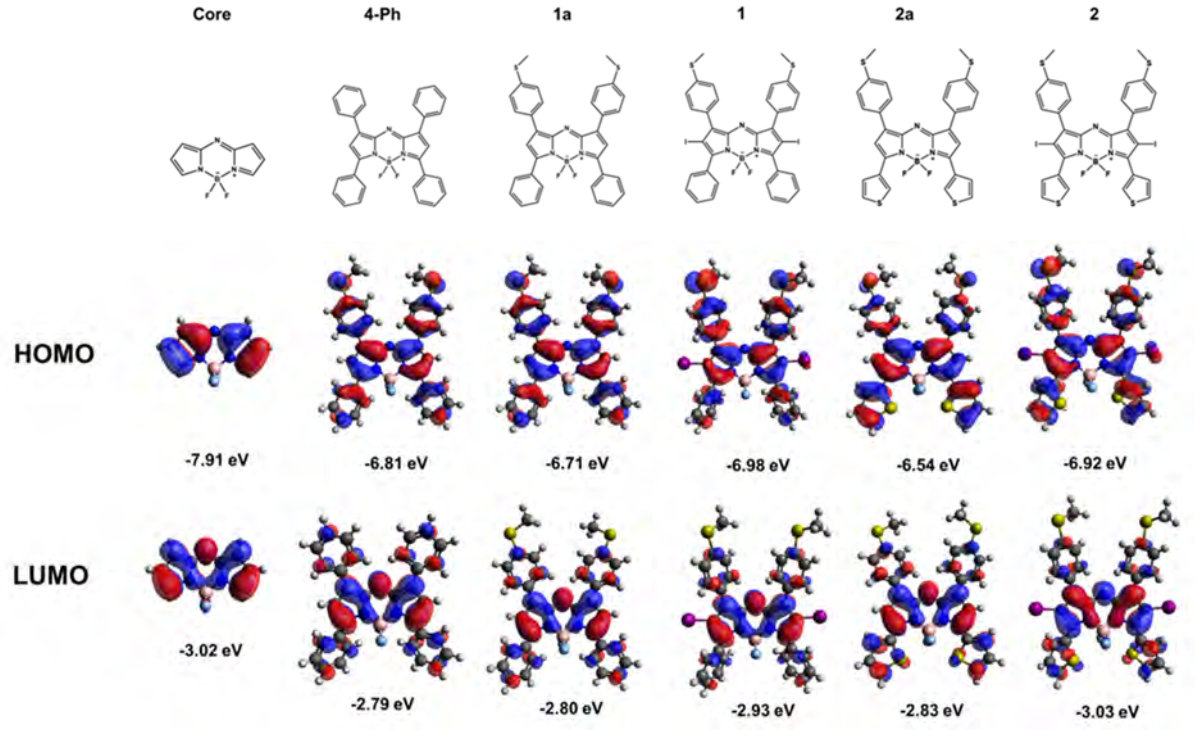

Figure 101. The angular nodal patterns (isosurface = 0.02 a.u.) and energies of the frontier MOs of aza-BODIPYs from TD-DFT calculations performed at the CAM-B3LYP/SDD level of theory.

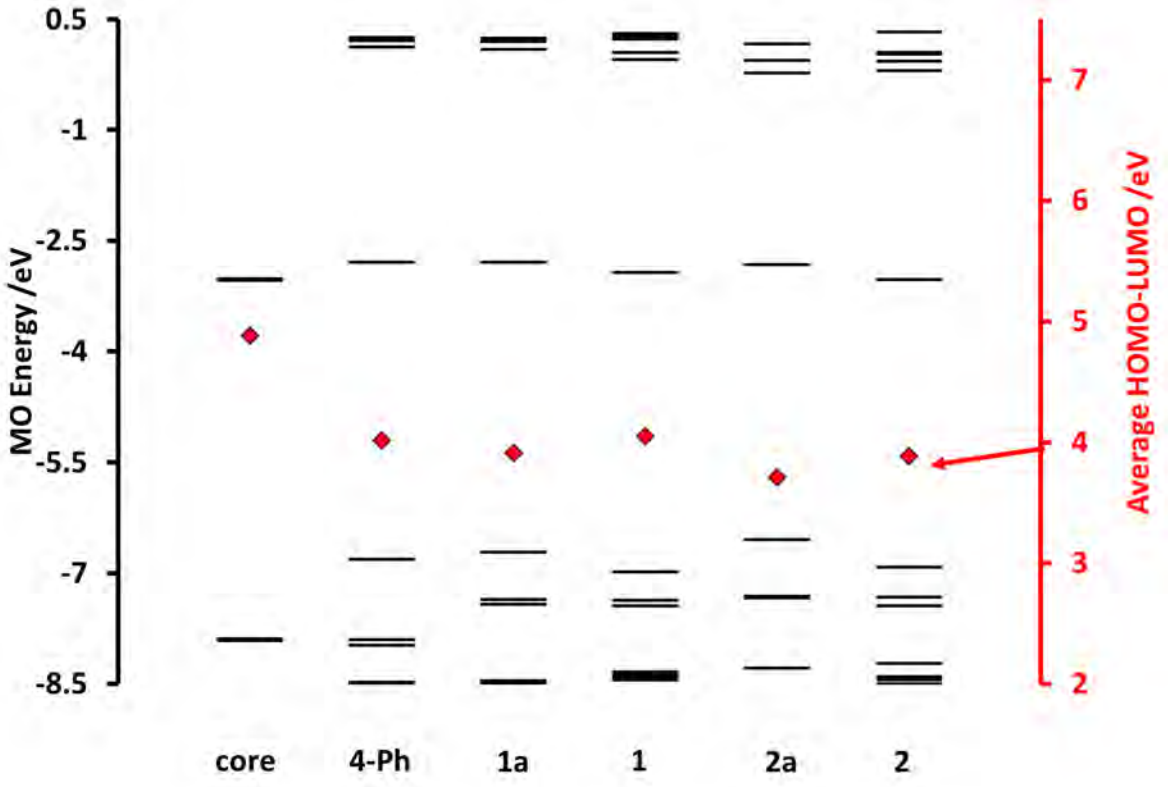

Figure 102. Frontier MO energies of the **core** and **4-Ph** model complexes, **1a** and **2a** and the diiodinated derivatives **1** and **2**, respectively. The HOMO–LUMO energy gaps are plotted against a secondary axis and are highlighted by red diamonds. Results obtained through TD-DFT calculations of aza-BODIPYs at the CAM-B3LYP/SDD level of theory.

9.4.2. Substitution at the 1,7- and 3,5-positions

This section compares the impact of substituting phenyl groups and thien-3-yl groups at the 1,7-positions and 4-methylthio groups at the 3,5-positions of aza-BODIPYs to determine how the optical characteristics of the dyes are affected. The aza-BODIPY **core** is the least red shifted compared to the other compounds since it has no substituents at the 1,7- and 3,5-positions. These substituents are responsible for the red shift of the main spectral bands of the aza-BODIPYs towards the NIR region.

Looking at **4-Ph** and **1a**, the introduction of 4-methylthio substituents resulted in a destabilisation of the LUMO. This resulted in the significant narrowing of the HOMO−LUMO energy gap (**Figure 102**), thus the red shift of the main spectral band of **1a** relative to that of **4-Ph**. Looking at **4-Ph** and **2a**, the presence of 4-methylthio substituents at the 1,7-positions and 3-thienyl substituents at 3,5-positions of **2a** resulted in a pronounced red shift of the main spectral band (**Figure 100**). This is due to the effects that the substituents had on the LUMO and HOMO of **2a.** The HOMO was slightly stabilised, while the LUMO was significantly destabilised. This resulted in a large decrease in the HOMO−LUMO energy gap (**Figure 102**). Thus, the red shift of the main spectral band of **2a** relative to that of **4-Ph**. According to the literature, the HOMO−LUMO energy gap can be narrowed by adding electron-rich substituents such as thienyl groups, producing NIR region aza-BODIPY derivatives [113, 114].

The absorption and emission wavelengths can be further pushed toward the near-infrared region of the electromagnetic spectrum by using push-pull systems. In this study, two push systems (electron-donating moieties) at the 1,7- and 3,5-positions were investigated. The HOMO can be destabilised by adding electron-donating groups to the *para*-positions of the aryl rings of the aza-BODIPYs. On the other hand, the LUMO-energy level can be stabilised by adding electron-donating groups to the *para*-positions of the aryl rings at the 3,5-positions of the aza-BODIPY. This can result in a decrease in the HOMO−LUMO energy gap and a red shift of the primary absorption band.

Moving from **1** to **2**, a pronounced red shift was observed due to the strongly electron-donating thienyl group compared to the phenyl group at the 3,5-positions in **1**, **Figure 100**. It can be concluded that adding electron-donating groups at the 3,5-positions is

an effective strategy to shift the main spectral bands of aza-BODIPYs towards the NIR. Similar trends were observed experimentally.

9.5. Effects of halogenation, substitution at the 1,7- and 3,5-positions and conjugation to folic acid of aza-BODIPY dyes in Series 3 and 4

9.5.1. Effect of halogenation at 2,6-positions

Figure 103 shows that a slight blue shift is predicted for the main spectral band following the halogenation of **3a** to **3**. Generally, the HOMOs of aza-BODIPYs have greater MO coefficients than the LUMOs at the 2,6-positions (**Figure 104**). Accordingly, there is a relative stabilisation of the HOMO due to the presence of iodine atoms at the 2,6-positions, **Figure 105**. As can be observed in the MO energy diagram, **Figure 105**, the blue shift was caused by the resulting increase in the HOMO−LUMO

energy gap. Following the iodination of **4a** to **4**, similar trends are predicted (**Figure 103-105**).

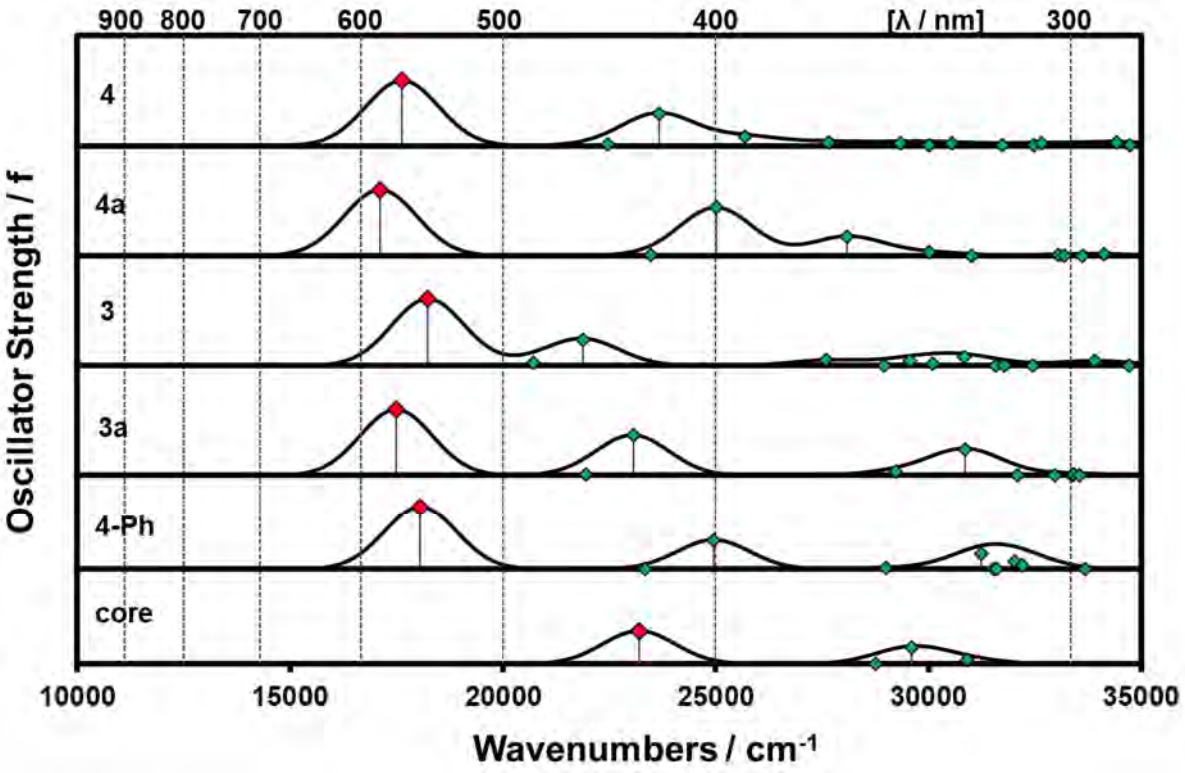

Figure 103. Calculated TD-DFT spectra of the B3LYP/SDD optimised geometries of aza-BODIPYs (**core**, **4-Ph**, **3a** and **4a**) and diiodinated derivatives (**3** and **4**) at the CAM-B3LYP/SDD level of theory. The main aza-BODIPY spectral bands are highlighted with red diamonds. Spectra were simulated by using the Chemcraft program with bandwidths fixed at 2000 cm^{-1}.

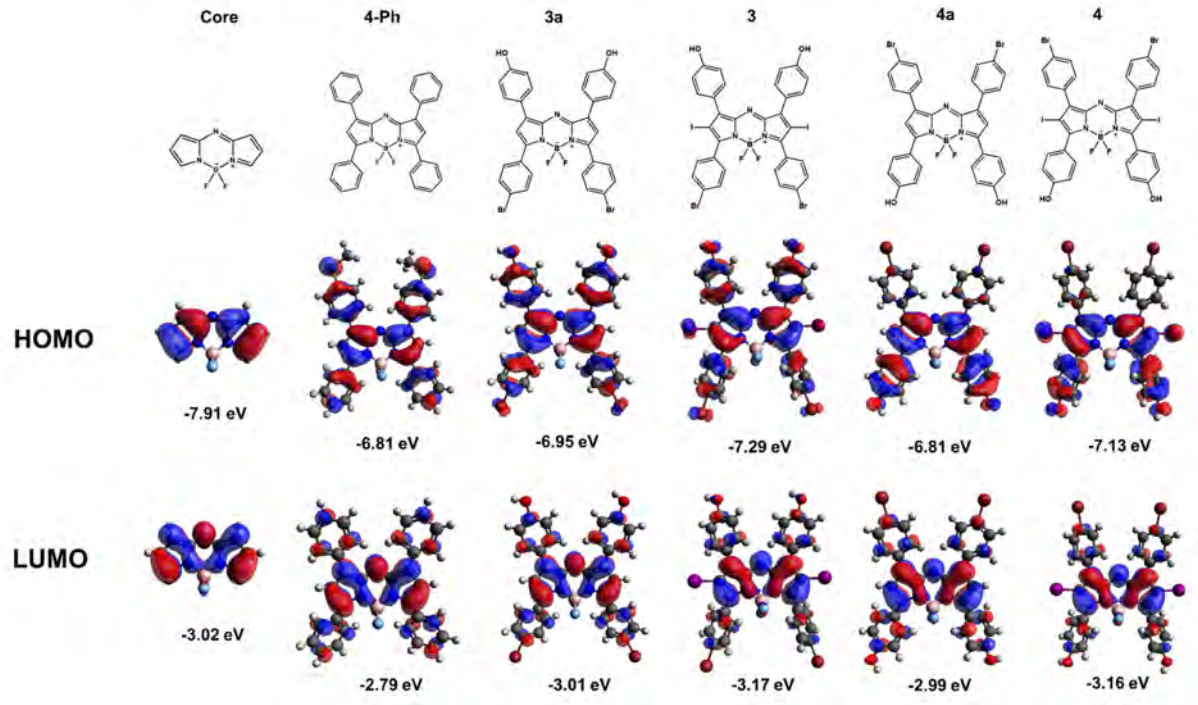

Figure 104. The angular nodal patterns (isosurface = 0.02 a.u.) and energies of the frontier MOs of aza-BODIPYs from TD-DFT calculations performed at the CAM-B3LYP/SDD level of theory.

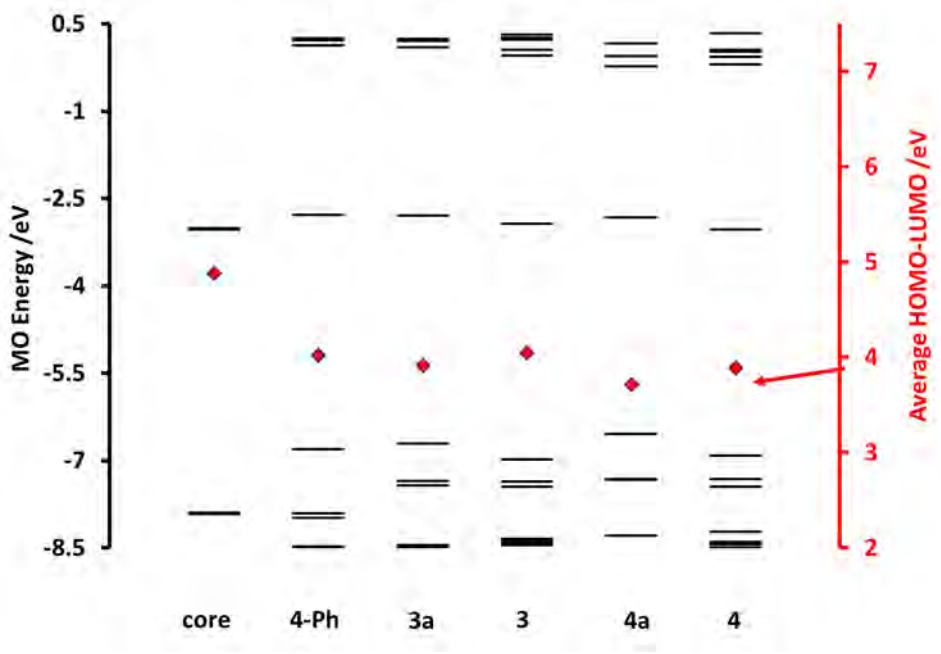

Figure 105. Frontier MO energies of the **core** and **4-Ph** model complexes, **3a** and **3a** and the diiodinated derivatives **3** and **4**, respectively. The HOMO–LUMO energy gaps are plotted against a secondary axis and are highlighted by red diamonds. Results obtained through TD-DFT calculations of aza-BODIPYs at the CAM-B3LYP/SDD level of theory.

9.5.2. Substitution at the 1,7- and 3,5-positions

The TD-DFT calculations show that the HOMO of the aza-BODIPYs possesses larger MO coefficients than the LUMO (**Figure 104**). Comparing the substituents added to the 1,7- and 3,5-positions of **3a** and **4a**, we observed that **4a** was more red-shifted than **3a**, **Figure 103**. This is due to the presence of electron-donating hydroxyl groups at the 3,5-positions of **4a** compared to the bromine atoms of **3a**. The effect of the EDGs is a slight destabilisation of the HOMO and a larger stabilisation of the LUMO, **Figure 105**. As a result, the main spectral band is significantly red-shifted in **Figure 103**. Similar trends were observed experimentally (**Table 2**).

9.5.3. Folic acid conjugation

Folic acid was introduced to the dyes' structures to form a targeted drug molecule for cancer treatment, so a series of calculations were carried out to investigate the effect of introducing folic acid moieties (**Figures 106-108**). This was achieved through conjugation *via* ester-bonds. This resulted in a narrowing of the HOMO−LUMO energy gap in the context of **3-FA** and, thus, a predicted red shift in the main spectral band, **Figure 106**. A slight red shift is predicted for the main spectral band of **4-FA** due to a slight increase in the HOMO−LUMO energy gap. Contrasting trends were observed experimentally, where the main spectral bands were broad and significantly blue-shifted, **Table 20**. This provides further evidence that significant aggregation occurs when **3-FA** and **4-FA** are formed.

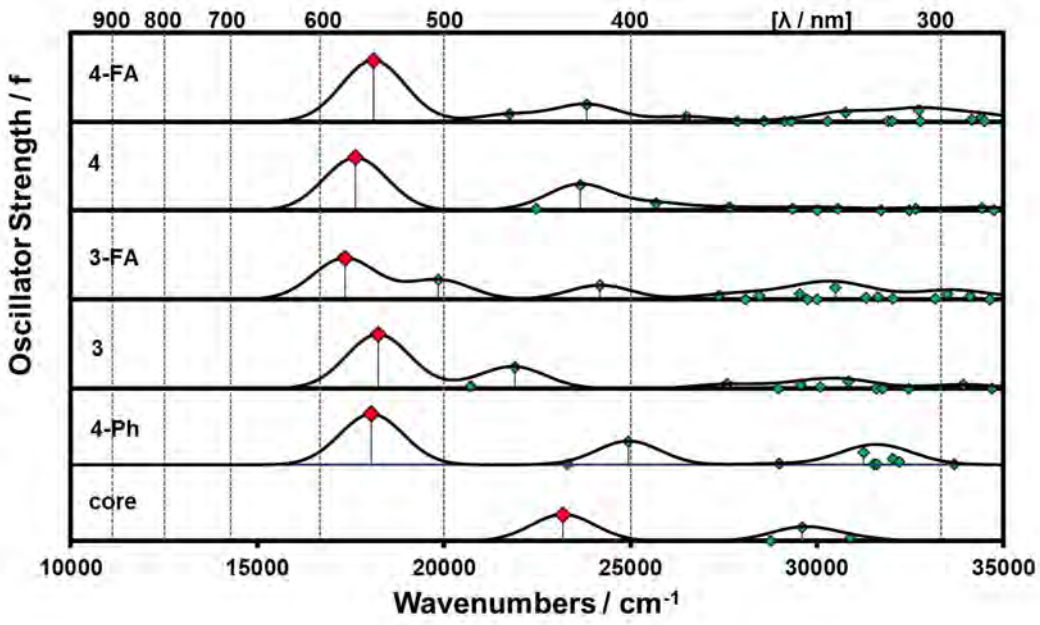

Figure 106. Calculated TD-DFT spectra of the B3LYP/SDD optimised geometries of the **core** and **4-Ph** model complexes, **3**, **4** and folic acid conjugates (**3-FA** and **4-FA**)

at the CAM-B3LYP/SDD level of theory. The main aza-BODIPY spectral bands are highlighted with red diamonds. Spectra were simulated by using the Chemcraft program with bandwidths fixed at 2000 cm^{-1}.

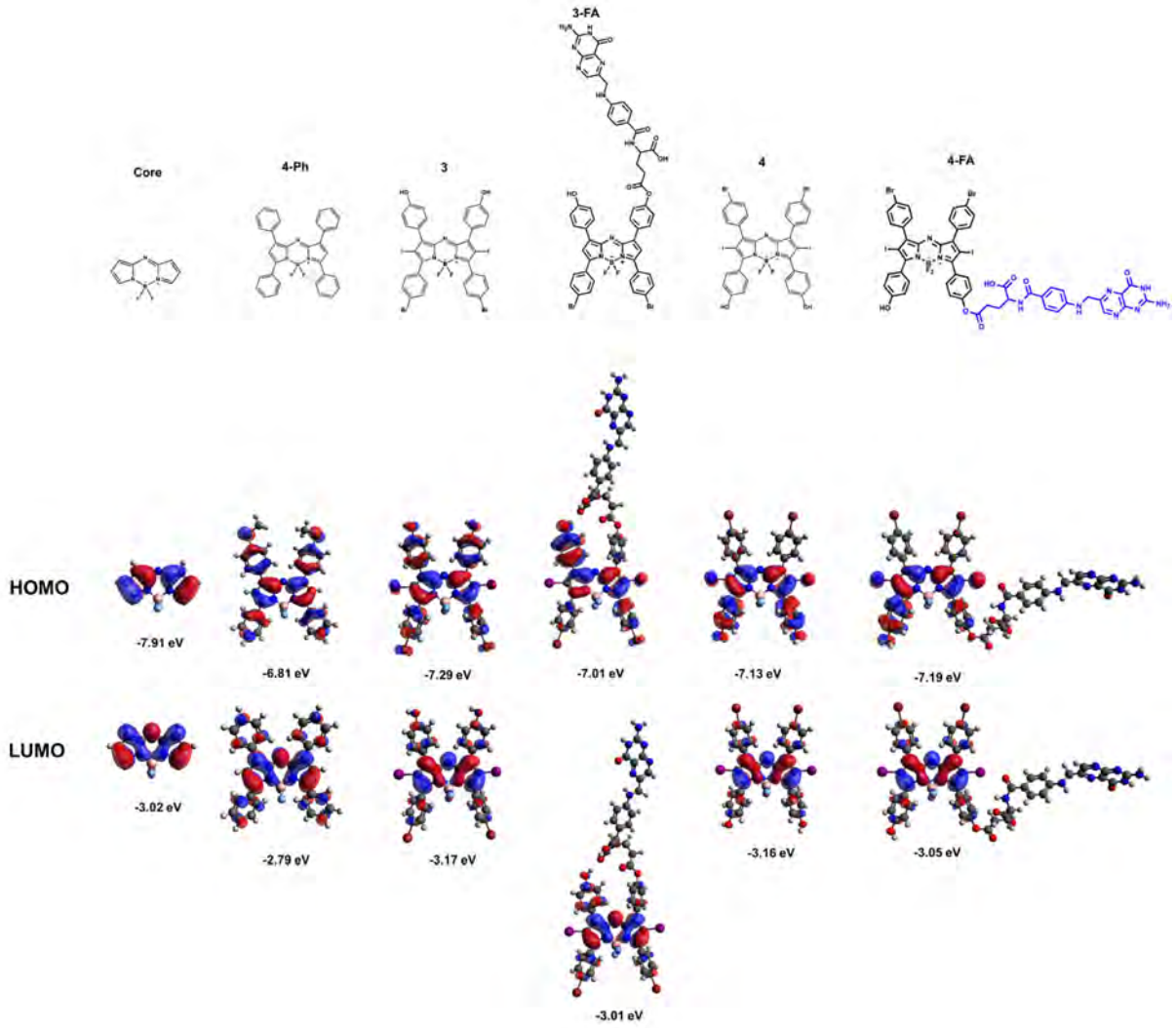

Figure 107. The angular nodal patterns (isosurface = 0.02 a.u.) and energies of the frontier MOs of aza-BODIPYs from TD-DFT calculations performed at the CAM-B3LYP/SDD level of theory.

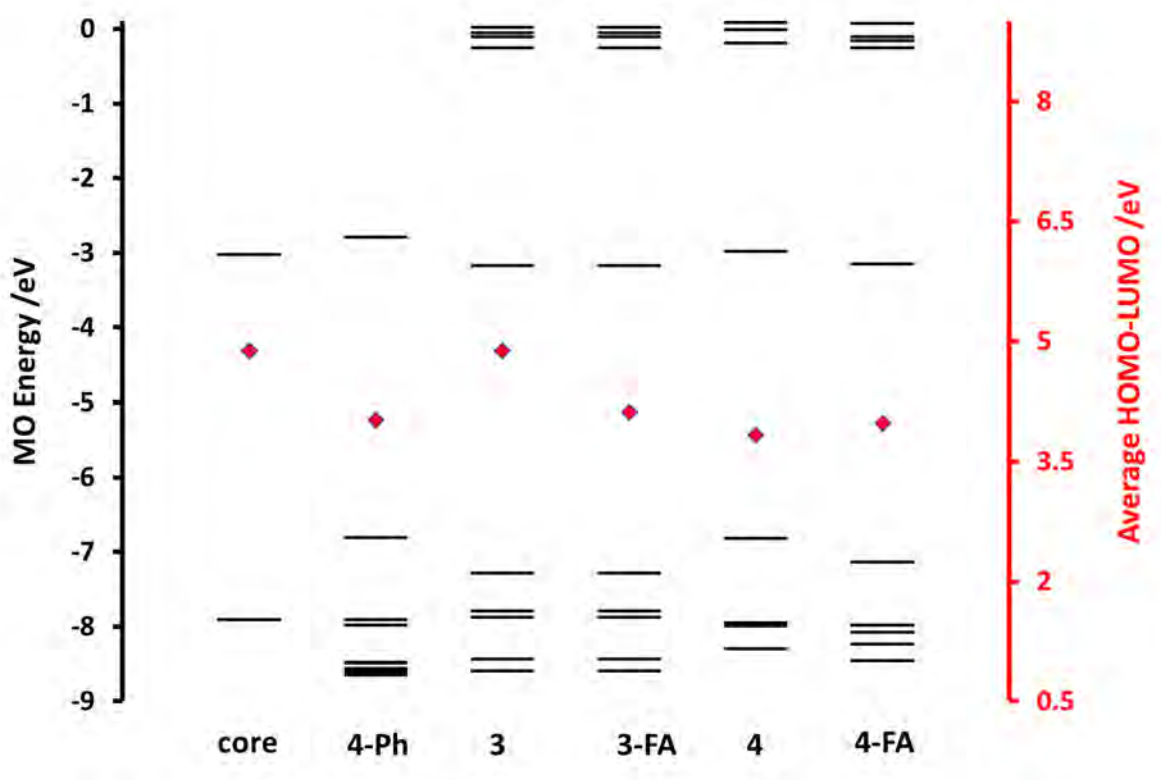

Figure 108. Frontier MO energies of the aza-BODIPYs, diiodinated aza-BODIPYs and folic acid conjugates of diiodinated aza-BODIPYs. The HOMO–LUMO energy gaps are plotted against a secondary axis and are highlighted with red diamonds.

Table 20. Experimental (λ_{exp}) and excitation wavelengths (λ_{calc}), calculated band energies (eV) and wavefunctions of the aza-BODIPYs.

	#[a]	E (eV)[b]	λ_{exp}[c]	λ_{calc}[d]	*f* [e]	Wavefunction[f]
Core	1	3.57	-	431	0.42	H→L (98%);…
4-Ph	1	2.24	-	554	0.82	H→L (99%);…
1a	1	2.16	681	574	0.78	H→L (98%);…
1	1	2.23	663	556	0.81	H→L (96%);…
2a	1	2.05	743	603	0.79	H→L (98%);…
2	1	2.13	730	583	0.81	H→L (97%);…

3a	1	2.17	685	572	0.84	H→L (99%);…
3	1	2.26	669	549	0.85	H→L (98%);…
3-FA	1	2.15	630	577	0.65	H→L (97%);…
4a	1	2.12	722	584	0.84	H→L (98%);…
4	1	2.19	720	567	0.83	H→L (98%);…
4-FA	1	2.25	643	552	0.96	H→L (97%);…

[a] – Excited state numbers in ascending energy from the TD-DFT calculations. [b] – Calculated band energies (eV). [c] – Experimental absorption band maxima in nm (solvent = DMSO). [d] – Calculated wavelengths in nm. [e] – Calculated band energy (10^3 cm^{-1}). [f] – Wavefunctions consisting of the one-electron transitions that generate the excited states based on the predicted eigenvectors. H and L refer to the HOMO and LUMO, respectively.

9.6. Concluding remarks

TD-DFT calculations were carried out to identify the structure-property relationships related to key trends in the spectroscopic properties of the different series of aza-BODIPY dyes that were prepared in this study. The iodination of the aza-BODIPY dyes and the addition of electron-donating groups at the 3,5-positions resulted in a large shift of the main absorption towards the NIR region. Precisely, the addition of 4-hydroxyphenyl groups at the 3,5-positions of **4a** and **4** resulted in a more pronounced red shift of the main spectral bands compared to the addition of 4-bromophenyl groups at the 3,5-positions of **3a** and **3**. Similar results were obtained for **1a**, **1**, **2a** and **2**, where the addition of thien-3-yl groups at the 3,5-positions of **2a** and **2** resulted in a more pronounced red shift of the main spectral bands compared to **1a** and **1** with phenyl groups at the 3,5-positions. The 3,5-positions of the HOMO of the aza-BODIPY π-system have larger MO coefficients than the 1,7-positions. As a result, introducing a more strongly electron-donating aryl group at these positions results in a relative destabilisation of the HOMO and a narrowing of the HOMO−LUMO gap.

The predicted properties of the aza-BODIPY dyes were compared to the corresponding experimental values, and a better understanding of their behaviour was established. Molecular modelling aided in visualising the structures and understanding the effects of introducing the different functional groups on the observed spectral trends. With the use of molecular modelling, the rational design of novel aza-BODIPY dyes for NLO, PDT and PACT can be facilitated.

Chapter 10: Conclusion and future prospects

10.1. General conclusions

Aza-BODIPY dyes are suitable for a wide range of applications since they are relatively easy to synthesise and provide extensive scope for further functionalisation. Using sequential reaction processes, including Aldol condensation, Michael addition, cyclisation of azadipyrromethenes, complexation, and electrophilic substitution, novel aza-BODIPY dyes **1a**, **1**, **2a**, **2**, **3a**, **3**, **4a**, and **4** were prepared as photosensitiser dyes for PDT research. Singlet oxygen-generating dyes with red-shifted spectral bands deep within the phototherapeutic window were successfully prepared for *in vitro* photodynamic activity studies. When the dyes were exposed to UV-visible region light, it was discovered that they were photostable. The encapsulation of the hydrophobic aza-BODIPY dyes **1** and **2** with Pluronic® F-127/L-121 was not successful, however, the focus was shifted instead towards the conjugation of aza-BODIPYs to gold nanoparticles. This was found to produce conjugates that are water-soluble. All the aza-BODIPY dyes' gold nanoparticle conjugates exhibited a significant reduction of MCF-7 breast cancer cell proliferation when their PDT activities were examined. As such, further in-depth research on aza-BODIPY dyes and their gold nanoparticle conjugates is merited to explore their utility for PDT.

Targeted drug delivery was also explored using aza-BODIPY-folic acid conjugates. The dyes conjugated to FA were **3** and **4**. The conjugated dyes were found to be significantly more effective in inhibiting the growth of MCF-7 cancer cells *in vitro.* Further studies on the use of folic acid as a targeting group for aza-BODIPYs in PDT are hence also merited.

Although porphyrins tend to π-π stack in solution, inserting folic acid as axial ligands in the porphyrins under study served as both a targeting ligand and bulky groups to

inhibit aggregation. The porphyrins were quartenised to create water-soluble conjugates. Enhanced aqueous solubility did not, however, enhance the ability to kill cancer cells. Better outcomes were obtained with folic acid-conjugated porphyrins. There was evidence of photocytotoxicity when the porphyrins' photodynamic activity was assessed on MCF-7 breast cancer cells. There is a need for more axial conjugation of other porphyrins to folic acid in future research. Based on the results obtained in this research, aza-BODIPYs exhibit superior inhibition of MCF-7 cancer cells and photoinactivation of *S. aureus* compared to the porphyrins studied. This can be attributed to the aza-BODIPYs having their main absorption bands absorbing deep in the biological window (NIR), where there is little to no interference by other biological molecules. On the other hand, the Q-bands of the porphyrins absorb very weakly in the therapeutic window and would experience interference from biological molecules, if a light source of shorter wavelength were to be used.

In the context of PACT, the four aza-BODIPY dyes were studied: **1**, **2**, **3** and **4**. Although the dyes had some ability to eradicate *S. aureus* colonies, with the exception of **1**, they were not as efficient in this context as they were in PDT activity studies. This could be due to their lack of solubility. Further in-depth studies are necessary to identify how to rationally enhance the PACT activity of aza-BODIPY dyes. In the context of porphyrins **18a**, **18**, **19a** and **19**, the introduction of a triphenylphosphonium was found to significantly enhance the PACT activity. A comparison with previous studies by Mack and coworkers [136] demonstrated that introducing lipophilic substituents can provide better Log_{10} reduction values against *S. aureus*.

Optical limiting studies on **1a**, **1**, **2a**, **2**, **3a**, **3**, **4a** and **4** demonstrated that iodination at the 2,6-positions enhances the RSA responses. A comparative study of the OL parameters for **1**, **2**, **3** and **4** with seven non-iodinated aza-BODIPY dyes reported

previously in the PhD thesis of Gugu Kubheka at Rhodes University [154] demonstrated that enhancing the dipole moment of the dye does not generally enhance the β_{eff} and γ values. Since the OL response on the nanosecond timescale depends on the cross-sections of the S_1 and/or T_1 in the context of ESA and from the S_0 state in the context of linear 1PA, the most important factor is minimising the linear absorption coefficient, α, by shifting the main aza-BODIPY spectral band as far to the red as possible. Molecular modelling demonstrates that this can be most readily achieved by introducing strongly electron-donating aryl groups at the 3,5-positions, since the mesomeric interactions result in a relative destabilisation of the HOMO, which has large MO coefficients at these positions.

10.2. Future prospects

In the case of PDT for cancer, since the use of folic acid as a targeting ligand has been proven to enhance the activity, the conjugation of aza-BODIPY dyes to various other targeting ligands, such as biotin, can be explored. Again, cationic derivatives, which can be quaternised, can be used *in vitro* to determine their suitability in killing cancer cells. Since the non-covalent conjugation of aza-BODIPY dyes to gold nanoparticles was also proven to work, the functionalisation of gold nanoparticles with stabilising agents and covalent conjugation to aza-BODIPYs can be explored. In the case of PACT, since most non-charged aza-BODIPYs did not perform well, quaternising agents such as ethyl iodide can be used to form cationic and water-soluble aza-BODIPYs and their effectiveness in the photoinactivation of both Gram-(+) strains such as *S. aureus* and Gram-(−) strains such as *E. coli* can be investigated in depth.

The folic acid-conjugated porphyrins have proved to have potential as PDT agents. The use of biotin and other targeting agents as axial ligands can be explored in future.

Since the tetra-quaternised porphyrins were found not to be efficient PDT agents due to excessive hydrophilicity, mono-substituted porphyrins with a single pyridyl substituent are worth investigating in this context.

The use of porphyrins **18a**, **18**, **19a** and **19** in PACT studies did not yield data that were as favourable as hoped. This work can be extended to include quaternised derivatives since the lack of solubility was a challenge. The quaternised derivatives can be used in the in-depth photoinactivation of *S. aureus* and other bacteria, such as Gram-(−) *E. coli* strains.

References

[1] Boisseau P, Loubaton B. Nanomedicine, nanotechnology in medicine. *Comptes Rendus Physique*, **12** (2011) 620−636.

[2] Lipson RL, Baldes, EJ. The photodynamic properties of a particular hematoporphyrin derivative. *Archives of Dermatology*, **82** (1960) 508−516.

[3] Dougherty TJ, Gomer CJ, Henderson BW, Jori G, Kessel D, Korbelik M, Moan J, Peng Q. Photodynamic therapy. *Journal of the National Cancer Institute*, **90** (1998) 889−905.

[4] Diamond I, Granelli SG, McDonagh AF, Nielsen S, Wilson CB, Jaenicke R. Photodynamic therapy of malignant tumours. *Lancet*, **2** (1972) 1175−1177.

[5] Ackroyd R, Kelty C, Brown N, Reed M. The history of photodetection and photodynamic therapy. *Photochemical and Photobiological Sciences*, **74** (2001) 656−669.

[6] Dolmans, DE, Fukumura D, Jain RK. Photodynamic therapy for cancer. *Nature Reviews Cancer*, **3** (2003) 380−387.

[7] Moan J, Peng Q. An outline of the hundred-year history of PDT. *Anticancer Research*, **23** (2003) 3591−3600.

[8] Yamamoto V, Suffredini G, Nikzad S, Hoenk ME, Boer MS, Teo C, Heiss JD, Kateb B. From Nanotechnology to Nanoneuroscience/Nanoneurosurgery and Nanobioelectronics. In *The Textbook of Nanoneuroscience and Nanoneurosurgery*, Springer, New York, 2013, pp 1−28.

[9] Kelly JF, Snell ME, Berenbaum MC. Photodynamic destruction of human bladder carcinoma. *British Journal of Cancer*, **31** (1975) 237−244.

[10] Dougherty TJ, Grindey GB, Fiel R, Weishaupt KR, Boyle DG. Photoradiation therapy. II. Cure of animal tumors with hematoporphyrin and light. *Journal of the National Cancer Institute*, **55** (1975) 115−121.

[11] Huang Z. A review of progress in clinical photodynamic therapy. *Technology in Cancer Research & Treatment*, **4** (2005) 283−293.

[12] Lipson RL, Baldes EJ, Olsen AM. The use of hematoporphyrin in tumor detection. *Journal of the National Cancer Institute*, **26** (1961) 1−11.

[13] Agostinis P, Berg K, Cengel KA, Foster TH, Girotti AW, Gollnick SO, Hahn SM, Hamblin MR, Juzeniene A, Kessel D, Korbelik M, Moan J, Mroz P, Nowis D, Piette J, Wilson BC, Golab J. Photodynamic therapy of cancer: an update. *A Cancer Journal for Clinicians*, **61** (2011) 250−281.

[14] Hamblin MR. Photodynamic therapy for cancer: What's past in prologue. *Photochemistry and Photobiology,* **96** (2020) 506−516.

[15] Dougherty TJ. An update on photodynamic therapy applications. *Journal of Clinical Laser Medicine and Surgery*, **20** (2002) 3−7.

[16] Lipson RL, Baldes EJ, Olsen AM. Hematoporphyrin derivative: A new aid for endoscopic detection of malignant disease. *The Journal of Thoracic and Cardiovascular Surgery*, **42** (1961) 623−629.

[17] Gregorie HB, Horger EO, Ward JL, Green JF, Richards T, Robertson Jr. HC, Stevenson TB. Hematoporphyrin-derivative fluorescence in malignant neoplasms. *Annals of Surgery*, **167** (1968) 820−828.

[18] Gomer CJ, Dougherty TJ. Determination of [3H]- and [14C] hematoporphyrin derivative distribution in malignant and normal tissue. *Cancer Research*, **39** (1979) 146−151.

[19] Wieman TJ, Mang TS, Fingar VH, Hill TG, Reed MW, Corey TS, Nguyen VQ, Render ER. Effect of photodynamic therapy on blood flow in normal and tumor vessels. *Surgery*, **104** (1998) 512−517.

[20] Agarwal ML, Clay ME, Harvey EJ, Evans HH, Antunez AR, Oleinick NL. Photodynamic therapy induces rapid cell death by apoptosis in L5178Y mouse lymphoma cells. *Cancer Research*, **51** (1991) 5993−5996.

[21] Xue LY, Chiu SM, Oleinick NL. Photochemical destruction of the Bcl-2 oncoprotein during photodynamic therapy with the phthalocyanine photosensitizer Pc 4. *Oncogene*, **20** (2001) 3420−3427.

[22] Kessel D, Oleinick NL. Cell death pathways associated with photodynamic therapy: An update. *Photochemical and Photobiological Sciences*, **74** (2018) 656−669.

[23] Kennedy JC, Pottier RH, Pross DC. Photodynamic therapy with endogenous protoporphyrin IX: Basic principles and present clinical experience. *Journal of Photochemistry and Photobiology B: Biology*, **6** (1990) 143–148.

[24] Cincotta L, Szeto, D, Lampros E, Hasan, T, Cincotta AH. Benzophenothiazine and benzoporphyrin derivative combination phototherapy effectively eradicates large murine sarcomas. *Photochemical and Photobiological Sciences*, **63** (1996) 229–237.

[25] Kleinovink JW, van Driel PB, Snoeks TJ, Prokopi N, Fransen MF, Cruz LJ, Mezzanotte L, Chan A, Löwik CW, Ossendorp F. Combination of photodynamic therapy and specific immunotherapy efficiently eradicates established tumors. *Clinical Cancer Research*, **22** (2016) 1459−1468.

[26] Tynga IM, Abrahamse H. Nano-mediated photodynamic therapy for cancer: Enhancement of cancer specificity and therapeutic effects. *Nanomaterials*, **8** (2018) 923.

[27] Malacarne MC, Banfia S, Caruso E. *In vitro* photodynamic treatment of cancer cells induced by aza-BODIPYs. *Photochemical and Photobiological Sciences*, **19** (2020) 790−799.

[28] Yu Z, Zhou J, Ji X, Lin G, Xu S, Dong X, Zhao W. Discovery of a Monoiodo Aza-BODIPY Near-Infrared Photosensitizer: *in vitro* and in vivo Evaluation for Photodynamic Therapy. *Journal of Medicinal Chemistry*, **63** (2020), 9950−9964.

[29] Li S, Lv M, Wang J, Zhang D, Xu Z, Jiang XD. Near-infrared absorbing aza-BODIPYs with 1,7-di-tert-butyl groups by low-barrier rotation for photothermal application. *Advanced Materials*, **3** (2022) 1254−1262.

[30] Shi Z, Han X, Hu W, Bai H, Peng B, Ji L, Fan Q, Li L, Huang W. Bioapplications of small molecule Aza-BODIPY: from rational structural design to *in vivo* investigations. *Chemical Society Reviews*, **49** (2020) 7533−7567.

[31] Gut A, Łapok L, Jamro´z D, Gorski A, Solarski J, Nowakowska M. Photophysics and redox properties of aza-BODIPY dyes with electron-withdrawing group. *New Journal of Chemistry*, **41** (2017) 12110−12122.

[32] Obłoza M, Łapok L, Pędziński T, Stadnicka KM, Nowakowska M. Synthesis, Photophysics and Redox Properties of Aza-BODIPY Dyes with Electron-Donating Groups. *ChemPhysChem*, **20** (2019) 2482−2497.

[33] Ng SY, Kamkaew A, Fu N, Kue CS, Chung LY, Kiew LV, Wittayakun J, Burgess K, Lee HB. Active targeted ligand-aza-BODIPY conjugate for near-infrared photodynamic therapy in melanoma. *International Journal of Pharmaceutics*, **579** (2020) 0378−5173.

[34] Sindelo A, Osifeko OL, Nyokong T. Synthesis, Photophysicochemical and photodynamic antimicrobial chemotherapy studies of indium pyridyl phthalocyanines: Charge versus bridging atom. *Inorganica Chimica Acta*, **476** (2018) 68−76.

[35] Mahmoudi H, Bahador A, Pourhajibagher M, Alikhani MY. Antimicrobial photodynamic therapy: an effective alternative approach to control bacterial infections. *Journal of Lasers in Medical Sciences*, **9** (2018) 154–160.

[36] Openda Y, Nyokong T. Combination of Photodynamic Antimicrobial Chemotherapy and Ciprofloxacin to Combat *S. aureus* and *E. coli* Resistant Biofilms. *Photodiagnosis and Photodynamic Therapy*, **42** (2022) 103142.

[37] Openda Y, Babu B, Nyokong T. Novel cationic-chalcone phthalocyanines for photodynamic therapy eradication of *S. aureus* and *E. coli* bacterial biofilms and MCF-7 breast cancer. *Photodiagnosis and Photodynamic Therapy*, **38** (2022) 102863.

[38] Mafukidze DM, Sindelo A, Nyokong T. Spectroscopic characterization and photodynamic antimicrobial chemotherapy of phthalocyanine-silver triangular nanoprism conjugates when supported on asymmetric polymer membranes.

Spectrochimica Acta A: Molecular and Biomolecular Spectroscopy, **5** (2019) 333−345.

[39] Sen P, Nyokong T. Promising photodynamic antimicrobial activity of polyimine substituted zinc phthalocyanine and its polycationic derivative when conjugated to nitrogen, sulfur, co-doped graphene quantum dots against *Staphylococcus aureus*. *Photodiagnosis and Photodynamic Therapy*, **34** (202) 1102300.

[40] Openda YI, Sen P, Managa M, Nyokong T. Acetophenone substituted phthalocyanines and their graphene quantum dots conjugates as photosensitizers for photodynamic antimicrobial chemotherapy against *Staphylococcus aureus*. *Photodiagnosis and Photodynamic Therapy*, **29** (2020) 101607.

[41] Rajesh S, Koshi E, Philip K, Mohan A. Antimicrobial photodynamic therapy: An overview. *Journal of Indian Society of Periodontology*, **4** (2011) 323−327.

[42] Moan J, Berg K. The photodegradation of porphyrins in cells can be used to estimate the lifetime of singlet oxygen. *Photochemistry and Photobiology*, **53** (1991) 549−553.

[43] Jiao L, Pang W, Zhou J, Wei Y, Mu X, Bai G, Hao E. Regioselective stepwise bromination of boron dipyrromethene (BODIPY) dyes. *The Journal of Organic Chemistry*, **76** (2011) 9988−9996.

[44] Zhu S, Zhang J, Vegesna G, Tiwari A, Luo F-T, Zeller M, Luck R, Li H, Green S, Liu H. Controlled Knoevenagel reactions of methyl groups of 1,3,5,7-tetramethyl BODIPY dyes for unique BODIPY dyes, *RSC Advances*, **2** (2012) 404−407.

[45] Shamova L, Zatsikha Y, Nemykin V. Synthetic pathways for the preparation of the BODIPY analogues: aza-BODIPYs, BOPHYs and some other pyrrole based acyclic chromophores. *Dalton Transactions*, **50** (2020) 1−43.

[46] Feng C, Li S, Fu L, Xiao X, Xu Z, Liao Q, Wu Y, Yao J, Fu H. Breaking Kasha's Rule as a Mechanism for Solution-Phase Room-Temperature Phosphorescence from High-Lying Triplet Excited State. *Journal of Physical and Chemistry Letters*, **11** (2020) 8246−8251.

[47] Redmond RW, Gamlin JN. A compilation of singlet oxygen yields from biologically relevant molecules. *Photochemistry and Photobiology*, **70** (1999) 391−475.

[48] Bhyrappa P, Suslick KS. Supramolecular Networks of Octahydroxy porphyrins. *Supramolecular Chemistry*, **9** (1998) 169−174.

[49] Yella A, Lee H-W, Tsao HN, Yi C, Chandiran AK, Nazeeruddin MK, Diau EW-V, Yeh CY, Zakeeruddin SM, Grätzel M. Porphyrin-sensitized solar cells with cobalt (II/III)–based redox electrolyte exceed 12 percent efficiency. *Science*, **334** (2011) 629−634.

[50] König K, Schneckenburger H, Rück A, Steiner R. *In vivo* photoproduct formation during PDT with ALA-induced endogenous porphyrins. *Journal of Photochemistry and Photobiology B: Biology*, **18** (1993) 287−290.

[51] Bolanos K, Kogan MJ, Araya E. Capping gold nanoparticles with albumin to improve their biomedical properties. *International Journal of Nanomedicine*, **14** (2019) 6387−6406.

[52] Camundeeswari M, Jeslin J, Verma ML. Nanocarriers for drug delivery applications. *Environmental Chemistry Letters*, **17** (2019) 849−865.

[53] Molupe N, Babu B, Oluwole DO, Prinsloo E, Gai L, Shen Z, Mack J, Nyokong T. The investigation of *in vitro* dark cytotoxicity and photodynamic therapy effect of a 2,6-dibromo-3,5-distyryl BODIPY dye encapsulated in Pluronic® F-127 micelles. *Journal of Coordination Chemistry*, **71** (2018) 3444−34.

[54] Molupe N, Babu B, Oluwole DO, Prinsloo E, Gai L, Shen Z, Mack J, Nyokong T. Photodynamic activity of 2,6-diiodo-3,5-dithienylvinyleneBODIPYs and their folate-functionalized chitosan-coated Pluronic® F-127 micelles on MCF-7 breast cancer cells. *Journal of Porphyrins and Phthalocyanines*, **24** (2020) 973−984.

[55] Sau TK, Murphy CJ. Room temperature, high-yield synthesis of multiple shapes of gold nanoparticles in aqueous solution. *Journal of the American Chemical Society*, **126** (2004) 8648−8649.

[56] Park J-E, Atobe M, Fuchigami T. Synthesis of multiple shapes of gold nanoparticles with controlled sizes in aqueous solution using ultrasound. *Ultrasonics Sonochemistry*, **13** (2006) 237−241.

[57] Grzelczak M, Perez-Juste J, Mulvaney P, Liz-Marzan LM. Shape control in gold nanoparticle synthesis. *Chemical Society Reviews*, **37** (2008) 1783−1791.

[58] Hieda J, Saito N, Takai O. Exotic shapes of gold nanoparticles synthesized using plasma in aqueous solution. *Journal of Vacuum Science & Technology A: Vacuum, Surfaces, and Films*, **26** (2008) 854−856.

[59] Mori T, Hegmann T. Determining the composition of gold nanoparticles: a compilation of shapes, sizes, and calculations using geometric considerations. *Journal of Nanoparticle Research,* **18** (2016) 1−36.

[60] Thakor AS, Jokerst J, Zavaleta C, Massoud TF, Gambhir SS. Gold nanoparticles: a revival in precious metal administration to patients. *Nanotechnology Letters*, **11** (2011) 4029−4036.

[61] Stark WJ, Stoessel PR, Wohlleben W, Hafner A. Industrial applications of nanoparticles. *Chemical Society Reviews*, **44** (2015) 5793−5805.

[62] Eberl C, Saif T. In situ mechanical testing of biological and inorganic materials at the micro-and nanoscales. *Materials Research Society Bulletin*, **35** (2010) 347−353.

[63] Ealias AM, Saravanakumar MP. A review on the classification, characterisation, synthesis of nanoparticles and their application. *Materials Science and Engineering*, **263** (2017) 1−15.

[64] Daniel M-C, Astruc D. Gold nanoparticles: assembly, supramolecular chemistry, quantum-size-related properties, and applications toward biology, catalysis, and nanotechnology. *Chemical Reviews*, **1** (2004) 293−346.

[65] Wangoo N, Bhasin KK, Mehta SK, Suri CR. Synthesis and capping of water-dispersed gold nanoparticles by an amino acid: bioconjugation and binding studies. *Journal of Colloid and Interface Sciences*, **2** (2008) 247−254.

[66] Dykman L, Khlebtsov N. Gold nanoparticles in biomedical applications: recent advances and perspectives. *Chemical Society Reviews*, **6** (2012) 2256−2282.

[67] Eberl C, Saif T. *In situ* mechanical testing of biological and inorganic materials at the micro-and nanoscales, *Materials Research Society Bulletin*, **35** (2010) 347−353.

[68] Chen Y, Gu X, Nie C-G, Jiang Z-Y, Xie Z-X, Lin C-J. Shape controlled growth of gold nanoparticles by a solution synthesis. *Chemical Communications*, **33** (2005) 4181–4183.

[69] Trindade AF, Frade RFM, Maçôas EMS, Graça C, Rodrigues CAB, Martinho JMG, Afonso CAM. “Click and go”: simple and fast folic acid conjugation. *Organic & Biomolecular Chemistry*, **12** (2014) 3181−3190.

[70] Figliola C, Marchal E, Groves BR, Thompson A. A stepwise synthetic approach is necessary to access γ-conjugates of folate: folate-conjugated prodigiosenes. *RSC Advances*, **9** (2019) 14078−14092.

[71] Stella B, Arpicco S, Peracchia MT, Desma D, Hoebeke J, Renoir M, D'Angelo J, Cattel L, Couvreur P. Design of folic acid-conjugated nanoparticles for drug targeting. *Journal of Pharmaceutical Sciences*, **89** (2000) 1452−1464.

[72] Yang S-J, Lin F-H, Tsai K-C, Wei M-F, Tsai H-M, Wong J-M, Shieh M-J. Folic Acid-Conjugated Chitosan Nanoparticles Enhanced Protoporphyrin IX Accumulation in Colorectal Cancer Cells. *Bioconjugate Chemistry,* **21** (2010) 679−68.

[73] Mohapatra S, Mallick SK, Maiti TK, Ghosh SK, Pramanik P. Synthesis of highly stable folic acid conjugated magnetite nanoparticles for targeting cancer cells. *Nanotechnology*, **18** (2007) 385102.

[74] Lee JW, Lu JY, Low PS, Fuchs PL. Synthesis and evaluation of taxol-folic acid conjugates as targeted antineoplastics. *Bioorganic & Medicinal Chemistry*, **10 (**2002) 2397−2414.

[75] Muller C, Schibli R. Folic acid conjugates for nuclear imaging of folate receptor-positive cancer. *Journal of Nuclear Medicine*, **52** (2011) 1−4.

[76] Zhang Z, Jia J, Lai Y, Ma Y, Weng J, Sun L. Conjugating folic acid to gold nanoparticles through glutathione for targeting and detecting cancer cells. *Bioorganic & Medicinal Chemistry*, **18** (2010) 5528−5534.

[77] Huang P, Xu C, Lin J, Wang C, Wang X, Zhang C, Zhou X, Guo S, Cui D. Folic acid-conjugated graphene oxide loaded with photosensitizers for targeting photodynamic therapy. *Theranostics*, **1** (2011) 240−250.

[78] Shawlow AI. Advances in Optical Masers. *Scientific American*, **209** (1963) 34−45.

[79] Hecht J. Short history of Laser development. *Applied Optics*, **49** (2010) 99−122.

[80] Zinth W, Laubereau A, Kaiser, W. The Long Journey to the Laser and its Rapid Development after 1960. *The European Physical Journal H*, **36** (2011) 153−181.

[81] Frenette M, Hatamimoslehabadi M, Bellinger-Buckley S, Laoui S, Bag S, Dantiste O, Rochford J, Yelleswarapu C. Nonlinear optical properties of multipyrrole dyes. *Chemical Physics Letters*, **608** (2014) 303−307.

[82] Juan EP, Barone V, Jackson KA. Site-specific polarizabilities from analytic linear-response theory. *Chemical Physics Letters*, **608** (2014) 24−27.

[83] Zyss J. Molecular Nonlinear Optics: Materials. Physics, and Devices. Academic Press, Cambridge MA, 2013.

[84] Samanta A, Maiti KK, Soh KS, Liao X, Vendrell M, Dinish U, Yun SW, Bhuvaneswari R, Kim H, and Rautela S. Ultrasensitive Near-Infrared Raman Reporters for SERS-Based *In vivo* Cancer Detection. *Angewandte Chemie*, **123** (2011) 6213−6216.

[85] Hussain SA, Dey D, Chakraborty S, Saha J, Roy AD, Chakraborty S, Debnath P, Bhattacharjee D. Fluorescence Resonance Energy Transfer (FRET) sensor. *Science Letters Journal*, **4** (2015) 119.

[86] Baudelet M. Laser Spectroscopy for Sensing: Fundamentals, Techniques and Applications, Elsevier, Amsterdam, 2014.

[87] Ngoy BP, Hlatshwayo Z, Nwaji N, Fomo G, Mack J, Nyokong, T. Photophysical and Optical Limiting Properties at 532 nm of BODIPY Dyes with *p*-Benzyloxystyryl Groups at the 3,5-Positions. *Journal of Porphyrins and Phthalocyanines*, **22** (2018) 413−422.

[88] Harris J. BODIPY Dyes for Singlet Oxygen and Optical Limiting Applications, MSc thesis, Rhodes University, Makhanda, South Africa, 2017.

[89] May AK, Majumdar P, Martynov AG, Lapkina LA, Troyanov SI, Gorbunova YuG, Tsivadze AY, Mack J, Nyokong T. Optical Limiting Properties, Structure and Simplified TD-DFT Calculations of Scandium Tetra-15-Crown-5 Phthalocyaninates. *Journal of Porphyrins and Phthalocyanines*, **24** (2020) 589−601.

[90] Kubheka G, Sanusi K, Mack J, Nyokong T. Optical Limiting Properties of 3,5-DipyrenylvinyleneBODIPY Dyes at 532 nm. *Spectrochimica Acta Part A: Molecular and Biomolecular Spectroscopy*, **191** (2018) 357−364.

[91] Kubheka G, Mack J, Kobayashi N, Kimura M, Nyokong T. Optical Limiting 210 Properties of 2,6-Dibromo-3,5-DistyrylBODIPY Dyes at 532 nm. *Journal of Porphyrins and Phthalocyanines*, **21** (2017) 523−531.

[92] Harris J, May AK, Ngoy BP, Mack J, Nyokong T. An Analysis of the Photophysical and Optical Limiting Properties of a Novel 1,3,5-TristyrylBODIPY Dye. *Journal of Porphyrins and Phthalocyanines*, **23** (2019) 63−75.

[93] Lan Y-Z, Gao Y-E, Kang H-L. A large enhancement of (hyper)polarizabilities of polyyne capped by Cu. *Chemical Physics Letters*, **608** (2014) 308–313.

[94] Sylvain D, Chang H-J, Lopes C, Brännlund C, Le Guennic B, Berginc G, Van Stryland E, Bondar MV, Hagan D, Jacquemin D, Andraud C, Maury O. Benzothiadiazole-Substituted Aza-BODIPY Dyes: Two-Photon Absorption Enhancement for Improved Optical Limiting Performances in the Short-Wave IR Range. *Chemistry − A European Journal*, **27** (2021) 3517−3525.

[95] Goldey MB, Head-Gordon M. Convergence of attenuated second-order Møller–Plesset perturbation theory towards the complete basis set limit. *Chemical Physics Letters*, **608** (2014) 249–254.

[96] Harris J, May AK, Ngoy BP, Mack J, Nyokong T. An Analysis of the Photophysical and Optical Limiting Properties of a Novel 1,3,5-TristyrylBODIPY Dye. *Journal of Porphyrins and Phthalocyanines*, **23** (2019) 63−75.

[97] Ndebele N, Hlatshwayo Z, Ngoy B. P, Kubheka G, Mack J, Nyokong T. Optical limiting properties of BODIPY dyes substituted with styryl or vinylene groups on the nanosecond timescale. *Journal of Porphyrins and Phthalocyanines*, **23** (2019) 701−717.

[98] Babu B, Mack J, Nyokong T. A Sn(IV) porphyrin with mitochondria targeting properties for enhanced photodynamic activity against MCF-7 cells. *New Journal of Chemistry*, **46** (2022) 5288−5295.

[99] Frisch G. W. T. M. J, Schlegel H. B, Scuseria G. E, Robb M. A, Cheeseman J. R, G. S, Barone V, Petersson G. A, Nakatsuji H, X. Li, M. Caricato, A. Marenich, J, B. G. J. Bloino, R. Gomperts, B. Mennucci, H. P. Hratchian, J. V. Ortiz, A. F. Izmaylov, J. L, D. W-Y. Sonnenberg, F. Ding, F. Lipparini, F. Egidi, J. Goings, B. Peng, A. Petrone, T, D. R. Henderson, V. G. Zakrzewski, J. Gao, N. Rega, G. Zheng, W. Liang, M. Hada, M. Ehara, K, R. F. Toyota, J. Hasegawa, M. Ishida, T. Nakajima, Y. Honda, O. Kitao, H. Nakai, T. Vreven, K, J. A. M. Throssell, Jr, J. E. Peralta, F. Ogliaro, M. Bearpark, J. J. Heyd, E. Brothers, K. N. Kudin,, T. K. V. N. Staroverov, R. Kobayashi, J. Normand, K. Raghavachari, A. Rendell, J. C. Burant, S. S, J. T. Iyengar, M. Cossi, J. M. Millam, M. Klene, C. Adamo, R. Cammi, J. W. Ochterski, R. L. Martin, O. F. K. Morokuma, J. B. Foresman, and D. J. Fox, Gausian 09, Revision 01, Gaussian, Inc., Wallingford CT, 2013.

[100] Kobayashi R, Amos RD. The application of CAM-B3LYP to the charge-transfer band problem of the zinc bacteriochlorin-bacteriochlorin complex. *Chemical Physics Letters*, **420** (2006), 106−109.

[101] Obłoza M, Łapok Ł, Pędziński T, Stadnicka K. M, Nowakowska M. Synthesis, Photophysics and Redox Properties of AzaBODIPY Dyes with Electron-Donating Groups. *ChemPhysChem*, **20** (2019) 2482−2497.

[102] Gut A, Łapok Ł, Jamróz D, Gorski A, Solarskib J, Nowakowska M. Photophysics and redox properties of aza-BODIPY dyes with electron-withdrawing groups. *New Journal of Chemistry*, **41** (2017) 12110−12122.

[103] Yeh Y-C, Creran B, Rotello VM. Gold Nanoparticles: Preparation, Properties, and Applications in Bionanotechnology. *Nanoscale*, **4** (2012) 1871−1880.

[104] Yazdani S, Daneshkhah A, Diwate A, Patel A, Smith J, Reul O, Cheng R, Izadian A, Hajrasouliha AR. Model for Gold Nanoparticle Synthesis: Effect of pH and Reaction Time. *ACS Omega*, **6** (2021) 16847−16853.

[105] Kotiaho A, Lahtinen R, Efimov A, Metsberg HK, Sariola E, LehtivuorI H, Tkachenko NV, Lemmetyinen H. Photoinduced charge and energy transfer in phthalocyanine-functionalized gold nanoparticles. *Journal of Physical Chemistry C*, **114** (2010) 162−168.

[106] Brückner C, Foss PCD, Sullivan JO, Pelto R, Zeller M, Birge RR, Crundwell G. Origin of the bathochromically shifted optical spectra of *meso*-tetrathien-2′- and 3′-ylporphyrins as compared to *meso*-tetraphenylporphyrin. *Physical Chemistry Chemical Physics*, **8** (2006) 2402−2412.

[107] Dennis PA. Aromatic ring currents illustrated-NMR spectra of tin(IV) porphyrin complexes: An advanced undergraduate experiment. *Journal of Chemical Education*, **65** (1988) 1111−1112.

[108] Ravindra KP, Norman F-YS, Smith W, Dougherty TJ, Smith KM. Syntheses of water-soluble cationic porphyrins and chlorins. *Tetrahedron*, **48** (1992) 7591−7600.

[109] Kaila BH, Hoff DJ, Lahren TJ, Mount DR, Squillace AJ, Burkhard LP. Estimating *n*-octanol-water partition coefficients for neutral highly hydrophobic chemicals using measured *n*-butanol-water partition coefficients. *Chemosphere*, **218** (2019) 616−623.

[110] Hodges G, Eadsforth C, Bossuyt B, Bouvy A, Enrici M-H, Geurts M, Kotthoff M, Michie E, Miller D, Müller J, Oetter G, Roberts J, Schowanek D, Sun P, Venzmer J. A comparison of log K_{ow} (n-octanol-water partition coefficient) values for non-ionic, anionic, cationic and amphoteric surfactants determined using predictions and experimental methods. *Environmental Sciences Europe*, **31** (2019) 1.

[111] Sadek P. *Solvent Miscibility and Viscosity Chart adapted from The HPLC Solvent Guide*. Wiley-Interscience, Accessed: March 1, 2022. Available: [chrome-extension://efaidnbmnnnibpcajpcglclefindmkaj/https://www.organometallics.it/wp-content/uploads/2022/01/Solvent-Miscibility-and-Polarity-Chart.pdf].

[112] Calloway D. Beer-Lambert Law. *Journal of Chemical Education*, **74** (1997) 744.

[113] Jiang XD, Li S, Guennic BL, Jacquemin D, Escudero D, Xiao L. Singlet oxygen generation properties of isometrically dibromated thienyl-containing aza-BODIPYs. *Journal of Physical Chemistry and Chemical Physics*, **18** (2016) 32686−32690.

[114] Antina EV, Bumagina NA. Tetraaryl-substituted aza-BODIPY: synthesis, spectral properties, and possible applications (microreview). *Chemistry of Heterocyclic Compounds*, **53** (2017) 39–41.

[115] Shaikha S, Neyadi A, Alzamly A, Al-Hemyari A, Tahir AM, Al-Meqbali S, Ahmad MAA, Bufaroosha M. An Undergraduate Experiment Using Microwave-Assisted Synthesis of Metalloporphyrins: Characterization and Spectroscopic Investigations. *World Journal of Chemical Education*, **7** (2019) 26−32.

[116] Arnold DP, Blok J. The coordination chemistry of tin porphyrin complexes. *Coordination Chemistry Reviews*, **248** (2004) 299−319.

[117] Dechan P, Bajju GD, Sood P, Dar UA. Crystallographic elucidations of indium (III) porphyrin conformations, morphology and aggregation behaviour: Comparative optical study of free base porphyrins and their indium(III) derivatives at varying pH. *Journal of Molecular Structure*, **1183** (2019) 87−99.

[118] Manaspon C, Viravaidya-Pasuwat K, Pimpha N. Preparation of folate-conjugated pluronic F127/chitosan core-shell nanoparticles encapsulating doxorubicin for breast cancer treatment. *Journal of Nanomaterials*, **2012** (2012) 593878.

[119] Basak R, Bandyopadhyay R. Encapsulation of hydrophobic drugs in Pluronic F-127 micelles: effects of drug hydrophobicity, solution temperature, and pH. *Langmuir*, **29** (2013) 4350−4356.

[120] Park H, Na K. Conjugation of the photosensitizer Chlorin e6 to pluronic F-127 for enhanced cellular internalization for photodynamic therapy. *Biomaterials*, **34** (2013) 6992−7000.

[121] Alexander-Bryant AA, Vanden Berg-Foels WS, Wen X. Chapter One - Bioengineering Strategies for Designing Targeted Cancer Therapies. *Advances in Cancer Research*, **118** (2013) 1−59.

[122] Cagel M, Tesan FC, Bernabeu E, Salgueiro M. J, Zubillaga MB, Moretton MA, Chiappetta DA. Polymeric mixed micelles as nanomedicines: Achievements and perspectives. *European Journal of Pharmaceutics and Biopharmaceutics*, **113** (2017) 211−228.

[123] Attia ABE, Ong ZY, Hedrick JL, Lee PP, Ee PLR, Hammond PT, Yang Y-Y. Mixed micelles self-assembled from block copolymers for drug delivery. *Current Opinion in Colloid & Interface Science*, **16** (2011) 182−194.

[124] Rathman JF, Scamehorn JF. Counterion binding on mixed micelles. *Journal of Physical Chemistry*, **88** (1984) 5807−5816.

[125] Haque ME, Das AR, Rakshit AK, Moulik SP. Properties of Mixed Micelles of Binary Surfactant Combinations. *Langmuir*, **12** (1996) 4084−4089.

[126] Manaspon C, Viravaidya-Pasuwat K, Pimpha N. Preparation of folate-conjugated pluronic F127/chitosan core-shell nanoparticles encapsulating doxorubicin for breast cancer treatment. *Journal of Nanomaterials*, **2012** (2012) 22.

[127] Managa M, Britton J, M/zhaya EK, Nyokong T. Photophysical properties of GaC1 5,10,15,20-tetra(1-pyrenyl)porphyrinato incorporated into Pluronic F127 micelle. *Journal of Luminescence*, **185** (2017) 34−41.

[128] Stella B, Arpicco S, Peracchia M. T, Desmaële D, Hoebeke J, Renoir M, D'Angelo J. Cattel L, Couvreur P. Design of Folic Acid-Conjugated

Nanoparticles for Drug Targeting. *Journal of Pharmaceutical Sciences*, **89** (2000) 1452−1464.

[129] Bonechi C, Donati A, Lampariello R, Martini S, Picchi M. P, Ricci M, Rossi C. Solution structure of folic acid: Molecular mechanics and NMR investigation. *Spectrochimica Acta Part A: Molecular and Biomolecular Spectroscopy*, **60** (2004) 1411−1419.

[130] Bagus PS, Ilton ES, Nelin CJ. The interpretation of XPS spectra: Insights into materials properties. *Surface Science Reports*, **68** (2013) 273−304.

[131] Geszke M, Murias M, Balan M, Medjahdi G, Korczynski J, Moritz M, Lulek J, Schneider R. Folic acid-conjugated core/shell ZnS:Mn/ZnS quantum dots as targeted probes for two photon fluorescence imaging of cancer cells. *Acta Biomaterialia*, **7** (2011) 1327−1338.

[132] Magaela B, Matshitse R, Babu B, Managa M, Prinsloo E, Nyokong T. Sn(IV) porphyrin-biotin decorated nitrogen doped graphene quantum dots nanohybrids for photodynamic therapy. *Polyhedron*, **213** (2022) 115624.

[133] Egan WJ, Merz KM, Baldwin JJ. Prediction of Drug Absorption Using Multivariate Statistics. *Journal of Medicinal Chemistry*, **43** (2000) 3867−3877.

[134] Dobson PD, Kell DB. Carrier-mediated cellular uptake of pharmaceutical drugs: an exception or the rule? *Nature Reviews Drug Discovery*, **7** (2008) 205−220.

[135] Dubazana, N. Azadipyrromethenes for applications in photodynamic antimicrobial chemotherapy, photodynamic therapy and optical limiting. MSc thesis, Rhodes University, Grahamstown, South Africa, 2020.

[136] Babu, B, Mack, J, Nyokong, T. Sn(IV)-porphyrinoids for photodynamic anticancer and antimicrobial chemotherapy. *Dalton Transactions*, **52** (2023) 5000–5018.

[137] Frimannsson, DO, Grossi, M, Murtagh J, Paradisi F, O'Shea DF. Light Induced Antimicrobial Properties of a Brominated Boron Difluoride (BF_2) Chelated Tetraarylazadipyrromethene Photosensitizer. *Journal of Medicinal Chemistry*, **53** (2010) 73385−7343.

[138] Andijani N, Wazzan NA. The effect of electron-donating substituents on tuning the nonlinear optical properties of pyrene-core arylamine derivatives: DFT calculations. *Results in Physics*, **11** (2018) 605−616.

[139] Khalid M, Hussain R, Hussain A, Ali B, Jaleel F, Imran M, Assiri MA, Khan MU, Ahmed S, Abid S, Haq S, Saleem K, Majeed S, Tariq CJ. Electron Donor and Acceptor Influence on the Nonlinear Optical Response of Diacetylene-Functionalized Organic Materials (DFOMs): Density Functional Theory Calculations. *Molecules*, **11** (2019) 2096.

[140] Marcano E, Squitieri E, Murgich J, Soscún H. Theoretical investigation of the static (dynamic) polarizability and second hyperpolarizability of DAAD quadrupolar push-pull molecules. A comparison among HF (TD-HF), DFT (TD-B3LYP), and MP2 (TD-MP2) methods. *Computational and Theoretical Chemistry*, **985** (2012) 72−79.

[141] Muhammad S, Al-Sehemi AG, Irfan A, Chaudhry AR, Gharni H, Alfaify S, Shkir M, Asiri AM. The impact of position and number of methoxy group(s) to tune the nonlinear optical properties of chalcone derivatives: a dual substitution strategy. *Journal of Molecular Modeling*, **22** (2016) 73.

[142] Xiaoting L, Ji-Long Z, Kai L, Xiaobo S, Zhijian W, Ai-Min R, Jikang F. New insights into two-photon absorption properties of functionalized aza-BODIPY dyes at telecommunication wavelengths: A theoretical study. *Physical Chemistry Chemical Physics*, **15** (2013) 4666−76.

[143] Harris J, Gai L, Kubheka G, Mack J, Nyokong T, Shen Z. Optical Limiting Properties of 3,5-Dithienylenevinylene BODIPY Dyes at 532 nm. *Chemistry − A European Journal*, **58** (2017) 14507−14514.

[144] Kubheka G, Mack J, Kobayashi N, Kimura M, Nyokong T. Optical limiting properties of 2,6-dibromo-3,5-distyrylBODIPY dyes at 532 nm. *Journal of Porphyrins and Phthalocyanines*, **21** (2017) 523−531.

[145] Sheik-Bahae M, Said AA, Wei T-H, Hagan DJ, Van Stryland EW. Sensitive measurement of optical nonlinearities using a single beam. *IEEE Journal of Quantum Electronics*, **26** (1990) 760−769.

[146] Pramodini S, Poornesh P, Sudhakar YN, Selva K. $\chi^{(3)}$ and optical power limiting measurements of Polyaniline and its derivative Poly(*o*-toluidine) under CW regime. *Optics Communications*, **293** (2013) 125−132.

[147] Mário JFC, Guo Y, Hanack M. Porphyrins and phthalocyanines as materials for optical limiting. *Synthetic Metals*, **141** (2004) 231−243.

[148] Shinkawa K, Ogusu K. Pulse-width dependence of optical nonlinearities in As_2Se_3 chalcogenide glass in the picosecond-to-nanosecond region. *Optics Express*, **16** (2008) 18231.

[149] Fahleson T. Derivation and application of response functions for nonlinear absorption and dichroisms. Division of Theoretical Chemistry & Biology School

of Engineering Sciences in Chemistry, Biotechnology and Health KTH Royal Institute of Technology Stockholm, Sweden, 2018.

[150] Salam A. On the manifestation of Casimir effects in intermolecular interactions *via* the method of induced moments. *Journal of Physics: Conference Series*, **161** (2009) 012040.

[151] Badran HA, Al-Hazam HA, Alfahed RKF, Ajeel KI. Second-order hyperpolarizability and nonlinear optical properties of novel organic compound-doped poly (*o*-methoxyaniline) polymer film. *Journal of Materials Science: Materials in Electronics*, **32** (2021) 14623−14641.

[152] Vladimir L, Sworin M, Richard K, Geurtsen G, Mordechai R. Nonlinear bleaching, absorption, and scattering of 532-nm-irradiated plasmonic nanoparticles. *Journal of Applied Physics*, **113** (2013) 053107-1.

[153] Stephen M, Lee T, Marvin K, George V. Optical Limiting with Reverse Saturable Absorbers. *The International Society for Optical Engineering*, **1307** (1990) 304−314.

[154] Xu W, Wang W, Li J, Wu Q, Zhao Y, Hou H, Song Y. Two-photon absorption property and excellent33 optical limiting response of three Schiff base derivatives with large conjugated system. *Dyes and Pigments*, **160** (2019) 1−8.

[155] Wu J-J, Tao Y-R, Wang J-N, Wu Z-Y, Fan L, Wu X-C. Reverse saturable absorption and nonlinear refraction of ultrathin ZrS_3 nanobelts. *Nanoscale*, **18** (2016) 10371−10379.

[156] Kubheka GP. BODIPY dyes for use in nonlinear optics and optical sensing. PhD thesis, Rhodes University, Makhanda, South Africa, 2020.

[157] Hanack M, Schneider T, Barthel M, Shirk JS, Flom SR, Pong RG. Indium phthalocyanines and naphthalocyanines for optical limiting. *Coordination Chemistry Reviews*, **219** (2001) 235−258.

[158] Saleh BE, Teich MC. *Fundamentals of Photonics.* John Wiley & Sons, New Jersey, 2019.

[159] He GS, Weder C, Smith P, Prasad PN. Optical power limiting and stabilization based on a novel polymer compound. *Quantum Electron*, **34** (1998) 2279−2285.

[160] Guo S-L, Xu L, Wang H-T, You X-Z, Ming N. Investigation of optical nonlinearities in $Pd(po)_2$ by Z-scan technique. *Optik*, **114** (2003) 58−62.

[161] De La Torre G, Vazquez P, Agullo-Lopez F, Torres T. Role of Structural Factors in the Nonlinear Optical Properties of Phthalocyanines and Related Compounds. *Chemical Reviews*, **104** (2004) 3723−3750.

[162] Eaton DF. Nonlinear Optical Materials. *Science,* **253** (1991) 281–287.

[163] Virgili T, Ganzer L, Botta C, Squeo BM, Pasini M. Asymmetric Aza-BODIPY with Optical Gain in the Near-Infrared Region. *Molecules*, **27** (2022) 4538.

[164] Matthes R, Cain CP, Courant D, Freund DA, Grossman BA, Kennedy PA, Lund DJ, Mainster MA, Manenkov AA, Marshall WJ. Revision of guidelines on limits of exposure to laser radiation of wavelengths between 400 nm and 1.4 μm. *Health Physics*, **79** (2000) 431−440.

[165] Sadikogullari BC, Koramaz I, Sütay B, Karagoz B, Özdemi AD. Application of aza-BODIPY as a Nitroaromatic Sensor. *ACS Omega*, **8** (2023) 25254−25261.

[166] Farfán-Paredes M, González-Antonio O, Tahuilan-Anguiano DE, Peón J, Ariza A, Lacroix PG, Santillan R, Farfán N. Physicochemical and computational insight of ^{19}F NMR and emission properties of *meso*-(*o*-aryl)-BODIPYs. *New Journal of Chemistry*, **44** (2020) 19459−19471.

[167] Cariati E, Pizzotti M, Roberto D, Tessore F, Ugo R. Coordination and organometallic compounds and inorganic–organic hybrid crystalline materials for second-order non-linear optics. *Coordination Chemistry Reviews*, **205** (2006) 1210–1233.

[168] Di Bella S, Dragonetti C, Pizzotti M, Roberto D, Tessore F, Ugo R. Coordination and organometallic complexes as second-order nonlinear optical materials. *In Molecular Organometallic Material for Optics*; Bozec, H., Guerchais, V., Eds.; Springer: Heidelberg, Germany, 2010; pp. 1–55.

[169] Suslick KS, Chen CT, Meredith GR, Cheng LT. Push-pull porphyrins as nonlinear optical materials. *Journal of the American Chemical Society*, **114** (1992) 6928–6930.

[170] Pizzotti M, Ugo R, Annoni E, Quici S, Ledoux-Rak I, Zerbi G, Del Zoppo M, Fantucci P, Invernizzi I. A critical evaluation of EFISH and THG non-linear optical responses of asymmetrically substituted *meso*-tetraphenyl porphyrins and their metal complexes*. Inorganica Chimica Acta*, **340** (2002) 70–80.

[171] LeCours SM, Guan HW, Di Magno SG, Wang CH, Therien MJ. Push-pull Arylethynyl Porphyrins: New Chromophores That Exhibit Large Molecular First-Order Hyperpolarizabilities. *Journal of the American Chemical Society*, **118** (1996) 1497–1503.

[172] Pizzotti M, Annoni E, Ugo R, Bruni S, Quici S, Fantucci P, Zerbi G, Del Zoppo M. A multitechnique investigation of the second order NLO response of a 10,20-diphenylporphyrinato nickel(II) complex carrying a phenylethynyl based push-pull system in the 5- and 15- positions. *Journal of Porphyrins and Phthalocyanines*, **8** (2004) 1311–1324.

[173] Annoni E, Pizzotti M, Ugo R, Quici S, Morotti T, Bruschi M, Mussini P. Synthesis, Electronic Characterization and Significant Second Order Non Linear Optical Responses of meso Tetraphenylporphyrins and their Zn(II) Complexes Carrying a Push or Pull Group in β Pyrrolic Position. *European Journal of Inorganic Chemistry*, **2005** (2005) 3857–3874.

[174] Tessore F, Biroli AO, Di Carlo G, Pizzotti M. Porphyrins for Second Order Nonlinear Optics (NLO): An Intriguing History. *Inorganics* **6** (2018) 81.

[175] Zhang A, Kwan L, Stillman MJ. The spectroscopic impact of interactions with the four Gouterman orbitals from peripheral decoration of porphyrins with simple electron withdrawing and donating groups. *Organic Biomolecular Chemistry*, **15** (2017) 9081–9094.

[176] Shamova LI, Zatsikha YV, Nemykin VN. Synthetic pathways for the preparation of the BODIPY analogues: azaBODIPYs, BOPHYs and some other pyrrole-based acyclic chromophores. *Dalton Transactions*, **50** (2020) 1–43.

[177] Majumdar P, Mack J, Nyokong T. Synthesis, characterization and photophysical properties of an acenaphthalene fused-ring expanded NIR absorbing aza-BODIPY dye. *Royal Society of Chemistry Advances*, **5** (2015) 78253–78258.

[178] Khan TK, Sheokand P, Agarwal N. Synthesis and Studies of Aza-BODIPY-Based π-Conjugates for Organic Electronic Applications. *European Journal of Organic Chemistry*, **2014** (2014) 1416–1422.

[179] Lu H, Mack J, Yang Y, Shen Z. Structural modification strategies for the rational design of red/NIR region BODIPYs. *Chemical Society Reviews*, **43** (2014) 4778–4823.

[180] Oliden-Sánchez A, Sola-Llano R, Bañuelos J, García-Moreno I, Uriel C, López JC, Gómez AM. Tuning the Photonic Behavior of Symmetrical Bis-BODIPY Architectures: The Key Role of the Spacer Moiety*. Frontier Chemistry*, **7** (2019) 1–18.

[181] Alkorta I, Legon A. Nucleophilicity of the boron atom in compounds R–B, (R = F, Cl, Br, I, CN, NC, CH_3, SiH_3, CF_3, H): a new look at the inductive effects of the group R. *Physical Chemistry Chemical Physics*, **24** (2022) 12804–12807.